I. The Superstition Hills, California, Earthquakes of 24 November 1987

II. Three-Dimensional Velocity Structure of Southern California

Thesis by

Harold William Magistrale

In Partial Fulfillment of the Requirements

for the Degree of

Doctor of Philosophy

California Institute of Technology

Pasadena, California

1990

(Submitted February 13, 1990)

Acknowledgements

I thank all the staff, faculty, and students of the division for making my time spent at Caltech pleasant. Hiroo Kanamori was my research advisor; I was fortunate to have been able to work with him. Particular thanks go to my research collaborators and co-authors: Chris Sanders, Lucy Jones, Pat Williams, Lorraine Hwang, and Hiroo Kanamori.

Most of this thesis is based on data collected on the southern California seismic array, so special thanks go to the array staff. Lucy Jones and Doug Given patiently answered questions about the array operations.

The work in chapters 7, 8, and 9 used codes written by Steve Roecker. Craig Jones provided the codes, answered many questions about using them, and contributed thoughtfully to many discussions. Rob Clayton installed the array data on the Sun and provided a fast sorting routine used in chapter 9. Leslie Sonder compiled some of the phase data used in chapter 8.

Cathy Smither dutifully reviewed chapters 1, 7, 8, and 9. Clarence Allen reviewed chapter 2. Dave Wald reviewed chapter 6. Craig Jones thoroughly reviewed chapters 7, 8, and 9.

The work in this thesis was supported by the U.S. Geological Survey under contract 14-08-001-G1354. Some funds for the study in chapter 5 were provided by the California Institute of Technology Earthquake Research Affiliates.

Abstract

Part 1 of this thesis is about the 24 November, 1987, Superstition Hills earthquakes. The Superstition Hills earthquakes occurred in the western Imperial Valley in southern California. The earthquakes took place on a conjugate fault system consisting of the northwest-striking right-lateral Superstition Hills fault and a previously unknown Elmore Ranch fault, a northeast-striking left-lateral structure defined by surface rupture and a lineation of hypocenters. The earthquake sequence consisted of foreshocks, the M_S 6.2 first main shock, and aftershocks on the Elmore Ranch fault followed by the M_S 6.6 second main shock and aftershocks on the Superstition Hills fault. There was dramatic surface rupture along the Superstition Hills fault in three segments: the northern segment, the southern segment, and the Wienert fault.

In Chapter 2, $M_L \geq 4.0$ earthquakes from 1945 to 1971 that have Caltech catalog locations near the 1987 sequence are relocated. It is found that none of the relocated earthquakes occur on the southern segment of the Superstition Hills fault and many occur at the intersection of the Superstition Hills and Elmore Ranch faults. Also, some other northeast-striking faults may have been active during that time.

Chapter 3 discusses the Superstition Hills earthquake sequence using data from the Caltech-U.S.G.S. southern California seismic array. The earthquakes are relocated and their distribution correlated to the type and arrangement of the basement rocks. The larger earthquakes occur only where continental crystalline basement rocks are present. The northern segment of the Superstition Hills fault has more aftershocks than the southern segment.

An inversion of long period teleseismic data of the second mainshock of the 1987 sequence, along the Superstition Hills fault, is done in Chapter 4. Most of the long period seismic energy seen teleseismically is radiated from the southern segment of the Superstition Hills fault. The fault dip is near vertical along the northern segment of the fault and steeply southwest dipping along the southern segment of the fault.

Chapter 5 is a field study of slip and afterslip measurements made along the Superstition Hills fault following the second mainshock. Slip and afterslip measurements were started only two hours after the earthquake. In some locations, afterslip more than doubled the coseismic slip. The northern and southern segments of the Superstition Hills fault differ in the proportion of coseismic and postseismic slip to the total slip.

The northern segment of the Superstition Hills fault had more aftershocks, more historic earthquakes, released less teleseismic energy, and had a smaller proportion of afterslip to total slip than the southern segment. The boundary between the two segments lies at a step in the basement that separates a deeper metasedimentary basement to the south from a shallower crystalline basement to the north.

Part 2 of the thesis deals with the three-dimensional velocity structure of southern California. In Chapter 7, an *a priori* three-dimensional crustal velocity model is constructed by partitioning southern California into geologic provinces, with each province having a consistent one-dimensional velocity structure. The one-dimensional velocity structures of each region were then assembled into a three-dimensional model. The three-dimension model was calibrated by forward modeling of explosion travel times.

In Chapter 8, the three-dimensional velocity model is used to locate earthquakes. For about 1000 earthquakes relocated in the Los Angeles basin, the three-dimensional model has a variance of the the travel time residuals 47 per cent less than the catalog locations found using a standard one-dimensional velocity model. Other than the 1987 Whittier earthquake sequence, little correspondence is seen between these earthquake locations and elements of a recent structural cross section of the Los Angeles basin. The Whittier sequence involved rupture of a north dipping thrust fault bounded on at least one side by a strike-slip fault. The 1988 Pasadena earthquake was deep left-lateral event on the Raymond fault. The 1989 Montebello earthquake was a thrust event on a structure similar to that on which the Whittier earthquake occurred. The 1989 Malibu earthquake was a thrust or oblique slip event adjacent to the 1979 Malibu earthquake.

At least two of the largest recent thrust earthquakes (San Fernando and Whittier) in the Los Angeles basin have had the extent of their thrust plane ruptures limited by strike-slip faults. This suggests that the buried thrust faults underlying the Los Angeles basin are segmented by strike-slip faults.

Earthquake and explosion travel times are inverted for the three-dimensional velocity structure of southern California in Chapter 9. The inversion reduced the variance of the travel time residuals by 47 per cent compared to the starting model, a reparameterized version of the forward model of Chapter 7. The Los Angeles basin is well resolved, with seismically slow sediments atop a crust of granitic velocities. Moho depth is between 26 and 32 km.

Table of Contents

Chapter 1

Introduction to the Superstition Hills, California, Earthquakes of 24 November, 1987

1.1 Introduction

The 24 November, 1987, Superstition Hills earthquakes occurred in the western Imperial Valley in southern California (Figure 1.1). The earthquakes took place on a conjugate fault system consisting of the northwest-striking right-lateral Superstition Hills fault and a previously unknown northeast-striking left-lateral structure defined by surface rupture and a lineation of hypocenters. The earthquake sequence consisted of foreshocks, the M_S 6.2 first main shock, and aftershocks on the northeast structure followed by the M_S 6.6 second main shock and aftershocks on the Superstition Hills fault.

The following chapters present the results of relocations of older, sparsely recorded earthquakes in the western Imperial Valley, locations and analysis of the 1987 earthquake sequence using the local array data, an inversion of teleseismic records of the mainshock on the Superstition Hills fault, and a field study of surface slip and afterslip along the Superstition Hills fault.

1.2 Tectonic Setting and Recent Seismicity

The 1987 earthquake sequence occurred in the western Imperial Valley, where the San Jacinto fault zone enters the Salton trough. The Salton trough is the sediment filled landward extension of the actively spreading Gulf of California (Figure 1.1, inset). Much of the Salton trough is below sea level but is separated from the gulf by the delta of the Colorado River. The

sediments in the trough are up to 6 km thick (Biehler *et al.*, 1964, Fuis *et al.*, 1982). Sea floor magnetic anomalies at the mouth of the Gulf of California show that the southern gulf opened 4 million years ago, yet sedimentary sequences in the gulf, and a dated volcanic unit in the Imperial Valley, require a Miocene age proto-gulf (Larson *et al.*, 1968, Moore and Buffington, 1968, Woodard, 1974). This indicates a long period of possibly sporadic crustal extension in the Salton trough. The Salton trough has been tectonically active throughout its sedimentary history as evidenced by unconformities, deformation, erosion, and redeposition in the sedimentary sequence of the Imperial Valley (Dibblee, 1954, Sharp, 1982).

Fuis *et al.* (1982) performed a large seismic refraction study in the Imperial Valley region. They combined seismic refraction, gravity measurements, and well data to define two types of basement rocks. The first type is metamorphosed sedimentary rocks that lie under the central Imperial Valley from about five to thirteen kilometers depth under the southern Salton Sea. Fuis *et al.* (1982), based on temperatures measured in drill holes at four km depth by Muffler and White (1969) and extrapolated to five km depth, suggest the metasediments have been altered to greenschist facies. The valley sediment fill and metasedimentary basement are characterized by a smooth increase of seismic velocity with depth (Fuis *et al.*, 1982), with a seismic velocity of 5.65 km/s at the top of the metasediments. The second type of basement rock, under the flanks of the Imperial Valley, are the pre-rifting continental crystalline plutonic and metamorphic rocks. Seismic velocity profiles near the Superstition Hills fault show an abrupt increase of seismic velocity, to about 5.9 km/s, at depths between 1 and 3 km. Kohler and Fuis (1986) interpreted the 5.9 km/s horizon as the top of continental crystalline

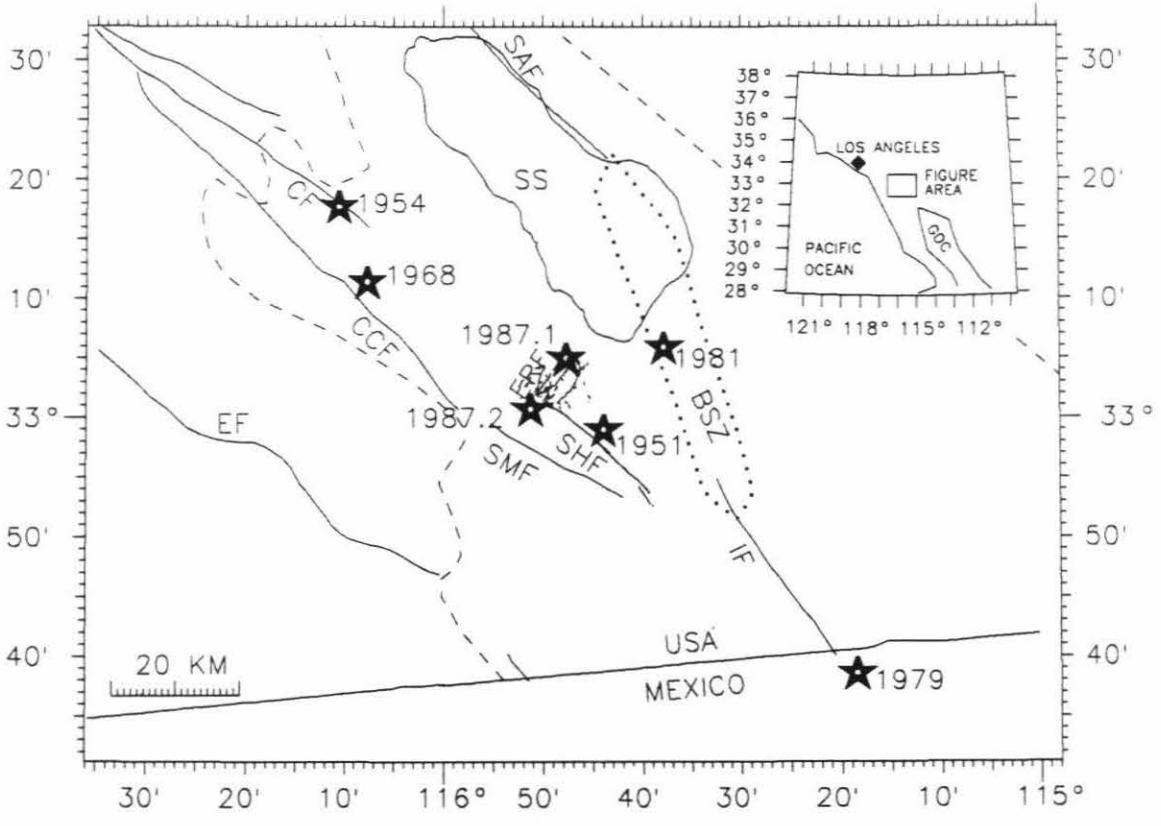

Figure 1.1. Reference map of the study area showing major faults and other features. Stars indicate earthquakes mentioned in text, labeled with year of occurrence. 1987.1 and 1987.2 indicate the first and second mainshocks, respectively, of the 24 November, 1987, sequence. Dashed lines indicate boundaries of the Salton trough. Area within dotted lines is the Brawley seismic zone. Abbreviations: SS, Salton Sea, SAF, San Andreas fault, CF, Clark fault, CCF, Coyote Creek fault, EF, Elsinore fault, SHF, Superstition Hills fault, SMF, Superstition Mountain fault, ERF, Elmore Ranch fault, IF, Imperial fault, BSZ, Brawley seismic zone, GOC, Gulf of California (in inset).

basement, indicating that continental crystalline basement is present beneath relatively thin sedimentary cover along the western border of the Salton trough. In this area the continental basement rocks are Cretaceous granitics of the southern California batholith, as are exposed in the Peninsular Ranges. Fuis *et al.* (1982) suggested that continental basement is absent within the central Salton trough. A steep basement gradient under the Superstition Hills fault separates the two basement types (Fuis *et al.*, 1982). Basement surfaces in the vicinity of the Superstition Hills fault, at depths of about 1.5, 2.5 and 4.5 km (Kohler and Fuis, 1986), are interpreted by Fuis *et al.* (1982) to represent down-faulted basement blocks, or terraces, at the western edge of the Salton trough. Some basement blocks, such as Superstition Mountain, rise above the sedimentary cover (Figure 3.14). The distribution of the continental crystalline basement rocks is shown in Figure 3.14. Note the complex distribution of those basement rocks in the vicinity of the Superstition Hills fault. The depth to the metasedimentary basement near the Superstition Hills fault is shown in Figure 5.1.

The northwest-striking San Jacinto fault zone enters the west margin of the Salton trough in two branches, the Clark fault and the Coyote Creek fault (Figure 1.1). The total offset of 24 km on the San Jacinto fault zone (Sharp, 1967) has produced an irregular western margin of the Salton trough. Both the Superstition Hills fault and the Superstition Mountain fault are members of the San Jacinto fault zone (Sharp, 1972). The strands of the San Jacinto fault zone are well defined by microseismicity trends (Figure 3.3). The Superstition Mountain fault probably connects to the Coyote Creek fault (Sharp and Clark, 1972). The relation of the Superstition Hills fault to the rest of the San Jacinto fault zone is uncertain. The Clark fault has no surface

expression east of 116° (Sharp, 1982) and there is no microseismicity trend linking the Clark fault to the Superstition Hills fault (Figure 3.3). The course of the San Jacinto fault zone southeast of the Superstition Hills and Superstition Mountain faults is also uncertain, but it probably joins the Imperial fault in some way (Sharp, 1967).

The San Andreas fault defines the northeast margin of the Salton trough. The Elsinore fault borders the southwest margin of the trough. These faults, and the San Jacinto fault zone, are elements of the San Andreas transform system that accommodates the Gulf of California sea floor spreading into right-lateral strike slip faulting in southern California (Elders *et al.*, 1972). The surface rupture and focal mechanisms of the 1987 earthquakes along the Superstition Hills fault were right-lateral, consistent with the overall transform system.

The Superstition Hills fault displayed minor surface rupture from a M_L 5.6 earthquake in 1951 (Allen *et al.*, 1965) (but see Chapter 2), and minor cracking in 1965 and 1969 (Allen *et al.*, 1972). Right-lateral triggered slip occurred following the 1968 M_L 6.5 Borrego Mountain earthquake on the Coyote Creek fault (Allen *et al.*, 1972), the 1979 M_L 6.6 Imperial Valley earthquake on the Imperial fault (Fuis, 1982), and the 1981 M_L 5.6 Westmorland earthquake on another northeast-trending seismic lineation (Sharp *et al.*, 1986). These earthquakes, and the 1954 M_L 6.2 Arroyo Salada earthquake on the Clark fault (Sanders *et al.*, 1986), were the largest recent earthquakes in this area (Figure 1.1).

The first main shock of the November 1987 sequence broke a previously unknown northeast-striking structure defined by left-lateral surface rupture and a lineation of hypocenters. The hypocenter lineation extends from the

north end of the Superstition Hills fault to the Brawley seismic zone (Figure 3.4). The surface rupture occurred in many northeast-trending strands (Sharp *et al.*, 1989, Hudnut *et al.*, 1989) in an area east of the northern 5 km of the Superstition Hills fault (Figure 1.2). One major strand, at the north end of the area, is the Elmore Ranch fault. The surface rupture extends 8.5 km northeast from the Superstition Hills fault, much less than the 28 km long hypocenter lineation. Here the entire hypocenter lineation will be referred to as the Elmore Ranch fault.

The Elmore Ranch fault is the third northeast-trending structure in the Imperial Valley to be defined by seismic activity during the last ten years. A large (M_L 5.8) aftershock of the 1979 Imperial Valley earthquake occurred in the southern Brawley seismic zone. Further aftershocks defined a northeast, left-lateral hypocenter lineation that was confined to the Brawley seismic zone (Johnson and Hutton, 1982). The 1981 M_L 5.6 Westmorland earthquake in the northern Brawley seismic zone was followed by aftershocks that defined a crooked lineation that reached to the Superstition Hills fault (Hutton and Johnson, 1981).

The second main shock of the November 1987 sequence produced right-lateral surface rupture along the Superstition Hills fault on three segments separated by right steps. The segments are named the northern Superstition Hills fault (14.9 km long), the southern Superstition Hills fault (12.1 km long), and the Wienert fault (4 km long) (Figure 1.2) (Sharp *et al.*, 1989). The extent of the surface rupture is coincident with that of the 1968 and 1979 triggered slip along the northern and southern segments of the Superstition Hills fault. No triggered slip has been recorded on the Wienert fault.

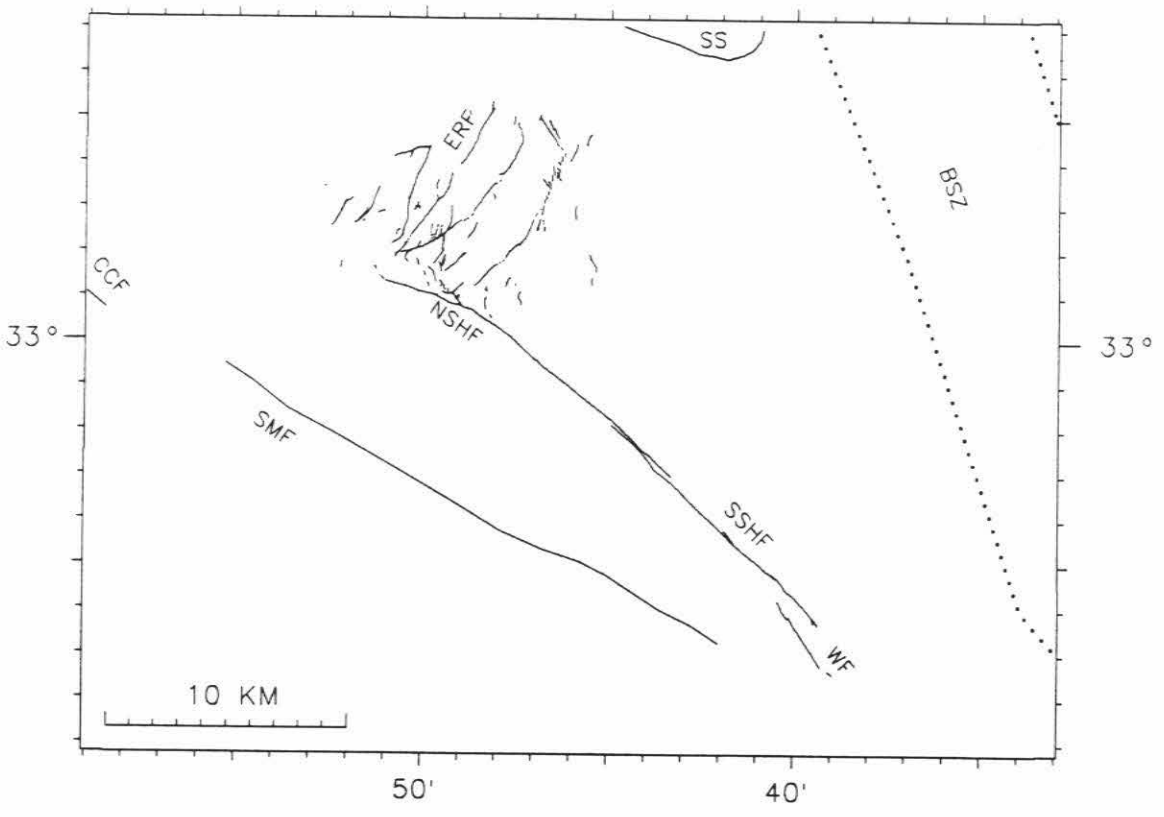

Figure 1.2. Reference map showing segments of the Superstition Hills fault and northeast striking faults that displayed surface rupture from the 24 November 1987 earthquake sequence (Sharp *et al.*, 1989). Area within dotted lines is the Brawley seismic zone. Abbreviations: ERF, Elmore Ranch fault, NSHF, north segment Superstition Hills fault, SSHF, southern segment Superstition Hills fault, WF, Wienert fault, other abbreviations as in Figure 1.1.

Figure 3.14 shows that the northern segment of the Superstition Hills fault borders the continental crystalline basement. The southern segment, and the Wienert fault, are surrounded by metasedimentary basement rocks. The fault segments behave differently in the studies discussed below.

The Superstition Hills and Superstition Mountain faults area had drawn attention prior to the 1987 earthquake sequence because of a change in seismic activity along the Superstition Mountain fault following the 7/8/86 M_L 5.9 North Palm Springs earthquake. The North Palm Springs earthquake was on the Banning fault, part of the San Andreas fault system, 120 km north of the Superstition Hills fault (Jones *et al.*, 1986). Figure 1.3 shows catalog locations of $M_L \geq 2$ earthquakes during 1984 and 1985 in the Superstition Hills fault area. Small, $M_L < 3$, events occur scattered along the Superstition Hills and Superstition Mountain faults. Earthquakes during the six months before the North Palm Springs earthquake are shown in Figure 1.4. No earthquakes occurred on the Superstition Hills fault, and few events occurred in the vicinity during that time. After the North Palm Springs earthquake, seismic activity increased on the Superstition Hills and Superstition Mountain faults (Figure 1.5). In contrast to the scattered earthquakes during 1984 and 1985, the increased activity occurs as mainshock-aftershock sequences. An M_L 3.2 earthquake on 8/24/86 along the Superstition Mountain fault was followed by six $M_L > 2$ aftershocks in eleven days. An M_L 3.4 earthquake just east of the Superstition Hills fault on 12/29/86 had five $M_L > 2$ aftershocks in just one and a half hours. These M_L 3+ earthquakes were the largest events in three years in the area.

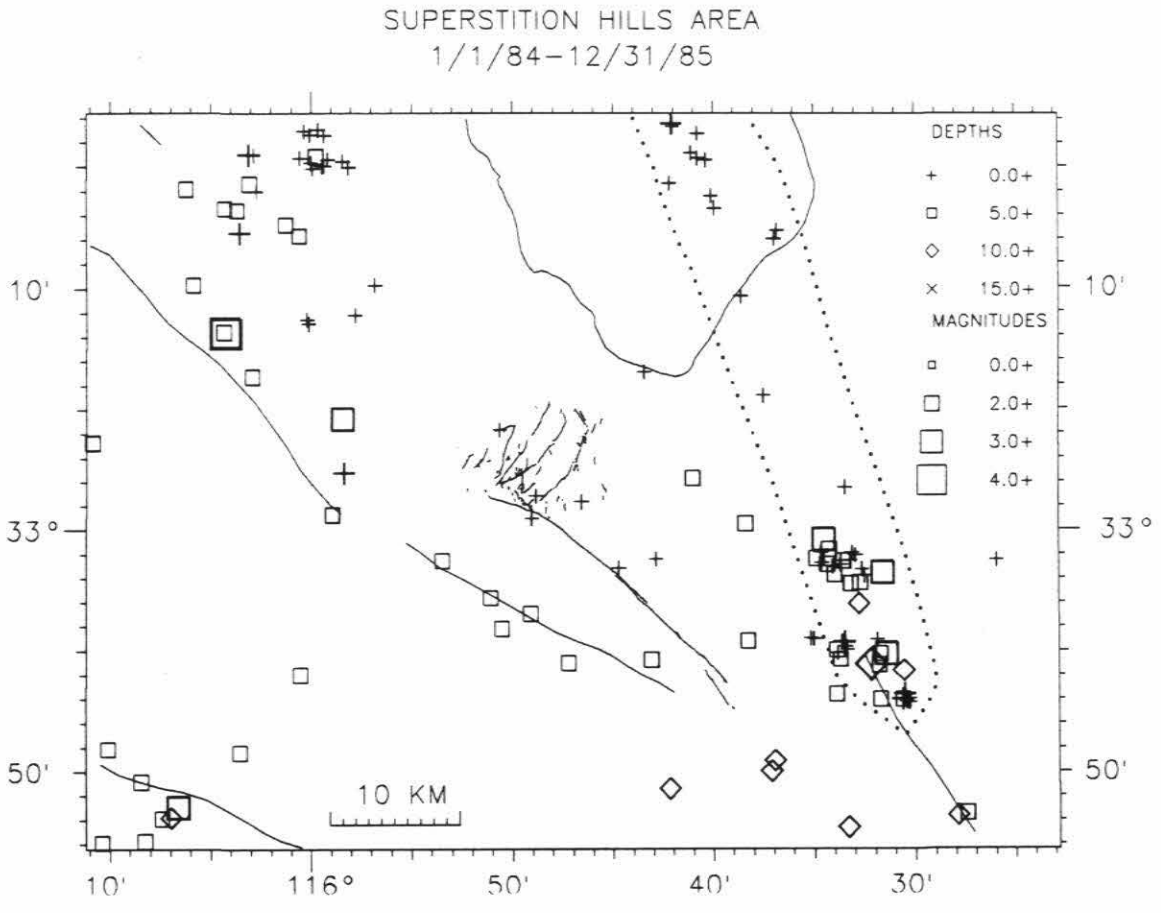

Figure 1.3. All $M_L \geq 2$ earthquake locations from the Caltech catalog from 1/1/84 to 12/31/85 in the Superstition Hills fault region. Earthquake symbol size is proportional to earthquake magnitude.

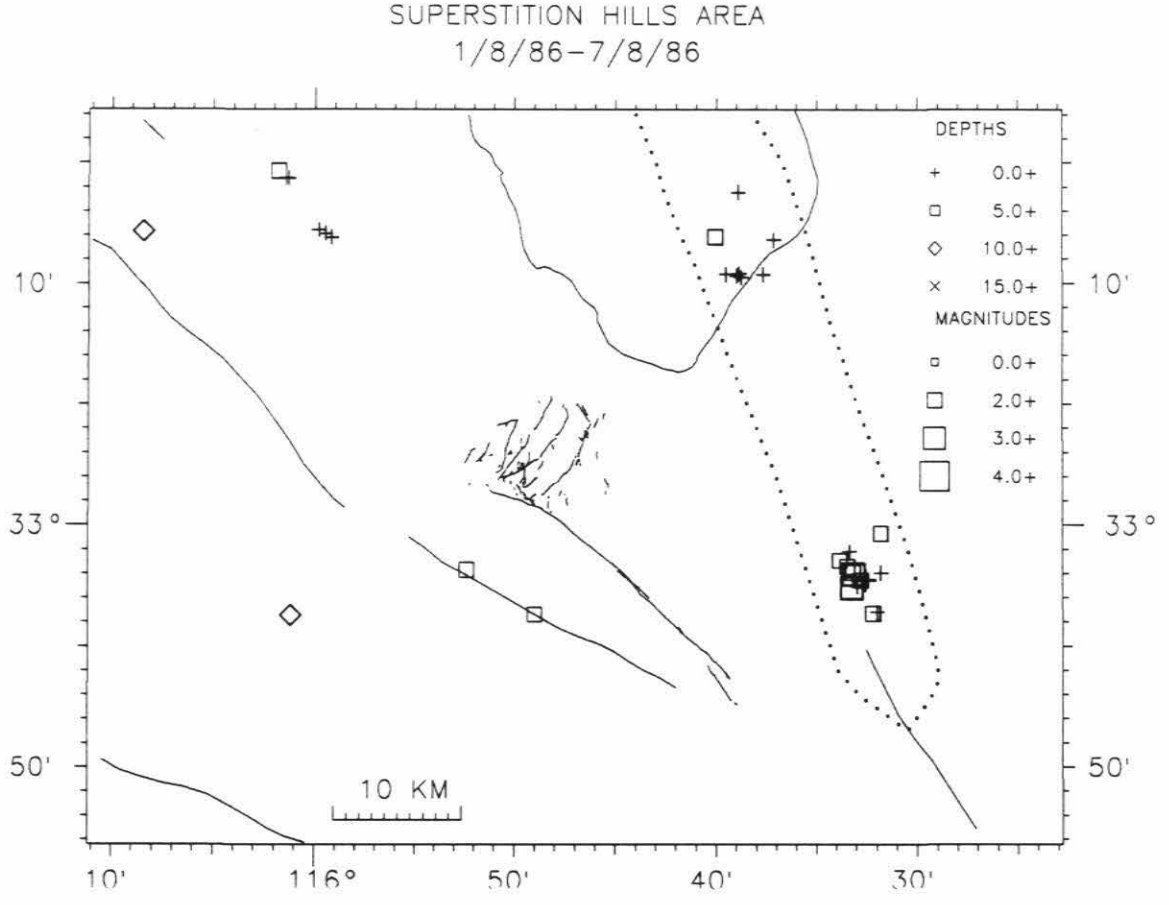

Figure 1.4. All $M_L \geq 2$ earthquake locations from the Caltech catalog from 1/8/86 to 7/8/86 (six months before the North Palm Springs earthquake) in the Superstition Hills fault region. Earthquake symbol size is proportional to earthquake magnitude.

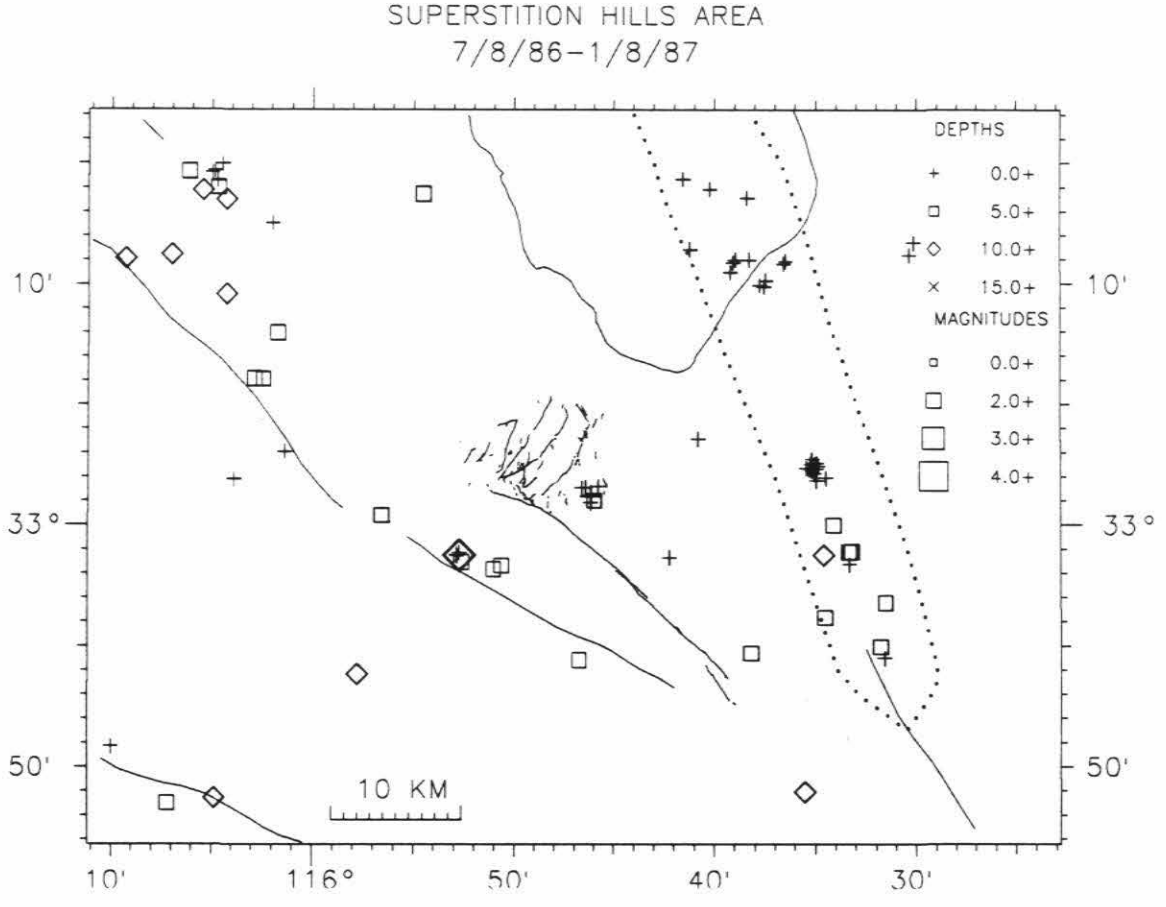

Figure 1.5. All $M_L \geq 2$ earthquake locations from the Caltech catalog from 7/8/86 to 1/8/87 (six months after the North Palm Springs earthquake) in the Superstition Hills fault region. Earthquake symbol size is proportional to earthquake magnitude.

1.3 Overview of Following Chapters

Chapter 2 is about the relocation of $M_L \geq 4.0$ earthquakes from 1945 to 1971 that have Caltech catalog locations near the 1987 sequence. It is new work. It is found that none of the relocated earthquakes occur on the southern segment of the Superstition Hills fault and many occur at the intersection of the Superstition Hills and Elmore Ranch faults. Also, some northeast-striking faults may have been active during that time.

Chapter 3 discusses the Superstition Hills earthquake sequence using data from the Caltech-U.S.G.S. southern California seismic array. The earthquakes are relocated and their distribution correlated to the type and arrangement of the basement rocks. The larger earthquakes occur only where continental crystalline basement rocks are present. The northern segment of the Superstition Hills fault has more aftershocks than the southern segment. This chapter is an extension of Magistrale, Jones, and Kanamori (1989).

Chapter 4 summarizes the results and interpretations of an inversion of long period teleseismic data of the second mainshock of the 1987 sequence, along the Superstition Hills fault. Most of the long period seismic energy seen teleseismically is radiated from the southern segment of the Superstition Hills fault. Chapter 4 is extracted from Hwang, Magistrale, and Kanamori (in press).

Chapter 5 is a field study of slip and afterslip measurements made along the Superstition Hills fault following the second mainshock. Slip and afterslip measurements were started only two hours after the earthquake. In some locations, afterslip more than doubled the coseismic slip. The northern and southern segments of the Superstition Hills fault differ in the proportion of coseismic and postseismic slip to the total slip, reflecting the difference in

basement rock types and sediment depth. This chapter is Williams and Magistrale (1989).

Chapter 6 reviews the results of Chapters 2, 3, 4, and 5 and discusses the implications. The reader seeking a concise discussion of the Superstition Hills earthquake sequence is advised to read Chapters 1 and 6 first.

Chapter 2

Relocations of older (1945-1972) M_L 4+ earthquakes near the Superstition Hills fault

2.1 Introduction

The 24 November 1987, Superstition Hills earthquakes occurred on a conjugate fault system consisting of the northwest-striking, right-lateral Superstition Hills fault and the northeast-striking, left-lateral Elmore Ranch fault. The earthquake sequence was complicated, with foreshocks, a mainshock, and aftershocks on the Elmore Ranch fault, followed by a mainshock and aftershocks on the Superstition Hills fault. The Elmore Ranch fault, as defined by aftershocks and surface ruptures, reaches from the northern end of the Superstition Hills fault to the northern end of the Brawley seismic zone. Many aftershocks occurred in the Brawley seismic zone. Thus the Elmore Ranch fault is an important northeast-striking seismogenic structure. It was not known to be active northeast of the surface traces cutting Quaternary strata (Dibblee, 1954) prior to the 1987 sequence.

The mainshock on the Superstition Hills fault initiated at the intersection of the Elmore Ranch fault and the Superstition Hills fault, and may have been triggered by the Elmore Ranch mainshock (Given and Stuart, 1988, Hudnut *et al.*, 1989). The Superstition Hills fault ruptured in two principal segments, the north and south segments. As discussed in other chapters, the two segments behave differently with respect to the number of aftershocks in the days following the mainshock, in the long period energy seen teleseismically, and in the behavior of afterslip.

The above observations suggest questions to be addressed by the relocation of older earthquakes (1945-1972) in the area of the Superstition Hills fault. Were any northeast-striking structures active during this time? If so, was earthquake activity on northeast-striking structures mistakenly associated with earthquakes on northwest-striking faults? Where have earthquakes during that time been along the Superstition Hills fault and has there been a difference in earthquake activity between the north and south segments of the Superstition Hills fault? The 1987 earthquakes are discussed in Chapter 3.

The older earthquakes are relocated using a master event technique. The seismograph station coverage is sparse and the velocity structure is complex. This complexity is accounted for by the introduction of empirical station corrections in the location program. The station corrections are the average of station residuals (observered travel time minus calculated travel time) of numerous earthquakes located in a plausible velocity structure. The station corrections are carefully determined from recent earthquakes well located by the contemporary dense seismograph array. This technique has been used with satisfactory results by Sanders *et al.* (1986) for earthquakes along the southern San Jacinto fault zone.

The earthquakes to be relocated were determined by sorting the Caltech catalog for events within the polygon shown in Figure 2.1 for the time period 1932 to 1987. A minimum M_L of 4 was used to ensure readable phase arrivals at the stations used (Figure 2.2, Table 2.2), and to limit the earthquakes to those that are tectonically significant. The 23 earthquakes selected occurred between 1945 and 1972. While sorting the catalog, it became clear that some selected earthquakes within the sort box were parts of sequences extending

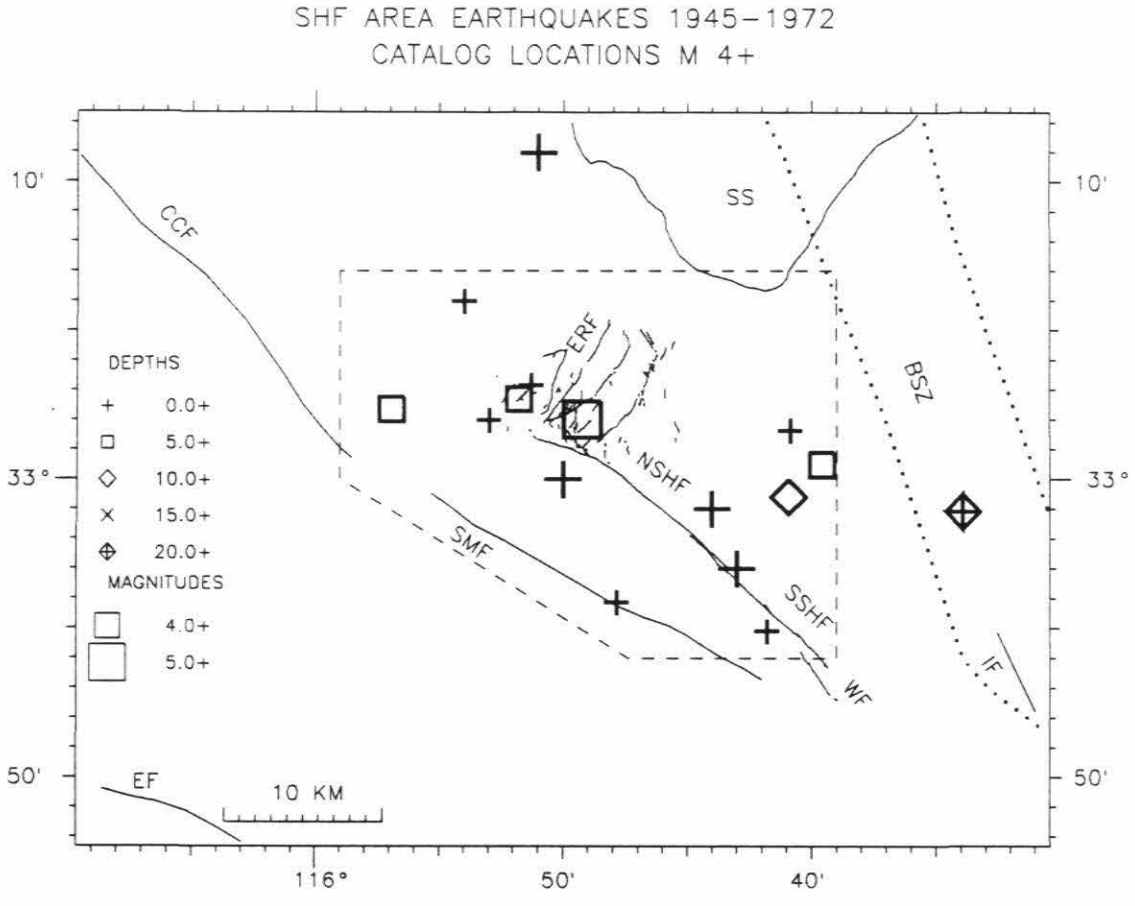

Figure 2.1. Catalog locations of the earthquakes to be relocated. The dashed line is the search window. Catalog locations are listed in Table 2.1. Area within dotted lines is the Brawley seismic zone. Abbreviations: NSHF, northern Superstition Hills fault, SSHF, southern Superstition Hills fault, WF, Wienert fault (part of the Superstition Hills fault), ERF, Elmore Ranch fault, SS, Salton Sea, CCF, Coyote Creek fault, EF, Elsinore fault, SMF, Superstition Mountain fault, IF, Imperial fault, BSZ, Brawley seismic zone.

Table 2.1

Relocated Earthquakes

Yr-Mo-Da	HrMn	New Location		Catalog Location		Magnitude	Model
45-08-27	1125	33 17.00	115 35.00	33 1.99	115 52.99	4.0	w
46-01-08	1854	33 6.20	115 56.70	33 0.00	115 50.00	5.4	w
51-01-24	717	32 57.54	115 31.84	32 59.00	115 43.99	5.6	w
51-01-24	733	33 1.96	115 31.80	32 59.00	115 43.99	4.0	w
53-06-14	417	32 51.16	115 43.19	32 57.00	115 43.00	5.5	w
53-06-14	429	32 47.00	115 48.00	32 57.00	115 43.00	4.8	w
57-04-25	2157	33 8.48	115 48.20	33 11.00	115 51.00	5.2	c
57-04-25	2205	33 11.10	115 43.50	33 5.99	115 54.00	4.2	c
57-04-25	2221	33 10.30	115 45.00	33 11.00	115 51.00	4.2	c
57-04-25	2224	33 8.73	115 47.75	33 11.00	115 51.00	5.1	c
57-04-25	2247	33 10.45	115 44.75	33 5.99	115 54.00	4.1	c
57-04-25	2249	33 9.50	115 46.60	33 5.99	115 54.00	4.2	c
63-05-23	636	33 0.22	115 37.92	32 54.90	115 41.81	4.3	c
63-05-23	906	33 0.35	115 38.82	32 58.92	115 33.93	4.6	c
63-05-23	1553	33 1.45	115 39.55	33 1.63	115 40.87	4.8	c
64-10-05	121	33 0.99	115 52.60	33 2.18	115 54.20	4.1	w
64-10-05	124	33 0.50	115 52.41	33 3.17	115 51.30	4.4	w
64-11-29	1425	32 57.76	115 36.97	32 59.40	115 40.94	4.2	c
65-06-17	740	33 5.74	115 31.09	33 0.47	115 39.58	4.1	c
68-05-06	1731	33 3.05	115 56.80	33 2.36	115 56.93	4.0	w
68-12-17	2253	33 1.30	115 51.67	33 2.69	115 51.79	4.7	w
71-09-30	2246	33 0.65	115 50.14	33 2.01	115 49.23	5.1	w
72-01-12	1231	33 1.50	115 49.80	32 55.87	115 47.87	4.0	w

In the model column, w indicates that the earthquake was relocated using the western Imperial Valley velocity model and station corrections, and c indicates the central Imperial Valley velocity model and station corrections. See Tables 2.3 and 2.4.

outside the sort box, in which case all the $M_L \geq 4$ earthquakes of the sequence were included. The catalog locations of the earthquakes are listed in Table 2.1 and shown in Figure 2.1.

The earthquake catalog locations come from Hileman *et al.*, (1973). Locations before 1961 were done graphically using empirical S-P versus Δ curves. Earthquakes after 1961 were located with a computer least squares routine using a 3 layer crustal model. The model included no correction for slow sedimentary surface layers. Aftershocks were often assigned the same location as the associated mainshocks. Location errors are $\pm$ 10 to 15 km.

Doser and Kanamori (1986a) used a master event technique to attempt to relocate every $M_L \geq 4.5$ earthquake from 1932 to 1973 in the Imperial Valley area, including many of the earthquakes studied here. The present work extends that effort by using better station corrections appropriate for the Superstition Hills fault area determined from tens of recent nearby events, rather than only two Borrego Valley events as in Doser and Kanamori (1986a). Also, this study uses independent P- and S-wave station corrections, which is very important for accurate relocations, instead of S-wave corrections based on the P-wave corrections. Some events rejected by Doser and Kanamori (1986a) for poor quality relocations are located here.

2.2 Method

The earthquakes are relocated using P- and S-wave arrivals from 2 to 5 of the Caltech seismograph stations Palomar (PLM), Riverside (RVR), La Jolla (LJC), Glamis (GLA), Perris (PRR), Big Bear (BBC), El Centro (ECC), Hayfield (HAY), Barrett (BAR) and Cedar Springs (CSP) (Figure 2.2) in the location program HYPOINVERSE (Klein, 1985). The station distances are

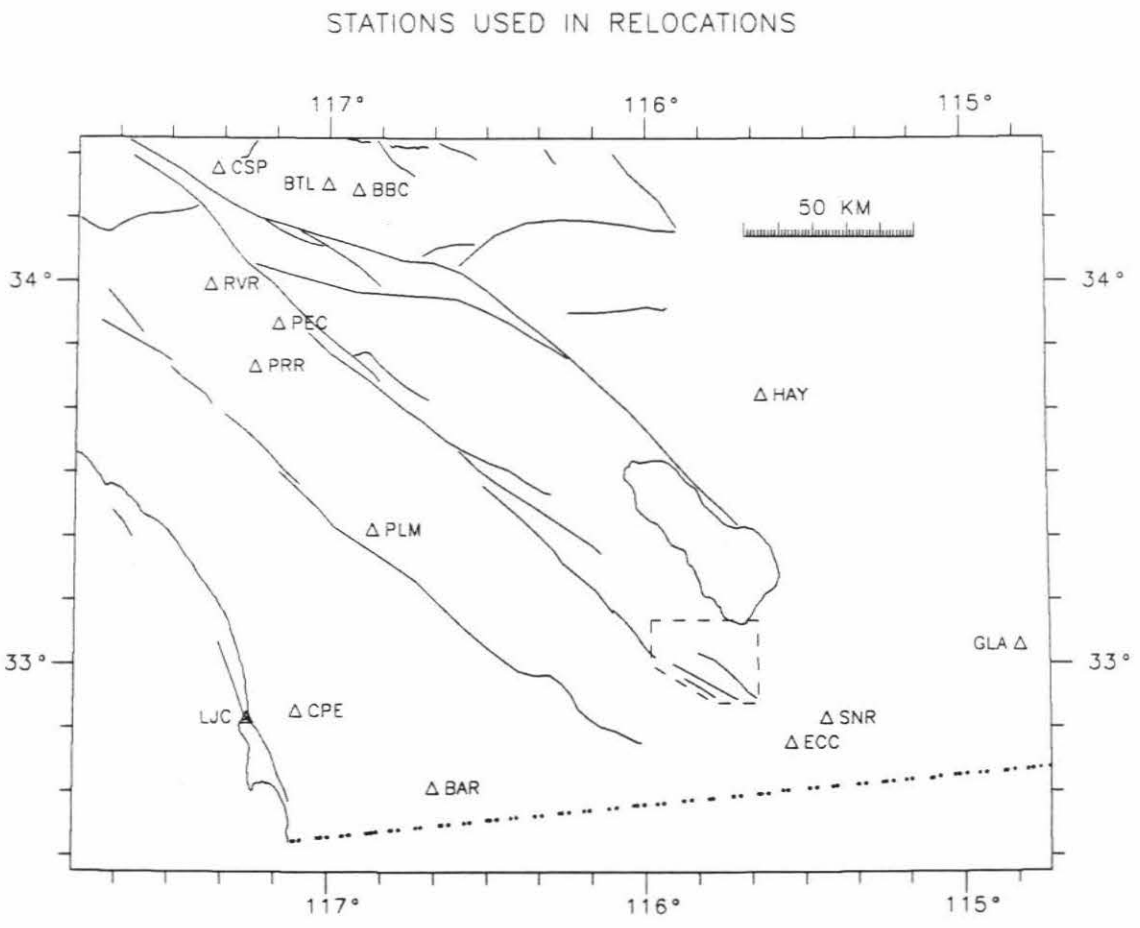

Figure 2.2. Stations used in the relocations. Station locations, shown by triangles, are listed in Table 2.2. The dashed line is the catalog search window from Figure 2.1. The dotted line is the international border.

Table 2.2
Station Information

Station	Latitude		Longitude		Elevation *meters*
BAR	32	40.80	116	40.30	510
PRR	33	46.80	117	14.00	430
ECC	32	47.90	115	32.90	-15
BBC	34	14.50	116	54.50	2060
LJC	32	51.80	117	15.20	8
CSP	34	17.87	117	21.33	1266
HAY	33	42.40	115	38.20	439
GLA	33	3.10	114	49.60	627
RVR	33	59.60	117	22.50	260
PLM	33	21.20	116	51.70	1692

from 20 to 210 kms. The station coverage is very sparse, and for some of the earthquakes the station azimuthal distribution is poor, so very accurate station corrections are needed to account for the deviation between the observed travel time through the real earth and the travel time calculated through the idealized crustal velocity models used in the location program. The station corrections are found by carefully locating many recent (1978 to 1988) large and small earthquakes using the current dense USGS-CIT seismograph network and stations within 80 km of the epicenters. The station residuals (observed travel time minus calculated travel time) of the recent earthquakes at the above named stations are averaged to define the station corrections (Table 2.4). Independent P-wave and S-wave station corrections are found. The station corrections are subtracted from the station travel times.

Experience with this location technique for earthquakes along the southern San Jacinto fault zone (Sanders *et al.*, 1986) showed that station corrections determined as above vary from earthquake source region to source region. The current study area has a velocity structure that differs between the western and central Imperial Valley (Fuis *et al.*, 1982), so different velocity models are used to define the station corrections and locate the earthquakes. Earthquakes in the central Imperial Valley had station corrections determined in, and are relocated in, a velocity model (Table 2.3) from Fuis *et al.* (1982, Fig. 22, east of shotpoint 13). Earthquakes in the western Imperial Valley near the Superstition Hills fault had station corrections determined in, and are relocated in, a dual velocity model. Stations west of the Superstition Hills fault use the velocity model of Hamilton (1970) (Table 2.3), which is appropriate for the thinner sediments

Table 2.3
Velocity Models

Central Imperial Valley		Western Imperial Valley, west		Western Imperial Valley, east	
P-Wave Velocity (km/sec)	Depth to Top of Layer (km)	P-Wave Velocity (km/sec)	Depth to Top of Layer (km)	P-Wave Velocity (km/sec)	Depth to Top of Layer (km)
2.0	0.0	2.5	0.0	2.5	0.0
3.1	1.0	5.1	0.4	4.5	1.5
3.8	2.0	6.0	2.9	6.2	3.0
4.6	3.0	7.1	14.0	7.0	12.5
5.3	4.0	7.9	25.0	7.9	25.0
5.8	4.8				
6.5	14.2				
7.3	15.4				
7.5	20.0				

and shallower basement of the western Imperial Valley. Stations east of the Superstition Hills fault use a velocity model from Fuis *et al.* (1982) (Fig. 22, east of shotpoint 1). The station residuals used to determine the station corrections were consistent for each area (Table 2.4). The velocity model used for each earthquake is flagged in Table 2.1. Because of sparse, distant station coverage, the depths of the earthquakes to be relocated were fixed at 10 km, consistent with the depth of many earthquakes during the 1987 Superstition Hills earthquake sequence (Chapter 3). The catalog locations were used as trial locations in the location program. S-wave velocities were calculated with $V_p / V_s = 1.73$ and S-wave arrivals were given one half the weight of P-wave arrivals.

The seismograph stations LJC, ECC, PRR, and BBC are no longer in operation so the nearby contemporary stations CPE, SNR, PEC, and BTL were used to determine station corrections for the old stations. All the stations are shown in Figure 2.2. CPE is 14 km east of LJC, SNR is 12 km northeast of ECC, PEC is 15 km northeast of PRR, and BTL is 8 km west of BBC. The elevations and site geology are similar in each case, so it was assumed that the station corrections determined at the modern stations are applicable to the old stations.

The P- and S-wave arrival times were repicked from the short period vertical and .8 sec torsion horizontal seismograms for about half the earthquakes studied. The repicked phase times were compared to the times on the archive phase cards, and most were found to agree within .2 sec. That agreement provides an estimation of .2 sec as the seismogram reading error. The phase card times were used for the other half of the earthquakes. Clock corrections assumed linear drift, a possible source of error in the arrival times.

As a test of the relocation quality, several recent earthquakes near the Superstition Hills fault were relocated using 4 or 5 stations (1 phase per station) and the appropriate station corrections. All relocated within 5 km of their catalog epicenters, indicating an accuracy of about 5 km for the relocations. The HYPOINVERSE code requires a minimum of four phases. For earthquakes with more than 4 phases, relocations were done with different subsets of the phases to check the differences in final locations for each subset. Most earthquakes relocated within 5 km for each subset, again indicating an accuracy of about 5 km for the relocations. Some earthquake relocations had large station residuals, or the relocations for different phase subsets varied widely. In these cases, final relocations were done by comparing P-O and S-P times of the earthquake in question to the P-O and S-P times of a well relocated earthquake.

2.3 Results

9/30/71 M_L 5.1 and 1/12/72 M_L 4.0 earthquakes. The 1971 earthquake is well located using P-wave arrivals from HAY, BAR, GLA, PLM, and CSP. The new location is near the north end of the Superstition Hills fault, 3 km southwest of the catalog location. Subsets of the 5 stations all give a location within 4 km of the location shown in Figure 2.3. Also, comparison of P-O times of PLM, BAR, HAY, and GLA of this earthquake to those of the well located earthquake of 12/17/68, discussed below, indicates this location. This earthquake is near the intersection of the Superstition Hills fault and the Elmore Ranch fault. Catalog locations of the 9 aftershocks in the 24 hours following this earthquake lie along the northern segment of the Superstition Hills fault, suggesting rupture to the southeast from the epicenter. No

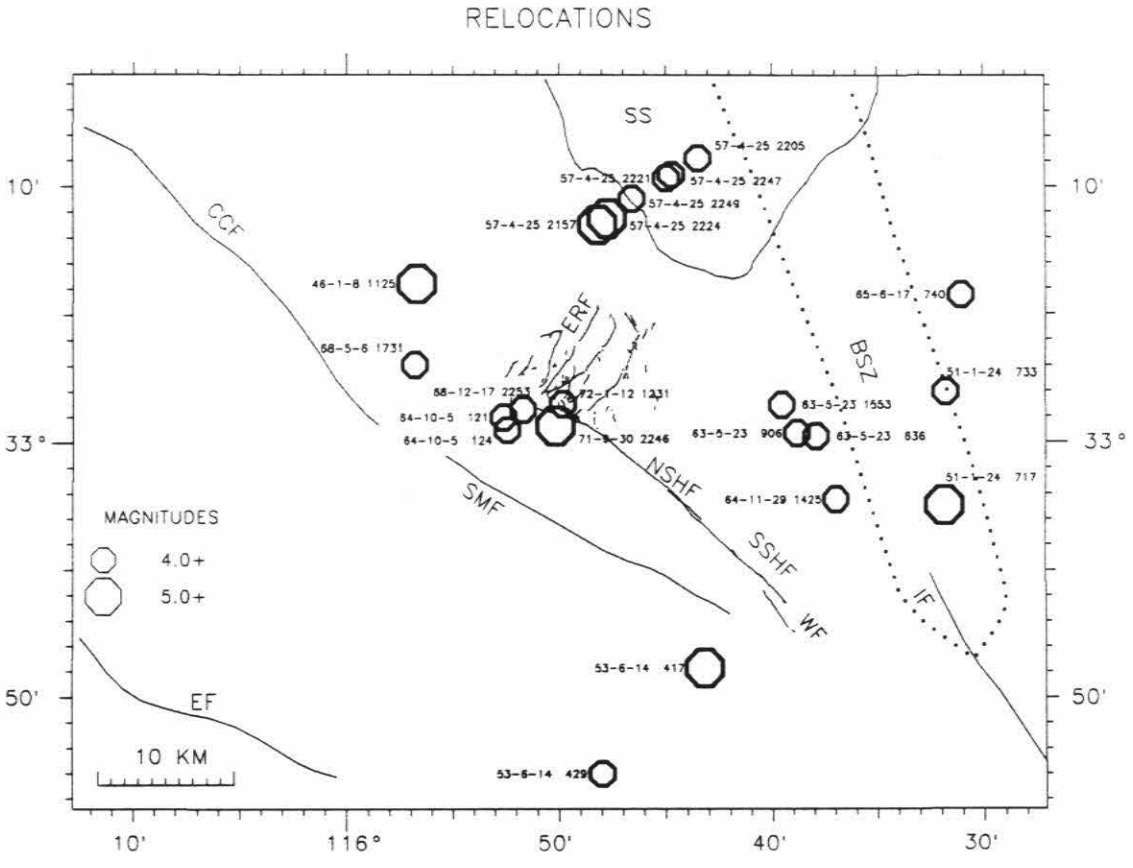

Figure 2.3. Events relocated in this study. The earthquakes are labeled with the yr-mo-da time of occurrence. The new locations are listed in Table 2.1. See text for discussion of relocations. Abbreviations as in Figure 2.1. Area within dotted lines is the Brawley seismic zone.

aftershocks are on the Elmore Ranch fault. Notes by Clarence Allen (pers. comm.) on field observations after the earthquake show that no surface rupture or creep was seen on the southern Superstition Hills fault, but fresh cracks were seen on the Imperial fault near old highway 80. From the location of the mainshock determined here, and the catalog locations of the aftershocks, this earthquake ruptured a few km of the northern segment of the Superstition Hills fault.

The 1972 earthquake location could not be well determined using the location program, so its location was found by comparison of P-O times of PLM, GLA, and CSP to those times of the 1971 earthquake. The new location, 1 to 2 km northeast of the 1971 earthquake, is about 10 km north of the catalog location in the middle of the surface trace of the Superstition Mountain fault. However, microseismicity of the Superstition Mountain fault diverges to the southwest of the surface trace of the fault, so the catalog location lacks plausibility. The new location places the earthquake near the intersection of the Superstition Hills fault and the Elmore Ranch fault. The catalog contains no aftershocks of this event, so it is not certain which of the two faults it occurred on.

5/6/68 M_L 4.0 and 12/17/68 M_L 4.7 earthquakes. The 12/17/68 earthquake was well located using P-wave times from HAY, BAR, GLA, and PLM. The new location is at the intersection of the Superstition Hills fault and the Elmore Ranch fault, 3 km south of the catalog location. The accuracy of the new location is about 2 km, as discussed below. The catalog lists 8 M_L 2+ aftershocks during the following two days. Some catalog aftershock locations are on the Superstition Hills fault, but some may be associated with the Elmore Ranch fault.

Table 2.4
Station Correction Information

	Central Imperial Valley velocity model average residual, sec						Western Imperial Valley velocity model average residual, sec					
Station	P	n	σ	S	n	σ	P	n	σ	S	n	σ
BAR	0.66	22	0.12	0.64	3	0.09	0.60	5	0.10	-0.56	5	0.16
PRR							-0.39	2	0.02			
ECC	0.25	6	0.07	0.19	2	0.06	0.33	35	0.10	0.19	2	0.06
BBC	1.05	2	0.11				0.54	3	0.04			
LJC							0.24	4	0.05			
CSP							0.62	3	0.03			
HAY	0.10	21	0.11				0.00	3	0.05			
GLA							-0.52	24	0.15			
RVR	0.63	3	0.44	3.17	1	0.00	-0.21	2	0.03	3.19	2	0.27
PLM	0.81	8	0.04				0.25	13	0.10	0.93	2	0.12

n is the number of earthquakes for which a residual to a given station was found, σ is the standard deviation of the average of n residuals, and a residual is observed travel time minus calculated travel time.

The 5/6/68 earthquake epicenter could not be confidently determined with the location program, so it was located by comparison of P-O times of PLM, GLA, and BAR to those times of the 12/17/68 earthquake. The 5/6/68 earthquake was an aftershock of the 4/9/68 M_L 6.8 Borrego Mountain earthquake on the Coyote Creek fault (Allen *et al.*, 1968). This aftershock's catalog location comes from Hamilton (1972) who used 18 nearby stations, mostly portables installed specifically to accurately locate Borrego Mountain aftershocks. The new location is only 2 km north of the very accurate catalog location. Since this location was determined relative to the 12/17/68 earthquake, this gives confidence to the new locations of both the 5/6/68 and 12/17/68 earthquakes. As mentioned above, the 1971 earthquake's P-O times tie the 1971 earthquake location to the 1968 earthquakes at the same level of accuracy. The 5/6/68 earthquake was on the Coyote Creek fault and, while small, serves as a test of accuracy of the relocations.

10/5/64 01:21 M_L 4.1 and 01:24 M_L 4.4 earthquakes. These earthquakes were located using P-wave times of HAY, BAR, PLM, and RVR in the location program. The new locations are near the intersection of the Superstition Hills fault and the Elmore Ranch fault. The new locations were checked by comparing P-O times of HAY, BAR, and PLM of these earthquakes to the 12/17/68 and 9/30/71 earthquakes. BAR and HAY P-O disagreements suggest an accuracy of about 5 km in absolute location. The catalog locations of the 1964 earthquakes are about 5 km north and northwest of the north end of the Superstition Hills fault, with an east-west separation of 4 km. This separation suggests a possible conjugate faulting sequence. However, the new locations colocate these earthquakes within a km. This small relative separation can be confirmed by differencing station arrival

times of each earthquake (for example, RVR-PLM arrival time) and comparing those differences. This eliminates possible origin time errors. The station arrival time differences agree within .2 sec for the two earthquakes, giving a relative separation of about a km. These earthquakes could still be conjugate, but their small source area size makes this difficult to judge. The catalog contains only 2 M_L 3+ aftershocks following the M_L 4 events, insufficient to define the causative structure. At any rate, these earthquakes occurred close to the intersection of the Superstition Hills and Elmore Ranch faults.

5/23/63 06:36 M_L 4.3, 09:06 M_L 4.6, 15:53 M_L 4.8, 11/29/64 M_L 4.2, and 6/17/65 M_L 4.1 earthquakes. These earthquakes were relocated with P-wave times from ECC and HAY, and P- and S-wave times from BAR and RVR in the location program. The 1964 event also used a PLM P-wave time. Alternate locations using subsets of the phases varied by only a km in the north-south direction, and by 4 km in the east-west direction for all the earthquakes other than the 1965 event, which varied tens of kms in the east-west direction. The 1963 and 1964 earthquakes move from 2 to 12 km from their curiously scattered catalog locations to their new locations 3 km west of the Brawley seismic zone. The 1963 earthquakes appear to be part of a swarm sequence rather than a mainshock-aftershock sequence. The catalog lists an M_L 3.3 event 7 hours before 06:36 and 10 M_L 3+ events between and after the M_L 4+ events. Also, the larger events increased in size over time. This is typical of Brawley seismic zone swarms (Johnson, 1979), so the 1963 earthquakes can be assigned to the Brawley seismic zone. The 3 km difference in the new location and the edge of the Brawley seismic zone is within the accuracy bounds of the new location. The 1964 event was preceded by 5 M_L

3+ earthquakes in three days, and so too can be assigned to the Brawley seismic zone on the basis of swarm behavior. The 1963 and 1964 events all lie in the section of the Brawley seismic zone between the northeast-striking structures defined by the 1981 Westmorland sequence (Hutton and Johnson, 1981) and the 1979 Imperial Valley aftershock sequence (Johnson and Hutton, 1982). The 1965 earthquake, poorly located here, was part of a major swarm during 6/16-6/17 that included 4 M_L 4+ events and 14 M_L 2.8+ events near Westmorland.

4/25/57 21:57 M_L 5.2, 22:05 M_L 4.2, 22:21 M_L 4.2, 22:24 M_L 5.1, 22:47 M_L 4.1, and 22:49 M_L 4.2 earthquakes. The 21:57 and 22:24 earthquakes were located with P-wave times from ECC, BBC, and RVR, and P- and S-wave times from BAR. The other four, smaller earthquakes were located relative to the two larger ones by comparison of BAR S-P times. The two larger earthquakes colocate within .6 km by comparison of P-O times and by comparison of station P-wave arrival time differences, which agree within .2 sec. They are then a double event. Only some of the smaller earthquakes fell within the search window used to select earthquakes from the catalog for this study. The larger earthquakes were included due to their clear association with the smaller earthquakes. The larger earthquakes relocate to just west of the southern Salton Sea, about 6 km south of their catalog locations. The new locations were confirmed by comparison of RVR and BAR P-O times of the larger 1957 events to the times of the 1987 Elmore Ranch earthquake and one of its foreshocks. This comparison suggests an accuracy of 2 to 3 km for the larger 1957 events. The catalog locations have the smaller earthquakes west of, or colocated with, the larger earthquakes, but the BAR S-P times indicate that all the smaller earthquakes must be 3 to 9 km east of the two M_L 5+

events.

Unfortunately, the ECC record was not available to provide north-south control on the smaller earthquake locations. This sequence also included 11 M_L 3+ aftershocks in the following ten hours.

6/14/53 04:17 M_L 5.5 and 04:29 M_L 4.8 earthquakes. The 04:17 earthquake was located using PLM and BBC P-wave arrivals, and S- and P-wave arrivals at RVR. These stations span only 30° in azimuth. Comparison of this earthquake's RVR and PLM P-O and RVR S-P times to the 1951 earthquake arrival times, described below, give an estimated accuracy of about 6 km along azimuth to those stations. The 04:29 aftershock was located by comparison of its PLM P-O and RVR and BAR S-P times to those of the mainshock. No clock correction was available for the BAR record, so only relative S-P times from that station could be used. The 04:29 event could only be located within a 10 by 15 km range, west of the first event. The catalog location of both earthquakes is near the middle of the surface trace of the Superstition Hills fault. The new location of the larger event is 11 km south of the catalog location, which places the earthquake on the seismicity trend of the Superstition Mountain fault, a few km southwest of that fault's surface trace. The earthquake occurred on the Superstition Mountain fault. The catalog lists 5 M_L 3+ additional aftershocks, assigned the same location as the mainshock.

1/24/51 07:17 M_L 5.6 and 07:33 M_L 4.0 earthquakes. These earthquakes were relocated with P- and S-wave arrival times from LJC and RVR, and P-wave times from PRR and PLM in the location program. These stations cover only 40° azimuth. Alternate locations determined from station subsets

vary over an area 6 km in diameter. The catalog places these events near the middle of the surface trace of the Superstition Hills fault. The new locations are 19 km east, in the Brawley seismic zone. This is a significant difference, because the larger earthquake was associated with slight displacement along 3 km of the Superstition Hills fault (Allen *et al.*, 1965). The longitude control for the new location comes from the LJC S-P time. That time, about 17 sec, is too large for the earthquakes to be on the Superstition Hills fault. The Brawley seismic zone was active during the time of these earthquakes. There was a large swarm from 7/27/50 to 8/22/50 with catalog locations 10 to 15 km north of the 1951 earthquakes' new locations. That swarm included many events of M_L 4+ and 5+. Three M_L 3.8 aftershocks the same day as the 1951 events were given the same catalog location as the 07:17 event, but two M_L 4+ earthquakes on 2/13/51 were given catalog locations the same as the new location for the 07:17 earthquake. The Superstition Hills fault ruptured by sympathetic slip during the 07:17 earthquake, just as it did during the 1981 Westmorland earthquake, an M_L 5.7 earthquake that also occurred in the Brawley seismic zone. The new locations of the two 1951 events are near the northeast trending seismic lineament that developed following the large aftershock of the 1979 Imperial Valley earthquake. They may have occurred on the same structure. The catalog location of the 07:17 event was based in part on felt reports. *MM VII* was reported 5.5 km southwest of Westmorland, close to the Superstition Hills fault. However, that felt report is very similar to those reporting *MM VI* from Brawley, Calexico, Calipatria, El Centro, Holtville, and Imperial (Murphy and Cloud, 1953), surrounding the Brawley seismic zone, so the new location for the 1951 earthquake is not inconsistent with the felt reports.

1/8/46 M_L 5.4 and 8/27/45 M_L 4.0 earthquakes. These earthquakes could not be well constrained using the location program, so they were located by comparing S-P times to RVR and LJC to those times of the 1951 and 1953 earthquakes. The 1946 event has a catalog location near the north end of the Superstition Hills fault. The new location is 13-20 km north, within a 10 by 5 km uncertainity range defined by different travel time comparisons. The new location places the earthquake on an active microseismicity trend that defines the north edge of an embayment in the crystalline basement rocks north of the Superstition Hills fault. This basement embayment is shown in Figures 3.14 and 3.17.

The 1945 earthquake has a catalog location 5 km northwest of the north end of the Superstition Hills fault. The new location is 40 km northeast, in the Brawley seismic zone under the Salton Sea. The new location is poorly constrained. This earthquake was 12 days after an M_L 5.7 event with a catalog location of $33^o 13^{'}, 116^o 8^{'}$, outside the current study area, but close to the 1968 M_L 6.8 Borrego Mountain earthquake location. The catalog contains no swarm activity to support a Brawley seismic zone location for the 1945 event.

2.4 Discussion and Conclusions

The relocations are shown in Figure 2.3 and listed in Table 2.1. In contrast to the catalog locations (Figure 2.1), no relocated earthquakes lie on the southern Superstition Hills fault. Along the northern Superstition Hills fault many relocated earthquakes occur near the intersection of the Superstition Hills fault and the Elmore Ranch fault. It is not surprising that the historic seismic activity occurred near the epicenter of the 1987

Superstition Hills earthquake. The pattern of historical seismicity mimics the aftershock pattern in the first four days following the November 24, 1987 Superstition Hills earthquake (Chapter 3), when most of the aftershocks occurred along the northern segment of the Superstition Hills fault. The northern and southern segments of the Superstition Hills fault behave differently in their recent seismic history.

The M_L 5.6, 24 January 1951 event is the only earthquake in this study that has been associated with surface rupture on the Superstition Hills fault (Allen *et al.*, 1965). The catalog location had placed it midway along the fault. Allen *et al.* (1965) noted it was a small earthquake to have been associated with surface rupture. The relocation determined here places the earthquake, and the M_L 4.0 aftershock, in the Brawley seismic zone. Therefore, the surface rupture of the Superstition Hills fault probably occurred by sympathetic slip instead of by direct rupture by the earthquake, as also happened during the M_L 5.7 26 April, 1981 Westmorland earthquake (Sharp *et al.*, 1986) that also occurred in the Brawley seismic zone (Hutton and Johnson, 1981). The Superstition Hills fault also had small surface rupture in 1965, 1968, 1969, and 1979 (Allen *et al.*, 1972, Fuis, 1982, Sharp *et al.*, 1986). The new locations of the 1951 earthquakes are near the northeast trending seismic lineament that developed following the large aftershock of the 1979 Imperial Valley earthquake (Johnson and Hutton, 1982). The 1951 earthquakes may have occurred on the same structure as the 1979 aftershocks.

The 1963 and November 1964 earthquakes were in the Brawley seismic zone, in a section of the zone delimited by the northeast trending seismic lineaments defined during the 1979 Imperial Valley aftershock sequence to the south and the 1981 Westmorland sequence to the north. The 1965 and 1945

earthquakes also were in the Brawley seismic zone, but their locations are not as well constrained. All but the 1945 earthquakes occurred during seismic swarms in the Brawley seismic zone well documented in the catalog.

The 1971, 1972, December 1968, and October 1964 earthquakes all occurred near the intersection of the Superstition Hills fault and the Elmore Ranch fault. Catalog locations of the 1971 aftershocks suggest the earthquake ruptured the northernmost part of the Superstition Hills fault. That earthquake also caused sympathetic slip on the Imperial fault (Allen, pers. comm.). The December 1968 and 1972 earthquakes, lacking sufficient aftershocks to define a fault plane, could have been on either the Superstition Hills fault or the Elmore Ranch fault. Because of their location near the fault intersection and close time of occurrence, the two October 1964 earthquakes may represent a conjugate pair of earthquakes involving the Elmore Ranch fault and the Superstition Hills fault. Their small source area and paucity of aftershocks make it equally plausible that both these earthquakes occurred on one fault or the other. It is noteworthy that no other earthquakes near the intersection of the Superstition Hills fault and Elmore Ranch fault occurred in a conjugate pair, as happened in the 1987 sequence.

The May 1968 earthquake occurred on the Coyote Creek fault as an aftershock of the May 9, 1968, Borrego Mountain earthquake (Hamilton, 1972). The first 1953 earthquake occurred on the Superstition Mountain fault. This is the largest earthquake (M_L 5.5) known to have occurred on the Superstition Mountain fault if one accepts the result of Sanders *et al.* (1986) that the 1942 M_L 6.3 earthquake was to the west of the fault. The second 1953 earthquake occurred on a structure to the west of the Superstition Mountain fault.

The 1957 and 1946 earthquakes probably took place on northeast-striking structures. The new location of the 1946 earthquake places it on a northeast-striking microseismicity trend that coincides with the north edge of an embayment in the continental basement rocks defined by the refraction study of Fuis *et al.* (1982). The 1957 earthquakes, a colocated doublet, lie on the projection of the south edge of this embayment. The faults bounding the embayment must be active because the shoreline of ancient Lake Cahuilla coincides with the basement embayment. This means the embayment area is dropping faster than the sedimentation rate, requiring active embayment bounding faults. The basement embayment is shown in Figure 3.14. If northeast-striking structures were active in 1946, 1951, and 1957, the idea of a simple south to north progression of seismic activity on northeast-striking structures (Hudnut *et al.*, 1989) would no longer hold.

The relocation of $M_L \geq 4.0$ earthquakes from the last 45 years near the Superstition Hills fault shows: 1. No large earthquakes occurred on the southern Superstition Hills fault during that time. Earthquakes assigned to the southern Superstition Hills fault in the catalog relocate to the Brawley seismic zone and the Superstition Mountain fault. The 1951 rupture observed on the Superstition Hills fault was due to sympathetic slip from a Brawley seismic zone earthquake. 2. Two northeast-striking faults north of the Superstition Hills fault have been active. Some of the Brawley seismic zone earthquakes may have also occurred on northeast-striking structures within the zone. 3. The intersection of the Superstition Hills fault and the Elmore Ranch fault has been very active during this time, but has no clear cut conjugate earthquake pairs before the 1987 sequence.

Chapter 3

The Superstition Hills, California, Earthquakes of 24 November, 1987

3.1 Introduction

The 24 November, 1987, Superstition Hills earthquakes occurred in the western Imperial Valley in southern California (Figure 3.1). The earthquakes took place on a conjugate fault system consisting of the northwest-striking Superstition Hills fault and a previously unknown northeast-striking structure defined by surface rupture and a lineation of hypocenters. The earthquake sequence consists of foreshocks, the M_S6.2 first main shock, and aftershocks on the northeast structure followed by the M_S6.6 second main shock and aftershocks on the Superstition Hills fault. This chapter presents the results of master event relocations of the earthquake sequence and relates the earthquake locations to the distribution of basement rocks in the western Imperial Valley.

The Superstition Hills fault is a member of the San Jacinto fault zone (Sharp, 1972). The fault displayed minor surface rupture from an M_L5.6 earthquake in 1951 (Allen *et al.*, 1965) (but see Chapter 2), and minor cracking in 1965 and 1969 (Allen *et al.*, 1972). Right-lateral triggered slip occurred following the 1968 M_L6.5 Borrego Mountain earthquake on the Coyote Creek fault (Allen *et al.*, 1972), the 1979 M_L6.6 Imperial Valley earthquake on the Imperial fault (Fuis, 1982), and the 1981 M_L5.6 Westmorland earthquake on a northeast-trending seismic lineament (Sharp *et al.*, 1986). These earthquakes were the largest recent earthquakes in this area (Figure 3.1). The second main shock of the November 1987 sequence

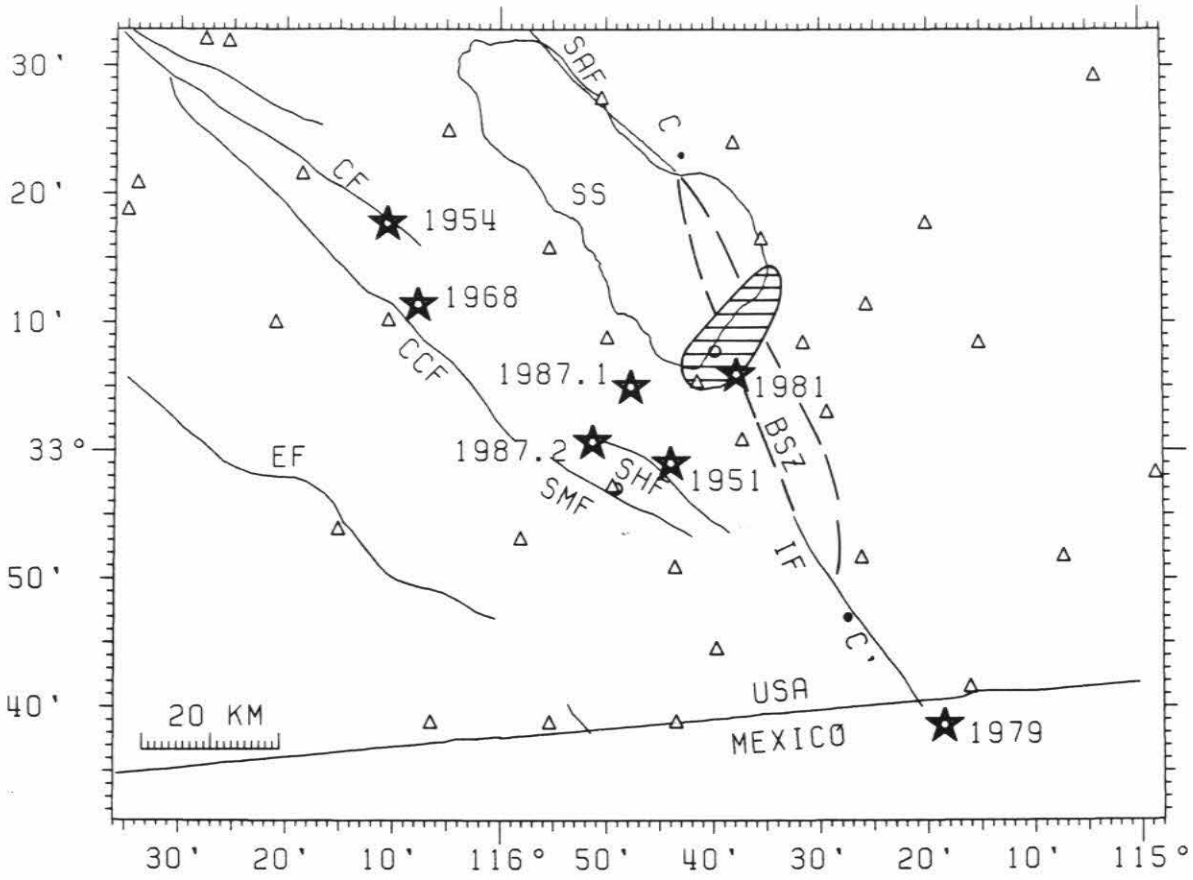

Figure 3.1. Reference map of the study area showing major faults and other features. Triangles are seismograph stations. Circles are strong motion instruments mentioned in text. Stars indicate earthquakes mentioned in text, labeled with year of occurrence. 1987.1 and 1987.2 indicate the first and second mainshocks, respectively, of the 24 November, 1987, sequence. Area of horizontal stripes is the Salton-Westmorland geothermal area. Area within dashed lines is the Brawley seismic zone. CC' is location of cross section shown in Figure 3.16. Abbreviations: SS, Salton Sea, SAF, San Andreas fault, CF, Clark fault, CCF, Coyote Creek fault, EF, Elsinore fault, SHF, Superstition Hills fault, SMF, Superstition Mountain fault, IF, Imperial fault, BSZ, Brawley seismic zone.

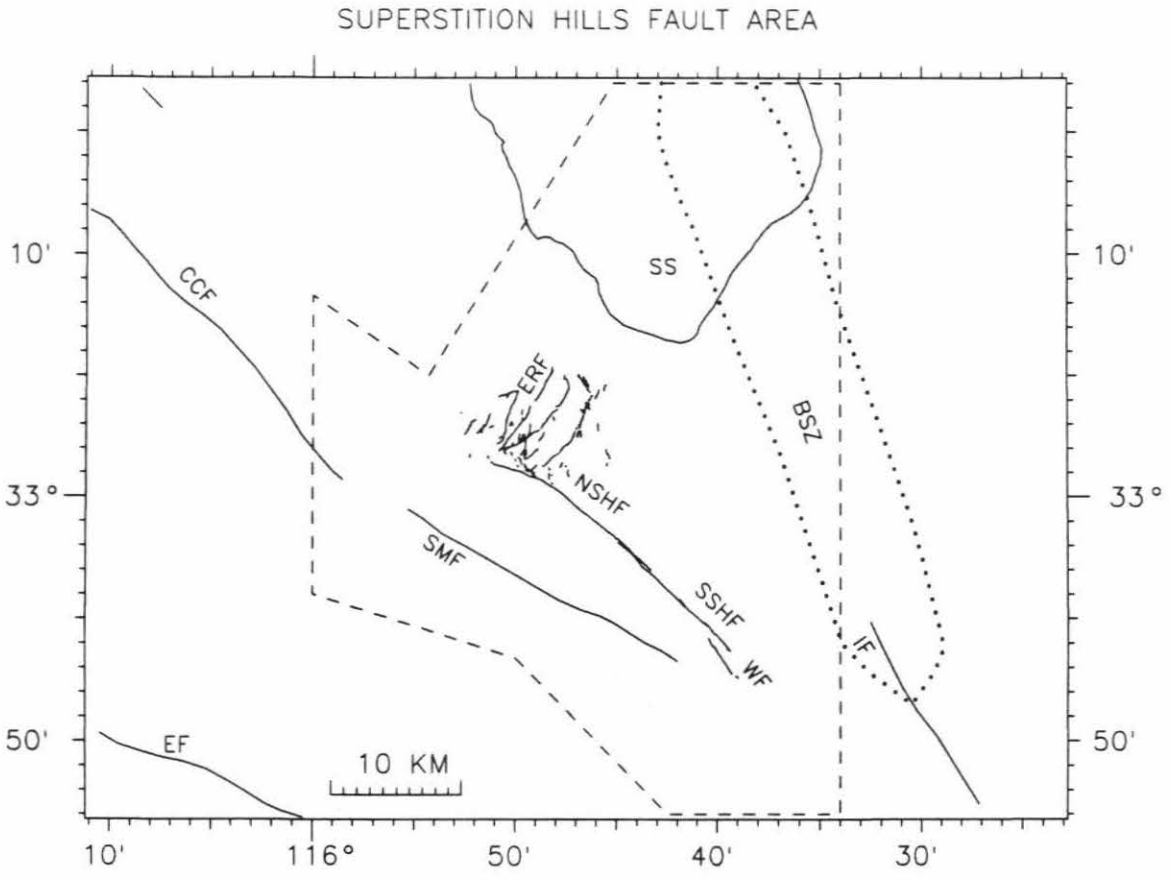

Figure 3.2. Close up reference map, showing segments of the Superstition Hills fault. Dashed lines enclose area within which all earthquakes from 11/24/87 to 2/9/89 were relocated. Area within dotted lines is the Brawley seismic zone. Abbreviations: ERF, Elmore Ranch fault, NSHF, north segment Superstition Hills fault, SSHF, southern segment Superstition Hills fault, WF, Wienert fault, other abbreviations as in Figure 3.1.

produced right-lateral surface rupture along the Superstition Hills fault on north and south segments separated by a right step. The extent of this rupture is coincident with that of the 1968 and 1979 triggered slip except at the southern end of the fault where a 4 km long en echelon fault segment, the Wienert fault, also ruptured during the 1987 earthquake (Figure 3.2) (Sharp *et al.*, 1989).

Background seismicity from the Caltech catalog (Figure 3.3) shows no obvious indication of the northeast-trending structure on which the first main shock took place (compare Figure 3.3 and Figure 3.4). The first main shock presumably caused the left-lateral surface rupture observed on numerous short faults striking northeast from near the north end of the Superstition Hills fault (Sharp *et al.*, 1989, Hudnut *et al.*, 1989), however, these faults were not field checked between the first and second main shocks. The first main shock did not produce surface rupture on the Superstition Hills fault (Kahle, *et al.*, 1988).

3.2 Data and Methods

The master event technique is used to relocate the earthquakes. The method works by carefully locating a master event earthquake in a given velocity model using no station travel time corrections. The station travel time residuals (observed travel time minus calculated travel time) of the master event are then used as station corrections to relocate the earthquakes of interest. The station corrections (also called station delays) account for complexities in the real earth velocity structure that are not present in the idealized velocity structure models used in the location program. Master events in different locations will produce different delays at a given station because the travel paths from the different events are not the same. The

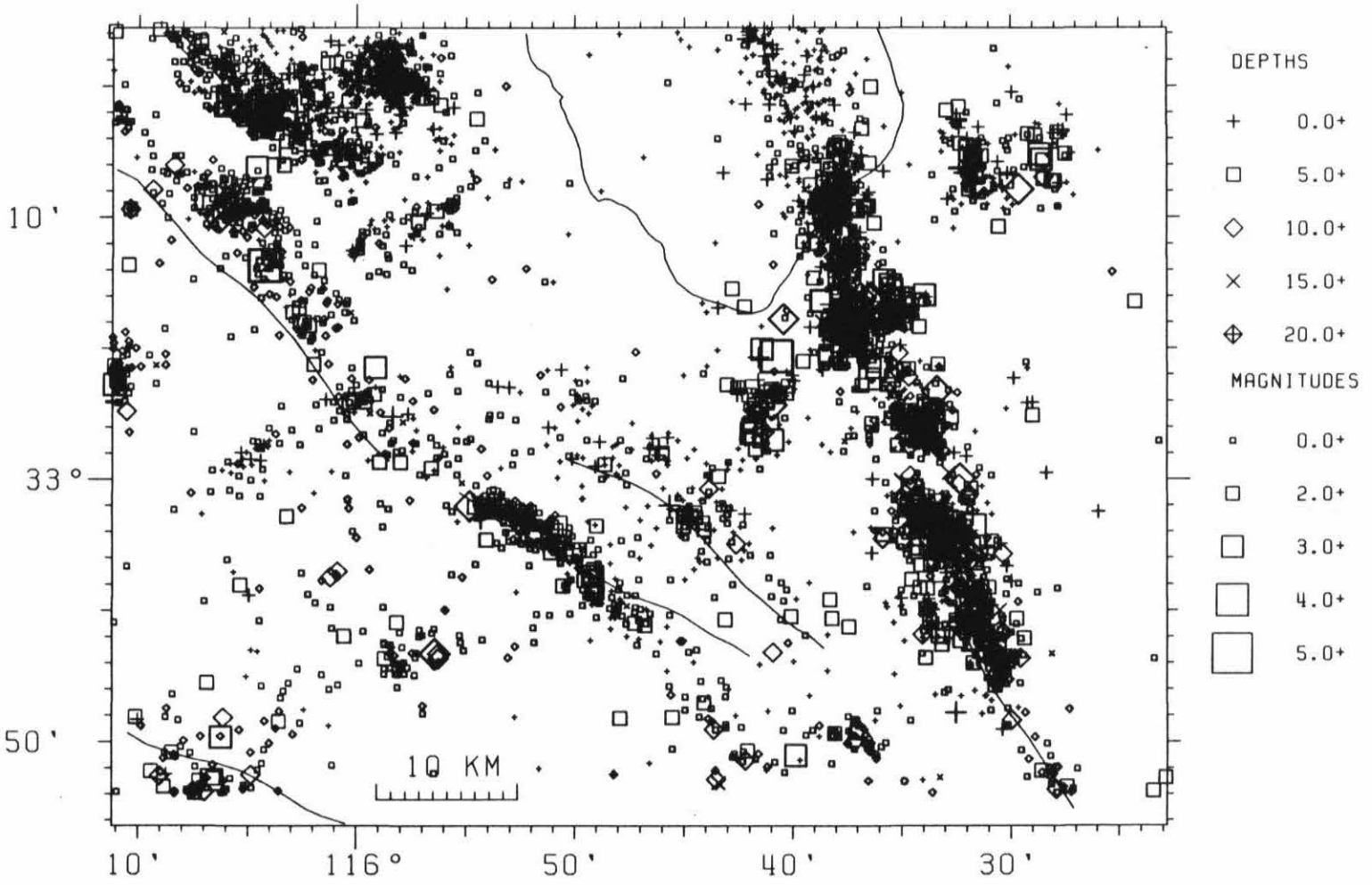

Figure 3.3. All earthquake locations from the Caltech catalog from 1980 to 1986 in the Imperial Valley region. The Westmorland sequence, mentioned in the text, is the alignment of events centered at $33^{o}2^{'}$ N, $115^{o}41^{'}$ W, between the Superstition Hills fault and the Brawley seismic zone.

various travel paths will sample different velocity complexities. It is therefore important to select appropriate master events.

The earthquakes were recorded on the Caltech-USGS seismic network in southern California. Routine processing (Given *et al.*, 1986) of events recorded from 24 November, 1987 to early February, 1989, produced the arrival times and first motions used here. To constrain the depth of the second main shock S-wave arrival times from a permanent station at Superstition Mountain and the temporary station KNB of the USGS Imperial Valley strong-motion network (Porcella *et al.*, 1987) and a KNB P-wave arrival time from a private seismograph network (I. Lutz, pers. comm.), are added to the phase file of the second main shock. The events are sorted into two groups according to their routine locations, those events that occur within the northeast trend along the Elmore Ranch fault, and those events that occur in the northwest trend along the Superstition Hills fault. Because the velocity structure differs between the western and the central Imperial Valley (Fuis *et al.*, 1982), different master events and velocity models are used in relocating the two groups. For the northeast group a well recorded foreshock serves as the master event, and a central Imperial Valley velocity model (Table 3.1) of Fuis *et al.* (1982, their Figure 22, southeast of shotpoint 13) is used.

The master event for the northwest-trending group is a 1985 earthquake from the Caltech catalog. Two velocity models are used for this group, depending on the azimuth of the seismic recording station from the second main shock. Stations west of a line through the second main shock epicenter and parallel to the San Jacinto fault zone use the velocity model of Hamilton (1970) (Table 3.1), which is appropriate for the thinner sediments and shallower basement of the western Imperial Valley. Stations east of the line

Table 3.1
Velocity Models

Central Imperial Valley		Western Imperial Valley, west		Western Imperial Valley, east	
P-Wave Velocity (km/sec)	Depth to Top of Layer (km)	P-Wave Velocity (km/sec)	Depth to Top of Layer (km)	P-Wave Velocity (km/sec)	Depth to Top of Layer (km)
2.0	0.0	2.5	0.0	2.5	0.0
3.1	1.0	5.1	0.4	4.5	1.5
3.8	2.0	6.0	2.9	6.2	3.0
4.6	3.0	7.1	14.0	7.0	12.5
5.3	4.0	7.9	25.0	7.9	25.0
5.8	4.8				
6.5	14.2				
7.3	15.4				
7.5	20.0				

The Western Imperial Valley velocity model is a hybrid model. A station west of a line drawn through the second mainshock and parallel to the strike of the San Jacinto fault zone uses the west model, a station to the east of the line uses the east model.

use a velocity model (Table 3.1) of Fuis *et al.* (1982, their Figure 22, east of shotpoint 1). The station locations and delays are listed in Table 3.2. Only P-wave delays were found from the master events. S-wave station delays were calculated from the P-wave delays by multiplication by the V_p / V_s ratio of 1.73.

The earthquakes are relocated using the program HYPOINVERSE (Klein, 1985) with station delays derived from the master events. To minimize uncertainties in the velocity models, only stations within 80 km are used. Stations within 40 km are given full weight, with the station weight tapering to zero at 80 km. S-wave arrivals are given one-half the weight of P-wave arrivals. In the hypocenter plots in the next section, only $M_L > 1$ earthquakes with horizontal and vertical location errors of less than 2 km, as indicated by the HYPOINVERSE parameters ERH and ERZ (Klein, 1985), are plotted. This filters out the earthquakes with poor depth control. Table 3.4 lists all the $M_L \geq 2$ earthquakes that have ERH and ERZ less than 1 km.

Focal mechanisms are determined for some $M_L \geq 3.0$ events that have more than 15 first motions by the grid searching program FPFIT (Reasenberg and Oppenheimer, 1985) after correcting the polarities of reversed seismometers with the information of Norris *et al.* (1986). The first motions were picked during routine processing and, except for the main shocks and the large aftershock of 1/28/88, not rechecked. Table 3.3 lists the fault plane solutions of all the focal mechanisms found.

3.3 Results

The first four days of the sequence. The relocated earthquakes are plotted in Figure 3.4 and most are listed in Table 3.4. The first main shock (0154:13.7 24 November 1987 GMT) location is $33^{o}\,4.9'$ N, $115^{o}\,47.7'$ W, at a

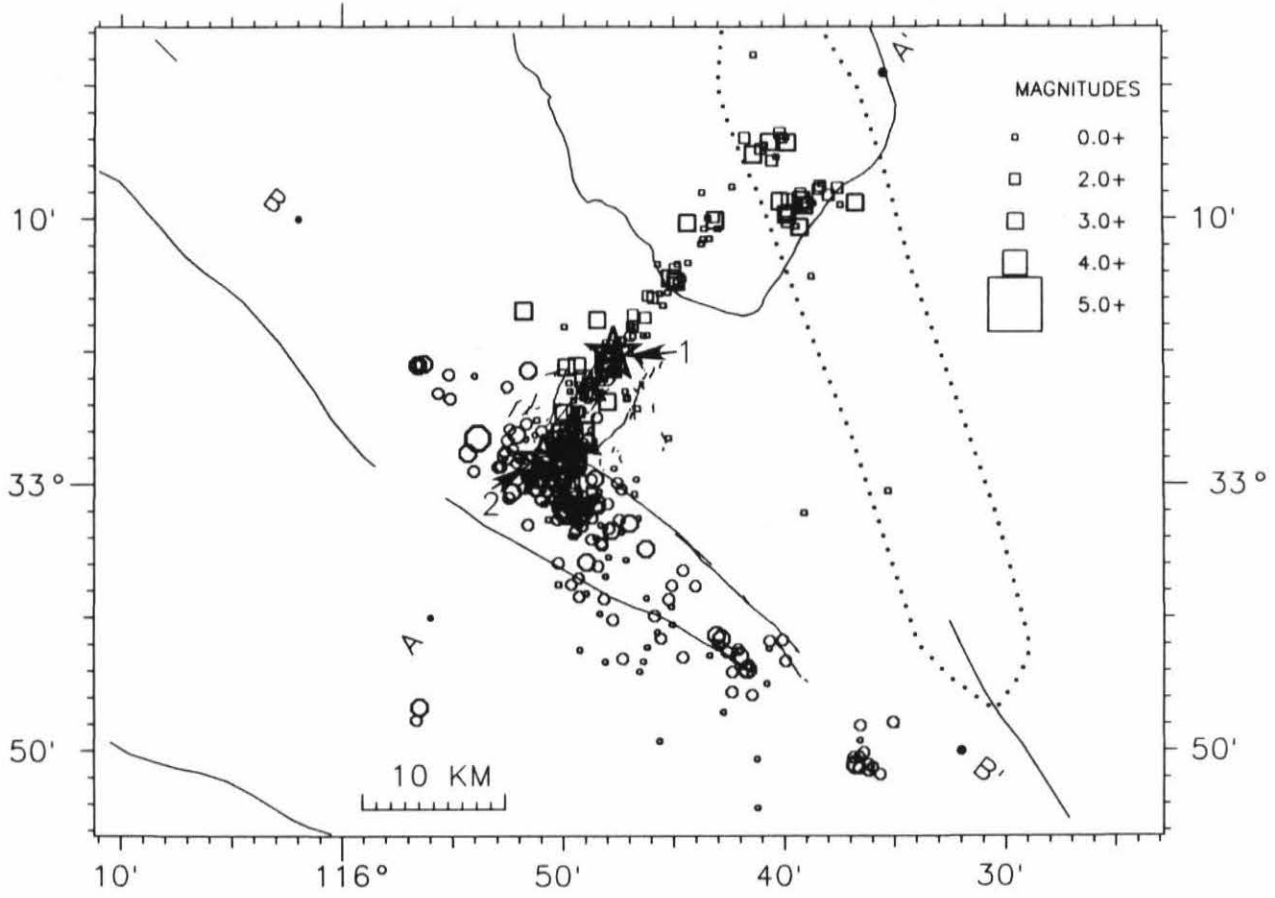

Figure 3.4. Events from 11/24/87 to 11/27/87 relocated in this study. Mainshocks are indicated by stars. The first and second mainshocks are labeled with 1 and 2, respectively. Events before the second mainshock are shown by squares. Events after the second mainshock are shown by octagons. AA' is location of the cross sections shown in Figures 3.5 and 3.9. BB' is location of cross sections shown in Figures 3.6 and 3.10. Only events of $M_L \geq 1$ and with ERH and ERZ ≤ 2 (see text) are plotted.

Table 3.2
Station Information and Delays

Station	Latitude	Longitude	Elevation *meters*	Central Imperial Valley velocity model delay *seconds*	Western Imperial Valley velocity model delay *seconds*	Model
AMS	33 8.48	115 15.25	140		-.12	e
BAT	33 27.54	115 50.46	-18		.05	e
BC2	33 39.42	115 27.67	1185	.16	.10	e
BON	32 41.67	115 16.11	14		.34	e
BRG	33 10.27	116 10.44	219		.12	w
CBK	32 54.94	116 15.16	390	.08	.16	w
CH2	33 17.77	115 20.17	347		-.20	e
CLI	33 8.45	115 31.64	-59	.06	.10	e
COK	32 50.95	115 43.61	-15	.10		
COY	33 21.63	116 18.56	232	.06	.00	w
CRR	32 53.18	115 58.10	98	-.09	.00	w
CTW	33 40.78	115 52.31	561	-.02	.00	e
ELR	33 8.84	115 49.95	-63	.25	.00	e
EMS	32 44.48	114 59.27	47	.51	.00	e
ERP	32 44.61	115 39.76	-9	.17	.30	w
FRG	33 45.43	116 03.69	934	.12	-.20	e
FRK	33 24.05	115 38.21	91		-.44	e
GLA	33 3.10	114 49.60	627	.13		
HAY	33 42.40	115 38.20	439	.20		
HOT	33 18.85	116 34.90	1963	.74	.40	w
IKP	32 38.93	116 6.48	957	-.06	-.17	w
ING	32 59.30	115 18.61	2	-.23	-.16	e
JUL	33 2.90	116 36.77	1292	.73	.48	w
LAQ	33 37.68	116 16.78	49		.12	e
LTC	33 29.34	115 4.20	458	.15	-.15	e
MEC	33 38.12	116 1.71	495	.12	.15	e
MIR	33 24.97	116 4.86	91		-.28	e
NW2	33 5.43	115 41.54	-68	-.19	-.07	e
ORK	33 33.97	115 46.15	1087	-.05		
RUN	32 58.33	114 58.63	152		.18	e
SGL	32 38.95	115 43.52	110		-.02	w
SLT	33 15.89	115 55.39	-50		.00	e
SMO	33 32.15	116 27.70	2437	.63	.30	w
SNR	32 51.71	115 26.21	-30	.32	.15	e
SUP	32 57.31	115 49.43	219	-.33	-.23	w
WIS	33 16.56	115 35.58	-68	-.21	-.10	e
WLK	33 3.08	115 29.44	-48	.11	.00	w
YAQ	33 10.08	116 21.00	441	.07	.06	w
YUH	32 38.86	115 55.38	186		-.10	w

The Model column flags which of the hybrid velocity models of the Western Imperial Valley model a station uses. 'e' is east, 'w' is west. See Table 3.1.

depth of 10.6 km. The first main shock, its foreshocks, and its aftershocks define a northeast-striking structure running from the northern end of the Superstition Hills fault to the northern end of the Brawley seismic zone defined by Johnson (1979). Many aftershocks occur within the Brawley seismic zone. Southwest of the first main shock the northeast structure bends to a more northerly strike and butts into the northwest trend, near the north end of the Superstition Hills fault. Here, the width of the northeast trend is about 5 km. Northeast of the first main shock, the trend is about 2 km wide.

The northeast trend events cluster in space and time. The first cluster consisted of the foreshocks and main shock. The seven foreshocks happened over a 22 minute period before the main shock, included two events of $M_L > 4.0$, and colocate with the main shock. A few minutes later events scatter to the north and west of the main shock, just off the main northeast trend. Twenty minutes to one hour after the main shock a group of events occurred near the intersection of the northeast structure and the Superstition Hills fault. This cluster remained active at a $M_L < 2.5$ level until the second main shock. Next, about two hours after the first main shock, a series of events occurred in the Brawley seismic zone, followed by aftershocks along the entire northeast trend.

The second main shock (1315:56.5 24 November 1987 GMT) occurred 12 hours after the first main shock at $33^{o}0.9^{'}$ N, $115^{o}50.9^{'}$ W, and at a depth of only 2 km. This location is at the intersection of the northeast trend defined by the aftershocks of the first main shock and the northwest trend defined by aftershocks of the second main shock. The aftershocks of the second main shock mostly lie west of the observed surface rupture on the Superstition Hills fault, in an area of low background seismic activity (Figure 3.3). The

aftershocks do not extend as far southeast on the Superstition Hills fault as the observed surface rupture. There is a group of aftershocks at the northwest end of the northwest trend. Excluding that group, the aftershocks extend only a few kilometers northwest of the surface rupture. North of $32^{o}58'$ the aftershock distribution has a sharp western boundary. The sharp boundary aligns with, but does not overlap the background seismicity trend that defines the Superstition Mountain fault (Figure 3.3). This boundary becomes more diffuse south of $32^{o}58'$ where the aftershock activity drops dramatically. A few aftershocks are off the main northwest trend, north of the second main shock. Aftershock activity on the northeast trend stopped almost completely after the second main shock.

Figure 3.5 is a cross section perpendicular to the strike of the Superstition Hills fault. Note the first main shock is deep (about 11 km) and the second is shallow (about 2 km). The maximum depth of aftershocks on both trends is the same (about 13 km), but most of the events on the northeast trend are deep and most of the earthquakes on the northwest trend are shallow. The deepest (10-13 km) northeast trend events are in two locations, west of the first main shock and in the Brawley seismic zone. Foci associated with the northwest trend, viewed along the azimuth of their trend, fill a volume between the Superstition Hills and Superstition Mountain faults, rather than defining a plane. Figure 3.6 is a cross section along strike of the Superstition Hills fault. A large (M_L 4.6) deep aftershock of the northwest trend occurs close to the join of the two trends.

The depth of the second main shock was tested in two ways. First, trial relocations at a range of fixed depths were made and travel time residuals to nearby seismograph stations were compared. The minimum residuals occur for

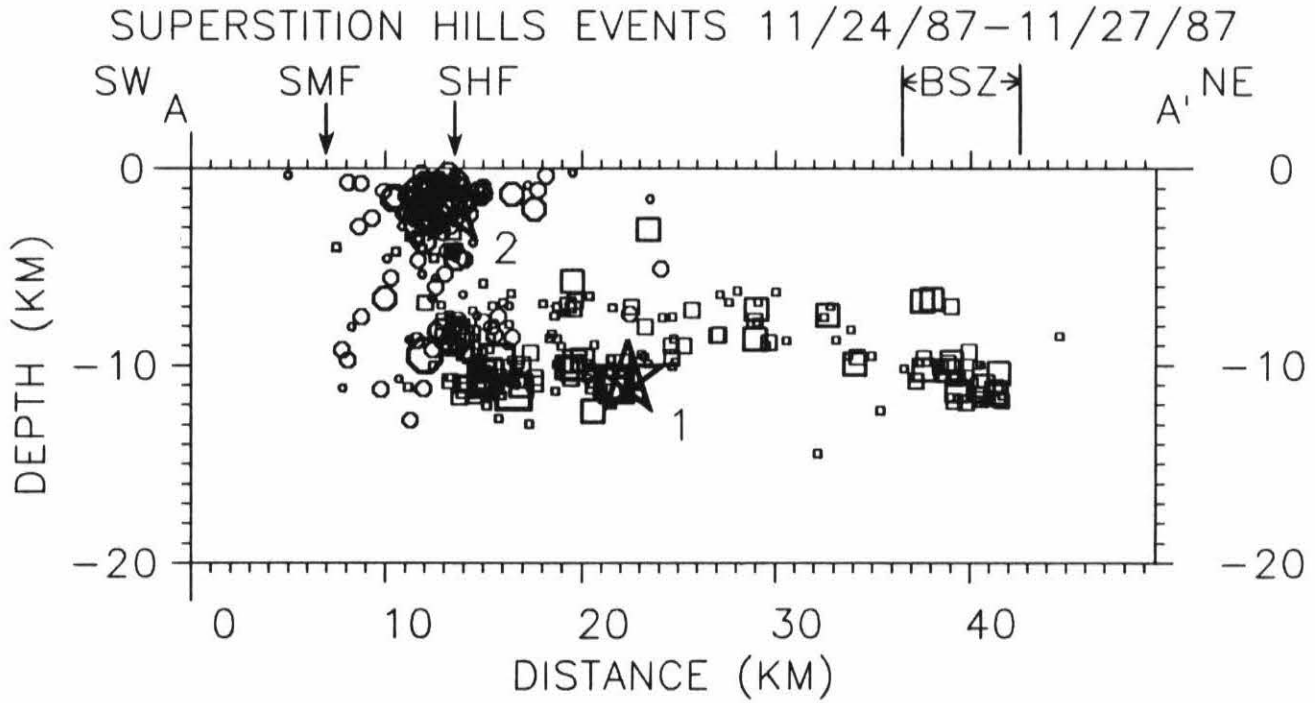

Figure 3.5. Cross section perpendicular to the Superstition Hills fault. All events in Figure 3.4 within 10 km of cross section are projected onto the plane of the figure. Intersections of cross section and faults are shown, with abbreviations as in Figure 3.1. Earthquake symbols as in Figure 3.4. Earthquake symbol size is proportional to earthquake magnitude.

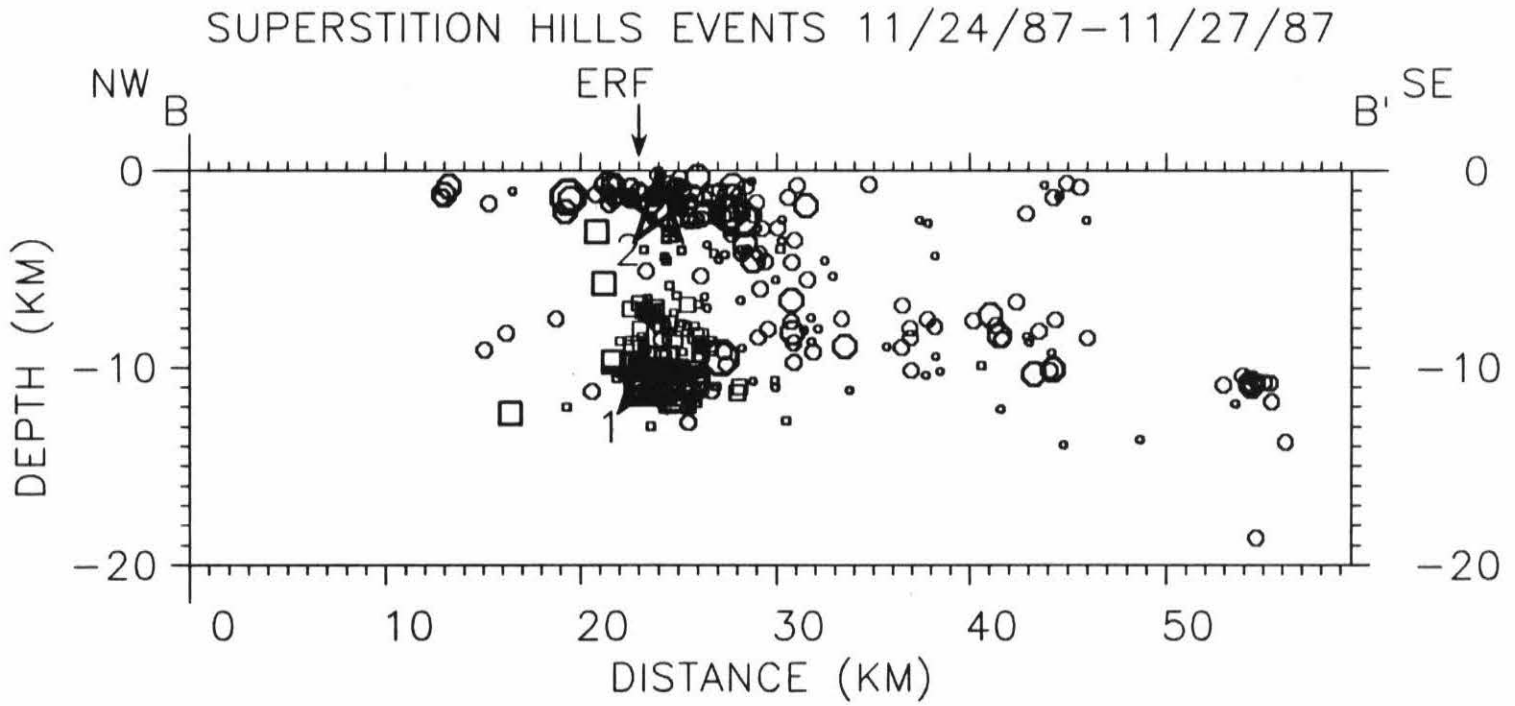

Figure 3.6. Cross section parallel to the Superstition Hills fault. All events in Figure 3.4 within 10 km of cross section are projected onto the plane of the figure. Earthquake symbols as in Figure 3.4. Earthquake symbol size is proportional to earthquake magnitude.

a shallow depth. Second, P-wave arrival times for nearby stations were swapped in and out of the phase file to ensure no erroneous pick was biasing the epicentral depth. The depth is insensitive to such swapping.

Focal mechanisms of $M_L \geq 3.0$ events for which 15 or more reliable first motions could be obtained are displayed in Figure 3.7 and listed in Table 3.3. A high quality mechanism for the first main shock could not be calculated because many of its first motions were obscured by an immediate foreshock. The mechanisms show mostly strike slip faulting, with some having a component of normal or reverse slip. The foreshocks (numbers 2 and 3 on Figure 3.7) and aftershocks of the first main shock (numbers 8, 9, 11, and 12) on the northeast trend have a nearly vertical fault plane parallel to the strike of the northeast trend. Because of observed left-lateral surface rupture and the hypocentral alignment, these events are most likely to be left-lateral. Some aftershocks of the first main shock form a short northwest lineation within the northeast trend (numbers 4-7 and 13) and have similar mechanisms, but because of their position in the short northwest lineation, they may be right-lateral on a northwest strike, representing activation of a northwest structure prior to the second main shock. The nodal-plane orientations of one event in the Brawley seismic zone (number 10) are different than the other aftershocks.

The mechanism of the second main shock (number 1) has a vertical northwest-striking fault plane that agrees with the strike of the Superstition Hills fault. South of the main shock, the fault plane for right-lateral motion of the aftershocks (numbers 16, 17, 20-25, 27-29) tends to strike more nearly east-west than that of the main shock. North of the main shock, the aftershock mechanisms (numbers 19 and 26) closely match the main shock mechanism. Mechanisms of events in the northernmost group (numbers 15

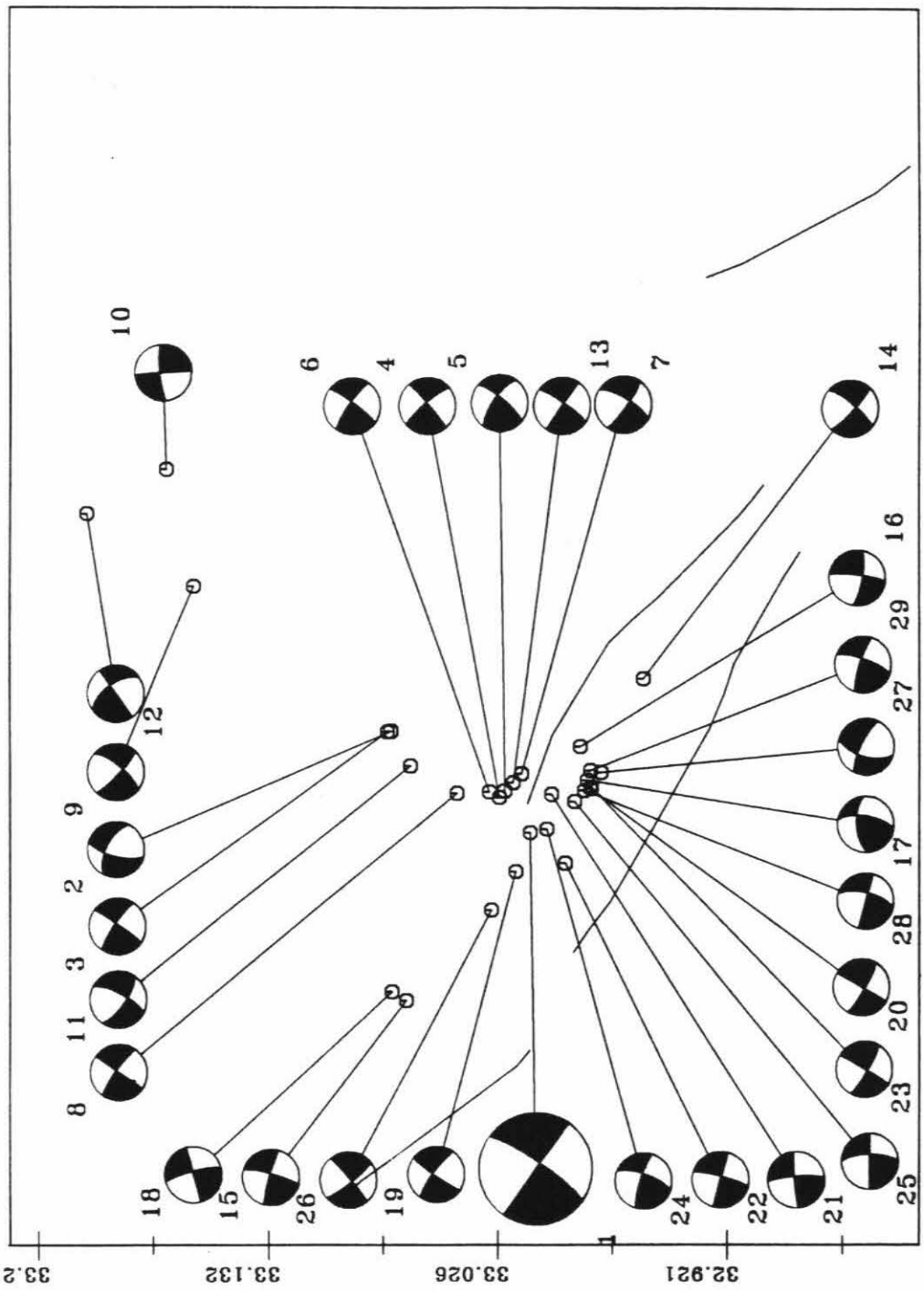

Figure 3.7. Focal mechanisms (lower hemisphere, compressional quadrants shaded) of selected $M_L \geq 3.0$ events during 11/24/87 to 11/27/87. Second mainshock shown by larger symbol. Numbers are for reference and do not indicate order of occurrence. Focal parameters are listed in Table 3.3.

Table 3.3

Fault Plane Solutions

Yr-Mo-Da	HrMn	Sec	Latitude		Longitude		Depth *km*	Magnitude	Focal Mechanism Dip dir	Dip	Rake
87-11-24	132	47.3	33	4.53	115	47.95	10.8	4.1	30	75	-150
87-11-24	153	2.4	33	4.63	115	47.97	11.0	4.0	305	85	-10
87-11-24	214	34.6	33	1.54	115	50.14	10.5	4.4	135	70	30
87-11-24	221	58.7	33	1.39	115	49.92	10.7	3.9	305	80	-20
87-11-24	252	59.9	33	1.81	115	49.95	9.8	4.7	305	85	-10
87-11-24	328	57.1	33	0.93	115	49.37	10.8	3.1	30	80	-150
87-11-24	343	54.2	33	2.71	115	49.99	11.0	3.8	125	80	10
87-11-24	400	44.3	33	9.95	115	43.13	9.9	3.2	315	85	-10
87-11-24	404	36.3	33	10.70	115	39.21	9.8	3.6	260	85	150
87-11-24	542	53.4	33	3.99	115	49.09	9.7	3.1	210	70	170
87-11-24	621	53.8	33	12.89	115	40.68	11.0	3.2	145	85	20
87-11-24	623	22.3	33	1.16	115	49.65	11.0	3.9	310	75	0
87-11-24	1315	56.4	33	0.69	115	51.31	1.9	6.3	125	85	0
87-11-24	1656	52.4	32	57.58	115	46.25	8.9	3.1	225	85	-160
87-11-24	1847	24.6	33	4.10	115	56.87	2.0	3.8	290	75	0
87-11-24	2344	53.3	32	59.31	115	48.48	4.5	3.1	185	55	120
87-11-25	133	30.0	32	59.12	115	49.58	2.3	3.0	110	70	40
87-11-25	208	30.7	33	4.50	115	56.57	1.2	3.0	165	90	-170
87-11-25	247	57.5	33	1.08	115	52.61	0.7	3.3	110	60	20
87-11-25	430	17.9	32	59.03	115	49.86	2.0	3.4	305	85	10
87-11-25	607	3.6	32	59.72	115	52.33	1.5	3.4	120	90	-10
87-11-25	1354	10.1	32	59.01	115	49.81	2.1	4.2	305	85	10
87-11-26	19	31.4	33	0.23	115	51.18	0.8	3.6	265	55	-30
87-11-26	156	27.6	32	59.46	115	50.28	2.0	3.7	90	65	0
87-11-26	1739	1.9	33	1.75	115	53.89	1.3	4.3	135	80	0
87-11-27	110	8.1	32	58.74	115	49.33	3.7	3.0	205	70	140
87-11-27	110	10.4	32	59.20	115	49.92	9.5	4.6	125	45	60
87-11-28	39	11.0	32	59.02	115	49.26	2.4	4.2	110	80	10
87-11-29	1719	48.0	33	0.95	115	52.62	1.4	3.0	225	70	-170
87-11-30	1954	49.0	32	58.74	115	48.92	2.8	3.0	115	65	40
87-12-02	403	6.2	33	0.19	115	49.53	1.9	4.6	30	90	180
87-12-03	205	27.2	32	55.51	115	42.85	1.3	2.4	30	85	180
87-12-03	1345	57.9	33	0.07	115	48.14	9.9	3.1	135	80	20
87-12-03	1904	36.5	33	0.73	115	53.49	1.1	3.8	20	90	170
87-12-04	523	54.1	32	59.17	115	49.25	5.6	3.1	100	45	50
87-12-08	636	5.9	33	0.42	115	50.78	2.0	3.1	95	75	-20
87-12-08	1845	33.1	33	0.22	115	52.26	1.1	3.4	170	85	-180
87-12-12	1820	49.0	32	59.98	115	48.93	7.1	3.0	150	80	30
87-12-13	1502	39.0	32	53.42	115	42.19	9.7	3.2	205	70	120
87-12-18	1326	15.1	32	48.27	115	41.52	11.3	2.3	165	75	-60
88-01-05	730	56.4	32	59.96	115	49.29	2.8	3.1	275	85	-30
88-01-21	1435	19.4	32	52.40	115	47.01	5.6	2.4	110	15	20
88-01-28	254	2.3	32	53.89	115	40.87	9.8	4.7	130	65	80
88-01-28	313	34.1	32	53.81	115	40.48	9.8	2.5	75	70	-140
88-01-29	2140	49.0	32	53.94	115	41.24	8.8	2.0	35	80	-130
88-02-02	1818	34.1	33	0.06	115	47.37	11.3	3.0	110	85	30
88-04-24	1213	38.9	32	53.28	115	38.41	10.5	3.1	295	70	0
88-07-03	1401	13.4	32	53.71	115	40.16	10.2	2.5	20	70	-170
88-07-03	2040	35.7	32	53.99	115	39.32	0.7	2.8	195	70	170
88-07-10	730	59.3	32	52.65	115	41.62	10.3	2.0	150	80	-10
88-07-20	300	40.3	33	1.83	115	50.72	1.6	3.0	135	75	20
88-07-30	823	22.2	32	53.29	115	41.15	10.0	2.9	120	85	50
88-11-08	434	33.1	32	52.13	115	39.75	10.4	3.2	205	65	-170
89-02-15	1350	41.5	33	1.62	115	50.99	2.2	3.6	130	80	10

and 18) differ. These events and the event in the Brawley seismic zone (number 10) did not occur on the principal conjugate fault system.

The sequence from 11/28/87 to 2/9/89. To observe the development of the earthquake sequence and identify active structures, about 1800 more aftershocks over fifteen months are relocated. These relocations are shown in Figures 3.8, 3.9, and 3.10. Only $M_L > 1$ earthquakes with horizontal and vertical location errors of less than 1 km, as indicated by the HYPOINVERSE parameters ERH and ERZ (Klein, 1985), are plotted in this section's figures and listed in Table 3.4. These magnitude and error cutoffs are chosen to eliminate those earthquakes with few picks that tend to get stuck on velocity interfaces during the location program. Every earthquake during this time period within the dashed lines in Figure 3.2 is relocated.

Relatively few additional earthquakes occur on the Elmore Ranch fault during this time (Figures 3.8 and 3.9), consistent with the shutoff of seismic activity on that fault following the mainshock on the Superstition Hills fault.

In the Brawley seismic zone, 2 new groups of seismic activity are seen. One group consists of a dozen small, $M_L < 2.8$ events that appear to be an extension of the Elmore Ranch fault to the east edge of the Brawley seismic zone. These earthquakes occurred throughout the entire time period. The other group is the cluster under the south edge of the Salton Sea. This cluster was active during the first few hours of the Elmore Ranch faulting, after which it was quiet until activity resumed between April and June 1988. During those months, a few dozen $M_L < 2.5$ earthquakes occurred. These earthquakes were in a 5 km long lineation oriented north-northwest in the middle of the earlier cluster. From October 1988 to February of 1989 an intense swarm occurred east of the previous activity. This swarm of over 100

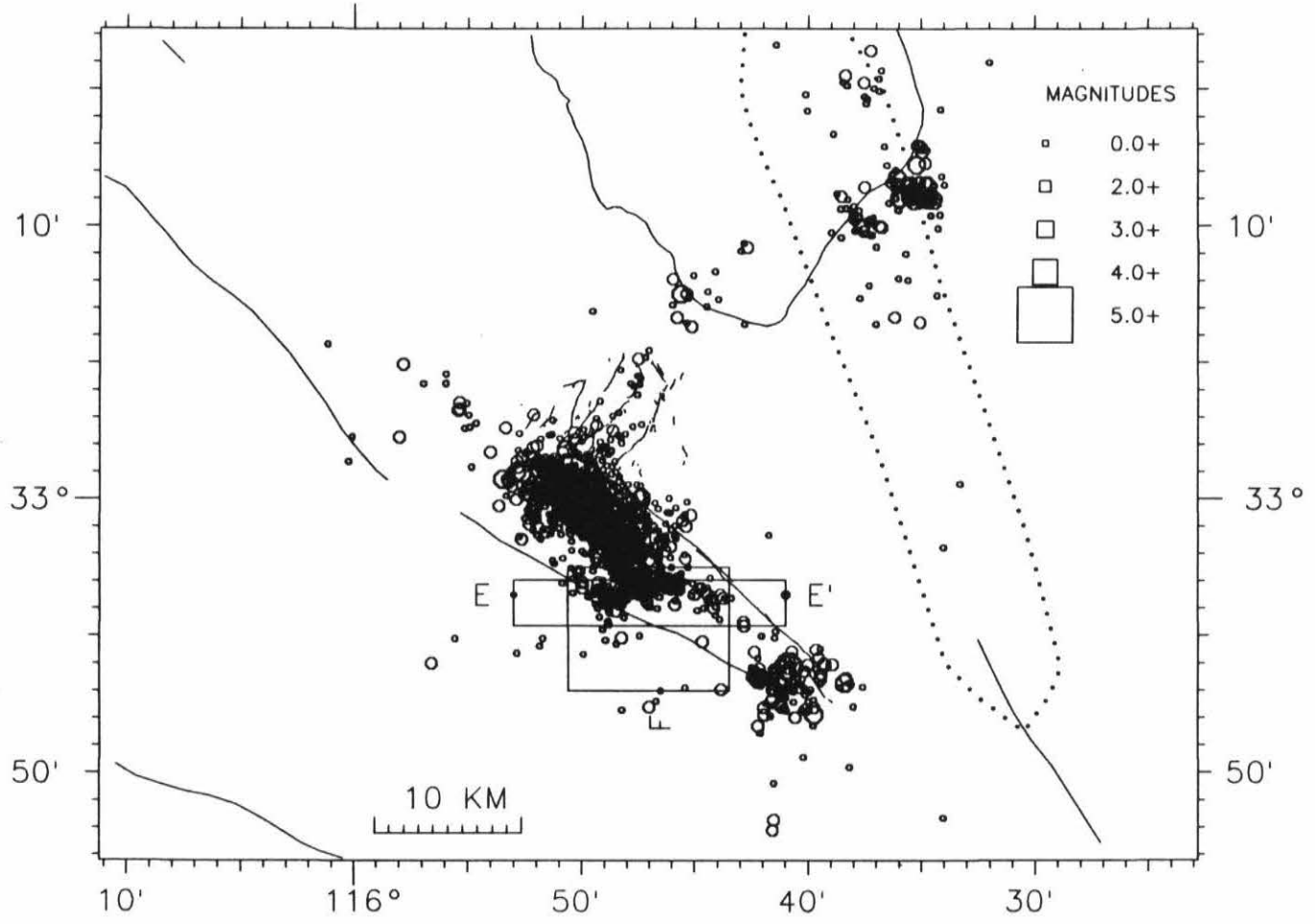

Figure 3.8. Events from 11/28/87 to 2/9/89 relocated in this study. Only events of $M_L \geq 1$ and with ERH and ERZ ≤ 1 (see text) are plotted. Symbols as in Figure 3.4. Boxes EE' and FF' enclose earthquakes plotted in cross sections in Figure 3.12.

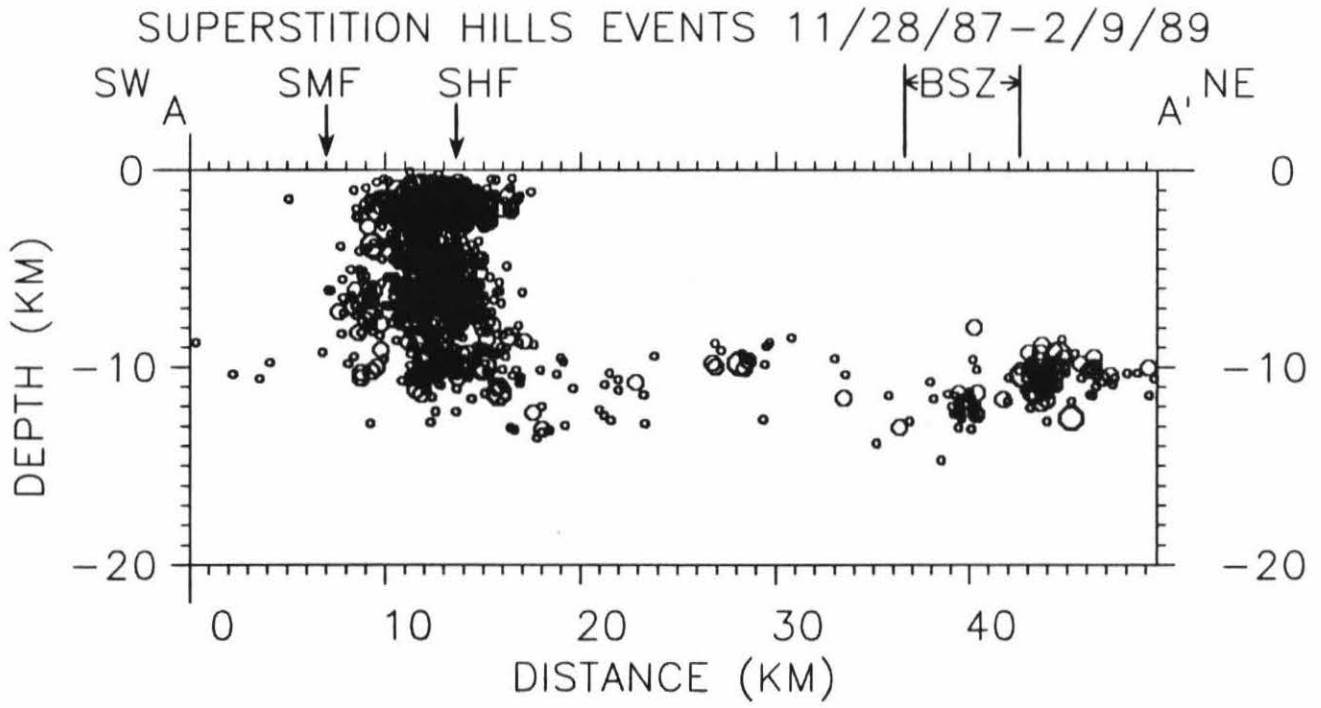

Figure 3.9. Cross section perpendicular to the Superstition Hills fault. All events in Figure 3.8 within 10 km of cross section are projected onto the plane of the figure. Intersections of cross section and faults are shown, with abbreviations as in Figure 3.1. Earthquake symbols as in Figure 3.4. Earthquake symbol size is proportional to earthquake magnitude.

earthquakes included 6 $M_L > 3$ events. All the above activity in the Brawley seismic zone was deep, about 10 km. The Elmore Ranch faulting caused aftershocks in the Brawley seismic zone early in the sequence, and the above swarms represent migration of Brawley seismic zone activity similar to that documented by Johnson (1979).

The aftershock activity along the Superstition Hills fault during this time can be divided into three groups (Figure 3.8). These groups are: 1. The region west of the northern Superstition Hills fault, similar to aftershock area described above for the first four days of the sequence. 2. An east-west band of small aftershocks at about latitude $32^{o}56.5^{'}$. 3. An area at the south end of the Superstition Hills fault. Each group is described below.

The first group occupies a volume similar to that defined by the aftershocks during the first four days of the sequence. The volume lies west of the surface trace of the northern Superstition Hills fault and has a sharply defined western boundary. The western boundary aligns with, but does not overlap, the background seismicity trend that defines the Superstition Mountain fault (Figure 3.3). The north boundary of the area is 2 km northwest of the intersection of the Superstition Hills and Elmore Ranch faults. Only a few aftershocks occur further northwest. To the southeast, this group of aftershocks extends to the northern side of the step between the north and south segments of the surface trace of the Superstition Hills fault. The northwest and southeast boundaries of this group both trend northeast. The volume filled by this group of aftershocks is vertical when viewed in cross section perpendicular to fault strike (Figure 3.9, km 10 to 15). Focal mechanisms (Figure 3.11 and Table 3.3) are similar to those from the first four days (Figure 3.7).

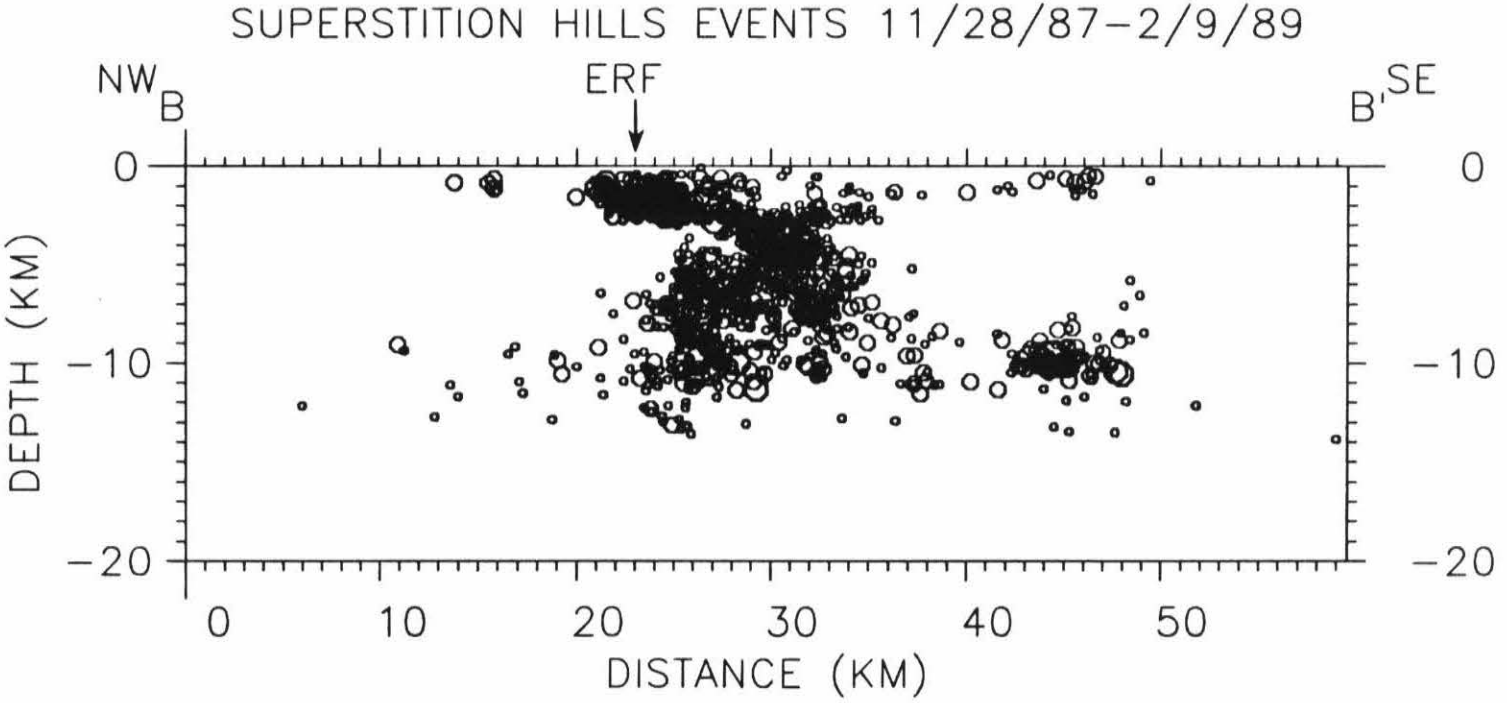

Figure 3.10. Cross section parallel to the Superstition Hills fault. All events in Figure 3.8 within 10 km of cross section are projected onto the plane of the figure. Earthquake symbols as in Figure 3.4. Earthquake symbol size is proportional to earthquake magnitude.

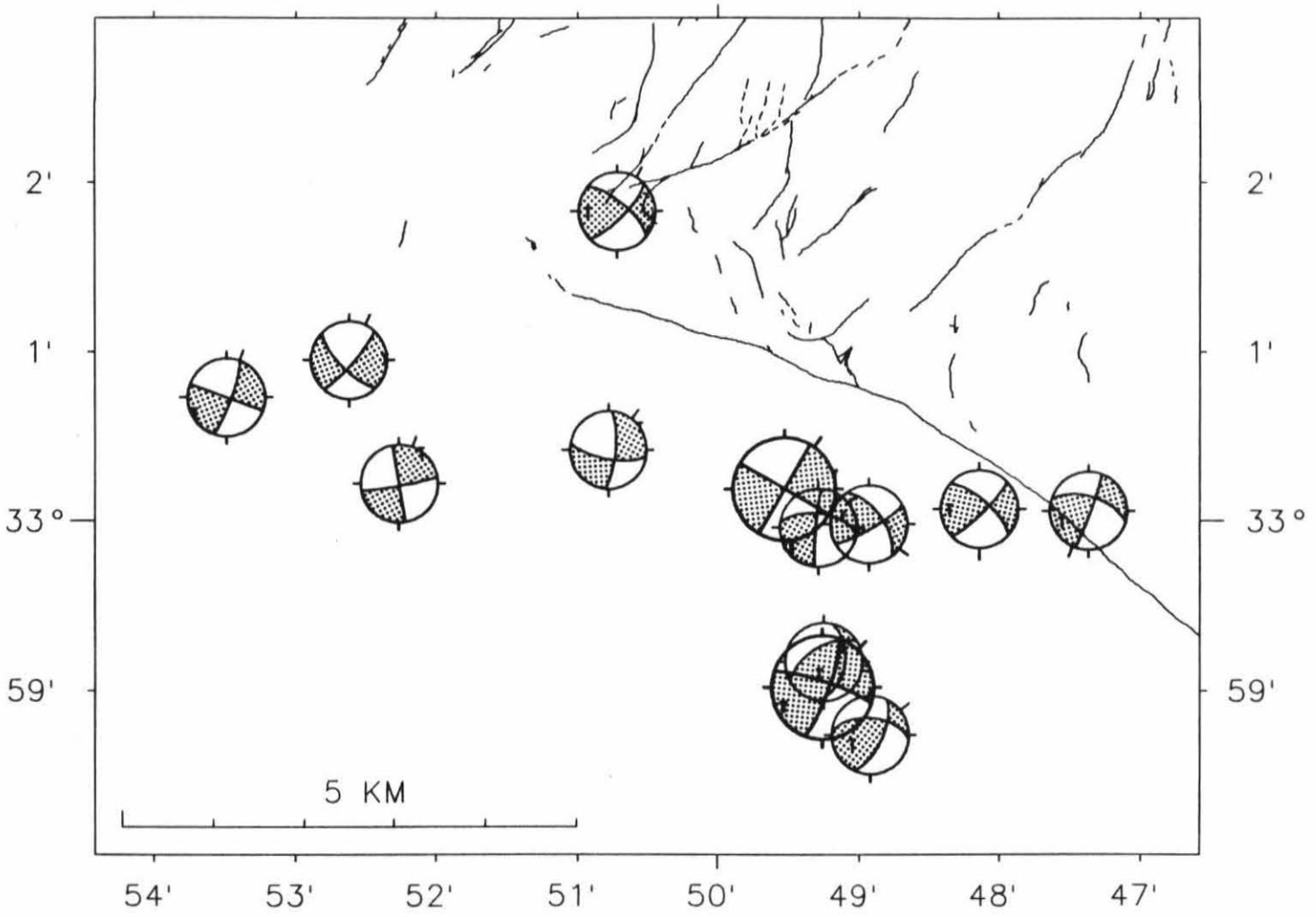

Figure 3.11. Focal mechanisms (lower hemisphere, compressional quadrants shaded) of selected $M_L \geq 3.0$ group 1 (see text) events during 11/28/87 to 2/9/89. Focal parameters are listed in Table 3.3.

The aftershocks of the first group occupy a volume rather than a plane. The volume is between the surface traces of the Superstition Hills and Superstition Mountain faults, in an area of very low background seismic activity (Figure 3.3). The Superstition Mountain fault has a very distinct definition in the background seismic activity, while the Superstition Hills fault has only a fuzzy definition. It is therefore difficult to predict the shape of an aftershock zone along the Superstition Hills fault, but nevertheless it is curious that the first group of aftershocks are all in a volume west of the surface trace and background seismicity of the fault. To test the relative locations of the aftershocks and the background seismicity trends of the Superstition Hills and Superstition Mountain faults, events from the seismicity trends of both faults were relocated by the same method as the aftershocks described above. Earthquakes from the Superstition Hills fault seismicity trend relocate a km or so west of their catalog locations, but still are east of the fault. Earthquakes from the Superstition Mountain fault seismicity trend also relocate about a km west of their catalog locations, further from the sharp western boundary of the aftershocks. The difference between the catalog locations and the relocations is mostly due to the use of the hybrid velocity model in the relocations that better models the lateral velocity variations in the region. The relocated background events do not move into the aftershock area, so the relative locations of the background seismicity trends and aftershocks are real.

The second group of aftershocks occupies an east-west trending zone near the middle of the Superstition Hills fault (Figure 3.8). These aftershocks define a narrow, vertical structure from 1 to 11 km depth (Figure 3.12). These aftershocks are small, with only 2 events with $M_L > 3$. The east and

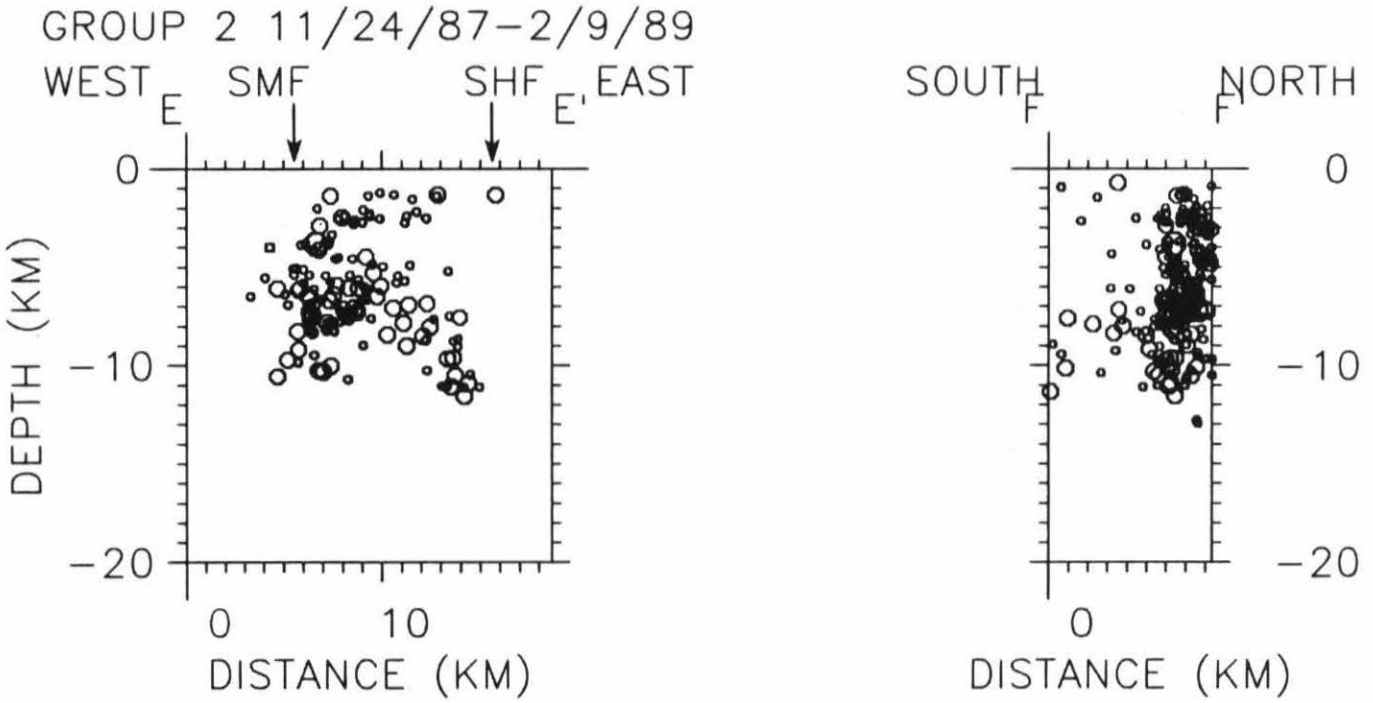

Figure 3.12. Cross sections of group 2 (see text) events from 11/24/87 to 2/9/89. Events within boxes on Figure 3.9 are plotted. Earthquake symbols as in Figure 3.4. Earthquake symbol size is proportional to earthquake magnitude.

west ends of the zone are bound by the Superstition Hills fault and the Superstition Mountain fault, respectively. The M_L 3+ events occurred at the intersection with the Superstition Mountain fault. This intersection also marks the place at which the background seismic trend leaves the surface trace of the Superstition Mountain fault. Reliable focal mechanisms are difficult to obtain for such small earthquakes, but those examined (not shown) have quite variable mechanisms and focal planes, so do not aid in a structural interpretation. This zone of aftershocks was most active during the first six weeks following the Superstition Hills mainshock to the north, but also had renewed activity following the M_L 4.7 1/28/88 aftershock to the south (described below). This feature is the only east-west trending structure in the Imperial Valley region.

The third group of aftershocks is at the south end of the Superstition Hills fault, at the right step to the Wienert fault. Activity in this group began three hours after the Superstition Hills mainshock with several M_L 3+ events along a northwest-striking lineation that, in map view, appears to lie under the Superstition Mountain fault but is east of that fault's background seismicity trend (Figure 3.3). Thus the lineation must be along the southern Superstition Hills or Wienert faults dipping to the west. Smaller aftershocks continued along the 5 km long lineation until a M_L 4.7 thrust event occurred just to the east of the lineation at 02:54 on 1/28/88. Aftershocks then spread a few km east and south. Most of the events in this group are in a narrow depth range, 8 to 11 km, (Figure 3.10) with a few small events at shallow depth. Focal mechanisms are shown in Figure 3.13 and listed in Table 3.3. The thrust mechanism of the 1/28/88 event is unexpected. From the narrow depth range of that event's aftershocks, the shallowly north-dipping fault

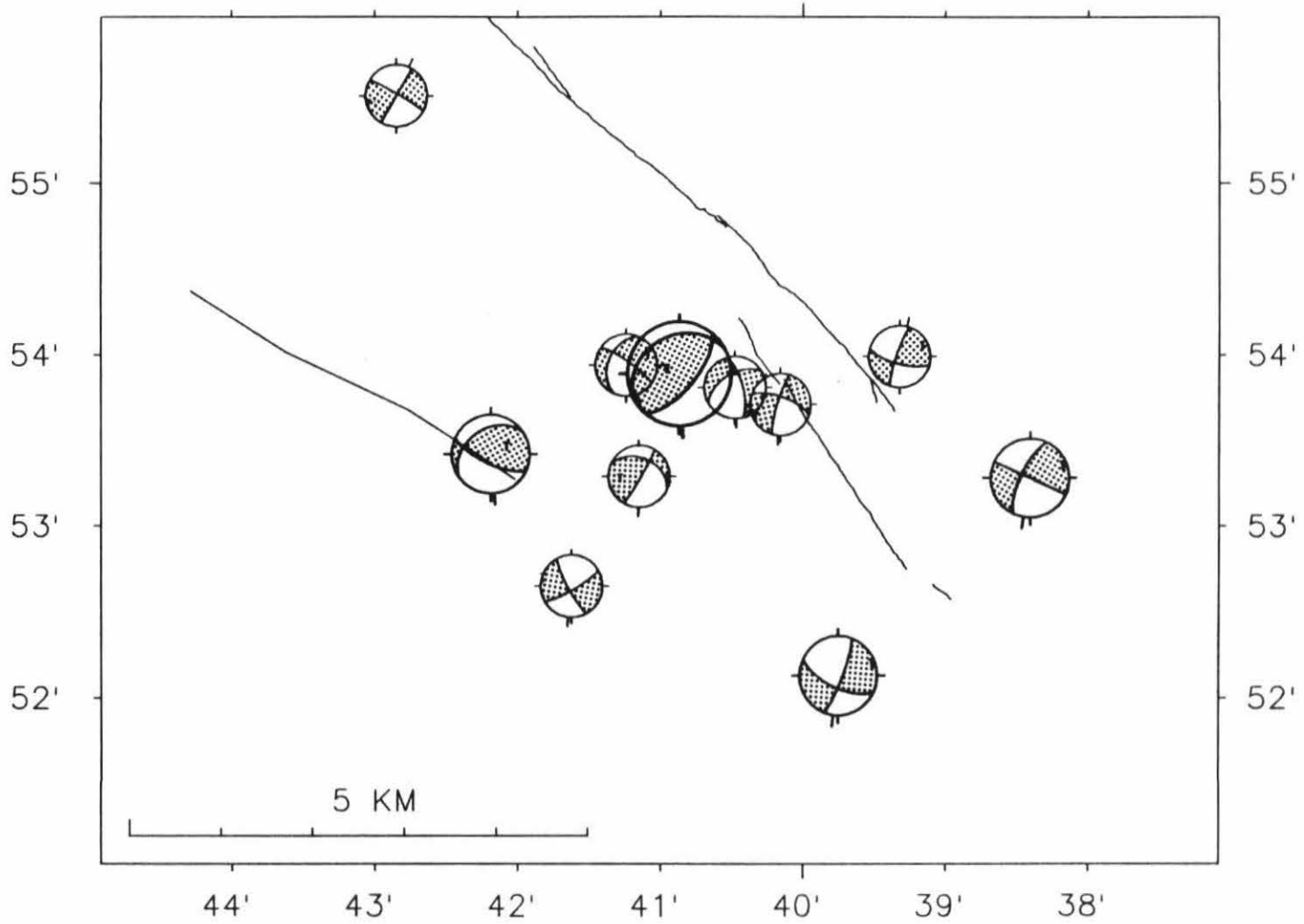

Figure 3.13. Focal mechanisms (lower hemisphere, compressional quadrants shaded) of selected $M_L \geq 3.0$ group 3 (see text) events during 11/28/87 to 2/9/89. Focal parameters are listed in Table 3.3.

plane is preferred. The other events have right-lateral strike-slip mechanisms, some with a strong thrust component. The 1/28/88 event is the largest aftershock along the Superstition Hills fault. It is the only $M_L > 4$ aftershock (out of seven) to occur outside the area of the first group. The third group of aftershocks, like the other two groups, occurs in an area of low background seismic activity (Figure 3.3).

3.4 Interpretation

The Imperial Valley lies astride the Salton trough, the sediment filled landward extension of the actively spreading Gulf of California (*e.g.*, Larson, 1972). Fuis *et al.* (1982) performed a large seismic refraction study in the Imperial Valley region. They combined seismic refraction, gravity, and well data to define two types of basement rocks. The first type, under the flanks of the Imperial Valley, are the pre-rifting continental crystalline plutonic and metamorphic rocks. These basement rocks are about two kilometers deep west of the Superstition Hills fault. The second type is metamorphosed sedimentary rocks under the central Imperial Valley at about five kilometers depth under the southern Salton Sea. A steep basement gradient under the Superstition Hills fault separates the two basement types (Fuis *et al.*, 1982). Reproduced in Figure 3.14 is a map of the structure and tectonics of the Imperial Valley area (from Fuis *et al.*, 1982) showing the inferred extent of continental crystalline basement rocks. Note the complex distribution of crystalline basement rocks in the area of the Superstition Hills earthquakes.

Figure 3.15 shows the extent of the basement from Figure 3.14 superposed on a map of the first four days of aftershocks. The first main shock and its foreshocks are located at a corner in the basement where the basement protrudes eastward into the Imperial Valley. Several aftershocks

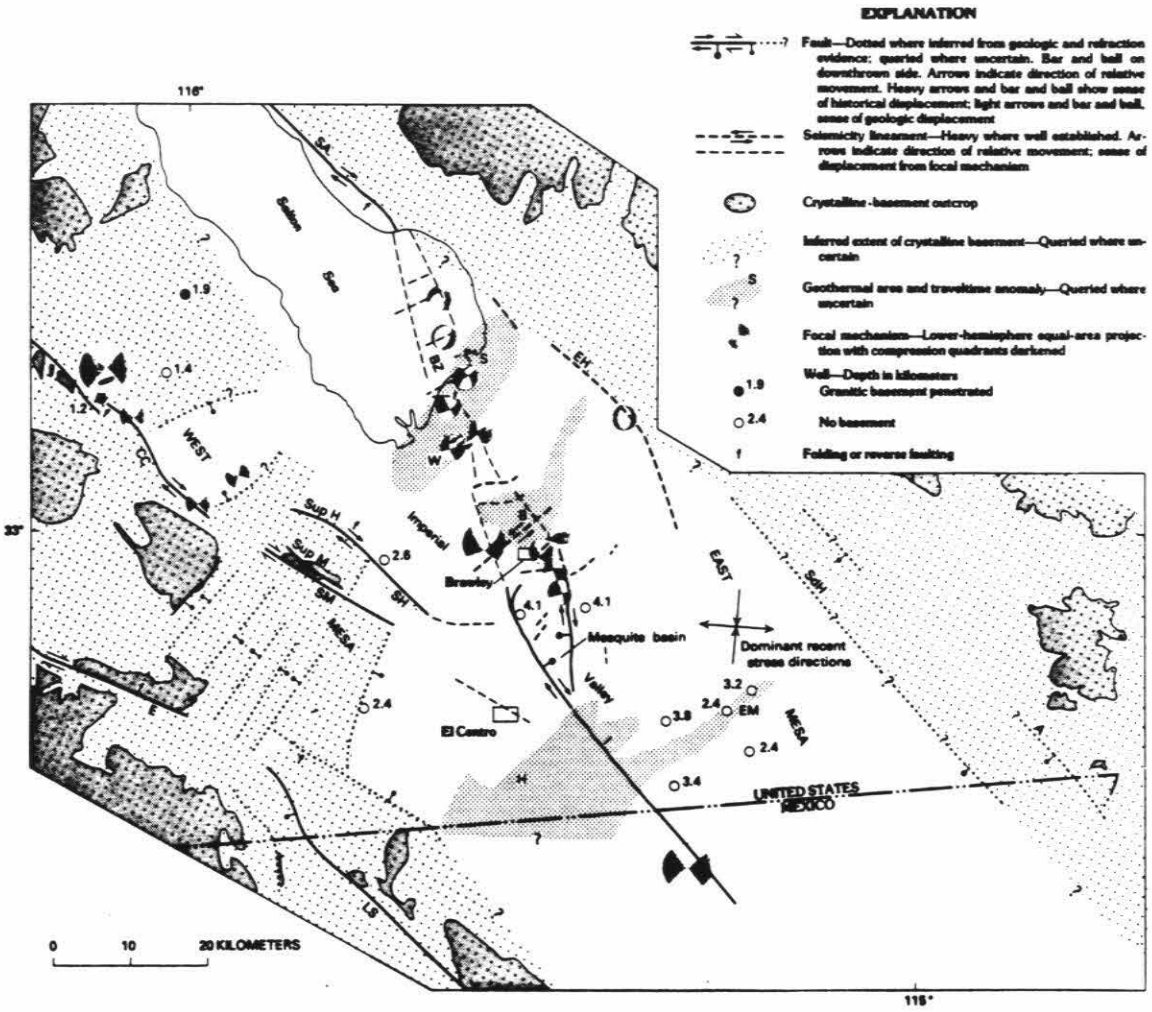

Figure 3.14. Figure 24 of Fuis *et al.*, (1982), showing tectonic and basement features of the Imperial Valley region as determined from refraction, gravity, and well data. Abbreviation: Sup M, Superstition Mountain.

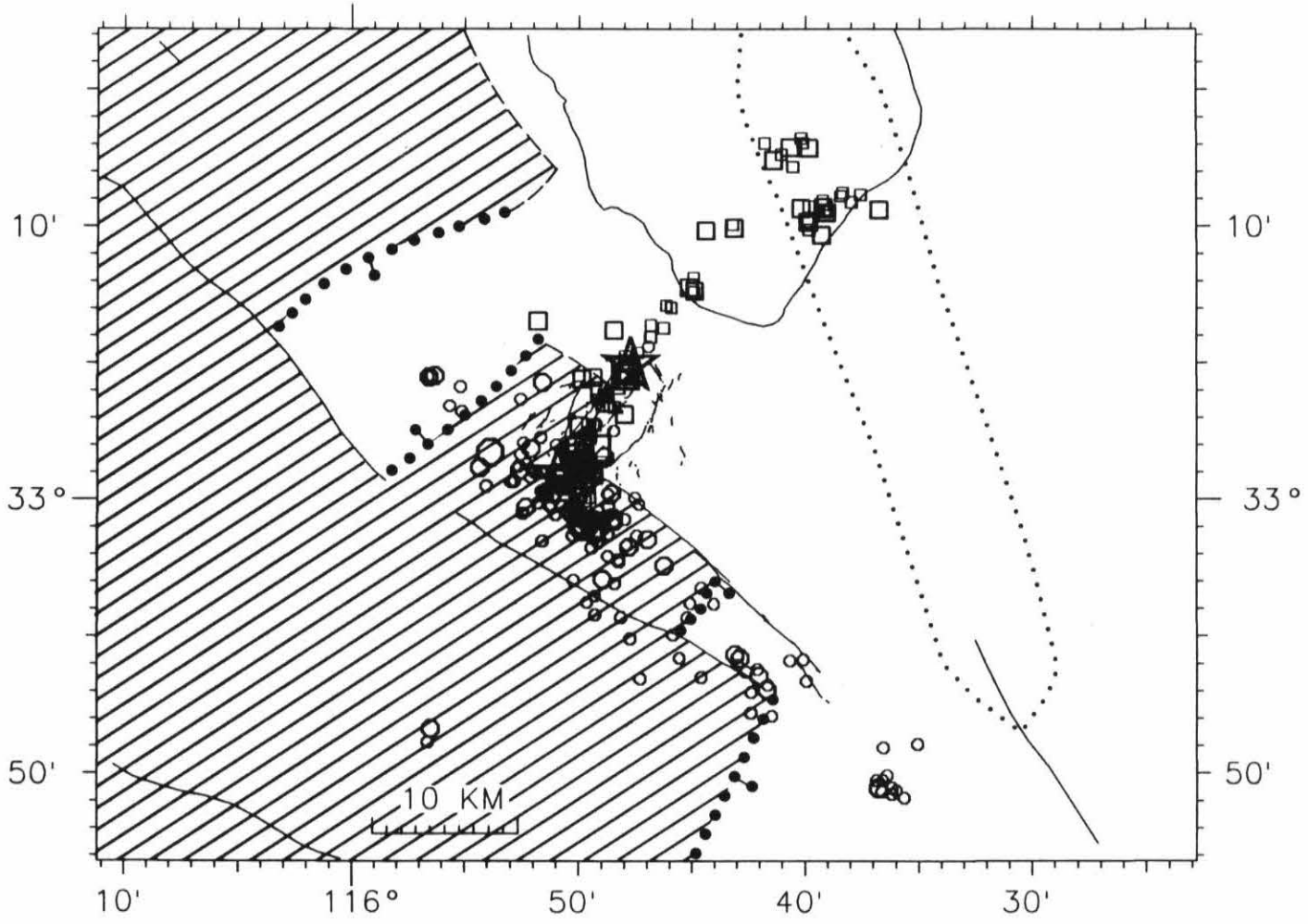

Figure 3.15. Basement features from Figure 3.14 superposed on $M_L \geq 2.0$ earthquake relocations from this study. Earthquakes from 11/24/87 to 11/27/87. Symbols as in Figure 3.4. Shading represents extent of crystalline basement.

are distributed in the rest of the protrusion. The larger ($M_L \geq 3.5$) aftershocks of the northeast trend lie no further northeast than the basement protrusion. The second main shock is at another, interior, corner of the basement. The aftershocks on the Superstition Hills fault end both to the southeast and to the northwest where the basement ends. The group of aftershocks at the northwest end of the northwest trend cluster at a basement edge. There is an alignment of aftershocks along the basement edge at the south end of the northwest trend. The west edge of the northwest trend aligns with the fault bounding Superstition Mountain. There is an epicenter lineation at the basement corner at the south end of the Superstition Mountain fault. It is concluded that the larger earthquakes tend to occur within, or along the edge of, the crystalline basement rocks.

The second and third groups of aftershocks along the Superstition Hills fault later during the sequence (described above) occur at right steps between strands of the fault. The step between the north and south segments of the Superstition Hills fault is coincident with the change in basement rock types. This suggests that the geometric complications of that step extend to depth. Sharp *et al.*, 1989, observe that the 3.6 km overlap of the fault segments is long with respect to the width, less than 300 m, of the step. This also suggests a deep extent of the step. The east-west band of aftershocks in the second group may be the edge of the crystalline continental basement rocks, or mark a terrace within those basement rocks. The northeast-trending southern edge of the first group of aftershocks may also be a terrace or other structure in the crystalline basement rocks. The southern edge of that aftershock group lines up with, and is parallel to, the northeast-trending 1981 Westmorland seismicity lineament to the east of the Superstition Hills fault

(Figure 3.2).

The M_L 4.7 1/28/88 aftershock in the third group of aftershocks along the Superstition Hills fault was a thrust rupture on a northeast-striking plane. It occurred at the right step between the southern Superstition Hills fault and the Wienert fault. A right step in a right-lateral fault produces extension, so the mechanism of the 1/28/88 aftershock is unexpected. The mechanism may be due to geometric complications in the step. A similar situation is reported by Sharp *et al.*, (1989), who report a thrust fault among many strike-slip faults in the step between the north and south segments of the Superstition Hills fault. A left step in a right-lateral fault will produce compression. The Superstition Hills fault joins the Imperial fault in some little understood way (Hill *et al.*, 1975, Sharp, 1972). The location of aftershocks to the west of the surface trace of the fault, and the results of a teleseismic inversion (Chapter 4) suggest that the southern Superstition Hills fault dips 70° to the west. That dip would place the large thrust aftershock east of the fault at 10 km depth, into a left step toward the Imperial fault. This may also explain the aftershock lineation seen in this group as the intersection of the dipping Superstition Hills fault with the vertical edge of the crystalline continental basement rocks, marked by the surface trace of the Superstition Mountain fault. The latter is quite speculative, but it is clear that the step played a role in nucleating the large thrust aftershock at 10 km depth, and so the step must extend to depth. Thus both right steps seen at the surface maintain identities to depth.

3.5 Discussion

The Superstition Hills earthquake sequence is unusual in two regards. First, a conjugate fault system was involved; the left-lateral northeast-striking

Elmore Ranch structure and the right-lateral Superstition Hills fault. Second, the depth of the second main shock initiation was shallow. That the first main shock on the northeast structure unlocked the Superstition Hills fault to produce the second main shock has a geometric appeal. The shallow initiation depth of the second main shock may be related to the unlocking mechanism. While the fault rupture started at a shallow depth, much of the seismic energy was released from deeper on the fault (see Chapter 4).

As seen in Figure 3.15, the larger events of the northeast trend occur in the crystalline basement rocks defined by Fuis *et al.* (1982) but the northeast trend clearly continues beyond those rocks to the Brawley seismic zone. The northeast seismicity trend passes just north of the Westmorland and Salton geothermal areas (Figures 3.1 and 3.14). These geothermal areas correlate with subtle anomalies in a traveltime contour map of Fuis *et al.*, (1982). Also, the Salton Buttes volcanoes, at the southeast end of the Salton Sea, contain granitic xenoliths that may indicate the presence of crystalline plutonic rocks at depth (Robinson *et al.*, 1976). Thus, it can be speculated that the northeast trend continues from along the edge of well defined continental crystalline basement rocks to either a metasedimentary basement feature or a bit of continent basement not resolved in the study of Fuis *et al.* (1982).

Figure 3.16 shows a north-south cross section of Caltech catalog locations of earthquakes in the Brawley seismic zone. The focal depths of events in the Brawley seismic zone shallow abruptly north of the junction of the northeast trend. This focal depth change may reflect basement structure. The northeast trend parallels a lineation within the Brawley seismic zone that developed during aftershocks of the 1979 Imperial Valley earthquake (Johnson and Hutton, 1982) and parallels the trend of the 1981 Westmorland sequence

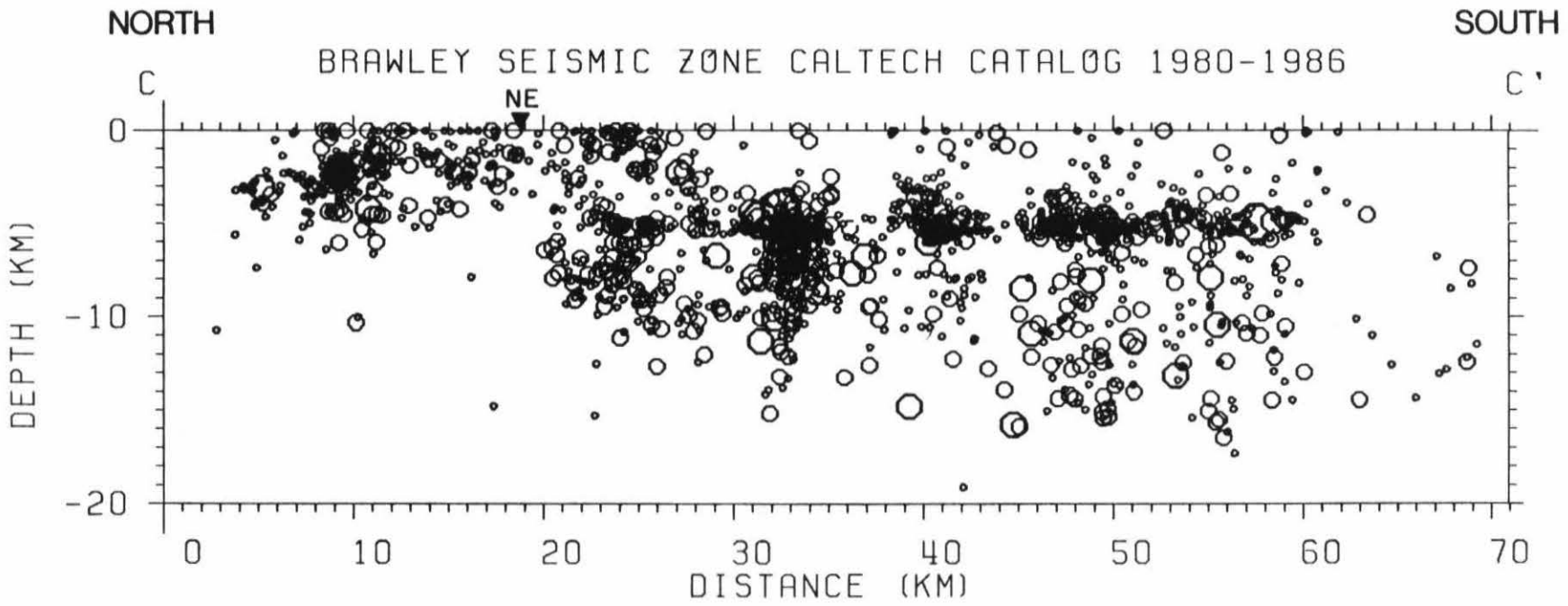

Figure 3.16. Cross section parallel to the Brawley seismic zone (see Figure 3.1) showing A and B quality earthquakes from the Caltech catalog from 1980 to 1986. Events within 6 km of cross section are projected onto the plane of the figure. NE indicates the intersection of the cross section with the northeast trend of the Superstition Hills sequence. Earthquake symbol size is proportional to earthquake magnitude.

(Figure 3.3). The Westmorland trend extended from the Brawley seismic zone to the Superstition Hills fault (Hutton and Johnson, 1981). This trend meets the Superstition Hills fault at the southern boundary of the first group of aftershocks (defined above), just north of the southern edge of the block of crystalline basement that lies between the Superstition Hills and Superstition Mountain faults. The southern edge of this block, as depicted by Fuis *et al.* (1982), also parallels the Westmorland trend, but may actually trend more easterly if the east-west trending aftershock group does represent the basement edge.

The current sequence illuminates the block of crystalline basement as a fault bounded structural unit. Many of the edges of the block are defined by aftershocks (Figure 3.15). Aftershock lineations, such as shown in Figure 3.7 (numbers 4-7, 13), illustrate this. The block is bordered on the west by the fault bounded Superstition Mountains (Figure 3.14). Aftershock activity does not extend under Superstition Mountain. Aftershocks of the 1954 Arroyo Salada earthquake, on the Clark strand of the San Jacinto fault zone, extend southeastward from the 1954 main shock (Sanders *et al.*, 1986) but do not cross the basement embayment just north of the Superstition Hills fault (Figure 3.17). Aftershocks of the 1968 Borrego Mountain earthquake (Hamilton, 1972) do not extend along the Coyote Creek fault past the southern edge of the basement embayment (Figure 3.17). Therefore the extent of rupture, as defined by aftershock zones, is controlled by the basement structure in the western Imperial Valley.

The three segments of the Superstition Hills fault are surrounded by different types of basement rock, and so have different aftershock behavior. The northern segment, with crystalline continental basement rock to the west,

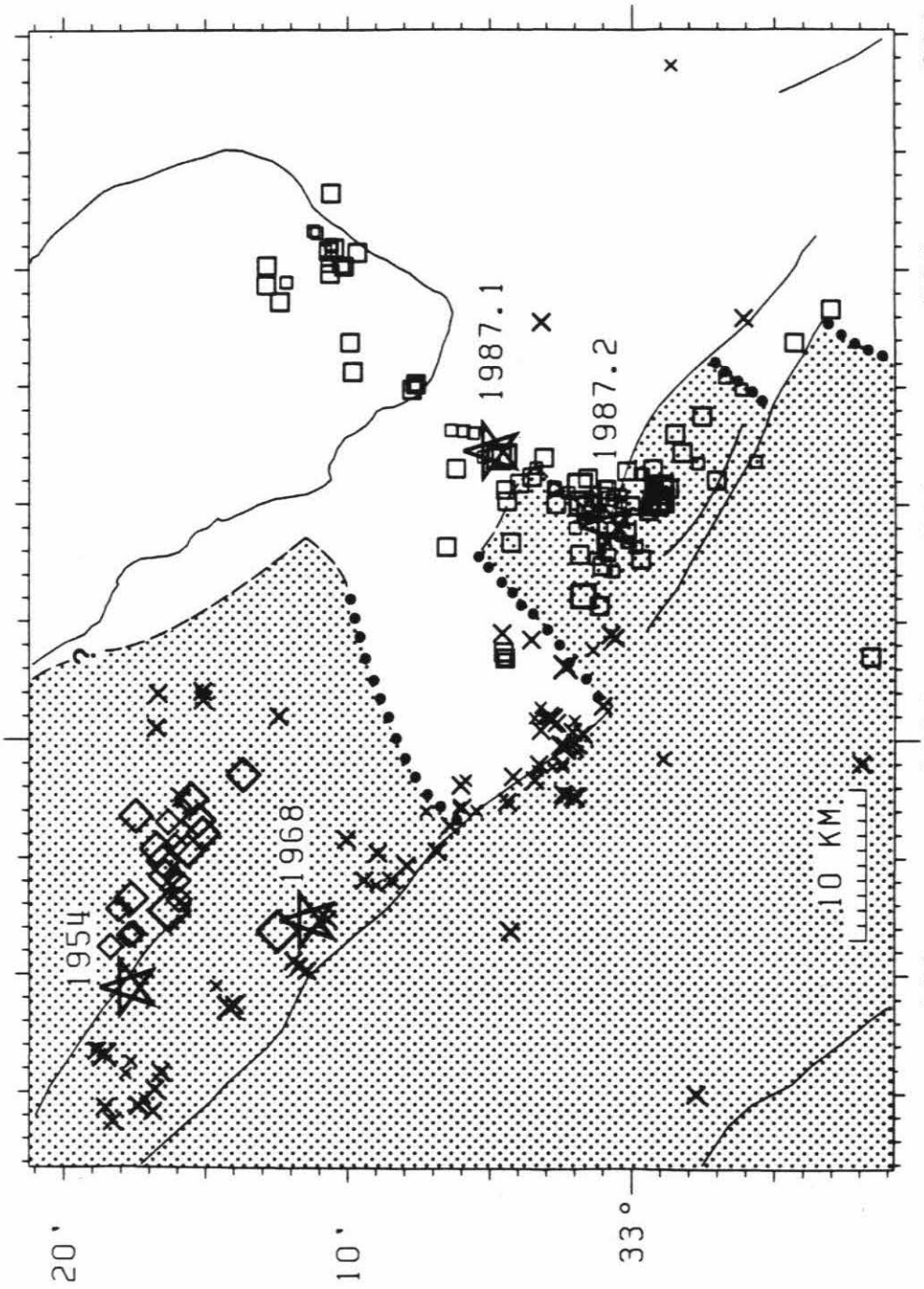

Figure 3.17. Aftershock zones of the 1954, 1968, and 1987 earthquakes with basement features from Figure 3.14. Mainshocks are indicated by stars, labeled with year of occurrence. Diamonds are 1954 $M_L \geq 3.9$ aftershocks, Xs are 1968 $M_L \geq 2.4$ aftershocks, and Squares are 1987 $M_L \geq 2.4$ aftershocks. Shading represents extent of crystalline basement.

has the most aftershocks. The aftershocks define a volume rather than a plane. This may be due to pervasive pre-existing fractures in the basement as might be expected from the crustal necking and thinning prior to the continental rifting that formed the Imperial Valley. The same could be said for the part of the Elmore Ranch fault that lies between the first, Elmore Ranch, mainshock, and the Superstition Hills fault (Figure 3.4). The southern segment of the Superstition Hills fault, and the Wienert fault, cut through the metasedimentary basement under the Imperial Valley fill. These segments have few aftershocks. The aftershocks that do occur are spatially associated with right steps between the segments. The depth of the aftershocks implies that the right steps persist down to the 12 km deep base of the seismogenic zone, so the Superstition Hills fault is as geometrically complicated at depth as it is at the surface.

3.6 Conclusions

The 24 November, 1987, Superstition Hills earthquakes occurred on a conjugate fault system consisting of the northwest-striking right-lateral Superstition Hills fault and a previously unknown northeast-striking left-lateral structure defined by a hypocenter plane that reaches from the Superstition Hills fault to the Brawley seismic zone. The plane parallels other northeast-trending epicenter alignments. The earthquake sequence is made up of foreshocks, a main shock, and aftershocks on the northeast trend, followed by a main shock and aftershocks on the northwest trend. Master event relocations show the following. The northeast trend main shock and its foreshocks colocate at about 11 km depth. The aftershocks of the first main shock cluster in time and space, with some aftershocks occurring in the Brawley seismic zone. The second main shock was 12 hours after the first

main shock and initiated at shallow depth, at the join of the two trends. The northwest trend aftershocks do not coincide with observed surface rupture on the Superstition Hills fault and occupy a volume between the Superstition Hills and Superstition Mountain faults. Most of the aftershocks are along the northern segment of the Superstition Hills fault. The northeast trend events are deep and the northwest trend events are both shallow and deep.

We compare the distribution of the earthquakes to the distribution of basement rocks defined by the refraction study of Fuis *et al.*, (1982). The earthquake locations and extent of aftershocks appear to be controlled by the presence of crystalline basement rocks. This observation is useful in understanding future and historical earthquakes in the western Imperial Valley.

Table 3.4

Best Located $M_L \geq 2$ Earthquakes

Yr-Mo-Da	Hr	Mn	Sec	Latitude		Longitude		Depth	Magnitude	rms	npicks
87-11-24	1	32	47.3	33	4.53	115	47.95	10.9	4.1	0.06	26
87-11-24	1	43	57.7	33	4.59	115	47.94	11.3	2.0	0.08	14
87-11-24	1	53	2.4	33	4.71	115	47.98	11.0	4.0	0.06	21
87-11-24	1	53	2.5	33	4.63	115	47.97	11.1	3.4	0.10	24
87-11-24	1	54	13.7	33	4.95	115	47.74	10.6	5.8	0.09	21
87-11-24	1	58	53.2	33	6.55	115	51.81	12.3	3.2	0.06	8
87-11-24	2	5	19.2	33	9.85	115	44.39	7.4	3.6	0.10	14
87-11-24	2	5	51.1	33	6.21	115	48.47	3.1	3.0	0.02	6
87-11-24	2	11	35.0	33	4.48	115	49.39	9.7	3.3	0.06	9
87-11-24	2	14	34.6	33	1.54	115	50.14	10.5	4.4	0.08	17
87-11-24	2	15	22.2	33	1.88	115	49.20	11.4	4.8	0.19	9
87-11-24	2	21	58.8	33	1.39	115	49.92	10.8	3.9	0.14	21
87-11-24	2	52	60.0	33	1.81	115	49.95	9.8	4.7	0.12	18
87-11-24	3	21	9.7	33	10.17	115	39.89	10.2	3.0	0.21	12
87-11-24	3	23	24.1	33	10.50	115	39.10	10.2	3.2	0.17	19
87-11-24	3	28	57.1	33	0.93	115	49.37	10.9	3.1	0.08	17
87-11-24	3	35	43.9	33	1.38	115	49.00	10.1	2.2	0.14	9
87-11-24	3	36	4.3	32	59.94	115	49.71	8.8	2.1	0.11	8
87-11-24	3	37	46.9	33	10.80	115	39.20	10.7	2.8	0.12	15
87-11-24	3	43	54.2	33	2.71	115	49.99	11.0	3.8	0.09	18
87-11-24	3	48	32.2	33	7.77	115	45.14	8.6	3.8	0.14	16
87-11-24	3	52	20.2	33	0.43	115	49.89	11.6	2.5	0.14	15
87-11-24	3	54	35.8	33	12.18	115	40.55	11.9	2.7	0.11	13
87-11-24	3	56	27.5	33	12.42	115	41.40	11.2	3.4	0.12	16
87-11-24	4	0	44.3	33	9.95	115	43.13	9.9	3.2	0.09	23
87-11-24	4	4	36.3	33	10.70	115	39.21	9.8	3.6	0.17	16
87-11-24	4	38	4.1	33	0.68	115	50.10	8.0	2.0	0.09	12
87-11-24	4	40	40.4	33	7.64	115	44.89	7.1	3.0	0.12	11
87-11-24	4	41	49.4	33	11.16	115	37.57	11.1	2.1	0.16	14
87-11-24	4	42	46.0	33	2.24	115	49.49	10.8	2.8	0.06	13
87-11-24	4	46	0.9	33	4.87	115	47.88	9.8	2.4	0.05	14
87-11-24	4	47	21.2	33	11.23	115	38.36	11.5	2.8	0.16	13
87-11-24	4	57	3.4	33	3.39	115	48.43	10.7	2.4	0.07	11
87-11-24	5	2	39.3	33	0.78	115	49.21	10.4	2.0	0.10	15
87-11-24	5	3	33.2	33	10.53	115	39.15	9.9	2.3	0.17	17
87-11-24	5	9	4.7	33	10.73	115	39.84	10.1	2.6	0.12	20
87-11-24	5	14	41.3	33	5.25	115	47.96	7.0	2.6	0.08	12
87-11-24	5	15	46.5	33	12.63	115	41.06	9.3	2.3	0.17	20
87-11-24	5	19	13.7	33	10.62	115	38.94	11.8	2.4	0.11	13
87-11-24	5	29	58.4	33	5.38	115	47.41	8.1	2.0	0.03	8
87-11-24	5	31	53.1	33	0.46	115	49.56	10.9	2.0	0.09	8
87-11-24	5	36	13.2	33	1.82	115	49.90	10.6	2.2	0.08	8
87-11-24	5	40	39.9	33	1.59	115	50.13	10.2	2.1	0.09	11
87-11-24	5	42	53.5	33	3.99	115	49.09	9.8	3.1	0.06	15
87-11-24	5	48	35.3	33	0.07	115	49.52	9.0	2.2	0.11	11
87-11-24	5	51	48.5	33	7.03	115	45.94	8.4	2.0	0.07	11
87-11-24	6	8	9.7	33	0.42	115	49.62	9.4	2.4	0.10	14
87-11-24	6	20	55.9	33	13.05	115	40.11	11.7	2.1	0.08	14
87-11-24	6	21	53.9	33	12.89	115	40.68	11.0	3.2	0.13	20
87-11-24	6	23	22.3	33	1.16	115	49.65	11.1	3.9	0.07	21
87-11-24	6	32	49.0	33	12.87	115	39.86	10.4	3.2	0.09	14
87-11-24	6	39	57.4	33	13.22	115	40.19	11.8	2.0	0.14	16
87-11-24	6	42	32.7	33	0.69	115	50.61	3.2	2.0	0.10	11
87-11-24	6	44	58.5	33	1.21	115	50.40	9.5	2.6	0.11	11
87-11-24	6	51	2.8	33	10.89	115	37.98	11.7	2.0	0.19	13
87-11-24	6	56	15.4	33	10.08	115	43.18	9.6	2.1	0.09	11
87-11-24	7	1	3.6	33	6.29	115	46.27	7.2	2.1	0.08	10
87-11-24	7	20	31.1	33	2.35	115	49.47	10.8	2.3	0.06	14
87-11-24	7	22	12.7	33	1.29	115	49.88	10.9	2.8	0.08	17
87-11-24	7	23	30.3	33	5.94	115	46.87	9.0	2.6	0.08	11
87-11-24	7	39	6.7	33	0.67	115	49.56	8.4	2.5	0.09	9
87-11-24	7	40	5.0	33	0.92	115	49.20	10.5	2.4	0.08	12
87-11-24	7	45	13.2	33	7.11	115	46.15	8.5	2.3	0.11	12
87-11-24	7	52	24.8	33	3.76	115	48.82	7.1	2.0	0.05	10
87-11-24	7	55	17.0	33	0.44	115	49.54	9.3	2.2	0.10	13
87-11-24	8	5	15.7	33	2.77	115	49.35	10.6	2.8	0.06	18
87-11-24	8	37	13.8	33	1.39	115	49.81	10.1	2.9	0.11	19
87-11-24	8	59	46.8	32	59.65	115	48.69	11.0	2.7	0.16	16
87-11-24	9	1	50.7	32	59.75	115	48.68	11.3	2.5	0.16	16
87-11-24	9	29	14.1	33	2.72	115	49.28	10.9	2.7	0.06	18
87-11-24	9	31	51.8	33	2.45	115	49.54	10.0	2.3	0.13	13
87-11-24	9	57	52.2	33	1.66	115	49.93	10.8	2.3	0.13	14

87-11-24	10	6	52.0	33	10.95	115	39.24	10.6	2.2	0.15	16
87-11-24	10	12	36.9	33	3.54	115	48.84	10.1	3.1	0.07	17
87-11-24	10	36	18.7	33	2.15	115	49.69	10.7	2.2	0.01	6
87-11-24	10	45	37.6	33	5.94	115	46.83	9.6	2.0	0.05	11
87-11-24	11	6	14.5	33	9.87	115	39.85	10.8	2.0	0.17	22
87-11-24	11	12	30.3	33	1.08	115	50.01	11.6	2.2	0.13	17
87-11-24	11	25	34.4	33	1.01	115	49.56	10.8	2.2	0.11	15
87-11-24	11	31	47.0	33	8.12	115	44.92	8.9	2.3	0.13	19
87-11-24	11	39	51.5	33	11.11	115	38.45	11.4	2.5	0.15	20
87-11-24	11	50	51.5	33	4.07	115	48.25	11.0	2.3	0.07	9
87-11-24	11	54	26.7	33	0.54	115	50.51	10.8	2.3	0.18	14
87-11-24	12	1	16.5	33	10.61	115	36.77	11.4	3.4	0.06	7
87-11-24	12	35	55.7	33	0.41	115	50.70	8.5	2.7	0.15	18
87-11-24	12	38	15.5	33	6.39	115	46.83	9.0	2.6	0.09	15
87-11-24	13	15	56.5	33	0.90	115	50.92	1.9	6.3	0.19	16
87-11-24	14	1	11.8	33	0.22	115	48.57	1.3	3.6	0.10	13
87-11-24	14	2	10.2	32	59.36	115	50.05	1.3	3.3	0.19	10
87-11-24	14	2	17.3	33	4.30	115	51.61	2.0	3.3	0.02	5
87-11-24	14	9	31.9	33	1.19	115	54.33	1.4	3.3	0.12	11
87-11-24	14	10	41.6	33	1.32	115	52.29	0.7	2.7	0.14	11
87-11-24	14	24	39.2	32	59.27	115	49.36	0.7	3.5	0.06	15
87-11-24	16	7	20.2	32	59.29	115	49.87	1.0	2.1	0.10	11
87-11-24	16	8	6.8	33	1.00	115	51.64	0.9	2.7	0.10	14
87-11-24	16	27	27.8	32	54.20	115	42.86	8.4	3.0	0.08	13
87-11-24	16	37	0.4	33	1.58	115	50.30	7.8	2.5	0.05	14
87-11-24	16	37	54.3	33	0.22	115	51.58	0.2	2.7	0.15	14
87-11-24	16	44	22.4	32	59.33	115	50.18	11.2	2.7	0.10	10
87-11-24	16	54	23.0	32	58.67	115	47.46	7.7	2.2	0.06	13
87-11-24	16	54	37.5	32	53.05	115	41.69	10.1	3.3	0.04	8
87-11-24	16	54	37.5	32	53.05	115	41.71	10.1	3.3	0.04	8
87-11-24	16	56	52.4	32	57.58	115	46.25	8.9	3.1	0.11	15
87-11-24	17	8	10.9	33	0.17	115	51.38	0.9	2.3	0.07	10
87-11-24	17	19	7.1	32	55.78	115	49.29	9.2	2.3	0.01	6
87-11-24	17	21	8.2	33	0.79	115	50.28	0.9	2.5	0.07	12
87-11-24	17	36	28.0	32	59.33	115	48.93	2.0	2.0	0.08	12
87-11-24	18	4	50.0	32	53.51	115	44.60	7.6	2.4	0.02	6
87-11-24	19	48	49.6	32	58.34	115	47.91	1.4	2.1	0.14	12
87-11-24	20	14	54.7	32	49.34	115	36.62	10.7	2.4	0.17	13
87-11-24	20	23	22.3	32	49.45	115	36.78	10.9	3.4	0.16	11
87-11-24	20	23	22.3	32	49.47	115	36.79	10.8	3.4	0.16	11
87-11-24	20	36	9.2	32	59.18	115	49.04	2.2	2.1	0.06	13
87-11-24	20	44	52.5	33	0.74	115	49.80	2.3	2.4	0.06	13
87-11-24	21	6	4.6	32	50.94	115	36.56	10.9	2.0	0.08	6
87-11-24	21	16	17.7	33	0.70	115	52.83	1.3	2.5	0.08	11
87-11-24	21	28	12.2	32	51.64	115	56.49	9.6	3.1	0.13	21
87-11-24	21	29	11.9	32	51.15	115	56.62	9.3	2.1	0.09	10
87-11-24	21	33	46.7	33	0.06	115	47.54	8.5	2.0	0.04	6
87-11-24	21	37	39.9	32	57.73	115	48.26	8.7	2.0	0.04	6
87-11-24	21	59	56.9	33	2.52	115	48.48	0.3	2.1	0.04	9
87-11-24	22	0	8.1	32	59.79	115	50.03	1.4	2.0	0.05	7
87-11-24	22	2	44.8	33	0.83	115	50.11	1.8	2.3	0.08	8
87-11-24	22	5	1.0	32	58.27	115	47.80	8.2	3.0	0.09	13
87-11-24	22	16	29.4	33	1.67	115	52.55	0.7	2.3	0.15	13
87-11-24	22	46	14.9	33	0.42	115	50.09	2.5	2.0	0.09	8
87-11-24	22	47	33.5	33	0.69	115	50.98	1.2	2.6	0.10	17
87-11-24	23	16	47.3	32	49.74	115	36.59	10.8	2.9	0.10	15
87-11-24	23	27	44.7	32	49.92	115	36.40	11.1	2.2	0.09	9
87-11-24	23	36	58.6	32	53.70	115	42.61	6.7	2.8	0.12	14
87-11-24	23	44	53.3	32	59.31	115	48.48	4.6	3.1	0.10	15
87-11-25	0	0	57.5	32	57.72	115	48.24	3.5	2.4	0.08	11
87-11-25	0	3	28.2	32	59.82	115	47.36	8.0	2.2	0.10	10
87-11-25	0	5	14.8	32	56.17	115	44.03	7.6	2.1	0.02	9
87-11-25	0	25	39.9	32	55.68	115	45.23	8.5	2.1	0.10	10
87-11-25	0	32	4.9	33	2.78	115	49.24	1.1	2.5	0.09	19
87-11-25	0	33	2.0	32	59.20	115	49.34	1.0	2.9	0.09	17
87-11-25	0	33	49.2	33	4.54	115	56.31	0.8	3.0	0.15	17
87-11-25	0	37	9.8	32	59.88	115	51.81	1.3	2.8	0.09	17
87-11-25	0	44	8.6	32	55.05	115	45.86	8.0	2.1	0.05	11
87-11-25	0	48	55.5	33	1.88	115	52.12	0.7	3.3	0.10	18
87-11-25	0	50	28.5	33	4.52	115	56.61	1.3	2.9	0.15	18
87-11-25	1	1	57.6	32	59.31	115	48.93	4.2	2.2	0.08	14
87-11-25	1	14	45.9	33	1.03	115	51.97	0.8	2.2	0.10	14
87-11-25	1	32	6.2	33	4.88	115	47.54	7.4	2.2	0.10	16
87-11-25	1	33	30.1	32	59.12	115	49.58	2.4	3.0	0.11	15
87-11-25	1	43	27.5	32	59.80	115	51.24	1.3	2.0	0.09	10
87-11-25	1	44	57.5	32	58.44	115	49.15	1.6	2.2	0.06	14
87-11-25	2	1	43.0	32	59.72	115	50.22	2.4	2.2	0.08	12
87-11-25	2	6	10.6	33	0.39	115	51.50	1.1	2.0	0.11	14

87-11-25	2	8	30.8	33	4.50	115	56.57	1.2	3.0	0.15	19
87-11-25	2	18	51.4	32	56.19	115	45.09	6.8	2.9	0.10	16
87-11-25	2	37	26.9	32	49.24	115	36.19	10.8	2.8	0.16	14
87-11-25	2	47	2.6	33	0.32	115	51.67	1.4	2.2	0.10	14
87-11-25	2	47	57.5	33	1.08	115	52.61	0.8	3.3	0.11	19
87-11-25	2	53	22.1	32	59.50	115	52.46	1.1	2.3	0.08	14
87-11-25	3	1	14.7	33	2.12	115	49.61	8.6	2.2	0.05	10
87-11-25	3	24	45.3	32	49.48	115	36.19	10.8	2.7	0.14	16
87-11-25	3	25	17.4	32	54.91	115	47.75	0.7	2.0	0.28	9
87-11-25	3	29	4.5	33	2.09	115	52.42	1.2	2.1	0.12	10
87-11-25	3	30	36.4	33	0.83	115	52.12	0.8	2.6	0.11	17
87-11-25	3	33	16.0	33	0.47	115	50.50	0.7	2.0	0.09	11
87-11-25	3	34	31.3	33	1.24	115	52.66	1.7	2.3	0.09	13
87-11-25	3	59	47.2	33	1.11	115	49.68	0.9	2.1	0.14	11
87-11-25	4	0	7.8	32	58.69	115	50.29	2.3	2.2	0.07	11
87-11-25	4	3	37.1	32	59.76	115	51.27	2.5	2.2	0.09	13
87-11-25	4	4	8.5	32	56.24	115	49.65	9.7	2.0	0.06	7
87-11-25	4	7	17.9	33	0.48	115	50.60	0.7	2.6	0.10	18
87-11-25	4	14	3.0	32	57.05	115	50.23	2.9	2.0	0.11	11
87-11-25	4	30	18.0	32	59.03	115	49.86	2.0	3.4	0.12	20
87-11-25	4	35	14.4	33	1.07	115	51.41	1.1	2.4	0.10	11
87-11-25	4	39	43.0	33	2.30	115	51.68	1.1	2.0	0.11	15
87-11-25	4	45	34.8	32	59.46	115	48.61	0.8	2.0	0.11	9
87-11-25	4	49	25.7	32	57.93	115	48.74	2.9	2.3	0.11	16
87-11-25	4	53	40.9	32	59.75	115	50.74	1.8	2.0	0.10	15
87-11-25	4	56	51.8	32	58.24	115	49.45	2.2	2.0	0.11	11
87-11-25	5	9	11.6	33	1.05	115	51.96	1.5	2.0	0.14	15
87-11-25	5	54	2.2	33	0.67	115	52.98	1.4	2.1	0.08	13
87-11-25	5	56	20.7	32	59.25	115	49.14	1.3	2.1	0.08	9
87-11-25	6	13	5.1	33	0.19	115	48.73	9.8	2.1	0.08	16
87-11-25	6	13	55.8	33	2.02	115	51.00	1.3	2.5	0.11	19
87-11-25	12	9	2.2	32	52.21	115	42.39	7.6	2.1	0.08	7
87-11-25	12	24	46.8	32	53.96	115	42.96	8.6	2.0	0.02	6
87-11-25	13	54	10.1	32	59.01	115	49.81	2.1	4.2	0.11	19
87-11-25	17	6	42.0	32	54.21	115	45.58	7.9	2.0	0.09	8
87-11-25	17	13	57.2	32	53.22	115	41.66	10.1	2.2	0.10	9
87-11-25	19	11	52.8	32	54.26	115	42.95	7.9	2.2	0.01	6
87-11-25	20	7	31.5	32	53.54	115	42.04	10.3	3.0	0.11	16
87-11-26	0	19	31.5	33	0.23	115	51.18	0.8	3.6	0.14	22
87-11-26	1	56	27.6	32	59.46	115	50.28	2.1	3.7	0.10	16
87-11-26	3	56	43.9	32	53.46	115	47.30	10.1	2.4	0.05	8
87-11-26	17	39	2.0	33	1.75	115	53.89	1.3	4.3	0.15	20
87-11-26	18	50	42.8	32	54.14	115	40.09	0.6	2.2	0.12	14
87-11-26	20	24	15.9	32	54.11	115	40.68	1.4	2.0	0.11	12
87-11-27	1	10	8.2	32	58.74	115	49.33	3.7	3.0	0.07	13
87-11-27	1	10	10.4	32	59.20	115	49.92	9.5	4.6	0.14	18
87-11-27	3	43	3.7	32	52.09	115	41.48	0.8	2.3	0.11	8
87-11-27	20	44	4.1	32	49.74	115	36.87	10.4	2.2	0.12	10
87-11-28	0	12	26.0	32	58.74	115	48.70	6.0	2.2	0.05	14
87-11-28	0	39	11.1	32	59.02	115	49.26	2.4	4.2	0.10	18
87-11-28	0	39	11.1	32	59.03	115	49.26	2.4	4.1	0.10	19
87-11-28	1	15	33.2	32	59.32	115	49.40	2.2	2.2	0.25	15
87-11-28	2	6	10.4	32	58.98	115	49.58	2.2	2.1	0.11	9
87-11-28	4	25	43.5	33	0.37	115	52.40	0.7	2.6	0.13	16
87-11-28	4	48	41.9	32	59.28	115	50.44	1.7	2.1	0.07	13
87-11-28	5	3	26.6	33	1.91	115	52.15	0.9	2.6	0.11	16
87-11-28	7	35	47.8	33	3.31	115	55.35	0.6	2.4	0.13	17
87-11-28	8	51	20.9	33	1.39	115	52.85	1.4	2.3	0.12	14
87-11-28	9	53	5.7	33	0.02	115	51.70	1.0	2.2	0.28	16
87-11-28	10	41	59.6	33	0.74	115	53.27	1.1	2.1	0.11	15
87-11-28	11	37	59.1	32	57.08	115	45.74	10.1	2.8	0.11	19
87-11-28	11	43	37.1	32	56.36	115	48.89	7.6	2.2	0.08	11
87-11-28	12	35	53.9	32	59.03	115	48.09	5.9	2.2	0.10	12
87-11-28	13	26	49.9	32	59.89	115	50.68	5.5	2.3	0.10	14
87-11-28	14	57	54.9	33	1.03	115	51.26	1.0	2.8	0.08	15
87-11-28	15	4	25.6	32	58.47	115	48.81	3.6	2.0	0.06	13
87-11-28	15	4	33.8	32	56.56	115	47.32	6.1	2.2	0.12	10
87-11-28	15	24	26.2	32	58.89	115	49.61	2.1	2.2	0.07	13
87-11-28	15	51	10.7	32	57.30	115	48.20	7.1	2.2	0.07	13
87-11-28	16	36	57.6	33	1.96	115	51.98	0.9	2.1	0.12	12
87-11-28	18	41	51.3	32	59.19	115	48.37	1.1	2.2	0.18	14
87-11-28	19	6	34.9	32	59.73	115	49.55	5.4	2.2	0.07	13
87-11-28	22	17	40.1	32	59.30	115	49.69	10.0	2.0	0.10	9
87-11-28	22	18	59.8	32	57.36	115	50.12	7.3	2.8	0.09	18
87-11-28	22	33	48.0	33	9.22	115	42.70	11.6	2.0	0.18	14
87-11-28	23	21	0.4	33	0.64	115	51.04	2.3	2.2	0.10	17
87-11-29	2	39	7.1	32	56.31	115	44.32	11.1	2.5	0.07	16
87-11-29	2	50	14.6	32	57.95	115	48.63	7.6	2.1	0.05	8

87-11-29	5	16	52.6	32	56.74	115	47.37	7.3	2.1	0.06	10
87-11-29	7	35	42.5	33	0.47	115	51.36	0.8	2.0	0.14	17
87-11-29	9	40	8.8	33	0.83	115	49.92	2.1	2.0	0.08	15
87-11-29	9	44	37.6	32	51.71	115	42.23	10.3	2.2	0.07	8
87-11-29	11	30	35.6	32	59.26	115	49.84	1.9	2.1	0.09	11
87-11-29	13	40	49.6	32	56.54	115	48.25	1.4	2.4	0.08	18
87-11-29	13	52	16.2	32	58.95	115	49.17	2.7	2.2	0.08	16
87-11-29	14	35	57.8	32	58.60	115	49.01	10.4	2.1	0.06	8
87-11-29	15	12	41.8	32	56.75	115	46.20	7.1	2.2	0.09	17
87-11-29	15	20	19.3	32	56.74	115	49.98	6.1	2.3	0.12	15
87-11-29	15	22	15.9	32	56.69	115	45.70	6.9	2.3	0.09	17
87-11-29	15	23	16.1	32	58.77	115	48.83	3.0	2.1	0.07	14
87-11-29	15	47	0.6	33	0.13	115	50.19	5.4	2.5	0.09	17
87-11-29	16	7	57.6	33	0.63	115	50.20	1.6	2.1	0.09	14
87-11-29	16	16	46.2	32	57.07	115	47.67	2.7	2.0	0.06	13
87-11-29	17	6	5.2	32	56.23	115	48.60	2.9	2.0	0.10	15
87-11-29	17	19	48.0	33	0.95	115	52.62	1.4	3.0	0.13	19
87-11-29	17	36	38.2	32	59.92	115	52.06	1.9	2.0	0.09	13
87-11-29	17	46	15.1	32	59.34	115	49.82	9.1	2.2	0.06	8
87-11-29	18	57	15.4	33	0.89	115	51.66	1.3	2.5	0.15	16
87-11-29	19	0	13.1	33	1.01	115	51.72	1.0	2.9	0.11	15
87-11-29	19	37	29.8	33	3.54	115	55.36	0.8	2.0	0.13	15
87-11-29	20	7	4.1	33	1.02	115	50.95	0.8	2.0	0.15	16
87-11-30	1	18	57.8	33	0.65	115	50.35	1.6	2.0	0.12	13
87-11-30	1	33	43.8	33	1.57	115	52.63	9.2	2.0	0.06	12
87-11-30	9	26	46.9	33	3.25	115	55.41	1.1	2.0	0.18	14
87-11-30	13	2	24.9	32	59.42	115	45.16	8.7	2.0	0.03	6
87-11-30	13	14	32.8	33	0.26	115	50.18	2.2	2.1	0.08	16
87-11-30	14	50	3.6	32	59.92	115	52.04	1.6	2.1	0.11	13
87-11-30	15	33	9.9	33	0.04	115	48.43	7.4	2.5	0.04	7
87-11-30	16	50	6.0	32	59.01	115	50.08	2.4	2.0	0.08	11
87-11-30	17	31	14.7	33	0.58	115	51.86	1.5	2.1	0.10	12
87-11-30	18	23	17.1	32	58.80	115	50.01	1.2	2.1	0.14	14
87-11-30	19	54	49.0	32	58.74	115	48.92	2.8	3.0	0.11	17
87-11-30	20	36	28.8	32	58.96	115	46.88	4.6	2.4	0.03	8
87-11-30	21	50	31.2	32	58.19	115	47.65	5.7	2.5	0.14	16
87-11-30	21	52	40.0	33	1.28	115	51.35	1.4	2.2	0.14	13
87-11-30	22	53	9.7	33	1.18	115	51.26	0.8	2.0	0.08	11
87-11-30	23	31	27.0	33	0.48	115	52.29	0.7	2.3	0.15	17
87-11-30	23	48	13.0	33	0.81	115	50.53	0.6	2.0	0.12	12
87-12- 1	2	39	20.9	33	1.21	115	51.21	1.5	2.1	0.08	12
87-12- 1	2	43	29.9	33	0.63	115	53.21	1.3	2.2	0.10	17
87-12- 1	3	9	42.8	32	56.82	115	45.76	9.0	2.1	0.13	15
87-12- 1	10	23	37.7	32	56.51	115	44.42	9.6	2.0	0.12	16
87-12- 1	11	0	6.8	33	2.70	115	49.35	12.3	2.2	0.22	20
87-12- 1	13	34	29.0	33	1.13	115	49.51	8.6	2.0	0.04	10
87-12- 1	13	48	19.3	32	59.02	115	50.08	1.3	2.3	0.07	11
87-12- 1	19	54	36.5	32	58.74	115	49.45	11.4	2.0	0.08	8
87-12- 1	21	11	34.1	33	0.42	115	51.41	1.4	2.1	0.11	11
87-12- 1	21	48	26.7	33	1.18	115	52.81	1.3	2.3	0.11	14
87-12- 1	22	10	45.5	33	6.66	115	45.78	9.8	2.6	0.20	16
87-12- 1	22	29	13.2	33	0.16	115	50.49	1.6	2.3	0.07	11
87-12- 2	3	3	18.6	33	0.31	115	50.78	2.0	2.0	0.10	10
87-12- 2	4	3	6.3	33	0.19	115	49.53	2.0	4.6	0.12	21
87-12- 2	10	59	53.9	33	0.78	115	49.90	1.2	2.7	0.12	21
87-12- 2	13	12	56.8	32	57.20	115	46.83	4.7	2.1	0.05	8
87-12- 2	14	8	30.6	33	0.63	115	50.92	1.4	2.2	0.12	19
87-12- 2	21	41	3.3	32	53.05	115	43.84	11.3	2.0	0.07	10
87-12- 3	1	9	45.9	32	58.93	115	48.51	9.4	2.0	0.07	15
87-12- 3	1	47	32.6	32	58.25	115	46.06	7.1	2.1	0.05	9
87-12- 3	2	5	27.2	32	55.51	115	42.85	1.3	2.4	0.16	20
87-12- 3	3	28	43.3	32	59.28	115	52.36	1.8	2.5	0.11	17
87-12- 3	3	30	52.5	32	59.41	115	50.39	0.6	2.1	0.07	10
87-12- 3	4	9	1.9	33	6.32	115	45.13	10.0	2.2	0.27	18
87-12- 3	4	32	4.8	32	59.08	115	52.32	2.2	2.0	0.10	16
87-12- 3	8	25	43.0	32	56.45	115	48.72	3.8	3.0	0.12	18
87-12- 3	9	43	8.6	32	58.41	115	48.64	5.0	2.1	0.16	19
87-12- 3	9	50	9.7	32	56.47	115	48.63	4.1	2.3	0.12	17
87-12- 3	10	18	45.0	33	0.06	115	50.34	2.5	2.3	0.15	17
87-12- 3	13	2	11.1	32	56.22	115	47.10	4.5	2.0	0.06	11
87-12- 3	13	45	57.9	33	0.07	115	48.14	10.0	3.1	0.12	20
87-12- 3	18	29	18.9	33	0.48	115	53.08	2.5	2.2	0.12	15
87-12- 3	19	4	36.5	33	0.73	115	53.49	1.1	3.8	0.14	23
87-12- 4	5	23	54.2	32	59.17	115	49.25	5.7	3.1	0.11	19
87-12- 4	6	4	43.1	32	58.99	115	48.91	6.4	2.6	0.11	20
87-12- 4	7	0	6.6	32	56.73	115	44.74	1.3	2.1	0.14	16
87-12- 4	7	37	0.6	33	0.20	115	49.29	1.2	2.2	0.13	17
87-12- 4	8	10	29.0	33	0.08	115	51.77	1.2	2.2	0.12	16

87-12- 4	8	56	59.6	33	0.99	115	52.88	0.8	3.1	0.14	21
87-12- 4	11	53	36.4	32	58.86	115	48.90	6.2	2.0	0.09	13
87-12- 4	17	32	20.9	32	58.17	115	48.21	4.3	2.1	0.08	11
87-12- 4	20	45	32.0	33	0.30	115	51.89	1.5	2.2	0.14	11
87-12- 5	0	24	20.7	33	1.40	115	51.86	1.1	2.3	0.11	11
87-12- 5	10	15	39.4	33	0.25	115	51.79	2.1	2.1	0.16	12
87-12- 5	18	40	56.6	32	59.61	115	48.56	5.4	2.3	0.12	17
87-12- 5	21	35	58.0	32	59.71	115	50.72	2.0	2.2	0.11	15
87-12- 6	2	37	4.8	32	53.45	115	38.34	8.9	2.1	0.10	7
87-12- 6	2	38	53.6	32	56.61	115	49.01	6.5	2.6	0.12	15
87-12- 7	6	27	32.7	32	54.49	115	39.65	0.6	2.0	0.15	13
87-12- 7	8	49	15.3	32	59.49	115	49.29	5.4	2.0	0.08	13
87-12- 7	9	30	2.2	32	58.99	115	51.96	1.4	2.2	0.12	13
87-12- 7	14	57	18.6	32	56.39	115	49.32	8.2	2.0	0.09	11
87-12- 7	17	55	9.7	32	53.28	115	41.57	9.9	2.1	0.10	10
87-12- 8	2	11	49.3	32	58.70	115	49.85	2.3	2.4	0.10	13
87-12- 8	6	36	5.9	33	0.42	115	50.78	2.1	3.1	0.12	16
87-12- 8	10	10	1.2	33	0.74	115	49.31	5.2	2.1	0.05	9
87-12- 8	10	26	34.5	33	2.45	115	50.34	1.3	2.7	0.14	16
87-12- 8	10	58	39.5	33	2.20	115	50.31	1.9	2.5	0.12	17
87-12- 8	13	56	37.8	33	1.04	115	51.95	2.0	2.4	0.13	19
87-12- 8	14	29	42.0	32	53.44	115	42.11	9.2	2.1	0.07	13
87-12- 8	14	39	19.0	33	1.25	115	51.34	2.4	2.0	0.07	10
87-12- 8	14	59	32.9	33	0.15	115	49.07	9.3	2.1	0.08	8
87-12- 8	17	46	29.5	33	0.53	115	48.34	7.9	2.1	0.09	11
87-12- 8	18	28	36.5	33	1.43	115	51.94	1.5	2.5	0.12	15
87-12- 8	18	45	33.2	33	0.22	115	52.26	1.1	3.4	0.13	21
87-12- 9	4	17	30.3	33	0.47	115	50.42	1.2	2.0	0.09	12
87-12- 9	4	34	48.0	32	59.98	115	52.88	1.4	2.8	0.12	19
87-12- 9	9	40	6.4	32	59.34	115	48.58	5.5	2.0	0.04	11
87-12- 9	9	52	38.2	32	53.49	115	41.83	0.7	2.0	0.13	14
87-12- 9	14	47	45.3	33	0.16	115	52.50	6.8	2.6	0.12	18
87-12-10	3	12	56.9	32	52.38	115	39.77	10.1	2.3	0.11	15
87-12-10	5	43	12.9	32	59.07	115	49.81	2.4	2.2	0.10	15
87-12-10	17	27	58.8	32	58.40	115	48.73	4.9	2.0	0.11	11
87-12-10	20	13	8.1	32	58.59	115	49.56	2.6	2.1	0.12	15
87-12-11	1	15	27.6	32	56.70	115	49.24	6.1	2.2	0.12	12
87-12-11	3	29	48.4	33	15.25	115	37.55	10.4	2.0	0.10	10
87-12-11	6	16	9.2	32	59.75	115	53.64	1.8	2.1	0.12	16
87-12-11	13	6	25.9	32	54.41	115	42.38	8.8	2.1	0.09	14
87-12-11	18	15	37.2	33	1.40	115	51.64	2.0	2.5	0.09	16
87-12-11	19	2	48.9	32	59.76	115	48.46	6.2	2.1	0.04	9
87-12-12	10	22	57.3	33	7.52	115	45.36	10.1	2.4	0.19	22
87-12-12	18	20	49.0	32	59.98	115	48.93	7.1	3.0	0.13	21
87-12-12	21	1	3.1	32	59.31	115	52.06	1.5	2.4	0.11	16
87-12-13	12	36	10.2	33	0.55	115	51.10	2.1	2.0	0.12	15
87-12-13	15	2	39.0	32	53.42	115	42.19	9.7	3.2	0.11	18
87-12-13	18	30	17.8	32	57.82	115	45.41	2.3	2.2	0.12	12
87-12-14	16	31	11.8	33	0.48	115	51.42	2.2	2.0	0.13	11
87-12-15	4	29	3.7	32	58.27	115	48.19	5.6	2.0	0.11	12
87-12-16	2	17	25.3	32	53.80	115	42.16	10.1	2.0	0.10	10
87-12-16	4	31	29.8	33	1.73	115	54.01	10.6	2.1	0.10	13
87-12-16	5	3	32.7	33	1.46	115	50.68	1.5	2.8	0.11	18
87-12-17	5	28	39.0	32	53.60	115	42.15	10.3	2.0	0.11	17
87-12-17	10	51	51.6	32	59.60	115	52.08	2.0	2.0	0.12	13
87-12-17	10	51	58.0	32	58.53	115	52.65	6.9	2.0	0.07	6
87-12-18	7	8	47.8	32	56.14	115	45.86	7.8	2.2	0.10	16
87-12-18	7	16	25.3	33	1.25	115	51.93	0.6	2.2	0.14	17
87-12-18	13	26	15.1	32	48.27	115	41.52	11.3	2.3	0.10	18
87-12-18	19	41	20.9	32	56.74	115	47.69	7.5	2.0	0.05	13
87-12-19	3	32	15.7	32	56.59	115	48.95	7.3	2.1	0.10	17
87-12-19	14	32	37.2	32	59.64	115	50.20	6.4	2.1	0.11	17
87-12-19	20	41	53.0	32	53.12	115	40.86	9.2	2.4	0.03	6
87-12-20	6	21	4.9	32	56.36	115	44.23	9.6	2.0	0.11	13
87-12-21	2	57	1.8	32	54.93	115	48.24	7.2	2.3	0.09	19
87-12-21	10	40	29.0	32	59.01	115	45.38	8.5	2.0	0.01	5
87-12-21	14	16	28.5	32	56.94	115	49.98	10.6	2.6	0.08	19
87-12-21	21	36	19.5	32	57.17	115	48.14	7.2	2.4	0.09	13
87-12-21	23	8	22.2	33	2.61	115	53.35	9.9	2.2	0.12	18
87-12-22	12	25	59.8	32	56.74	115	47.88	2.5	2.3	0.13	15
87-12-24	5	34	58.7	32	53.47	115	41.59	9.9	2.2	0.07	20
87-12-24	10	24	42.0	32	59.79	115	48.87	9.3	2.0	0.02	10
87-12-25	7	26	4.6	32	59.49	115	50.11	6.9	2.1	0.12	19
87-12-25	18	15	48.1	33	7.52	115	45.61	9.8	3.5	0.19	23
87-12-26	21	22	51.2	32	53.71	115	42.38	10.1	2.0	0.09	17
87-12-27	0	30	28.0	33	4.94	115	57.82	9.1	2.3	0.12	20
87-12-27	1	19	59.4	32	56.93	115	46.40	8.4	2.2	0.08	13
87-12-27	16	42	55.9	33	1.56	115	52.10	1.4	2.8	0.14	16

87-12-27	21	13	47.7	32	53.49	115	42.46	9.8	2.1	0.08	15
87-12-28	2	20	16.4	33	5.14	115	47.50	10.8	2.1	0.14	17
87-12-28	7	27	35.0	32	59.28	115	48.86	0.9	2.1	0.25	19
87-12-29	9	25	46.0	32	53.42	115	39.46	10.0	2.0	0.09	11
87-12-29	19	7	45.9	32	57.00	115	46.60	5.9	2.1	0.10	11
87-12-30	7	36	4.7	33	0.54	115	50.84	1.6	2.1	0.11	15
87-12-30	11	22	21.3	33	0.50	115	50.74	1.8	2.1	0.11	12
87-12-30	14	39	55.3	32	57.89	115	47.37	10.1	2.2	0.08	15
87-12-30	18	14	17.1	32	57.08	115	46.89	6.3	2.4	0.09	9
87-12-31	2	40	9.4	32	56.89	115	46.74	6.5	2.0	0.06	10
88- 1- 2	18	9	17.4	32	55.90	115	48.50	10.3	2.1	0.06	11
88- 1- 4	18	23	25.6	33	1.10	115	50.55	7.2	2.0	0.08	12
88- 1- 4	21	2	34.1	32	56.94	115	49.28	6.1	2.2	0.09	11
88- 1- 5	7	18	34.3	32	59.91	115	51.18	1.5	2.0	0.14	12
88- 1- 5	7	30	56.4	32	59.96	115	49.29	2.8	3.1	0.11	17
88- 1- 5	15	13	29.3	33	0.73	115	49.22	10.3	2.1	0.04	13
88- 1- 7	14	35	55.2	32	59.70	115	52.17	2.4	2.2	0.12	17
88- 1- 8	3	34	37.5	33	0.87	115	50.44	2.4	2.0	0.11	16
88- 1- 8	14	34	37.7	33	0.50	115	50.54	2.7	2.3	0.11	18
88- 1- 9	8	11	54.2	32	56.51	115	45.00	8.0	2.0	0.08	11
88- 1-10	8	29	53.1	32	58.59	115	48.88	4.2	2.1	0.10	14
88- 1-13	15	2	37.2	32	52.02	115	40.57	10.0	2.3	0.07	12
88- 1-13	20	0	54.2	33	0.37	115	51.77	2.2	2.1	0.12	15
88- 1-13	23	38	31.2	32	56.63	115	46.84	5.3	2.1	0.11	14
88- 1-14	5	56	7.3	32	58.23	115	48.88	3.5	2.1	0.09	13
88- 1-17	9	20	29.5	32	59.60	115	49.23	5.9	2.1	0.11	10
88- 1-20	7	12	10.9	33	0.03	115	50.48	5.8	2.2	0.12	17
88- 1-21	14	35	19.4	32	52.40	115	47.01	5.6	2.4	0.14	18
88- 1-22	22	26	17.2	32	57.93	115	47.56	5.2	2.1	0.11	11
88- 1-26	5	10	45.8	32	53.42	115	41.56	9.6	2.0	0.05	10
88- 1-26	13	40	25.8	33	0.33	115	51.55	1.5	2.5	0.14	19
88- 1-28	2	54	2.3	32	53.89	115	40.87	9.8	4.7	0.11	21
88- 1-28	3	13	34.2	32	53.81	115	40.48	9.9	2.5	0.09	16
88- 1-28	6	0	30.5	32	53.76	115	41.35	10.1	2.3	0.11	18
88- 1-28	8	52	15.8	32	54.41	115	40.71	10.2	2.0	0.06	9
88- 1-29	21	40	49.1	32	53.94	115	41.24	8.9	2.0	0.12	17
88- 1-30	6	46	27.8	32	53.61	115	40.88	10.0	2.0	0.05	9
88- 1-31	23	40	39.3	33	0.30	115	51.03	7.0	2.1	0.13	16
88- 2- 2	18	17	43.7	33	0.11	115	47.42	10.9	2.9	0.11	19
88- 2- 2	18	18	34.1	33	0.06	115	47.37	11.3	3.0	0.13	18
88- 2- 5	23	5	21.2	32	57.87	115	48.09	5.2	2.1	0.09	11
88- 2- 9	4	14	42.2	33	0.68	115	50.59	2.2	2.1	0.11	15
88- 2-10	9	25	52.6	32	52.40	115	41.16	9.2	2.1	0.08	11
88- 2-12	12	0	35.5	32	52.38	115	41.96	8.3	2.1	0.04	10
88- 2-15	14	18	11.9	32	59.56	115	51.04	10.5	2.3	0.11	18
88- 2-15	14	18	30.4	32	59.41	115	50.70	11.2	2.2	0.13	14
88- 2-15	22	45	17.7	32	52.51	115	41.25	8.2	2.0	0.05	7
88- 2-17	3	20	8.2	33	0.08	115	50.90	2.5	2.1	0.14	10
88- 2-17	23	10	3.1	32	58.86	115	48.66	4.1	2.5	0.11	14
88- 2-18	17	56	56.1	32	52.32	115	40.11	9.4	2.0	0.04	6
88- 2-18	18	47	56.4	32	59.21	115	45.53	2.0	2.1	0.12	11
88- 2-21	2	46	7.5	32	54.00	115	56.58	7.8	2.1	0.12	18
88- 2-23	11	9	8.2	32	59.17	115	48.45	2.7	2.1	0.05	7
88- 2-23	14	53	27.8	32	58.74	115	49.55	2.3	2.1	0.08	10
88- 2-26	15	15	18.0	32	59.52	115	48.49	6.6	2.0	0.12	10
88- 2-26	21	7	2.0	33	1.33	115	49.25	11.1	2.6	0.07	15
88- 2-27	1	55	41.9	33	0.35	115	49.30	5.2	2.2	0.08	15
88- 2-28	13	55	1.4	33	0.75	115	51.14	1.4	2.2	0.14	17
88- 3- 3	2	10	32.6	32	47.90	115	41.58	11.7	2.1	0.06	12
88- 3- 4	1	45	19.2	32	53.78	115	41.50	9.3	2.1	0.11	18
88- 3- 4	2	32	41.0	32	56.37	115	43.75	10.9	2.8	0.14	21
88- 3- 4	23	48	50.9	32	59.54	115	50.50	6.1	2.1	0.16	17
88- 3- 8	11	34	58.9	33	0.40	115	51.09	2.6	2.0	0.11	13
88- 3-10	6	41	46.7	32	57.15	115	47.91	2.4	2.0	0.10	11
88- 3-10	7	29	59.1	32	57.13	115	48.04	2.7	2.2	0.11	12
88- 3-11	19	27	24.5	32	56.96	115	48.05	5.9	2.0	0.11	13
88- 3-13	15	28	5.8	32	58.24	115	47.87	2.7	2.1	0.12	15
88- 3-14	15	52	56.0	32	57.90	115	48.67	2.5	2.0	0.10	13
88- 3-15	1	59	19.5	32	56.88	115	47.65	6.1	2.0	0.02	8
88- 3-16	21	19	31.8	32	57.99	115	48.47	4.3	2.4	0.10	15
88- 3-16	22	41	39.4	32	57.98	115	48.25	4.6	2.2	0.10	13
88- 3-19	2	3	35.9	32	54.79	115	44.66	8.4	2.0	0.03	10
88- 3-19	14	29	32.9	32	57.45	115	47.26	4.8	2.1	0.09	13
88- 3-20	19	4	6.1	32	58.51	115	48.58	3.7	2.2	0.09	12
88- 3-22	5	4	30.3	32	57.39	115	47.92	4.6	2.2	0.13	10
88- 3-22	7	8	46.5	32	56.49	115	43.87	11.6	2.2	0.10	10
88- 3-22	23	28	25.5	33	0.49	115	48.93	4.5	2.2	0.05	11
88- 3-24	20	20	30.8	32	58.57	115	48.53	4.0	2.0	0.11	10

88- 3-25	0	13	10.6	32	56.40	115	48.65	10.2	2.8	0.14	21
88- 3-25	1	18	30.8	32	56.30	115	48.24	10.0	2.1	0.11	13
88- 3-26	22	42	39.7	33	2.51	115	48.62	13.1	2.1	0.21	23
88- 3-27	22	21	1.4	32	57.80	115	49.34	2.6	2.0	0.08	12
88- 3-28	3	8	18.0	33	0.54	115	49.19	1.5	2.1	0.11	16
88- 3-29	5	47	9.5	33	0.22	115	49.67	6.3	2.0	0.06	11
88- 3-29	20	10	43.7	33	0.16	115	49.78	2.4	2.4	0.13	17
88- 3-29	21	51	55.0	33	0.35	115	49.70	1.8	2.6	0.13	16
88- 3-31	3	42	30.3	32	59.40	115	50.00	6.8	2.0	0.11	13
88- 4- 1	15	39	49.0	32	56.15	115	48.31	6.7	2.0	0.09	14
88- 4- 1	20	2	51.3	33	15.52	115	38.37	10.5	2.0	0.11	15
88- 4- 3	1	13	51.6	32	57.12	115	47.18	4.2	2.0	0.04	9
88- 4- 3	4	6	13.0	32	59.92	115	49.95	8.7	2.1	0.12	15
88- 4- 3	7	8	5.4	32	53.60	115	39.45	10.6	2.0	0.16	16
88- 4- 3	21	49	56.5	33	6.66	115	36.19	13.1	2.0	0.21	20
88- 4- 8	9	30	49.2	32	53.11	115	40.41	9.7	2.0	0.11	13
88- 4-11	22	31	58.1	33	11.42	115	37.53	11.6	2.2	0.07	8
88- 4-12	10	28	4.6	32	57.61	115	48.77	4.2	2.4	0.16	20
88- 4-13	11	0	33.4	32	59.27	115	49.63	0.6	2.1	0.15	19
88- 4-13	11	2	22.0	32	58.99	115	49.10	2.6	2.0	0.10	11
88- 4-13	20	38	8.6	33	0.28	115	51.03	2.7	2.0	0.15	16
88- 4-22	15	26	46.9	33	11.09	115	38.56	8.0	2.0	0.26	17
88- 4-24	12	13	39.0	32	53.28	115	38.41	10.6	3.1	0.14	25
88- 4-27	20	1	18.3	32	59.56	115	48.07	7.3	2.1	0.08	13
88- 4-30	2	37	18.3	32	54.19	115	39.54	0.8	2.1	0.17	20
88- 4-30	6	32	59.7	32	53.93	115	40.02	10.9	2.0	0.05	6
88- 4-30	12	18	11.7	32	53.95	115	38.93	0.5	2.0	0.21	8
88- 5- 6	16	33	31.3	33	9.99	115	36.85	12.4	2.0	0.05	10
88- 5- 9	18	12	30.9	32	57.76	115	46.99	5.4	2.0	0.06	9
88- 5-10	15	54	21.0	32	56.99	115	48.16	6.4	2.1	0.10	14
88- 5-18	19	13	43.4	33	10.29	115	37.90	11.8	2.1	0.19	24
88- 5-19	4	3	25.2	32	52.12	115	41.95	10.3	2.0	0.21	15
88- 5-19	7	38	9.2	32	58.17	115	47.24	4.3	2.0	0.09	9
88- 5-21	14	7	43.2	33	1.04	115	51.08	8.0	2.2	0.08	16
88- 5-25	16	23	14.3	32	57.21	115	48.05	4.4	2.1	0.12	15
88- 6- 2	5	23	6.3	32	59.63	115	48.54	0.7	2.0	0.05	8
88- 6- 2	6	25	56.3	32	59.92	115	47.92	2.7	2.0	0.09	10
88- 6- 2	6	26	7.2	33	0.01	115	47.77	2.6	2.0	0.07	8
88- 6- 5	13	58	8.4	33	9.81	115	37.56	11.3	2.5	0.28	24
88- 6- 7	0	46	40.4	33	0.87	115	50.93	9.9	2.5	0.12	18
88- 6- 7	11	58	55.3	33	0.12	115	50.57	10.2	2.0	0.09	16
88- 6- 7	19	45	0.6	32	56.33	115	48.92	6.5	2.0	0.06	9
88- 6- 7	23	46	52.3	33	9.95	115	36.76	11.3	2.1	0.11	11
88- 6- 8	21	48	37.5	32	59.08	115	48.67	5.1	2.2	0.13	10
88- 6-11	18	18	57.0	32	58.03	115	47.26	4.8	2.2	0.07	7
88- 6-21	8	37	34.2	33	0.68	115	49.43	6.5	2.2	0.08	14
88- 6-29	22	11	29.4	32	59.43	115	51.09	8.7	2.1	0.14	22
88- 7- 2	5	19	9.6	32	58.41	115	47.97	8.9	2.0	0.03	6
88- 7- 2	8	43	2.5	33	2.27	115	57.98	0.8	2.0	0.09	13
88- 7- 3	13	52	37.6	32	53.93	115	39.25	0.5	2.0	0.19	16
88- 7- 3	14	1	13.4	32	53.71	115	40.16	10.3	2.5	0.17	20
88- 7- 3	15	2	37.8	32	59.48	115	48.97	2.1	2.1	0.16	21
88- 7- 3	20	40	35.8	32	53.99	115	39.32	0.8	2.8	0.17	22
88- 7- 6	5	32	0.4	32	58.59	115	47.72	6.1	2.1	0.03	7
88- 7-10	7	30	59.3	32	52.65	115	41.62	10.3	2.0	0.11	16
88- 7-11	7	46	16.7	32	58.11	115	48.04	4.8	2.1	0.13	14
88- 7-11	9	4	21.7	32	57.96	115	47.91	4.4	2.1	0.14	14
88- 7-20	3	0	40.3	33	1.83	115	50.72	1.7	3.0	0.14	22
88- 7-21	7	1	2.3	32	53.01	115	41.56	10.0	2.1	0.07	12
88- 7-28	1	29	57.2	32	56.55	115	48.37	7.8	2.0	0.10	12
88- 7-30	8	23	22.2	32	53.29	115	41.15	10.1	2.9	0.15	18
88- 7-30	9	28	9.3	32	59.61	115	48.89	10.2	2.3	0.12	21
88- 7-30	9	31	9.6	32	59.62	115	48.85	10.5	2.5	0.11	18
88- 7-30	9	41	38.0	32	59.57	115	48.99	10.1	2.5	0.13	17
88- 7-31	15	19	5.5	33	0.09	115	50.66	8.2	2.2	0.09	13
88- 8- 1	14	37	27.6	32	59.44	115	50.74	7.3	2.3	0.10	13
88- 8- 2	15	47	52.9	32	59.71	115	48.65	6.2	2.4	0.13	15
88- 8- 7	10	23	18.1	32	58.79	115	51.60	9.1	2.2	0.13	18
88- 8- 8	17	22	11.0	33	3.09	115	52.13	1.5	2.7	0.12	20
88- 9- 7	14	56	19.8	33	6.47	115	35.06	12.8	2.7	0.17	29
88- 9-11	4	17	34.2	32	59.92	115	51.04	2.2	2.0	0.12	13
88- 9-21	16	6	32.5	33	0.35	115	50.63	2.3	2.1	0.14	15
88- 9-22	5	58	36.7	32	57.94	115	48.52	4.4	2.1	0.15	21
88-10- 4	1	29	37.8	32	59.72	115	50.71	10.3	2.1	0.15	17
88-10- 6	11	30	3.1	33	0.73	115	51.56	1.5	2.0	0.14	16
88-10- 9	13	18	38.9	33	1.73	115	50.84	1.5	2.1	0.12	15
88-10-10	20	6	46.2	33	8.06	115	45.96	9.7	2.1	0.23	23
88-10-15	19	52	4.5	33	11.54	115	36.08	10.3	2.4	0.21	23

88-10-19	16	52	46.7	32	59.00	115	48.44	6.8	2.1	0.06	10
88-10-19	22	47	53.9	33	11.02	115	35.99	10.4	3.7	0.25	27
88-10-19	22	55	47.0	33	11.75	115	36.09	10.8	3.4	0.18	21
88-10-20	1	49	3.0	33	12.29	115	34.83	9.8	2.5	0.23	22
88-10-20	2	5	42.8	33	12.93	115	35.06	10.0	2.1	0.23	14
88-10-22	2	30	44.1	33	12.95	115	35.19	10.0	2.4	0.17	20
88-10-23	10	31	25.4	33	11.42	115	36.10	11.3	2.0	0.13	11
88-11- 6	19	49	32.9	33	12.69	115	34.98	10.2	2.6	0.24	23
88-11- 8	4	34	33.2	32	52.13	115	39.75	10.4	3.2	0.12	20
88-11-29	14	38	4.0	32	55.36	115	42.83	10.9	2.2	0.12	17
88-11-30	8	11	51.5	33	12.88	115	34.99	9.5	2.1	0.19	16
88-12- 2	2	6	15.2	33	11.35	115	35.46	10.4	2.0	0.12	13
88-12- 2	2	54	25.4	33	11.09	115	35.39	11.4	2.0	0.13	14
88-12- 2	2	59	13.7	33	11.49	115	35.68	11.8	2.0	0.07	7
88-12- 2	4	1	52.7	33	11.59	115	35.67	11.3	2.3	0.19	16
88-12- 2	5	26	46.2	33	11.29	115	35.55	10.9	2.0	0.18	15
88-12- 2	15	36	5.9	33	11.59	115	36.34	10.0	2.3	0.27	19
88-12- 7	8	43	59.9	32	58.79	115	49.70	2.7	2.1	0.17	21
88-12- 8	3	4	43.1	32	58.08	115	48.56	3.0	2.9	0.18	19
88-12- 8	5	59	22.5	33	11.60	115	34.80	9.9	2.5	0.22	24
88-12-22	2	1	7.4	33	11.58	115	35.12	10.9	2.4	0.20	21
88-12-22	2	3	59.0	33	11.46	115	34.73	9.3	3.1	0.23	23
88-12-22	2	6	56.8	33	11.61	115	35.09	9.9	2.9	0.22	21
88-12-22	13	42	22.4	32	57.54	115	48.61	4.6	2.1	0.13	14
88-12-22	13	43	7.7	32	57.55	115	48.66	4.6	2.2	0.14	16
88-12-22	15	9	20.5	32	58.10	115	46.28	2.8	2.1	0.08	11
88-12-22	18	40	16.9	32	59.59	115	50.03	9.1	2.0	0.07	12
88-12-23	0	6	3.7	32	57.53	115	48.59	4.4	2.4	0.15	18
88-12-24	0	23	31.5	32	57.46	115	48.06	3.1	2.1	0.16	13
88-12-24	5	53	32.2	32	57.58	115	48.57	4.0	2.3	0.15	19
88-12-29	3	33	24.3	33	10.98	115	34.72	10.8	3.0	0.22	26
89- 1- 4	5	5	10.9	32	56.02	115	44.17	10.5	2.3	0.12	21
89- 1- 6	20	30	3.0	33	12.23	115	35.22	12.6	3.2	0.10	9
89- 1-11	10	31	16.3	33	16.41	115	37.24	10.0	2.0	0.15	15
89- 1-22	8	43	1.4	33	11.35	115	35.27	10.1	2.0	0.21	20
89- 1-26	15	14	31.3	33	11.00	115	34.34	9.2	2.0	0.22	10
89- 1-26	15	14	47.7	33	11.61	115	34.73	9.5	2.1	0.17	11
89- 2- 3	3	45	29.5	33	11.07	115	35.13	9.3	2.3	0.23	21
89- 2- 3	7	48	51.3	33	10.92	115	35.01	10.7	2.0	0.21	19
89- 2- 3	14	10	7.6	33	10.97	115	34.64	11.7	2.1	0.29	16
89- 2- 3	18	14	22.6	33	10.85	115	34.39	10.4	2.3	0.19	15
89- 2- 3	23	30	27.6	33	10.98	115	34.93	8.9	2.0	0.16	8
89- 2- 3	23	37	11.8	33	10.82	115	35.36	9.3	2.2	0.20	13
89- 2- 3	23	48	46.1	33	11.10	115	35.50	10.4	3.4	0.29	25
89- 2- 8	16	35	57.8	33	11.15	115	34.53	9.8	2.1	0.17	8

Depth is in kilometers. Rms is the rms travel time residual. Npicks is the number of P and S times used in the earthquake location.

Chapter 4

Teleseismic Source Parameters and Rupture Characteristics of the 24 November 1987, Superstition Hills Earthquake

4.1 Introduction

The 24 November 1987, Superstition Hills earthquake sequence occurred in the western Imperial Valley in southern California. The earthquakes took place on a conjugate fault system consisting of the right-lateral, northwest-striking Superstition Hills fault and the left-lateral, northeast-striking Elmore Ranch fault (Figure 4.1). The earthquake sequence consisted of foreshocks, an M_s 6.2 mainshock, and aftershocks on the Elmore Ranch fault followed by an M_s 6.6 mainshock and aftershocks on the Superstition Hills fault (Magistrale *et al.*, 1989, see also Chapter 3). The epicenter of the Superstition Hills mainshock is located near the intersection of the two faults. The Superstition Hills fault ruptured the surface in three strands (Sharp *et al.*, 1989): the north and south segments of the Superstition Hills fault, and the Wienert fault to the south (Figure 4.1). The fault strands are separated by narrow right steps. Previous geologic and seismologic investigations (Hanks and Allen, 1989) provide useful constraints for this teleseismic study. The strike of the surface rupture (Sharp *et al.*, 1989) constrains the plane of fault rupture and the distribution of aftershocks (Magistrale *et al.*, 1989) indicates a depth range of moment release to investigate.

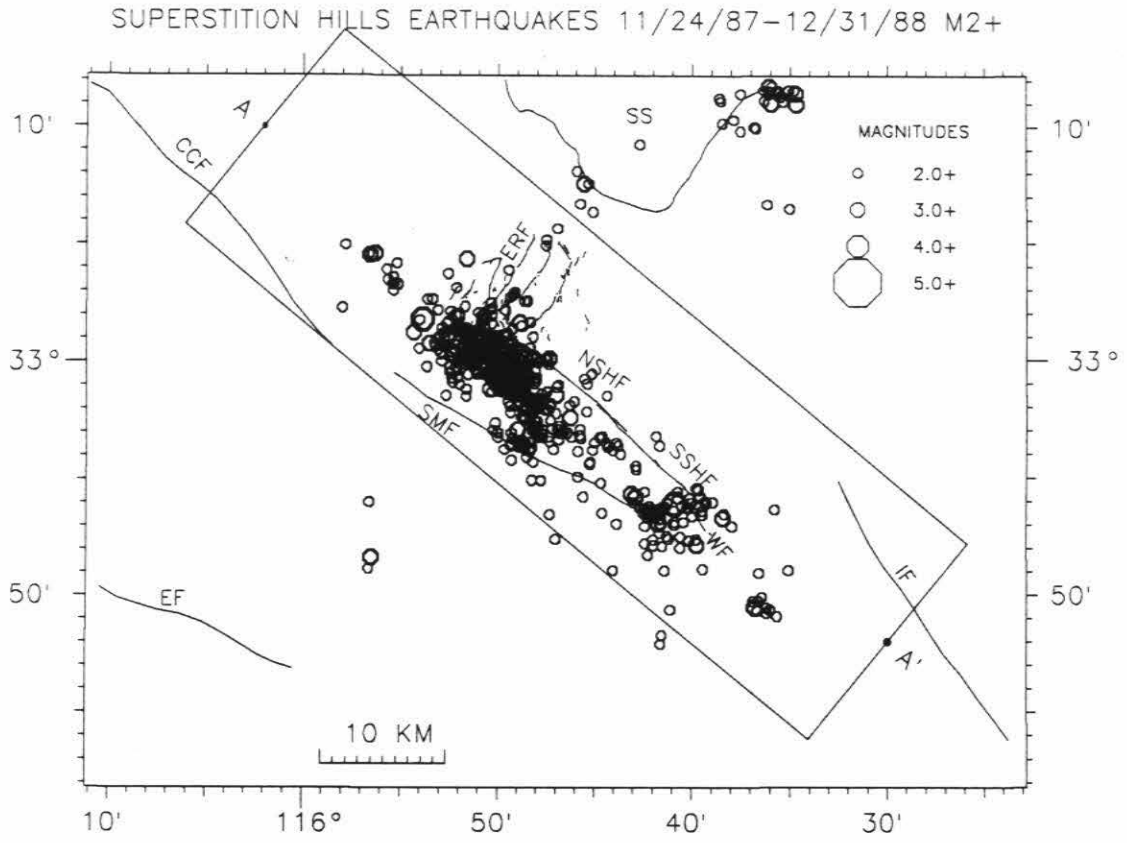

Figure 4.1 The 24 November 1987 Superstition Hills earthquake (star, obscured by aftershocks) and $M_L \geq 2$ aftershocks from 11/24/87 to 12/31/88. Symbol size is scaled to earthquake magnitude. Box AA' encloses earthquakes shown in the cross section of Figure 4.2. Earthquake location technique is described in Chapter 3. The trace of the Elmore Ranch and Superstition Hills fault rupture is from Sharp *et al.*, 1989. Abbreviations: NSHF, northern segment of the Superstition Hills fault; SSHF, southern segment of the Superstition Hills fault; WF, Wienert fault; ERF, Elmore Ranch Fault; SMF, Superstition Mountain fault; CCF, Coyote Creek fault; EF, Elsinore fault; IF, Imperial fault; and SS, Salton Sea.

4.2 Body Wave Modeling

The Superstition Hills earthquake was recorded by nearby strong motion instruments, and local and teleseismic seismic networks. Source studies of this earthquake by several authors utilize these data and provide a general picture of this earthquake over a broad frequency range.

Frankel and Wennerberg (1989) inverted high frequency strong motion recordings using a tomographic source inversion technique to determine timing, location, one-dimensional extent and rupture velocity of three subevents. The effective rupture velocity between the two principal subevents, their subevents 2 and 3, is very slow but the individual subevent rupture velocities are greater than or equal to the shear wave velocity of the medium, respectively. Depth was determined from waveform complexity.

Frankel and Wennerberg (1989) investigated rupture to the northeast of the epicenter along the Elmore Ranch fault. This rupture direction improved the waveform and amplitude fits to strong motion records to the northeast, but records at other azimuths had worse or similar fits to their preferred model of rupture along the Superstition Hills fault. Wald and Somerville (1988) also propose that a subevent ruptured the Elmore Ranch fault. However, Frankel and Wennerberg (1989) point out that the lack of aftershocks along the Elmore Ranch fault following the Superstition Hills earthquake does not support rupture of the Elmore Ranch fault during the Superstition Hills earthquake.

Bent *et al.* (1989) forward modeled long-period regional and teleseismic P- and SH-waveforms using a method based on ray summation (Langston and Helmberger, 1975). They determined focal mechanism, depth, timing and source separation distance for two subevents that have different mechanisms.

For their second subevent, they investigated both point and distributed source models. The solutions for the different models were not significantly different. Their preferred model explains the event as two distinct point sources separated in time and space. They placed their second subevent due south of the first subevent. The distance between subevents is poorly resolved. If their first subevent is near the north end of the Superstition Hills fault, their preferred model would place the second subevent substantially off the surface trace of the Superstition Hills fault. Alternatively, restricting the first subevent to lie on the Elmore Ranch fault and the second subevent to lie on the Superstition Hills fault would place the first subevent at least 16 km northeast from the epicenter.

Sipkin (1989) inverted teleseismic long-period waveforms using a time-dependent moment-tensor algorithm to resolve a time varying moment tensor and a detailed source time function. He modeled this earthquake with a complex source time function consisting of two subevents with no significant change in focal mechanism. In his model, sources were constrained to occur at the same location and focal depth, so he does not consider spatial separation of subevents.

Source parameters from the above studies are summarized in Table 4.1. Several important questions are not well resolved by these studies. No model clearly determines whether any moment release occurred on the Elmore Ranch fault during the Superstition Hills earthquake and if all the segments of the Superstition Hills fault ruptured coseismically. By using an inverse method that allows for multiple source parameterizations, an improvement on the resolution of directivity, rupture velocity and spatial extent of the sources can be made.

Table 4.1
Model Parameters

Model	Strike deg	Dip deg	Slip deg	Depth km	Delay sec	Velocity km/sec	Distance km	Azimuth deg	Moment dyne−cm×10^{25}
MJK	305	90	180	2	-	-	-	-	-
FW#	128	90	180	9	0	-	-	-	-
	128	90	180	9	3	5.3	2	-	0.37*
	128	90	180	9	9.7	3	8	-	1.4*
S	303	89	-180	10	5-9	-	0	0	10
HRV	133	78	178	15	-	-	-	-	7.2
BHSH	305	80	175	10	0	-	0	0	3.6
	320	80	175	6	7.5	-	30	180	7.2
HMK1	120	88	194	4	0	-	0	0	2.4
	126	69	182	6	8.1	-	20	125	5.2
HMK2	122	82	194	4	0	-	0	0	3.1
	125	63	178	6	8.2	2.5	22.5	125	4.8

* moment at ~1 Hz

assumed focal mechanism

MJK: Magistrale et al. (1989)

FW: Frankel and Wennerberg (1989)

S: Sipkin (1989)

HRV: Harvard Centroid Moment Tensor

BHSH: Bent et al. (1989)

HMK1: Hwang et al. (in press), Model 1

HMK2: Hwang et al. (in press), Model 2

4.3 Data Preparation, Method, and Results

Teleseismic body waves were simultaneously inverted in a least-squares sense using the method of Nabelek (1984, 1985). This method can invert for multiple sources and solves simultaneously for focal mechanism, centroid depth and source time function for each source and solves for the separation time, distance and azimuth between the sources. Point and line sources were investigated. Data preparation, modeling technique, and error analysis are discussed in detail in Hwang *et al.*, (in press) and are only briefly mentioned here. That paper also displays the waveform data, not shown here.

The data set consists of long-period Global Digital Seismic Network (GDSN), Worldwide Standard Seismograph Network (WWSSN), and Canadian Network (CAND) P- and SH-waveforms restricted to the distance range $30^\circ \leq \Delta \leq 90^\circ$ for P-waves and $30^\circ \leq \Delta \leq 80^\circ$ for SH-waves to avoid regional and core effects. The crustal velocity structure for the source region was taken after Fuis *et al.* (1982). It is the same as the east part of the hybrid velocity model of the western Imperial Valley used in Chapters 2 and 3 (Tables 2.3 and 3.1). The modeling results are only mildly sensitive to the source crustal model used.

Data from the Southern California seismograph network define the source dimensions and location of this event (Magistrale *et al.*, 1989, see also Chapter 3). In the inversion, the locally determined focal mechanism (strike 305°, dip 90°, slip 180°) was used as the starting mechanism. The nucleation point of the first subevent is constrained to the locally determined hypocentral depth of 2 km but the centroid depth may differ. Aftershock data defines the bottom of the seismogenic zone at a depth of 12 km, and extends this zone to a distance of 30 km striking northwest along the Superstition

Hills fault (Figure 4.2). Multiple sources were constrained to lie along the fault plane with rupture velocities up to the shear wave velocity of the medium, 3.5 km/sec. For Subevent 1, sources along the Superstition Hills fault (out to 30 km) and Elmore Ranch fault (out to 25 km) were investigated. The above depth, distance and velocity ranges are systematically searched for the best solution assuming a source time function of approximately 15 sec duration based on inspection of the waveforms.

Single point and single line source models were unable to explain the data. A two source (two subevents) model provides a much better fit. For Subevent 1, centroid locations along the Elmore Ranch fault were tested. Solutions worsen as Subevent 1 is moved further away from the epicenter. However, a point source closer than 10 km to the epicenter is unresolvable from a point source at the epicenter. Either moment release along the Elmore Ranch fault during Subevent 1 was not a substantial portion of the long-period moment release or it occurred within 10 km to the epicenter of the event. In the final models, Subevent 1 is a point source located at the epicenter. Since the epicenter lies near the intersection of the Elmore Ranch and Superstition Hills faults and has a focal plane parallel to each fault, the choice of fault plane is ambiguous. The northwest striking Superstition Hills fault plane is chosen for the sake of discussion.

Investigation of various double source models suggests two possible source parameterizations. Model 1 consists of two temporally and spatially separate point sources. Spatial separation of the two sources is investigated by placing Subevent 2 at 5 km intervals southeast of Subevent 1 along the strike of the fault, 305°. Model 2 consists of one point source and one time-delayed propagating line source. Rupture velocity was modeled at 0.5 km/sec

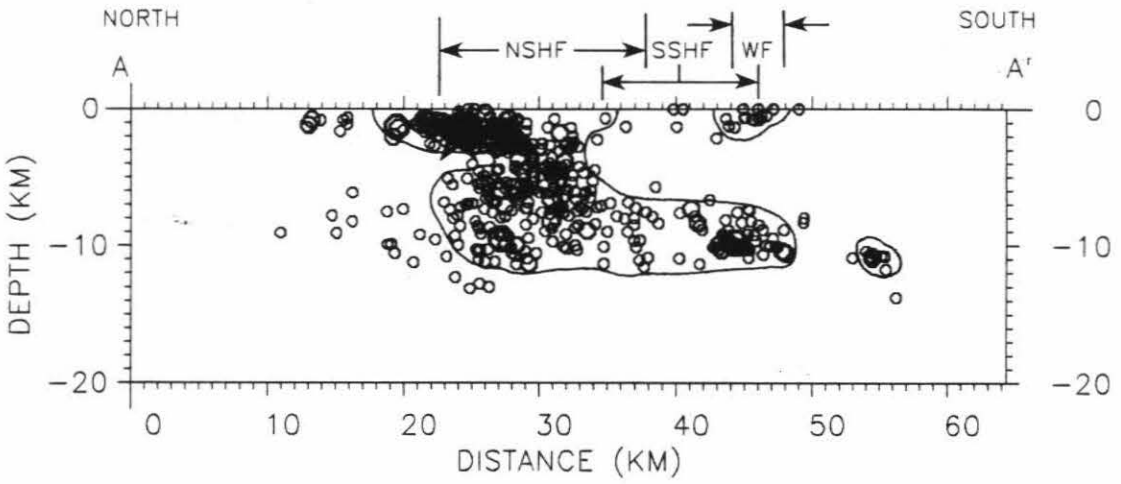

Figure 4.2 Cross section parallel to the Superstition Hills fault. All events in Figure 4.1 within 10 km of cross section are projected onto the cross section. The aftershock zone is outlined. Earthquake symbols and abbreviations are the same as in Figure 4.1.

intervals. In Model 2, the line source remains within a specified focal plane as the plane changes its orientation during the inversion. Final solutions for both models are given in Table 4.1.

The best solution has the centroid depths of Subevent 1 and Subevent 2 at 4 and 6 km, respectively. Centroid depth of Subevent 1 is not robust, and Subevent 2 can have a range of 4 to 8 km in centroid depth. In the inversion, formal errors for each solution are small. A more realistic estimation of the model errors is determined from the range of acceptable solutions. In Model 1, Subevent 2 can occur at a distance range of 15-20 km from Subevent 1. In Model 2, the rupture velocity may be as low as 1.5 km/sec up to the preferred velocity of 2.5 km/sec. This velocity is 0.7 V_{sh} of the shear wave velocity in the layer. Within the above depth, distance and velocity ranges, the strike is well constrained to $\pm 1^\circ$ and the dip and rake are resolved to approximately $\pm 5^\circ$ for both models and subevents (Table 4.1).

The total moment for both models is less than but in good agreement with that of Bent *et al.* (1989) and Sipkin (1989) and comparable to the Harvard CMT solution (Table 4.1). Total moment corresponds to a M_w 6.5.

4.4 Discussion

Figure 4.3 summarizes the fault rupture models in this and previous studies along with aftershock, afterslip, and structural data. Symbols as noted in the figure represent point sources for different models. Line sources are represented by bold arrows.

In this study, both Model 1 and Model 2 give a reasonable fit to the data. Both solutions indicate a steep, westerly-dipping fault plane for Subevent 1 and a 70° westerly-dipping fault plane for Subevent 2. The

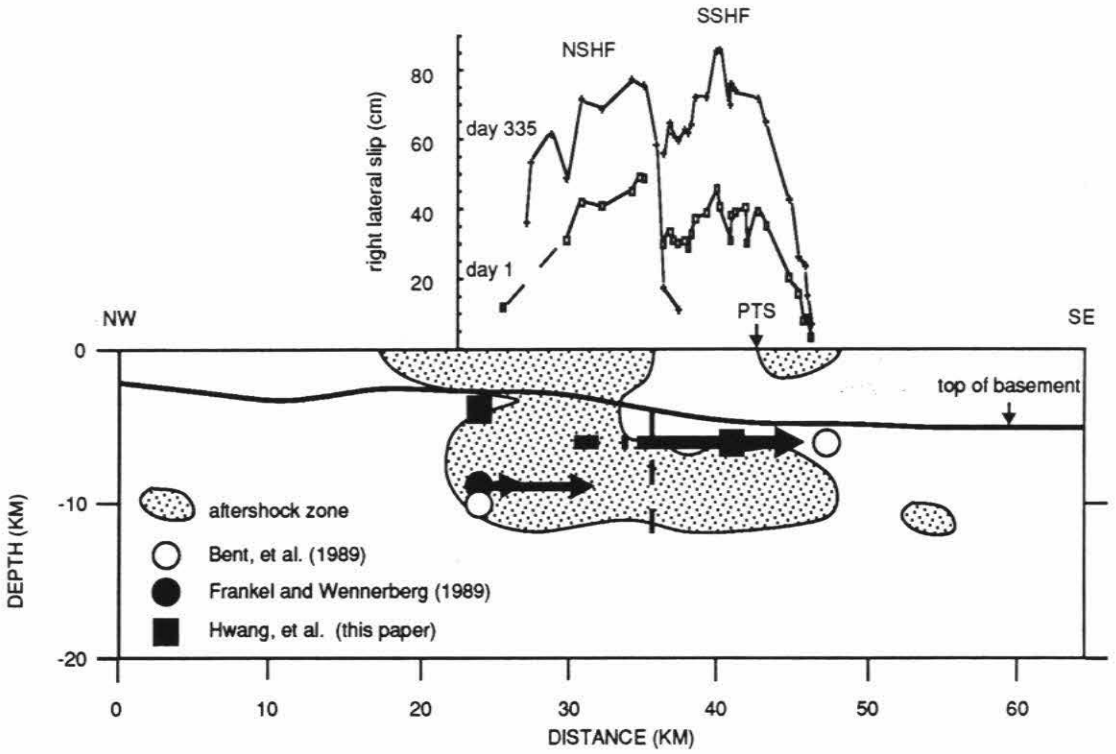

Figure 4.3 Northwest-southeast cross section parallel to the Superstition Hills fault summarizing fault rupture models and slip history along the fault. The top figure shows afterslip plotted along the fault for 1 day and 335 days after the earthquake (from Chapter 5). The bottom figure outlines the aftershock area (thin line, see Figure 4.2) and basement topography (bold line, after Kohler and Fuis, 1986). The bold dashed line separates crystalline basement to the north (left) from metasedimentary basement to the south (right). Symbols as noted in the figure show source location and lateral extent for rupture models from this and previous studies. Abbreviations are the same as Figure 4.1. See Table 4.1 for source parameters.

western dip agrees broadly with the location of the aftershocks to the west of the surface trace of the fault (Figure 4.1). In both models, the centroid for Subevent 1 lies at or near the epicenter. Subevent 1 nucleates at a depth of 2 km but has a centroid depth of 4 km. The nucleation point is recorded as the hypocenter by the local southern California seismic array. Fault rupture proceeds from northwest to southeast. Most of the moment release for Subevent 2 lies along the southern segment of the Superstition Hills fault at a depth of 6 km. For Subevent 2, Model 1 places a point source between 15-20 km southeast of Subevent 1 along the strike of the fault. Model 2 distributes the source along a line at a distance of 10 to 22 km southeast from Subevent 1. Assuming a lower rupture velocity of 1.5 km/sec would move this to a distance of 6 to 14 km. This lower distance bound is illustrated by a bold dashed line in Figure 4.3. The upper distance bound, 22 km, agrees with the extent of surface rupture along the Superstition Hills fault (Sharp *et al.*, 1989). Moment release along the southern segment accounts for 2/3 of the total moment release for this earthquake. No significant moment release is seen along the Wienert fault.

The timing of the two subevents proposed by Bent *et al.* (1989) correlates with the timing of the two subevents in Model 1 and Model 2, but their locations differ substantially. Bent *et al.* (1989) place their second subevent due south of their first subevent at a preferred separation distance of 30 $\pm$10 km. Constraining the first subevent to lie along the Elmore Ranch fault and the second subevent to lie along the Superstition Hills fault would place their first subevent between 16 and 33 km northeast of the epicenter and their second subevent between 11 and 31 km southeast of the epicenter. A distance greater than 10 km northeast from the epicenter for the first subevent is not

supported by this study. The lack of afterslip and aftershocks also does not support a large moment releasing subevent along the Elmore Ranch fault for the first subevent (Frankel and Wennerberg, 1989). Placing Bent *et al.*'s (1989) first subevent on the Superstition Hills fault would place the second subevent well off the surface trace of the southern Superstition Hills fault.

The model of Frankel and Wennerberg (1989) shows some similarities to Model 1 and Model 2. Subevent 1 correlates with their subevent 1 and 2 where their subevent 1 represents the nucleation point of the earthquake. The timing of their subevent 3 correlates with Subevent 2 but the position of the sources differ. Slip for their subevent 3 starts at 0 km and does not extend past 8 km (see Figure 4.3). All their subevents occur on the northern segment of the Superstition Hills fault. Total moment for their model is 1/6 of what is observed at long periods (see Table 4.1). Hence, their model may not account for all of the slip along the fault.

Model 1 and Model 2 are still consistent with the raw strong motion data. The record from PTS located 18 km from the epicenter on the Superstition Hills fault suggests that significant moment release did not go beyond that station (Frankel and Wennerberg, 1989). Even though surface rupture continued along the trace of the fault out to 24 km, the magnitude of surface slip dies off rapidly beyond PTS (see Figure 4.3). This distance falls within the range of the estimate of the position and extent of Subevent 2 in both models. If the maximum extent for Subevent 2 is 18 km, this would imply a slightly slower rupture velocity in Model 2 of 2.25 km/sec. The strong motion data also indicate directivity towards the northeast along the Elmore Ranch fault (Frankel and Wennerberg, 1989; Wald and Sommerville, 1989). Any moment release within 10 km of the epicenter along the Elmore

Ranch fault is not resolvable from the long-period data.

Figure 4.3 compares the depth of moment release determined here, 4 to 8 km, to the depth distribution of the aftershocks. The aftershocks lie mostly between 1 to 11 km depth. Along the northern segment of the fault, relatively few aftershocks lie between 2.5 to 5 km depth and in the south, between 2 to 8 km. This is in agreement with studies of slip distribution along faults that find fewest aftershocks in areas of greatest slip (Doser and Kanamori, 1986b, Mendoza and Hartzell, 1988) and greatest moment release (Schwartz *et al.*, 1989) on the fault plane. Here it is assumed regions of greatest moment release correspond to areas of high slip. The centroid depths of both subevents in this study are generally shallower than the depths determined in the previous studies.

The model of Frankel and Wennerberg (1989) suggests that high frequency energy radiated predominately from the northern end of the fault. Combined with the results from Model 1 and 2, this suggests that both high frequency and low frequency energy radiated in the epicentral region along the northern segment of the Superstition Hills fault while only low frequency energy radiated from the southern segment. This agrees with previous studies that indicate a different behavior for the two fault segments. In Model 1 and Model 2, the northern segment dips near vertically and the southern segment dips steeply towards the west. The northern segment had a smaller proportion of afterslip than the southern segment (Chapter 5), and more aftershocks (Chapter 3). The boundary between the northern and southern segments lies at a step in the basement. This step separates the deeper sediments (4 to 5 km thick) of the southern segment that overlie metasedimentary basement from the thinner sediments (2 km thick) of the

northern segment that overlie crystalline basement (Figure 4.3).

4.5 Conclusion

Teleseismic body waves of the 24 November 1987 Superstition Hills earthquake are inverted using the method of Nabelek (1984,1985). Two multiple source models are obtained. In both models, Subevent 2 begins 8 sec after the initiation of Subevent 1 and has 2/3 of the total moment . The total moment for both models is about 8×10^{25} dyne-cm. In Model 1, the first point source occurs under the epicenter, followed by a second point source 15 to 20 km away southeast along strike of the fault. In Model 2, the first point source is followed by a line source of 8 sec duration rupturing southeast at 1.5 to 2.5 km/sec. Sources for both models are between 4 to 8 km depth. The fault dip changes from near vertical near its northern end to about 70° near its southern end.

Moment release for Subevent 1 occurs in the epicentral region and radiates both short and long-period energy. A small portion of the Elmore Ranch fault ($<$ 10 km) may have reruptured during Subevent 1 or alternatively, all moment release for both subevents was confined to the Superstition Hills fault. The second subevent ruptured the southern segment of the Superstition Hills fault radiating a substantial portion of the long-period energy resolved in this study. The difference in rupture characteristics and fault dips seen teleseismically is also reflected in aftershock and afterslip data, and crustal structure underlying the two fault segments.

Chapter 5

Slip Along The Superstition Hills Fault Associated With The 24 November 1987 Superstition Hills, California, Earthquake

5.1 Introduction

The 24 November M_s 6.6 Superstition Hills earthquake was part of a complex sequence of earthquakes in late 1987. Kahle *et al.* (1988) found no slippage across the Superstition Hills fault during a visit about 2.5 hours before the Superstition Hills earthquake, but they observed dextral surface displacement of about 15 cm across the fault 30 minutes after the event. Those observations demonstrate that rupture of the Superstition Hills fault was the primary cause of the 24 November event. Aftershock distribution verifies this interpretation (Magistrale *et al.*, 1989, see also Chapter 3). A first-motion focal mechanism of right-lateral strike slip on a vertical plane striking 305° (Magistrale *et al.*, 1989, see also Chapter 3) for the Superstition Hills earthquake is compatible with the strike and sense of slip of the Superstition Hills fault.

The M_s 6.2 Elmore Ranch earthquake preceded the Superstition Hills earthquake by 11 hours. This earlier event involved primarily left-lateral rupture of northeast-striking faults oriented perpendicular to the northern Superstition Hills fault (Figure 5.1) (Hudnut *et al.*, 1989, Sharp *et al.*, 1989, Magistrale *et al.*, 1989).

In the process of documenting displacement of the Superstition Hills fault associated with the Superstition Hills earthquake, it became apparent that afterslip was proceeding rapidly. Repeated measurements of fault

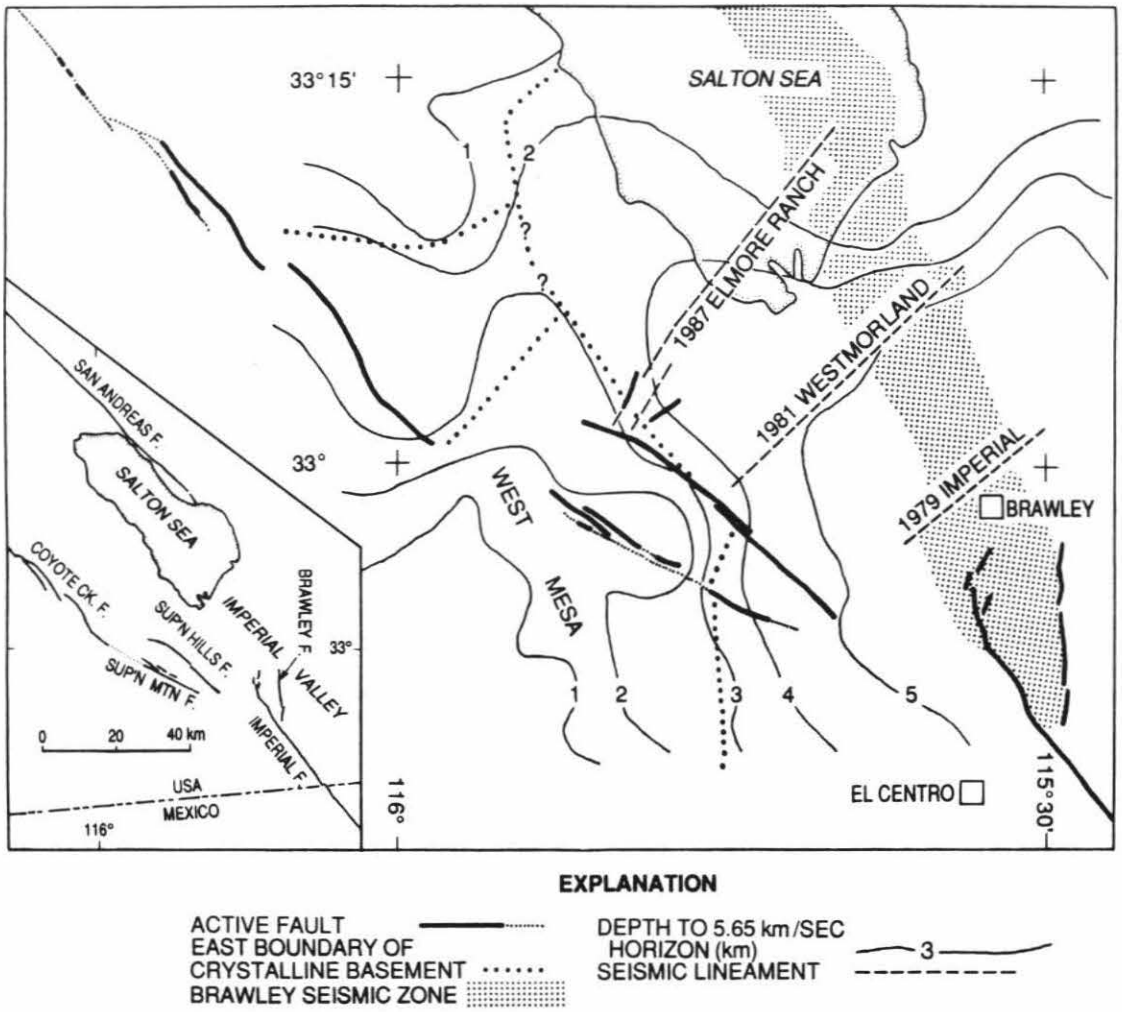

Figure 5.1 Tectonic environment of the Superstition Hills fault. Shown in the inset are the Brawley, northern Imperial and southern San Andreas faults. Branches of the southern San Jacinto fault zone including the Coyote Creek, Superstition Mountain and Superstition Hills faults are also shown. Most fault locations are from Sharp, 1982. Major northeast-trending seismic lineaments are dashed. These were expressed in association with the 1979 Imperial Valley (Johnson and Hutton, 1982), the 1981 Westmorland (Hutton and Johnson, 1981), and the 1987 Elmore Ranch earthquakes (Magistrale *et al.*, 1989). Contours correspond to depth in kilometers to the 5.65 km/s seismic velocity associated by Kohler and Fuis (1986) with the base of unmetamorphosed sediments. The bold dotted line indicates the boundary of continental basement as inferred by Fuis and Kohler (1984). A basin in the area adjacent and east of the southern Coyote Creek fault was detected by analysis of residuals in earthquake locations obtained with portable stations (Hamilton, 1970) and by refraction methods (Kohler and Fuis, 1986).

displacement were made in order to attempt to discover relationships between afterslip parameters and the geological character of the fault. Afterslip behavior correlates with prominent geometric features of the fault trace including a bend and a right-step, to a large increase in the thickness of sedimentary cover from north to south along the fault, and to the presence of buried continental crystalline basement along the fault's northern half.

Tectonic setting. The Superstition Hills fault is one of the prominent northwest- trending faults at the transition from the East Pacific Rise - Gulf of California spreading system to the southern California continental transform system. This fault appears to cut from crust that lies within the extensional Gulf of California province to continental crust at the edge of the Peninsular Ranges province (Fuis *et al.*, 1982). Rupture of faults adjacent to the Superstition Hills fault caused a number of significant earthquakes during the past 20 years. These include the 1968 rupture of the Coyote Creek fault (Clark, 1972), 1940 and 1979 ruptures of the Imperial fault (Richter, 1958, Sharp *et al.*, 1982), and the rupture of an unnamed northeast-striking fault in the 1981 Westmorland earthquake (Figure 5.1) (Hutton and Johnson, 1981). Of the larger, mapped, active faults within the Salton Trough, only the San Andreas and Superstition Mountain faults have not ruptured in the past 20 year period (Figure 5.1).

5.2 Methods

Surface displacements were measured along the 24-km-length of the Superstition Hills fault at successive times, from two hours to 11 months after the 24 November, 1987, Superstition Hills earthquake. During reconnaissance along two major segments of the fault rupture, many relatively simple

sections of the fault were identified. These sections of the fault are single stranded and are locally parallel to the overall strike of the Superstition Hills fault. Most of the displacement measurements were made within these simple sections where a large fraction of surface displacement occurred across a narrow zone.

Initial measurements. Determination of initial slip was accomplished by matching features across the fault. Most of our measurements were made across small extensional fault jogs and offset tire tracks. A few fresh and well- defined channel offsets were measured. (See Williams and Magistrale, 1989, for photographs of offset features.) These features allowed precise determination of right-lateral displacement parallel to the mean local strike of the fault. At some sites, several features were offset, so measurements were combined for a mean site displacement. The uncertainty of most initial measurements was 5 mm. Each site was named (Figure 5.2), and alignment marks were made across the fault by painting a 1- to 2-m- long reference line directly on the ground surface. Even on sandy surfaces the paint lines were durable for at least several weeks. This durability allowed accurate slip determinations after the original offset features eroded. Primary and successive slip measurements are necessarily small in aperture (*i.e.*, 1 to 2 m) because initial offsets could be accurately determined only for discrete fractures.

Remeasurements. Many sites were revisited several times within 12 days of the earthquake. The most comprehensive surveys were made on 25 November and 5-6 December, 1987, and 25-26 January and 24 October, 1988. On 24 November, 1987, 14 sites were measured and marked with paint alignments. By 27 November, 1987, 35 sites were established. These sites

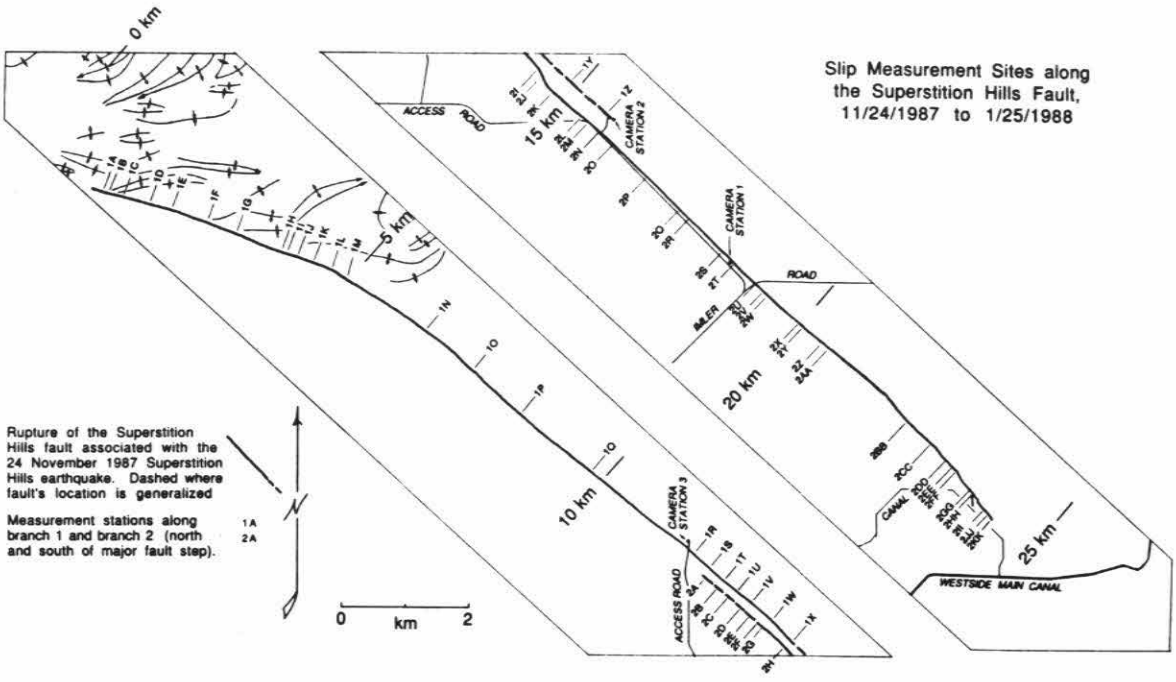

Figure 5.2 Reference map of Superstition Hills fault and slip measurement sites. Sites are numbered from north to south. Sites along the northern segment are denoted 1A to 1Z, sites along the southern segment are denoted 2A to 2KK. Note the bend of the fault between kilometers 4 and 5, and closely spaced tight folds in the Borrego Fm. adjacent to the northern 6 km of the fault as mapped by Dibblee (1984). Folds in the same unit farther south along the fault are much more open. The zone of fault step-over, discussed in the text, is located between kms 12.4 and 15.6.

were remeasured and remonumented, and 18 additional sites were established on 5-6 December, 1987. On 25-26 January, 1988, 49 sites were remeasured and on 24 October, 1988, 33 sites were remeasured. Additional measurements were made at intermediate and subsequent times at some very accessible sites.

During site visits paint-line offsets were measured, remaining original offset features were measured, and more durable alignment monuments were established to replace deteriorated paint-lines. At most sites linear arrays of nails were pushed into the soil and covered with stone cairns. Offsets were measured with the aid of two straight edges and a measuring tape. Uncertainty in these measurements was generally less than 3 mm, except at sites where substantial degradation of reference marks occurred.

5.3 Data

Fault segments. The fault is composed of two major segments (Figure 5.2) that are distinguished by a right stepping zone of complex faulting. The northern and southern segments are approximately 14.9 and 12.1 km in length, respectively. These two segments overlap across a 3.5-km-long zone, thus the rupture along the Superstition Hills fault was about 23.5 km in length, corresponding to the previously known extent of the fault. Sharp *et al.*, (1989) have mapped ruptures that extend 4 km south of the previously known extent of the Superstition Hills fault. Slip across those ruptures is not described here.

Character of afterslip accumulation. A sample of the afterslip data is presented in Figure 5.3. The most complete records of fault slippage during the first 1800 hour period were acquired at sites about 6 km south of the mid-point of the Superstition Hills fault (sites 2T and 2U, Figure 5.2).

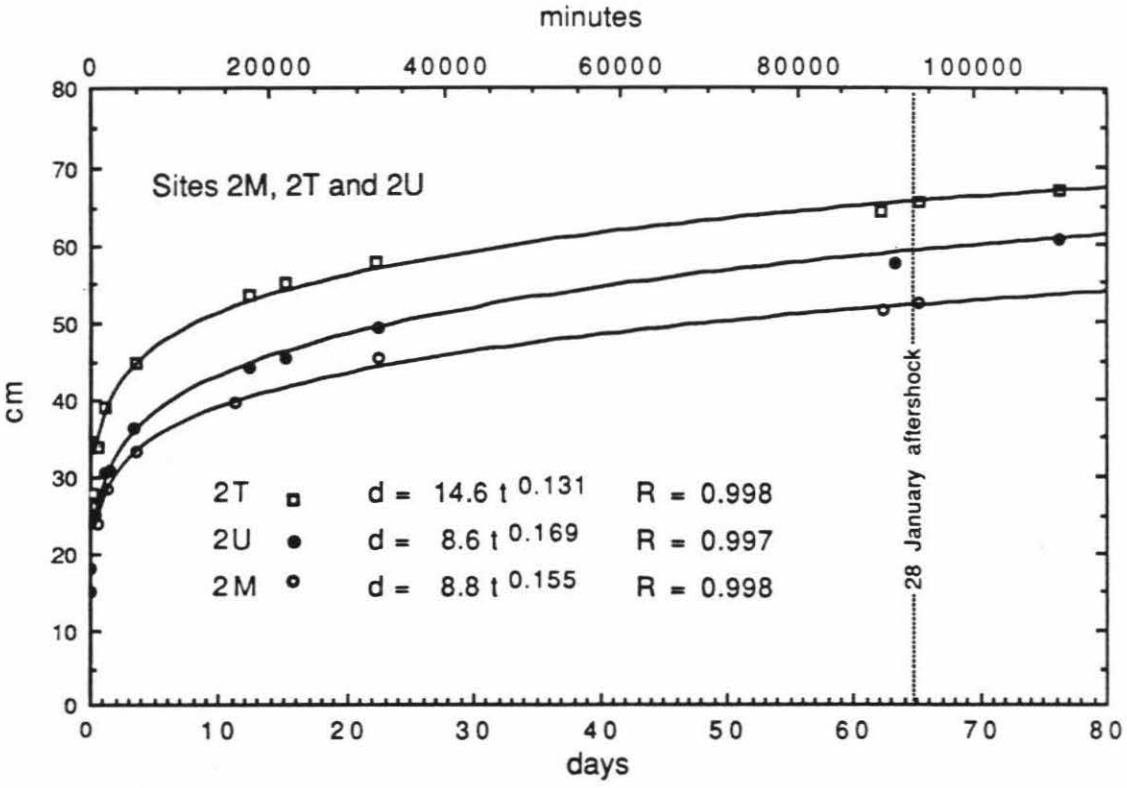

Figure 5.3 Slip decay curves for sites 2M, 2T, and 2U. Note the increase of displacement at sites 2M and 2T after a large aftershock (M_L 4.7) on the 28th of January, 1988. To the right of the key are power law equations of the form, $d=at^b$ ($b<1$), where d is displacement in cm, t is time in minutes, a and b are constants. Also listed is the correlation coefficient R.

Displacement at site 2T was 28 cm at 2.75 hours, 39 cm at 28 hours, and 67 cm at 1829 hours (about 11 weeks). Displacement at site 2U was 18.3 cm at 2.15 hours, 31 cm at 27.5 hours, and 61 cm at 1832 hours. Slip measurements for all sites are presented in Table 5.1.

Afterslip behavior during the initial 1800 hours at thirteen sites is summarized in Figure 5.4. These afterslip data display a decrease in rate that is well described by the power law

$$d = at^b \quad (b < 1) \tag{5.1}$$

where d is displacement, t is time after the earthquake, a is a constant indicating displacement at $t=1$, and b is a rate constant. The data plotted in Figure 5.4 are from sites that were initially measured between 2.15 and 35 hours after the mainshock. Very similar afterslip behavior was observed at sites 1P and 1Q, and at 2H, 2I, 2J, 2K, and 2M (locations shown in Figure 5.2), so data from the single most completely described site are plotted. A larger number of sites for the southern segment reflects earlier investigation of that area.

The data summarized in Figure 5.4 are illustrated together with least-square regressions. Assuming constant power-law behavior throughout the initial 1800 hour period of earthquake afterslip, the estimated slip at t=1 minute after the mainshock origin time and its 95 per cent confidence interval are shown in Figures 5.4a and 5.4b. The 95 per cent confidence intervals are ±10 to 35 per cent of the inferred coseismic slip for the northern segment and ±5.5 to 104 per cent along the southern segment.

Distribution of slip along the fault. The spatial distribution of displacement at six intervals after the earthquake is illustrated in Figure 5.5.

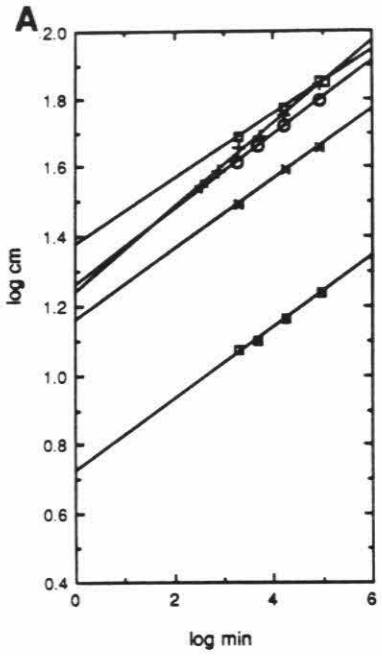

key

▫	1U
+	1R
o	1Q
✱	1O
■	1G

	A	B	R	CI
d =	22.9	$t^{0.099}$	1.000	10.0
d =	17.3	$t^{0.122}$	0.998	10.0
d =	18.2	$t^{0.108}$	0.998	12.0
d =	14.3	$t^{0.102}$	0.999	35.0
d =	5.3	$t^{0.103}$	0.999	14.0

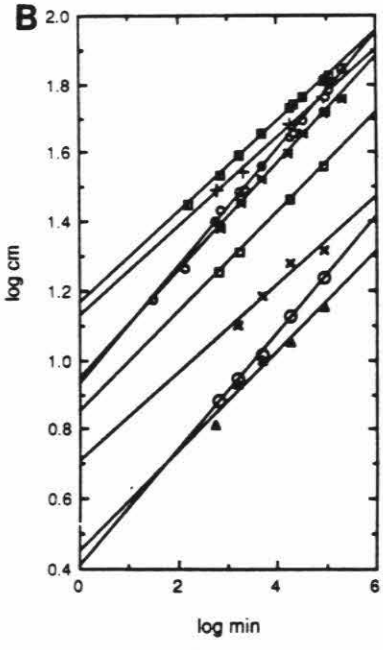

key

■	2T
+	2Z
o	2U
✱	2M
▫	2BB
×	2FF
o	2EE
▲	2CC

	A	B	R	CI
d =	14.6	$t^{0.131}$	0.998	5.5
d =	13.4	$t^{0.129}$	0.998	22.0
d =	8.6	$t^{0.169}$	0.997	6.5
d =	8.8	$t^{0.155}$	0.998	8.5
d =	7.1	$t^{0.144}$	1.000	6.5
d =	2.8	$t^{0.144}$	0.986	41.0
d =	2.6	$t^{0.167}$	0.999	21.5
d =	5.1	$t^{0.127}$	0.971	104.0

Figure 5.4 Logarithmic plots of slippage along the Superstition Hills fault. Part A and part B show data from 5 sites along the northern fault segment, and 8 sites along the southern segment, respectively. The first measurement at site 2U was made by Kahle *et al.* (1988). Power-law equations and correlation coefficients are listed to the right as in Figure 5.3. The 95% confidence interval (CI) cited is a percentage of slip at t=1 minute, for example, at site 1U there is 95% confidence that the displacement at t=1 minute was 22.9 ± 10% (22.9 ± 2.3 cm).

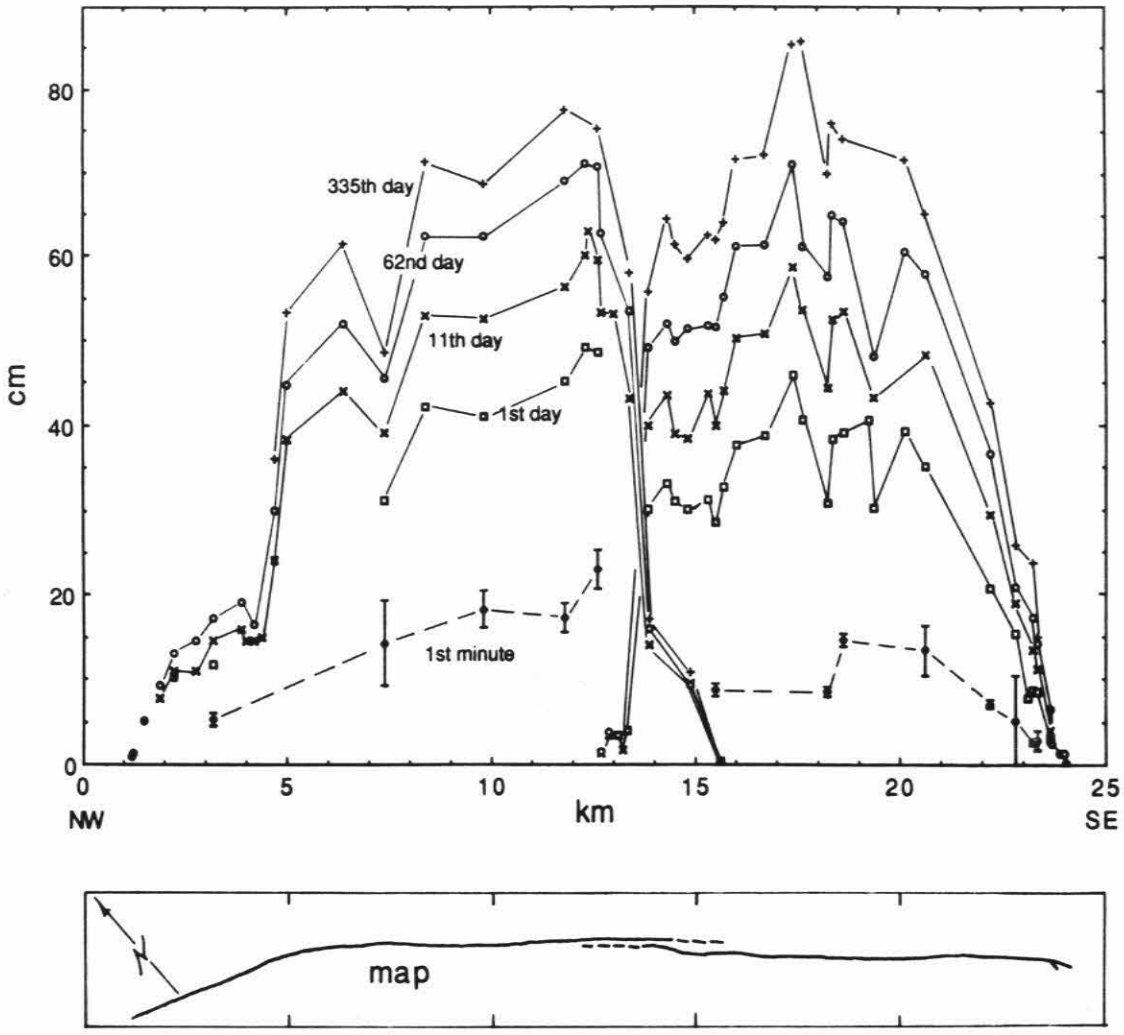

Figure 5.5 Afterslip plotted along the fault. The illustrated displacements were observed on 25 November and 5-6 December 1987, and on 25 January and 24 October 1988. Solid dots illustrate measurements of the northern extent of the surface rupture made on 27 November 1987. Dashed lines connect displacements inferred at t=1 minute after the mainshock in Figure 5.4. 95% confidence intervals for these points are shown with error bars. The fault is plotted in map view below. Note that the fault is a composite of two segments and that smaller displacements occurred where the segments overlap. Note also the sudden increase in slip near an abrupt fault bend about 5 km from the northeast end of the fault. These features are discussed in the text.

A high rate of afterslip is evident at some localities. Also apparent are some deviations from a simple distribution of slip along the fault. Two apparently anomalous features in Figure 5.5 are defined by several measurements. From the north, these are an abrupt step in the displacement profile at km 4.5, and a broad "saddle" in the profile between km 12.4 and 15.6.

5.4 Discussion

Tectonic features and subsurface geometry of the Imperial Valley. The Imperial Valley is a topographic expression of the Salton Trough in southeastern California. The trough formed by continental rifting at the northern tip of the Gulf of California (Lomnitz *et al.*, 1970, Elders *et al.*, 1972). Dominating the modern tectonic setting of the Salton Trough is a through-going system of transform faults: the Imperial fault, the San Andreas fault, and southern branches of the San Jacinto fault system including the Superstition Hills, Superstition Mountain, and Coyote Creek faults (Figure 5.1). Rupture of faults that define, or are near, the western margin of the Salton Trough caused the 1987 Superstition Hills earthquake sequence.

Seismic refraction data indicate that sediment thickness in the Salton Trough is greater than 4 to 5 km across most of the width of the Imperial Valley (Figure 5.1) (Fuis *et al.*, 1982). Fuis *et al.* presented seismic velocity profiles within the valley showing a smooth increase of velocity to depths of about 5 km. Quite different velocity profiles were found in the "West Mesa" area, west of and adjacent to the Superstition Hills fault (Figure 5.1). Those profiles show an abrupt increase of seismic velocity, to about 5.9 km/s, at depths between 1 and 3 km. Kohler and Fuis (1986) interpreted the 5.9 km/s horizon as the top of continental crystalline basement. These data indicate

that continental crystalline basement is present beneath relatively thin sedimentary cover along the border of the western Salton Trough. In addition Fuis *et al.* (1982) suggested that continental basement is absent within the Salton Trough itself, and that metasedimentary rocks dominate at depths from 5.5 to 13 km.

Major basement surfaces in the vicinity of the Superstition Hills fault, at depths of about 1.5, 2.5 and 4.5 km (Kohler and Fuis, 1986), are interpreted by Fuis *et al.* (1982) to represent down-faulted basement blocks at the western edge of the Salton Trough. The Superstition Hills fault appears to bound and to cut an escarpment defining the eastern boundary of the 2.5-km-deep basement surface (Figure 5.1)

Association of slip distribution with surficial geometry of the fault. Displacement of the Superstition Hills fault correlates with the fault's geometry. Two distinctive departures from a simple elliptically-shaped along-fault displacement profile occur at a bend and a step that define boundaries of fault segments. At km 4.5 (Figure 5.5) an 18° fault bend is associated with an abrupt increase of slip magnitude to the south. The more westerly striking part of the fault to the north cuts through a zone of uplifted and closely folded Pleistocene strata of the Borrego Formation (Figure 5.2). Geologic mapping of this area by Dibblee (1984) indicates that Plio-Pleistocene strata are much more tightly folded near the northernmost Superstition Hills fault than elsewhere along the fault. Displacement in this area is presumably taken up in local folding of the Borrego Formation or in uplift of the whole of the northern Superstition Hills area (Figure 5.1).

The M_s 6.2 rupture of left-lateral faults that are located northeast of, and strike perpendicular to, the northern Superstition Hills fault occurred just

12 hours prior to the Superstition Hills earthquake (Figure 5.1) (Magistrale *et al.*, 1989, see also Chapter 3). This event suggests a second candidate for causing the abrupt increase of slip observed at km 4.5. Presumably, movement of several left-lateral fault strands in the 23 November earthquake produced higher normal stresses across the Superstition Hills fault northwest of the intersection of the right- and left-lateral faults. If normal stress across the Superstition Hills fault was reset by the earlier event (Given and Stuart, 1988), displacement in the subsequent Superstition Hills earthquake may have been locally impeded. Because the zone of intersecting left-lateral faults is widely distributed and located northwest of the prominent step in the slip profile (Hudnut *et al.*, 1989, Sharp *et al.*, 1989), it is probable that the 18° bend of the Superstition Hills fault, not the action of intersecting left-lateral faults, principally caused the abrupt change in slip magnitude at km 4.5.

A "saddle" in the slip profile is associated with a 3.5-km-long zone where fault segments extending from the north and south overlap (km 12.4 to 15.6, Figure 5.5). Slip must be transferred between the overlapping faults in this zone. Locally within this zone the magnitude of slip accounted for by summing slip across adjacent sites on the two main strands is close to the maxima outside the area of the right step and so the decrease of observed slip is only apparent. The efficiency of slip transfer between the two echelon strands may be due to the step's "releasing" geometry. The position of this segment boundary corresponds to the projection of a prominent lineation defined by aftershocks of the the 1981 Westmorland earthquake (Hutton and Johnson, 1981) and is near to a steep subsurface escarpment at the edge of continental crystalline basement rocks between the Superstition Hills and Superstition Mountain faults (Fuis and Kohler, 1984, Kohler and Fuis, 1986)

(Figure 5.1). The above suggests that fault complexity in the right-stepping zone probably reflects the location of a major boundary between basement blocks beneath the step.

Creep across the Superstition Hills fault in 1968, 1979, and 1981 was triggered by local earthquakes (Allen *et al.*, 1972, Fuis, 1982, Sharp *et al.*, 1986). The location of 1987 surface rupture corresponds closely to the mapped trace of the recent aseismic displacements. Some details of the 1987 rupture pattern, however, were not observed in earlier triggered aseismic slip events. Surface fractures associated with the 1968 and 1979 events were mapped continuously through a prominent bend and the northern and southern branches of the fault were connected (Figure 5.2). This suggests that the earlier aseismic ruptures were much less complicated than the rupture pattern associated with the 1987 earthquake.

Association of afterslip behavior with subsurface geology. An abrupt change in afterslip behavior near km 13 (Figure 5.2) correlates with the boundary of the two overlapping fault segments discussed earlier, to a large increase in the thickness of sedimentary rock southeastward, and to a marked boundary of basement rock type (Figure 5.1). The northern segment of the Superstition Hills fault experienced a significantly smaller amount of afterslip than the southern segment during the time periods 30 to 280 hours and 30 to 1500 hours after the Superstition Hills shock. The percentage increase of afterslip is compared in Figure 5.6 between field measurements made 30 ± 5, 283 ± 17, and 1505 ± 15 hours after the earthquake. The increase of slip from 30 to 280 hours is 24.5 ± 2 per cent, $n = 7$ (where n is the number of sites measured in all time periods), along the northern segment of the fault and 35.5 ± 7 per cent, $n = 21$, along the southern segment. Between 30 and

1505 hours slip increased 48 ± 3 per cent, n = 7, along the northern segment of the fault and 69 ± 10.5 per cent , n = 22, along the southern segment (Figure 5.6). Because total displacement along the two fault segments is similar, this result suggests that a greater proportion of coseismic slip or early aseismic slip occurred along the northern segment (Figure 5.5).

Although the slip increase cited for the northern segment is defined by only seven data points, behavior is clearly more uniform there than that along the southern segment. This indicates that factors controlling the magnitude of coseismic slip and rate of afterslip must be relatively consistent along the northern segment. It is speculated that the presence of a large block of continental crystalline basement buried at relatively uniform depth along the northern segment moderated slip behavior there. This idea is suggested by the location crystalline basement proposed by Fuis *et al.* (1982) and Fuis and Kohler (1984).

The depth of young sedimentary cover and the geometry of buried basement blocks along the boundary of Salton Trough appear to have strongly influenced the slip behavior of different segments of the Superstition Hills fault. The northern segment appears to have experienced larger coseismic, or early aseismic slip, than the southern segment, but the rate of slip was significantly larger across the southern segment between 35 and 1800 hours after initial rupture. According to Fuis *et al.*, (1982) and Kohler and Fuis (1986), 2.5 to 3.5 km of young sedimentary cover overlies old continental basement along the northern Superstition Hills fault, but at least 4- to 5-km of sedimentary cover overlies metasedimentary rock along the southern part of the fault. The presence of shallow continental basement and thinner sedimentary cover are thus correlated with larger early, probably coseismic

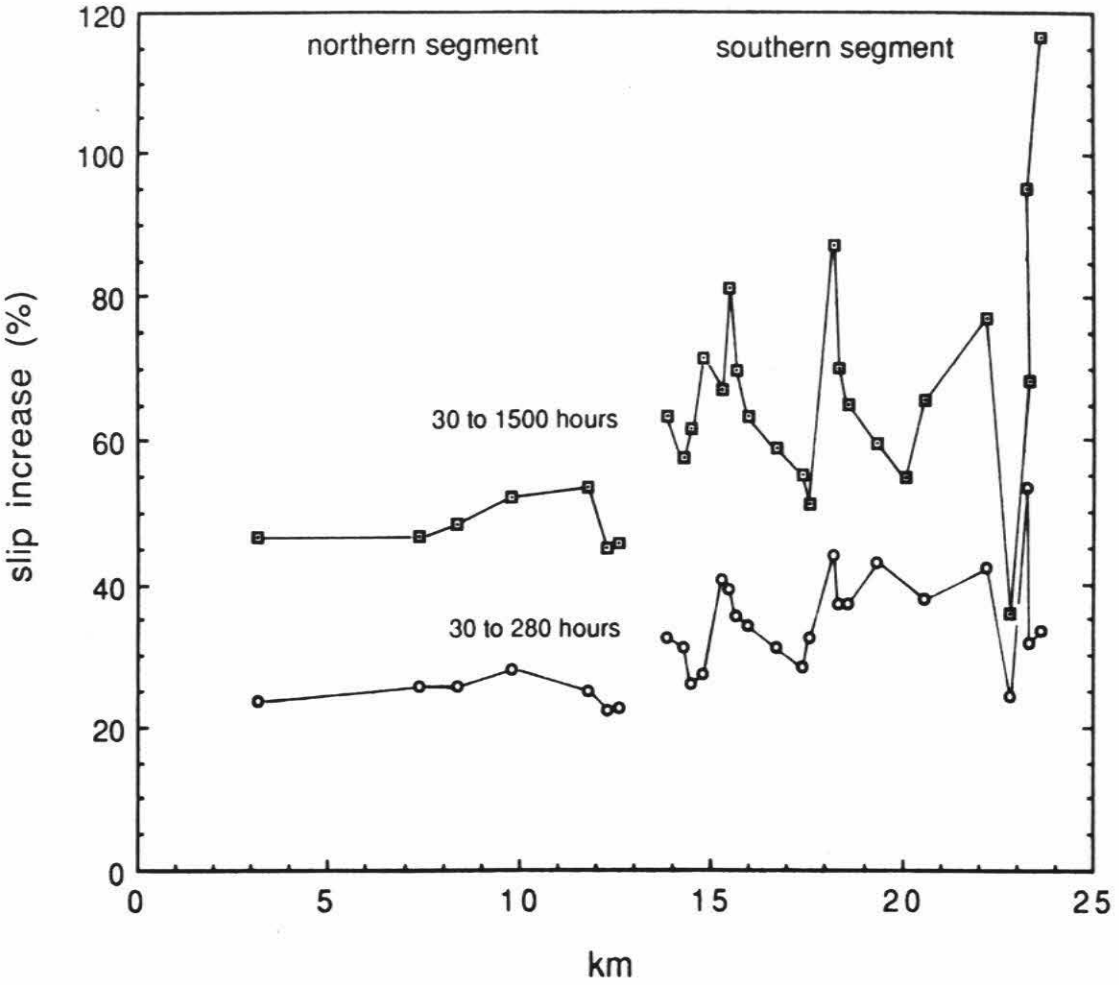

Figure 5.6 The percentage increase in afterslip between field measurements made at three times 30 ± 5, 283 ± 17, and 1505 ± 15 hours after the earthquake. The increase of slip from 30 to 280 hours was 24.5 ± 2% and 35.5 ± 7% along the northern and southern branches of the fault, respectively. Between 30 and 1505 hours the slip increased 48 ± 3% along the northern segment of the fault and 69 ± 10.5% along the southern segment.

displacement of the northern branch of the fault. Reciprocally, a greater depth to basement and substantially thicker sedimentary cover are correlated with smaller coseismic (or early aseismic) displacements and to more rapid aseismic surficial slip over the first several days of the postseismic period. Substantially different behavior of the northern and southern fault segments is further supported by the observation of Magistrale *et al.* (1989, see also Chapter 3) that aftershocks during the four days following the mainshock were densely clustered along the northern Superstition Hills fault segment, but were sparse and were generally smaller in magnitude along the southern segment.

Afterslip distributions associated with some earlier, well-described strike-slip earthquakes, indicate that the geometry of basement rocks, and sediment thickness appear to play roles in the distribution of net surface displacement between coseismic and aseismic processes. Slip behavior along the three Coyote Creek fault segments that ruptured in association with the April 1968 Borrego Mountain earthquake was closely correlated to the depth of basement rocks and sedimentary thickness. Continental basement rocks are present at depths of 0 to 1000 m on both sides of the northern 13 km of the 1968 rupture (Hamilton, 1970, Fuis *et al.*, 1982). Almost no afterslip was detected along this segment (Clark, 1972). An increase of fault slip of between 25 to 800 per cent occurred aseismically during the initial three month postseismic period along the central and southern segments of the fault (Clark, 1972). Burford (1972) correlated the large afterslip observed along the central Coyote Creek fault segment to the depth of sedimentary strata in that area (up to 3.5 km, Hamilton, 1970, Kohler and Fuis, 1986). Fuis *et al.* (1982) suggested that continental basement may be absent on the northeast side of the southern

Coyote Creek fault segment (Figure 5.1). Although refraction data are too sparse to distinguish unambiguously the presence or absence of buried continental crystalline basement there (G. S. Fuis, personal communication, 1988), the results of Hamilton (1970) and Kohler and Fuis (1986) both indicate the presence of an at least 3 to 3.5 km thickness of sedimentary cover northeast of the southern Coyote Creek fault (Figure 5.1). The occurrence of large amounts of afterslip was thus confined to sections of the Coyote Creek fault where continental basement rocks are juxtaposed against an at least 3.5 km thickness of young sedimentary rock across the fault. This agrees with Burford (1972) that boundaries between zones of differing slip behavior were probably controlled by sediment thickness in the 1968 rupture and suggests that such a relationship also held for the 1987 Superstition Hills rupture.

Supporting this idea are observations of afterslip behavior along the 1979 Imperial fault surface rupture (Sharp *et al.*, 1982) (Figure 5.7). The Imperial fault cuts a homogeneous stratigraphic section consisting of a 5 km thickness of young sedimentary rocks overlying metasedimentary rocks (Fuis *et al.*, 1982). Unlike the 1968 and 1987 ruptures, dramatic changes of slip behavior were not detected along the 1979 Imperial fault rupture. The afterslip behavior observed after the 1979 event is consistent with small variation of sediment thickness along the Imperial fault.

The occurrence of aseismic surficial fault displacement in areas with substantial accumulations of poorly consolidated sediment indicates the existence of a physical mechanism for velocity strengthening of poorly consolidated sedimentary rock (Marone and Scholz, 1988, Scholz, 1989). Marone and Scholz presented experimental data showing evidence of velocity

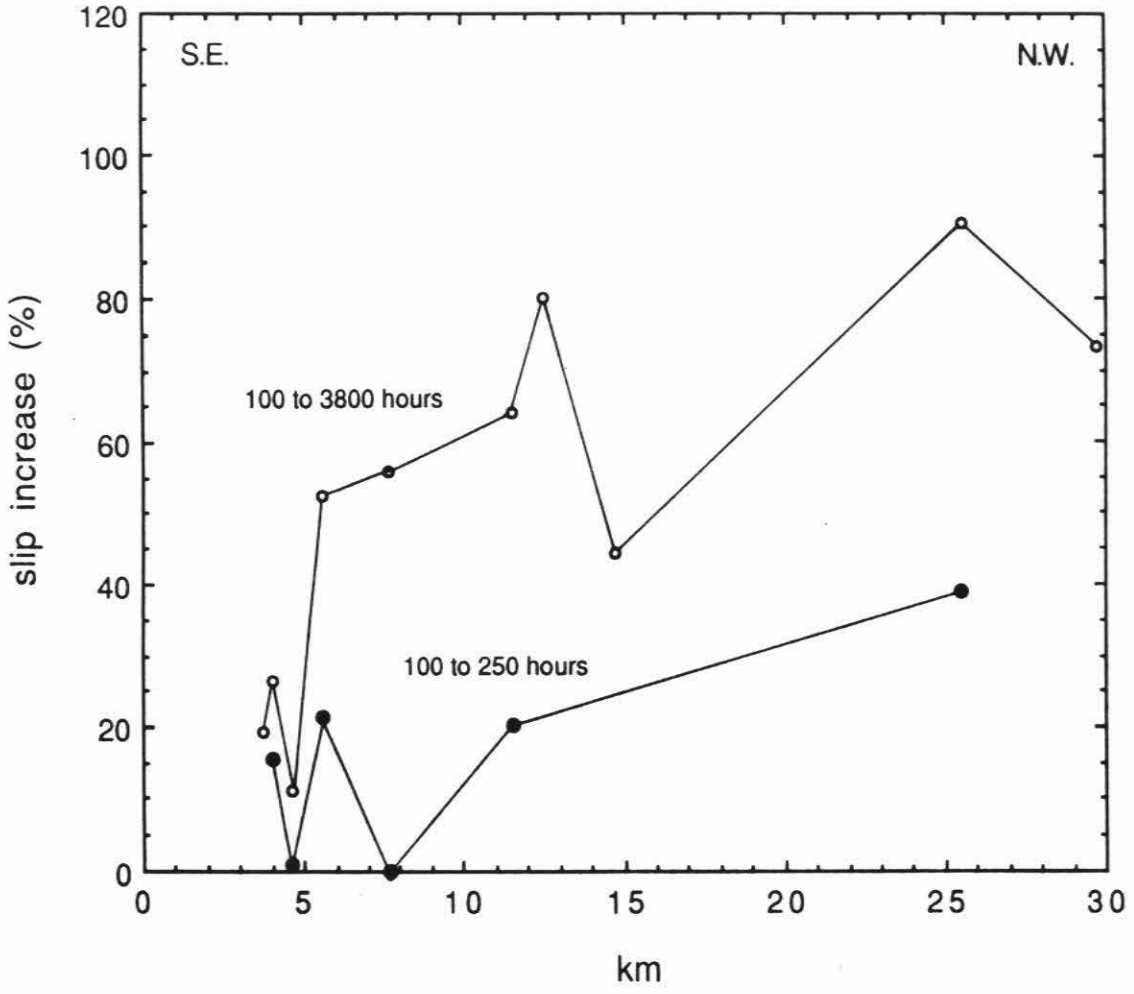

Figure 5.7 The percentage increase of slip between 4 and 10 days and 4 and 160 days after the Imperial Valley earthquake as measured by Sharp *et al.* (1982).

strengthening in poorly-consolidated granular quartz. They argue that aseismic surficial slip results from velocity strengthening in poorly consolidated fault gouge. This mechanism is plausible for aseismic afterslip of the Superstition Hills fault where, as has been described, young sedimentary rock extends to several kilometers depth.

That aseismic slip appears to have a larger contribution to total displacement where young sedimentary cover is deeper along the Superstition Hills fault suggests that magnitudes of coseismic slip and afterslip are in part a function of the thickness of poorly consolidated material overlying a fault.

For convenience, coseismic slip is defined as displacement that occurred during the first minute after the mainshock origin time. Although no primary observations or records demonstrate that coseismic slip occurred at the surface along the Superstition Hills fault, the power-law fit of the repeated measurements of subsequent aseismic slip (Figures 5.4a and 5.4b) suggests that as much as 23 cm of coseismic surface slip occurred (Figure 5.5).

Apparently no significant slip of the Superstition Hills fault occurred prior to the 24 November earthquake. A creepmeter at Camera Station 2 (Figure 5.2), recorded no slip between 12 January and 27 October 1987 (McGill *et al.*, 1989), and no observable surface displacement had occurred at Imler Road (site 2U) as of 2.5 hours before the earthquake (Kahle *et al.*, 1988). However, Sharp and Saxton, (1989), based on a regression of their surface slip data, suggest that the northernmost end of the fault had about 10 cm surface rupture in response to the first, 23 November, mainshock on the Elmore Ranch fault.

Power-law slip behavior. Afterslip described by a simple logarithmic law was documented in association the Parkfield, Borrego Mountain and Imperial

Valley, California, earthquakes (Scholz *et al.*, 1969, Burford, 1972, Cohn *et al.*, 1982). In marked contrast, slip of the Superstition Hills fault associated with the 1987 earthquake followed a power law during the first several-hundred hour postseismic period.

Plotted on Figure 5.4 are several least-square regressions to afterslip data. The regressions indicate that equations of the power-law form successfully describe the initial several hundred hours of postseismic slip data. The validity of these regressions is supported by a 15 cm displacement measured 30 minutes after the earthquake by Kahle *et al.* (1988). That point, measured at site 2U, is plotted in Figure 5.4b. It plots precisely on the site 2U regression line.

The afterslip data presented in Figure 5.4 are not well-described by logarithmic functions in time. Slip at early times was much larger than indicated by logarithmic regression lines (Figure 5.8). The first dextral offset measured after the earthquake, at site 2U (Kahle *et al.*, 1988), is several centimeters larger than inferred by logarithmic regression of data collected over the subsequent weeks. In addition, collective plots of these data retain a concave upward non-linearity when plotted on semi-log coordinates (Figure 5.8). An unacceptable result of the logarithmic regression is the inference that most fault displacements at t = 1 minute were significantly less than zero.

Some of the small deviations of individual measurements from the general form of the power-law decay curves (Figures 5.3 and 5.4) must partly result from the intermittent occurrence of slip episodes in which several millimeters of slip occur (Bilham, 1989). In addition, the occurrence of slip at sites 2M and 2T between 26 and 28 January, 1988 (Figure 5.3) was probably associated with a large aftershock (M_L 4.7) at 02:54 GMT on 28 January

1988. Significant retardation of afterslip at three sites was observed shortly before the aftershock. Remeasurement at two of these sites within a few hours after the aftershock suggests that ground shaking triggered rapid slippage of the fault and total displacement stepped abruptly up to the trend of measurements at earlier and subsequent times.

Wesson (1988) investigated the dynamics of aseismic fault slippage. He modeled afterslip of the 1966 Parkfield and 1979 Imperial Valley earthquakes as the response of several aseismically-slipping strips to a deeper, instantaneous, brittle rupture. The model utilized a quasi-plastic rheology in the aseismically slipping layers and assumes zero external stress on the fault plane and zero coseismic slip at the surface. This model successfully fits the observations of afterslip in the 1966 and 1979 earthquakes, except at small times (Figure 9 in Wesson, 1988). The afterslip data fit by Wesson's model can be described by a simple function of the form:

$$d = a + b \log t \tag{5.2}$$

where d is surface displacement, t is time after coseismic rupture, and a and b are constants. Wesson suggests that poor fit at small times may be due to the neglect of coseismic slip, which would require a more complex rheology in his model. The observation here of power-law decay of afterslip at small times and Wesson's success at modeling log decay, suggests that at short times external stress may be a significant factor in driving the observed surface slip.

Projected total surface displacement. The afterslip data invite predictions of the course of fault displacement over the coming months and years. Slip data measured across the Imperial fault subsequent to the 1979 Imperial Valley earthquake as reported by Cohn *et al.* (1982) and Louie *et al.*, (1985) and from C. R. Allen, (personal communication, 1988), demonstrate

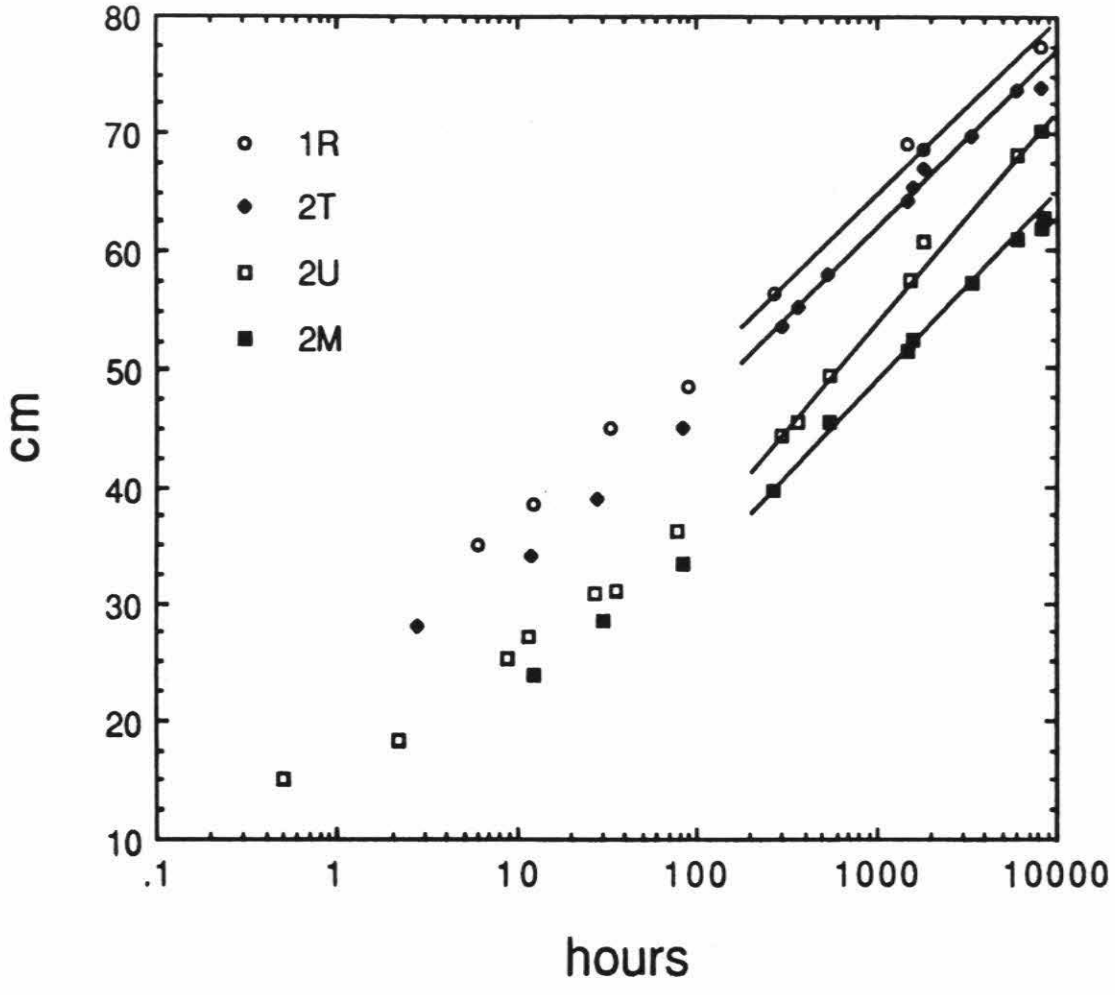

Figure 5.8 Displacements at sites 1R, 2M, 2T and 2U (Figure 5.2) between 0 and 335 days after the Superstition Hills earthquake plotted in a semi-log field. Measurements made two weeks to 335 days after the event are relatively well described by a logarithmic function, as shown by straight-line fits to those data. Measurements made within the first two weeks do not fit the later log trend and are better fit by a power law as illustrated in Figures 5.3 and 5.4.

continuing logarithmic increase in afterslip between 18 hours and eight years after that event. The slippage is described by simple logarithmic functions of the form shown in equation (5.2), above. While the Superstition Hills afterslip data from the initial few hundred hour period are poorly fit by this equation, as discussed earlier, behavior subsequent to this is well described by the simple logarithmic expression. This suggests that over long periods afterslip follows a logarithmic form as was formerly suggested. Assuming continuation of the current logarithmic behavior at sites 1R, 2M, 2T and 2U (Figure 5.8), in 10 years displacements there will approach about 93, 78, 91 and 90 cm, respectively. These displacements are consistent with estimates of coseismic displacement at seismogenic depths as inferred from regional geodetic data (Lisowski and Savage, 1988) and as can be deduced from the moment estimates of Bent *et al.* (1989) and Hwang *et al.* (in press, see also Chapter 4). In addition, the projected slip over a 10 year period across the 150- m-wide Caltech alignment array (400 m south of site 2T) is just 5 cm greater than that suggested by extrapolation of current logarithmic behavior at site 2T (McGill *et al.*, 1989).

5.5 Conclusions

The afterslip displacement along the Superstition Hills fault has been predictable during the period of this study, and that it is well described by a power law, $d=at^b$ $(b<1)$, during the initial several weeks after the mainshock (d is displacement, t is time after the earthquake, and a and b are constants). Regression of power-law functions to $t=$ 1 minute after the earthquake suggests that up to about 23 cm of surface slippage along the Superstition Hills fault occurred coseismically.

Most sites that were monitored during the 280 to 8000 hour postseismic interval exhibit slip behavior that is well described by simple logarithmic function, $d = a + b \log t$. The apparent change of behavior from power-law to logarithmic slip-decay is not explained. However, simple logarithmic behavior has been observed for the nine years following the the nearby Imperial fault rupture of 1979, and is thus precedented. Extrapolation of logarithmic fits to the data collected up to October, 1988 suggest that displacement will reach about 90 cm by November of 1997, 10 years after the rupture.

The geometry of the Superstition Hills fault correlates well to details of the earthquake slip-profile. The amount of slip towards the northwest end of the fault decreased abruptly at a prominent fault bend that is associated with uplift and tight folding of sedimentary rocks. Change of slip magnitude is also observed at a major right-step near the center of the fault.

Afterslip behavior correlates well with subsurface geology as interpreted from seismic refraction studies. A relatively larger percentage of afterslip appears to have occurred where the fault cuts a thicker section of late Cenozoic sedimentary strata and more uniform afterslip behavior occurred where the fault cuts continental crystalline basement. Change in slip behavior along the fault thus appears to be strongly dependent on the constitutive properties of rocks bounding the fault.

Table 5.1
Displacement Measurements

Site	Date	Time *P.S.T.*	Displacement *cm*	Position *km*	Uncertainty *cm*
1A	27 NOV 87	1500	1.0	1.20	0.25
1B	27 NOV 87	1500	1.3	1.25	0.25
1C	27 NOV 87	1430	5.1	1.50	0.25
1D	06 DEC 87	1325	7.8	1.90	0.25
	26 JAN 88	1503	9.3		0.25
1E	27 NOV 87	1400	10.3	2.25	0.50
	06 DEC 87	1310	11.1		0.20
	26 JAN 88	1452	13.1		0.15
1F	06 DEC 87	1252	11.0	2.75	0.25
	26 JAN 88	1442	14.6		0.25
1G	25 NOV 87	1617	11.8	3.20	0.25
	27 NOV 87	1320	12.6		0.20
	06 DEC 87	1130	14.6		0.20
	26 JAN 88	1335	17.3		0.20
1H	06 DEC 87	1145	16.0	3.90	0.25
	26 JAN 88	1411	19.1		0.25
1I	06 DEC 87	1225	14.5	4.00	0.50
1J	06 DEC 87	1200	14.5	4.20	1.50
	26 JAN 88	1408	16.5		1.50
1K	06 DEC 87	1210	15.0	4.40	2.5
1L	06 DEC 87	1055	24.0	4.70	0.25
	25 JAN 88	1700	30.0		0.25
	24 OCT 88	1700	36.0		0.5
1M	06 DEC 87	1003	38.3	5.00	0.25
	25 JAN 88	1646	44.8		0.25
	24 OCT 88	1630	53.3		1.5
1N	06 DEC 87	0940	44.0	6.40	0.25
	25 JAN 88	1633	52.0		0.25
	24 OCT 88	1650	61.3		0.25
1O	25 NOV 87	1515	31.9	7.40	0.5
	05 DEC 87	1621	40.2		0.5
	25 JAN 88	1622	46.4		0.25
	24 OCT 88	1633	49.4		1.0
1P	25 NOV 87	1400	42.0	8.40	1.0
	05 DEC 87	1609	52.8		0.25
	25 JAN 88	1615	62.3		0.25
	24 OCT 88	1615	71.2		
1Q	25 NOV 87	1323	41.0	9.80	1.0
	27 NOV 87	1520	45.7		0.25
	05 DEC 87	1553	52.5		0.25
	25 JAN 88	1600	62.3		0.25
	24 OCT 88	1600	68.5		0.5
1R	24 NOV 87	1120	35.0	11.80	2.0
	24 NOV 87	1748	38.5		0.25
	25 NOV 87	1435	45.0		0.25
	27 NOV 87	1545	48.5		0.25
	05 DEC 87	1018	56.3		0.25

	25 JAN 88	1230	69.0		1.8
	08 FEB 88	1145	68.6		2.0
	24 OCT 88	1425	77.5		0.5
1S	05 DEC 87	1040	45.1	12.10	3.0
1T	05 DEC 87	1100	63.0	12.40	1.0
1U	25 NOV 87	1402	48.5	12.60	3.0
	05 DEC 87	1136	59.5		3.0
	25 JAN 88	1311	70.7		
	08 FEB 88	1215	70.1		1.0
	24 OCT 88	1445	75.3		0.5
1V	06 DEC 88	1145	53.2	12.70	0.75
	25 JAN 88	1355	62.7		0.25
1W	06 DEC 87	1317	53.0	13.00	2.0
1X	06 DEC 87	1321	43.0	13.40	1.0
	25 JAN 88	1445	53.4		0.25
	24 OCT 88	1500	58.2		2.0
1Y	27 NOV 87	1620	13.0	13.90	0.25
	05 DEC 87	1335	14.0		0.25
	25 JAN 88	1500	15.9		1.0
	24 OCT 88	1320	17.1		0.5
1Z	05 DEC 87	1450	9.5	14.90	0.50
	25 JAN 88	1420	9.2		0.50
	24 OCT 88	1530	10.8		0.4
1AA	26 JAN 88	1130	0.4	15.60	0.20
2A	05 DEC 87	1230	0.4	12.20	0.10
2B	05 DEC 87	1215	3.0	12.40	0.20
	25 JAN 88	1258	3.4		0.20
2C	05 DEC 87	1158	1.4	12.70	0.20
	25 JAN 88	1350	1.5		0.20
2D	05 DEC 87	1250	3.5	12.90	0.20
	25 JAN 88	1406	3.7		0.20
2E	05 DEC 87	1300	3.4	13.10	0.20
	25 JAN 88	1425	3.4		0.20
2F	05 DEC 87	1315	1.8	13.25	0.20
2G	05 DEC 87	1330	4.0	13.35	0.20
	25 JAN 88	1427	4.0		0.20
2H	25 NOV 87	1325	30.0	13.85	0.20
	27 NOV 87	1620	33.0		0.35
	05 DEC 87	1347	39.8		0.75
	25 JAN 88	1505	49.0		0.25
	24 OCT 88	1430	55.7		1.0
2I	25 NOV 87	1310	33.0	14.30	1.0
	05 DEC 87	1420	43.3		1.0
	25 JAN 88	1508	52.0		1.0
	24 OCT 88	1400	64.5		1.5
2J	25 NOV 87	1255	30.9	14.50	1.0
	05 DEC 87	1425	38.9		1.0
	25 JAN 88	1450	49.9		1.0
	24 OCT 88	1330	61.4		1.0
2K	25 NOV 87	1245	30.0	14.80	0.25
	05 DEC 87	1435	38.2		0.25
	25 JAN 88	1408	51.4		0.25

	24 OCT 88	1300	59.7		1.0
2L	25 NOV 87	1200	31.0	15.30	1.0
	05 DEC 87	1452	43.6		0.25
	25 JAN 88	1330	51.7		0.25
	24 OCT 88	1230	62.5		0.5
2M	24 NOV 87	1730	24.0	15.50	2.0
	25 NOV 87	1120	28.5		0.25
	27 NOV 87	1637	33.4		0.25
	05 DEC 87	0932	39.7		0.25
	25 JAN 88	1320	51.6		0.25
	28 JAN 88	1121	52.5		0.25
	13 APR 88	1838	57.2		0.25
	03 AUG 88	1820	61.1		0.5
	24 OCT 88	1200	61.9		0.5
2N	25 NOV 87	1345	32.5	15.70	1.0
	05 DEC 87	0922	44.0		1.0
	25 JAN 88	1308	55.1		0.20
	24 OCT 88	1140	64.0		0.5
2O	25 NOV 87	1125	37.5	16.0	0.50
	05 DEC 87	0858	50.3		0.20
	25 JAN 88	1255	61.2		0.20
	24 OCT 88	1120	71.6		0.5
2P	25 NOV 87	1100	38.7	16.70	1.0
	05 DEC 87	0842	50.7		0.20
	25 JAN 88	1245	61.4		0.20
	24 OCT 88	1100	72.2		1.0
2Q	25 NOV 87	1035	45.8	17.40	0.30
	05 DEC 87	0820	58.8		0.20
	25 JAN 88	1235	71.0		0.20
	24 OCT 88	1040	85.5		0.8
2R	25 NOV 87	1025	40.5	17.60	1.5
	05 DEC 87	0810	53.7		0.20
	25 JAN 88	1210	61.2		0.20
	24 OCT 88	1020	75.9		0.5
2S	25 NOV 87	0945	38.3	18.35	0.25
	05 DEC 87	0743	52.5		0.20
	25 JAN 88	1140	65.0		0.20
	24 OCT 88	1000	76.0		0.5
2T	24 NOV 87	0800	28.0	18.60	2.0
	24 NOV 87	1656	34.0		2.0
	25 NOV 87	0913	39.0		2.0
	27 NOV 87	1655	45.0		2.0
	06 DEC 87	1420	53.5		0.30
	09 DEC 87	1020	55.3		0.40
	16 DEC 87	1420	58.0		0.25
	25 JAN 88	1110	64.3		0.25
	28 JAN 88	1110	65.5		0.30
	08 FEB 88	1100	67.1		0.60
	13 APR 88	1815	69.9		0.25
	03 AUG 88	1810	73.7		0.5
	24 OCT 88	0900	74.0		0.5
2U	24 NOV 87	0725	18.3	19.10	0.75

	24 NOV 87	1359	25.3		0.25
	24 NOV 87	1640	27.3		0.25
	25 NOV 87	0855	30.8		0.25
	25 NOV 87	1653	31.0		0.25
	27 NOV 87	1200	36.2		0.25
	06 DEC 87	1435	44.3		0.25
*	09 DEC 87	0830	45.5		2.0
	16 DEC 87	1615	49.5		2.0
	26 JAN 88	1200	57.6		2.0
	08 FEB 88	1345	60.8		2.0
	03 AUG 88	1836	68.2		2.0
	24 OCT 88	0830	70.3		2.0
2V	24 NOV 87	1414	35.5	19.25	4.0
	25 NOV 87	0916	40.5		0.25
	27 NOV 87	1210	46.0		0.25
2W	24 NOV 87	1435	25.2	19.35	4.0
	24 NOV 87	1626	26.0		4.0
	25 NOV 87	0928	30.2		1.0
	27 NOV 87	1220	35.7		1.0
	06 DEC 87	1720	43.2		1.0
	25 JAN 88	1640	48.2		1.0
2Y	24 JAN 87	1511	34.0	20.10	2.0
	25 NOV 87	0956	39.2		0.25
	25 JAN 88	1000	60.6		0.25
	24 OCT 88	1030	71.7		2.0
2Z	24 NOV 87	1537	31.0	20.60	3.0
	25 NOV 87	1021	35.0		3.0
	06 DEC 87	1657	48.3		0.25
	25 JAN 88	1017	58.0		0.25
	24 OCT 88	1100	65.2		1.0
2AA	24 JAN 87	1853	14.0	20.65	2.0
	25 JAN 87	1029	17.0		2.0
	06 DEC 87	1646	29.0		2.0
2BB	24 NOV 87	1520	18.0	22.20	1.0
	25 NOV 87	0809	20.6		0.25
	06 DEC 87	1623	29.3		0.25
	25 JAN 88	1115	36.5		0.25
	24 OCT 88	1135	42.7		0.5
2CC	25 NOV 87	0800	12.5	22.80	0.50
	27 NOV 87	1128	15.3		0.20
	06 DEC 87	1615	19.0		0.20
	25 JAN 88	1100	20.8		0.20
	24 OCT 88	1200	25.7		0.5
2DD	25 NOV 87	0736	7.75	23.10	0.25
2EE	24 NOV 87	1600	7.6	23.25	0.20
	25 NOV 87	0744	8.8		0.20
	27 NOV 87	1119	10.3		0.20
	06 DEC 87	1605	13.5		0.20
	25 JAN 88	1020	17.2		0.20
	24 OCT 88	1230	23.7		0.5
2FF	24 NOV 87	1400	6.5	23.35	0.50
	25 NOV 87	0719	8.5		0.50

	27 NOV 87	1110	10.0		0.50
	06 DEC 87	1558	11.2		0.50
	25 JAN 88	1035	14.3		0.75
	24 OCT 88	1300	16.7		1.0
2GG	24 NOV 87	1430	3.0	23.65	0.40
	25 NOV 87	0706	3.0		0.40
	06 DEC 87	1537	4.0		0.20
	25 JAN 88	0905	6.5		0.50
	24 OCT 88	1318	6.7		0.25
2HH	24 NOV 87	1415	1.0	23.75	0.20
	25 NOV 87	0655	1.0		0.20
	27 NOV 87	1059	1.0		0.20
	06 DEC 87	1530	1.0		0.20
	25 JAN 88	1010	1.0		0.20
2II	25 JAN 88	0915	2.5	23.70	0.20
2JJ	25 JAN 88	0930	1.3	23.90	0.20
2KK	25 JAN 88	0945	1.4	24.00	0.20
2LL	25 JAN 88	1000	0.1	24.05	0.10

* Monument 2U moved 20 m southeast on 6 December 1987. Position is km along fault, see Figure 5.2.

Chapter 6

Summary and Discussion

6.1 Summary of Results

The four studies of the 24 November, 1987, Superstition Hills earthquake sequence in this thesis allow the Elmore Ranch fault and the segments of the Superstition Hills fault to be considered from a variety of viewpoints. The northern and southern segments of the Superstition Hills fault act differently in each study. The north segment had $M_L \geq 4$ earthquakes over the last 50 years while the south segment had none. The north segment had more aftershocks in the 1987 sequence than the south segment. The south segment radiated most of the long period seismic energy recorded teleseismically, and had a greater percentage of afterslip relative to total slip than the north segment. These differences are due to the difference in basement rock type and sediment thickness along the fault segments. The results of each study are summarized below.

Master event relocations of the Superstition Hills earthquake sequence. The 24 November, 1987, Superstition Hills earthquakes occurred on a conjugate fault system consisting of the northwest-striking right-lateral Superstition Hills fault and a previously unknown northeast-striking left-lateral structure, the Elmore Ranch fault, defined by a planar hypocenter distribution that reaches from the Superstition Hills fault to the Brawley seismic zone. The Elmore Ranch fault parallels other northeast-trending epicenter alignments. The earthquake sequence is made up of foreshocks, a main shock, and aftershocks on the Elmore Ranch fault, followed by a main

shock and aftershocks on the Superstition Hills fault. Master event relocations show the following. The first, Elmore Ranch, main shock and its foreshocks colocate at about 11 km depth. The aftershocks of the first main shock cluster in time and space, with some aftershocks occurring in the Brawley seismic zone. The second, Superstition Hills, main shock was 12 hours after the first main shock and initiated at shallow depth, at the join of the two trends. The northwest trend aftershocks do not coincide with observed surface rupture on the Superstition Hills fault and occupy a volume between the Superstition Hills and Superstition Mountain faults. Most of the aftershocks are along the northern segment of the Superstition Hills fault. Aftershocks along the southern Superstition Hills fault are spatially associated with the two right steps that separate segments of the Superstition Hills fault. The northeast trend events are deep and the northwest trend events are both shallow and deep.

The distribution of the earthquakes is compared to the distribution of basement rocks defined by the refraction study of Fuis *et al.*, (1982). Along the northern Superstition Hills fault the earthquake locations and extent of aftershocks are controlled by the presence of crystalline basement rocks. The extent of the aftershock zones of the 1954 Arroyo Salada earthquake, on the Clark strand of the San Jacinto fault zone, and the 1968 Borrego Mountain earthquake, on the Coyote Creek fault, also are controlled by the basement structure in the western Imperial Valley. Along the southern Superstition Hills fault the locations of aftershocks appear to be controlled by the presence of right steps in the fault. The steps may extend to the bottom of the fault.

Relocations of older $M_L \geq 4$ earthquakes near the Superstition Hills fault. The relocation of $M_L \geq 4.0$ earthquakes from the last 45 years near the

Superstition Hills fault shows the following. No large earthquakes occurred on the southern Superstition Hills fault during that time. Earthquakes assigned to the southern Superstition Hills fault in the Caltech catalog relocate to the Brawley seismic zone and the Superstition Mountain fault. The 1951 rupture observed on the Superstition Hills fault was due to sympathetic slip from a Brawley seismic zone earthquake. Two northeast-striking faults that form the boundaries of the embayment into continental crystalline basement rocks north of the Superstition Hills fault have been active. Some of the Brawley seismic zone earthquakes may have also occurred on northeast striking structures within the zone. The intersection of the Superstition Hills fault and the Elmore Ranch fault has been very seismically active during this time, but has no clear cut conjugate earthquake pairs before the 1987 sequence.

Teleseismic source parameters and rupture characteristics. Long-period teleseismic body waves of the Superstition Hills earthquake are inverted using the method of Nabelek (1984, 1985). The earthquake is a complex event with two spatially distinct subevents. Two multiple source models are obtained. In both models, Subevent 2 begins 8 sec after the initiation of Subevent 1 and has 2/3 of the total moment. The total moment for both models is about 8×10^{25} dyne-cm. In Model 1, the first point source occurs under the epicenter, followed by a second point source 15 to 20 km away southeast along strike of the fault. In Model 2, the first point source is followed by a line source of 8 sec duration rupturing southeast at 1.5 to 2.5 km/sec. Sources for both models are between 4 to 8 km depth. The fault dip changes from near vertical near its northern end to about 70° near its southern end.

Moment release for Subevent 1 occurs in the epicentral region and radiates both short and long-period energy. A small portion of the Elmore

Ranch fault (<10 km) may have reruptured during Subevent 1 or alternatively, all moment release for both subevents may have been confined to the Superstition Hills fault. The second subevent ruptured the southern segment of the Superstition Hills fault, radiating a substantial portion of the long-period energy resolved in this study.

Surface slip and afterslip along the Superstition Hills fault. Surficial slip along the Superstition Hills fault was monitored by repeated measurements at dozens of sites along the fault. Dextral slip was as high as 48.5 cm one day after the Superstition Hills main shock and 71 cm two months later. The afterslip displacement along the Superstition Hills fault is well described by a power law, $d=at^b$ $(b<1)$ during the initial several weeks after the main shock (d is displacement, t is time after the earthquake, and a and b are constants). Regression of power-law functions to $t=$ 1 minute after the earthquake suggests that co-seismic slip ranged from 5 to 23 cm along the fault. Most sites that were monitored during the 280 to 8000 hour postseismic interval exhibit slip behavior that is well described by simple logarithmic function, $d=a+b\log t$. The apparent change of behavior from power-law to logarithmic slip-decay is not explained. However, simple logarithmic behavior has been observed for the nine years following the the nearby Imperial fault rupture of 1979, and is thus precedented. Extrapolation of logarithmic fits to the data collected up to October, 1988 suggest that displacement will reach about 90 cm by November of 1997, 10 years after the earthquake.

The geometry of the Superstition Hills fault correlates well to details of the earthquake slip-profile. The amount of slip towards the northwest end of the fault decreased abruptly at a prominent fault bend that is associated with uplift and tight folding of sedimentary rocks. Change of slip magnitude is

also observed at a major right-step near the center of the fault that separates the north and south segments of the fault. Maximum slip on both segments is similar.

Afterslip behavior correlates well with subsurface geology as interpreted from seismic refraction studies. A relatively larger percentage of afterslip appears to have occurred where the fault cuts a thicker section of late Cenozoic sedimentary strata and more uniform afterslip behavior occurred where the fault cuts continental crystalline basement. Change in slip behavior along the fault thus appears to be strongly dependent on the constitutive properties of rocks bounding the fault.

6.2 Discussion

Fault segmentation. The Superstition Hills earthquake sequence illustrates two types of fault segmentation. The first type is that seen along the Superstition Hills fault, where a right step separates the north and south segments of the fault. The right step corresponds to a change in the basement rock type and sediment thickness. Aftershocks up to 11 km deep are spatially associated with the right step between the segments, suggesting that the step extends to depth. The north and south fault segments act differently. The north segment had $M_L \geq 4$ earthquakes over the last 50 years while the south segment had none. The north segment had more aftershocks in the 1987 sequence than the south segment. The south segment radiated most of the long period seismic energy recorded teleseismically, and had a greater percentage of afterslip relative to total slip than the north segment. These differences are due to the difference in basement rock type and sediment thickness along the fault segments.

The second type of segmentation involves seismically active northeast-striking fault structures that interact with the San Jacinto fault zone. Such structures have, for example, controlled the extent of the aftershock zones of three strike-slip earthquakes on the San Jacinto fault zone. Northeast-striking faults bound the embayment in the continental crystalline basement rocks northwest of the Superstition Hills fault (Figure 3.14). The 1987 Superstition Hills sequence does not extend northwest beyond the southern edge of the embayment (Figure 3.17). Aftershocks of the 1954 Arroyo Salada earthquake, on the Clark strand of the San Jacinto fault zone, extend southeastward from the 1954 main shock (Sanders *et al.*, 1986) but do not cross the northern edge of the basement embayment (Figure 3.17). Aftershocks of the 1968 Borrego Mountain earthquake (Hamilton, 1972) do not extend along the Coyote Creek fault past the southern edge of the basement embayment (Figure 3.17). In these earthquakes the extent of the aftershock zones are controlled by the northeast-striking faults.

The faults bounding the north and south edges of the basement embayment were apparently active in 1946 and 1957, respectively. The new location of the 1946 earthquake (Chapter 2) places it on a northeast-striking microseismicity trend that coincides with the north edge of the embayment in the continental basement rocks. The 1957 earthquakes, a colocated doublet, lie on the northeast projection of the south edge of this embayment (Figures 2.3 and 3.17). The faults bounding the embayment must be active because the shoreline of ancient Lake Cahuilla coincides with the basement embayment. This means the embayment area is dropping faster than the sedimentation rate, requiring active embayment bounding faults. These faults can then be added to the list of northeast-striking structures identified in the

Imperial Valley: a lineation within the Brawley seismic zone that developed during aftershocks of the 1979 Imperial Valley earthquake (Johnson and Hutton, 1982), the trend of the 1981 Westmorland sequence (Figure 3.3), and the Elmore Ranch trend of the 1987 Superstition Hills sequence (Figure 3.4). If northeast-striking structures were active in 1946 and 1957, the idea of a simple south to north progression of seismic activity on northeast-striking structures (Hudnut *et al.*, 1989), would no longer hold.

The 1951 earthquake produced rupture on the Superstition Hills fault but relocated to the Brawley seismic zone (Figure 2.3), requiring the displacement on the Superstition Hills fault to be due to triggered slip. This moves the earliest known example of triggered slip from the 1968 Borrego Mountain earthquake (Allen *et al.*, 1972) to 1951. The occurrence of triggered slip 17 years earlier during the ≈330 year interval between the last two large earthquakes on the Superstition Hills fault (Hudnut and Sieh, 1989) supports the conclusion of McGill *et al.*, (1989), that triggered slip is a long-term behavioral style of some faults, and is not specific to any particular stage in the earthquake cycle.

While not addressed in this work, mention should be made of the role of rupture of the Elmore Ranch fault in triggering failure of the Superstition Hills fault (Given and Stuart, 1988, Hudnut, 1989). Double events are common in the Imperial Valley (Richter, 1958), but the relocations of older earthquakes along the Superstition Hills fault (Chapter 2) and in the Imperial Valley (Doser and Kanamori, 1986a), indicate the 1987 Elmore Ranch and Superstition Hills earthquakes are unique as a conjugate pair.

Influence of basement rocks and sediment thickness. The north and south segments of the Superstition Hills fault are surrounded by different types of

basement rock, and covered by different thicknesses of late Cenozoic sediment. The northern segment, with crystalline continental basement rock to the west, has the most aftershocks (Figures 3.4 and 3.8) and all the recent $M_L \geq 4$ earthquakes on the fault (Figure 2.3). The aftershocks along the north segment of the Superstition Hills fault define a volume rather than a plane. The same is true of the aftershocks along the part of the Elmore Ranch fault that lies between the first, Elmore Ranch, main shock, and the Superstition Hills fault (Figure 3.4) where crystalline continental basement rocks are also present (Fuis *et al.*, 1982). This part of the Elmore Ranch seismic lineation is about 5 km wide, compared to the 2 km width of the seismic lineation east of the Elmore Ranch main shock (Figure 3.4). The width of the aftershock zones may be due to pervasive pre-existing fractures in the continental basement as might be expected from the crustal necking and thinning prior to, and during, the continental rifting that formed the Imperial Valley.

The southern segment of the Superstition Hills fault, and the Wienert fault, cut through the metasedimentary basement under the Imperial Valley fill. These segments have few aftershocks (Figures 3.4 and 3.8) and no recent $M_L \geq 4$ earthquakes (Figure 2.3). The aftershocks that do occur are spatially associated with right steps between the segments. This suggests that the aftershocks are due to geometric complications along the fault. The depth of the aftershocks implies that the right steps persist down to the 11 km deep base of the seismogenic zone, so the Superstition Hills fault is as geometrically complicated at depth as it is at the surface.

Seen teleseismically, the north and south segments of the Superstition Hills fault ruptured in different subevents during the earthquake. Moment release along the southern segment accounts for 2/3 of the total moment

release of 8×10^{25} dyne-cm. (No significant moment release is seen along the Wienert fault.) The strong-motion modeling of Frankel and Wennerberg (1989) suggests that high frequency energy radiated predominately from the northern end of the fault, similar to the aftershock behavior. Combined with the teleseismic results, this suggests that both high frequency and low frequency energy radiated in the epicentral region along the northern segment of the Superstition Hills fault while only low frequency energy radiated from the southern segment (Figure 4.3). The south segment of the fault, underlain by the uniform metasedimentary basement, ruptured smoothly, in contrast to the fractured crystalline basement under the north segment of the fault. The metasedimentary basement is more uniform because it postdates the continental rifting that produced the Imperial Valley.

A larger percentage of afterslip relative to total slip occurred along the south segment of the fault (Figure 5.6). The rate of afterslip was higher along the south segment of the fault than along the north segment from 30 to 1500 hours after the earthquake. Total slip on the north and south segments of the fault was similar (Figure 5.5), so a greater proportion of co-seismic slip occurred on the north segment. A more uniform afterslip increase occurred on the north segment (Figure 5.6). Thus, the metasedimentary basement and thick sediments of the south segment of the Superstition Hills fault correlate to smaller co-seismic displacements and larger post-seismic slip, while the crystalline basement and thin sediments of the north segment correlate to larger co-seismic displacements.

Unusually shallow earthquakes. One of the most striking features of the earthquake locations in Chapter 3 is the shallow initiation depth of the Superstition Hills main shock, and the shallow depth of many of the

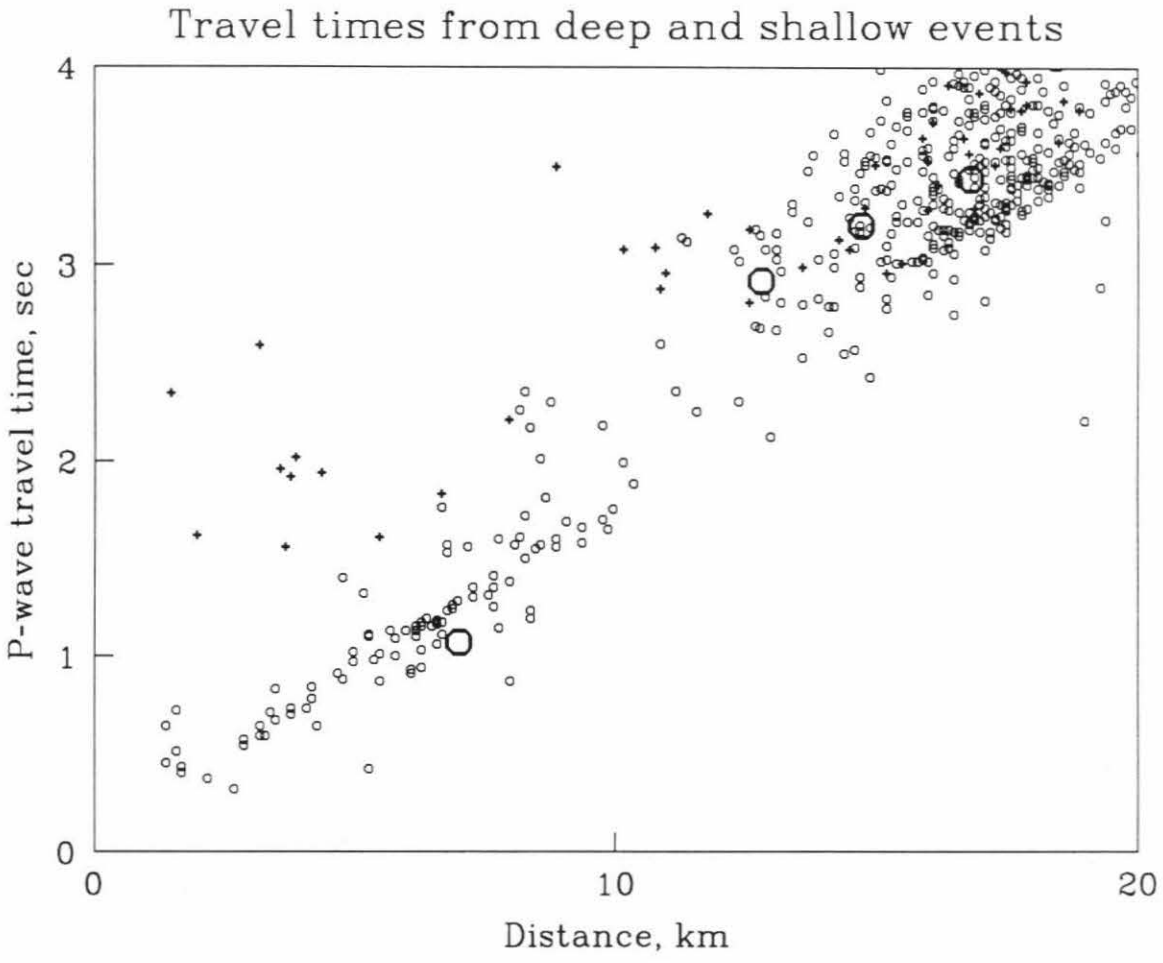

Figure 6.1 Travel time data for the Superstition Hills mainshock and aftershocks along the northern segment of the Superstition Hills fault. + (crosses) are data for aftershocks deeper than 9 km, o (small circles) are data for aftershocks shallower than 3 km, O (large circles) are data for the mainshock. Note separation of travel time data at small distances for deep and shallow events, and how main shock lies on shallow event data line.

aftershocks along the north segment of the Superstition Hills fault (Figure 3.5). During the location processing, the depth of the Superstition Hills main shock was tested in two ways. First, trial relocations at a range of fixed depths were made and travel time residuals to nearby seismograph stations were compared. The minimum residuals occur for a shallow depth. Second, S- and P-wave arrival times for nearby stations were swapped in and out of the phase file to ensure no erroneous pick was biasing the epicentral depth. The depth is insensitive to such swapping.

A more convincing argument for shallow earthquakes can be made by comparing travel times of shallow and deep earthquakes to nearby seismograph stations as in Figure 6.1. Recall that travel time data plotted on a travel time versus distance diagram will form a straight line for shallow earthquakes and, at small distances, will plot a convex downward curved line for deep earthquakes. Figure 6.1 shows such lines formed by travel times from many shallow ($\leq$3 km depth) and deep ($\geq$9 km depth) events along the north Superstition Hills fault. The separation of the travel time data for deep and shallow events, and the continuation of the shallow travel time data toward the plot origin support the location of earthquakes at shallow depths. The Superstition Hills main shock travel-time data lies on the line of shallow event data.

The shallow earthquakes along the north Superstition Hills fault, deep earthquakes along the south Superstition Hills fault, and the difference in afterslip behavior of the fault segments can be interpreted in terms of Marone and Scholz's (1988) discussion of minimum depth of earthquakes. They define a fault to be well developed if it has a thick gouge from undergoing significant net displacement. An undeveloped fault has undergone little net displacement

and so has little or no gouge. They find thick gouge to exhibit velocity strengthening. Well developed faults with thick gouge have no earthquakes at shallow depths. However, well developed faults with thick gouge exhibit afterslip because the co-seismic rupture dies out near the surface due to the velocity strengthening, resulting in a slip deficit that produces afterslip upon relaxation. Undeveloped faults do have shallow earthquakes because such faults have velocity weakening. Undeveloped faults would then show smaller afterslip and greater co-seismic slip. On the Superstition Hills fault, the north segment has shallow aftershocks, more co-seismic slip, and less afterslip. The south segment has few, deep aftershocks, less co-seismic slip, and more afterslip. In terms of Marone and Scholz (1988), the north segment behaves as an undeveloped fault and the south segment is well developed. It could be argued that the north and south segments are different ages, with different amounts of total offset, accounting for the difference in development. It is more likely, however, that both segments are the same age and that the different rock types surrounding each of the fault segments age or develop differently per given amount of fault offset. Presumably the softer rock along the south segment of the fault generates gouge quicker per unit fault offset and so acts well developed. The harder rock along the north segment generates less gouge per unit fault offset and so behaves undeveloped. The age and total offset of the Superstition Hills fault is unknown. Sedimentary and fault interactions between the Superstition Hills fault and the northeast-striking faults indicate a minimum Pleistocene age (Sharp *et al.*, 1989).

It is worth emphasizing that the shallow depth found for the Superstition Hills main shock from the local array data represents only the initiation point of the earthquake. The teleseismic study (Chapter 4) found most of the

seismic energy of the main shock to come from deeper on the fault. Figure 4.3 compares the depth of moment release determined in Chapter 4, 4 to 8 km, to the depth distribution of the aftershocks, which lie mostly between 1 to 11 km depth. Along the northern segment of the fault, relatively few aftershocks lie between 2.5 to 5 km depth and in the south, between 2 to 8 km. This is in agreement with studies of slip distribution along faults that find fewest aftershocks in areas of greatest slip (Doser and Kanamori, 1986b, Mendoza and Hartzell, 1988) and greatest moment release (Schwartz *et al.*, 1989) on the fault plane. Here it is assumed regions of greatest moment release correspond to areas of high slip.

Crustal block rotation. Nicholson *et al.* (1986) have proposed that northeast-striking faults in the Imperial Valley area act as the sides of rotating crustal blocks between the San Andreas fault and the San Jacinto fault zone. In terms of crustal blocks, the Elmore Ranch fault and the Superstition Hills fault would define a corner of a block. Rotation of that block is implied by the near simultaneous activity of both faults. Rotation of the block into the Superstition Hills fault should produce compressional and extensional focal mechanisms near the intersection of the faults, depending on the sense of rotation. However, the best constrained focal mechanisms near the fault intersections are all strike-slip (Figure 3.7) and so block rotation apparently did not play a role in this earthquake sequence. Block rotation has also been cited in the nucleation of earthquakes at fault intersections that represent block corners. Models of the Elmore Ranch earthquake triggering the Superstition Hills earthquake have been proposed (Given and Stuart, 1988, Hudnut *et al.*, 1989) without calling on block rotation.

It is interesting that the Elmore Ranch main shock nucleated where it did. The Elmore Ranch seismic activity is the only one of three northeast-trending seismic lineation during the last ten years that did not start within the Brawley seismic zone. Figure 3.15 shows the Elmore Ranch main shock occurred at a corner in the crystalline basement rock. Sharp *et al.* (1989) speculated that the Elmore Ranch seismic lineation was a coincidental juxtaposition of two northeast-striking faults. The join of the faults is at the site of the main shock, and the width of the seismic lineation differs to either direction from the main shock. As seen in Figure 3.15, the larger events of the northeast trend occur in the crystalline basement rocks southwest of the Elmore Ranch main shock where the seismic lineation is wider (5 km). The Elmore Ranch seismic lineation continues beyond those rocks to the Brawley seismic zone. The seismicity lineation passes just north of the Westmorland and Salton geothermal areas (Figures 3.1 and 3.14). These geothermal areas correlate with subtle anomalies in a traveltime contour map of Fuis *et al.*, (1982). Also, the Salton Buttes volcanoes, at the southeast end of the Salton Sea, contain granitic xenoliths that may indicate the presence of crystalline plutonic rocks at depth (Robinson *et al.*, 1976). It can be speculated that the northeast trend continues from along the edge of well defined continental crystalline basement rocks to either a metasedimentary basement feature or a bit of continent basement not resolved in the study of Fuis *et al.* (1982).

The continental crystalline basement along the north segment of the Superstition Hills fault and the southwest end of the Elmore Ranch fault does act as a fault bounded structural unit or block. This block is defined on the east by the Superstition Hills fault, to the north by the south edge of the basement embayment, to the west by the faults along which Superstition

Mountain was uplifted, and to the south by the basement step (Figure 3.15). The basement step is marked by aftershocks. This block is analogous to the islands in the western Gulf of California that apparently separated from Baja California by strike-slip faulting (*e.g.*, Ness *et al.*, 1986) as gulf spreading progressed. In the same way, the Superstition Mountain and Superstition Hills faults separate pieces of continental basement from the mainland.

Chapter 1 to 6 References

Allen, C. R., P. St. Amand, C. F. Richter, and J. M. Nordquist (1965). Relationship between seismicity and geologic structure in the southern California region, *Bull. Seism. Soc. Am.* **55**, 753-797.

Allen, C. R., A. Grantz, J. N. Brune, M. M. Clark, R. V. Sharp, T. G. Theodore, E. W. Wolfe, and M. Wyss (1968). The Borrego Mountain, California, earthquake of 9 April 1968: a preliminary report, *Bull. Seism. Soc. Am.* **58**, 1183-1186.

Allen, C. R., M. Wyss, J. N. Brune, A. Grantz, and R. E. Wallace (1972). Displacements on the Imperial, Superstition Hills, and San Andreas faults triggered by the Borrego Mountain earthquake, in *The Borrego Mountain earthquake of April 9, 1968, U.S. Geol. Surv. Profess. Paper 787*, 87-104.

Bent, A.L., D.V. Helmberger, R.J. Stead, and P. Ho-Liu (1989). Waveform modeling of the November 1987 Superstition Hills earthquake, *Bull. Seism. Soc. Am.* **79**, 500-514.

Biehler, S., R. L. Kovach, and C. R. Allen (1964). Geophysical framework of northern end of Gulf of California, in *Marine geology of the Gulf of California*, T. H. van Andel and G. G. Shor Jr. (Editors), AAPG Memoir 3, 126-143.

Bilham R. G. (1989). Surface slip subsequent to the 24 November 1987 Superstition Hills, California, earthquake monitored by digital creepmeters, *Bull. Seism. Soc. Am.* **79**, 424-450.

Burford, R. O. (1972). Continued slip of the Coyote Creek fault after the Borrego Mountain earthquake, in *The Borrego Mountain earthquake of April 9, 1968, U.S. Geol. Surv. Profess. Paper 787*, 105-111.

Clark, M. M. (1972). Surface rupture along the Coyote Creek fault, in *The Borrego Mountain earthquake of April 9, 1968, U.S. Geol. Surv. Profess. Paper 787*, 55-86.

Cohn, S. N., C. R. Allen, R. Gilman, and N. R. Goulty (1982). Preearthquake and postearthquake creep in the Imperial fault and the Brawley fault

zone, in *The Imperial Valley, California, earthquake of October 15, 1979, U.S. Geol. Surv. Profess. Paper 1254*, 161-167.

Dibblee, T. W., Jr. (1954). Geology of the Imperial Valley region, in Geology of southern California, *Bull. Calif. Div. Mines* **170**, 21-28.

Dibblee, T. W., Jr. (1984). Stratigraphy and tectonics of the San Felipe Hills, Borrego Badlands, Superstition Hills, and vicinity, in *The Imperial Basin - Tectonics, Sedimentation and Thermal Aspects*, C.A. Rigsby (Editor), Pacific Section SEPM, Los Angeles, 31-44.

Doser, D. I. and H. Kanamori (1986a). Spatial and temporal variations in seismicity in the Imperial Valley (1902-1984), *Bull. Seism. Soc. Am.* **76**, 421-438.

Doser, D. I. and H. Kanamori (1986b). Depth of seismicity in the Imperial Valley region (1977-1983) and its relationship to heat flow, crustal structure, and the October 15, 1979 earthquake, *J. Geophys. Res.* **91**, 675-688.

Elders, W. A., R. W. Rex, T. Meidav, P. T. Robinson, and S. Biehler (1972). Crustal spreading in southern California, *Science* **178**, 15-24.

Frankel, A. and L. Wennerberg (1989). Rupture process of the M_s 6.6 Superstition Hills earthquake determined from strong-motion recordings: application of tomographic source inversion, *Bull. Seism. Soc. Am.* **79**, 515-541.

Fuis, G. S. (1982). Displacement on the Superstition Hills fault triggered by the 1979 Imperial Valley earthquake, in *The Imperial Valley, California, earthquake of October 15, 1979, U.S. Geol. Surv. Profess. Paper 1254*, 145-154.

Fuis, G. S., W. D. Mooney, J. H. Healey, G. A. McMechan, and W. J. Lutter (1982). Crustal structure of the Imperial Valley region, in *The Imperial Valley, California, earthquake of October 15, 1979, U.S. Geol. Surv. Profess. Paper 1254*, 25-50.

Fuis, G. S. and W. M. Kohler (1984). Crustal structure and tectonism of the

Imperial Valley region, California, in *The Imperial Basin-tectonics, Sedimentation and Thermal Aspects*, C.A. Rigsby (Editor), Pacific Section SEPM, Los Angeles, 1-13.

Given, D. D., R. Norris, L. M. Jones, L. K. Hutton, C. E. Johnson, and S. Hartzell (1986). The southern California network bulletin January through June, 1986, *U.S. Geol. Surv., Open-File Rept. 86-598*, 28pp.

Given, D. D. and W. D. Stuart (1988). A fault interaction model for triggering of the Superstition Hills earthquake of November 24, 1987 (abstract), *Seism. Res. Lett.* **59**, 48.

Hamilton, R. M. (1970). Time term analysis of explosion data from the vicinity of the Borrego Mountain, California, earthquake of 9 April 1968, *Bull. Seism. Soc. Am.* **60**, 367-381.

Hamilton, R. M. (1972). Aftershocks of the Borrego Mountain earthquake from April 12 to June 12, 1968, in *The Borrego Mountain earthquake of April 9, 1968, U.S. Geol. Surv. Profess. Paper 787*, 31-54.

Hanks, T.C. and C.R. Allen (1989). The Elmore Ranch and Superstition Hills earthquakes of 24 November 1987: introduction to the special issue, *Bull. Seism. Soc. Am.* **79**, 231-238.

Hileman, J. A., C. R. Allen, and J. M. Nordquist (1973). Seismicity of the southern California region 1 January 1932 to 31 December 1972, Seismological Laboratory, California Institute of Technology, Pasadena, California.

Hill, D. P., P. Mowinckel, and L. G. Peake (1975). Earthquakes, active faults, and geothermal areas in the Imperial Valley, California, *Science* **188**, 1306-1308.

Hudnut, K., L. Seeber, and J. Pacheco (1989). Cross-fault triggering in the November 1987 earthquake sequence, *Geophys Res. Lett.* **16**, 199-202.

Hudnut, K., L. Seeber, T. Rockwell, J. Goodmacher, R. Klinger, S. Lindvall, and R. McElwaun (1989). Surface ruptures on cross-faults in the 24 November 1987 Superstition Hills, California, earthquake sequence, *Bull.*

Seism. Soc. Am. **79**, 282-296.

Hudnut, K. and K. Sieh (1989). Behavior of the Superstition Hills fault during the past 330 years, *Bull. Seism. Soc. Am.* **79**, 304-329.

Hutton, L. K. and C. E. Johnson (1981). Preliminary study of the Westmorland, California, earthquake swarm (abstract), *Eos Trans. AGU* **62** 957.

Hwang, L., H. Magistrale, and H. Kanamori (1989). Teleseismic source parameters and rupture characteristics of the 24 November 1987 Superstition Hills earthquake, *Bull. Seism. Soc. Am.* (in press).

Johnson, C. E. (1979). CEDAR-An approach to the computer automation of short period local seismic networks; seismotectonics of the Imperial Valley of southern California, *Pasadena, California Institute of Technology, Ph. D. thesis*, 343pp.

Johnson, C. E. and L. K. Hutton (1982). Aftershocks and preearthquake seismicity, in *The Imperial Valley, California, earthquake of October 15, 1979, U.S. Geol. Surv. Profess. Paper 1254*, 59-76.

Jones, L. M., L. K. Hutton, D. D. Given, and C. R. Allen (1986). The North Palm Springs, California, earthquake sequence of July 1986, *Bull. Seism. Soc. Am.* **76**, 1830-1837.

Kahle J. E., C. J. Wills, E. W. Hart, J. A. Treiman, R. B. Greenwood and R. S. Kaumeyer (1988). Preliminary report, surface rupture, Superstition Hills earthquakes of November 23 and 24, 1987, *California Geology* **41**, 75-84.

Klein, F. W. (1985). User's guide to HYPOINVERSE, a program for VAX and PC350 computers to solve for earthquake locations, *U.S. Geol. Surv., Open-File Rept. 85-515*, 24pp.

Kohler, W.M. and G.S. Fuis (1986). Travel-time, time-term, and basement depth maps for the Imperial Valley Region, California, from explosions, *Bull. Seism. Soc. Am.* **76**, 1289-1303.

Langston, C.A. and D.V. Helmberger (1975). A procedure for modelling shallow dislocation sources, *Geophys. J. R. Astron. Soc.* **42**, 117-1390.

Larson, R. L. (1972). Bathymetry, magnetic anomalies, and plate tectonic history of the mouth of the Gulf of California, *Geol. Soc. Am. Bull.* **83**, 3345-3360.

Larson, R. L., H. W. Menard, and S. M. Smith (1968). Gulf of California: A result of ocean-floor spreading and transform faulting, *Science* **161**, 781-784.

Lisowski, M. and J. C. Savage (1988). Deformation associated with the Superstition Hills, California, earthquakes of November 1987 (abstract), *Seism. Res. Lett.* **59**, 35.

Lomnitz, C., F. Mooser, C. R. Allen, J. N. Brune, and W. Thatcher (1970). Seismicity and tectonics of the northern Gulf of California region, Mexico: preliminary results, *Geofisica Internacional* **10**, 37-48.

Louie, J. N., C. R. Allen, D. C. Johnson, P.C. Haase, and S. N. Cohn (1985). Fault slip in southern California, *Bull. Seism. Soc. Am.* **75**, 811-833.

Magistrale, H., L. Jones, and H. Kanamori (1989). The Superstition Hills, California, Earthquakes of 24 November 1987, *Bull. Seism. Soc. Am.* **79**, 239-251.

Marone, C., and C. H. Scholz (1988). The depth of seismic faulting and the upper transition from stable to unstable slip regimes, *Geophys. Res. Lett.* **15**, 621-624.

McGill, S. F., C. R. Allen, K. W. Hudnut, D. C. Johnson, W. F. Miller and K. E. Sieh (1989). Slip on the Superstition Hills fault and on nearby faults associated with the 24 November 1987 Elmore Ranch and Superstition Hills earthquakes, southern California, *Bull. Seism. Soc. Am.* **79**, 362-375.

Mendoza, C. and S.H. Hartzell (1988). Aftershock patterns and main shock faulting, *Bull. Seism. Soc. Am.* **78**, 1438-1449.

Moore, D. G. and E. C. Buffington (1968). Transform faulting and growth of

the Gulf of California since the late Pliocene, *Science* **161**, 1238-1241.

Muffler, L. J. P. and D. E. White (1969). Active metamorphism of upper Cenozoic sediments in the Salton Sea geothermal field and the Salton Trough, southeastern California, *Geol. Soc. Am. Bull.* **80**, 157-181.

Murphy, L. M. and W. K. Cloud (1953). United States earthquakes, 1951, *Serial 748, U. S. Coast and Geodetic Survey.*

Nabelek, J. (1984). Determination of earthquake source parameters from inversion of body waves, *Massachusetts Institute of Technology, Ph. D. Dissertation*, 360 pp.

Nabelek, J. (1985). Geometry and mechanism of faulting of the 1980 El Asnam, Algeria, earthquake from inversion of teleseismic body waves and comparison with field observations, *J. Geophys. Res.* **90**, 12713-12728.

Ness, G. E., S. V. Francisco, and C. R. Gustavo (1986). Geophysical structure and late Neogene history of Gulf and Peninsular province of the Californias (abstract), *AAPG Bull.* **70**, 932.

Nicholson, C., L. Seeber, P. Williams, and L. Sykes (1986). Seismic evidence for conjugate slip and block rotation within the San Andreas fault system, southern California, *Tectonics* **5**, 629-648.

Norris, R., C. E. Johnson, L. M. Jones, and L. K. Hutton (1986). The southern California network bulletin, *U.S. Geol. Surv., Open-File Rept. 86-96*, 31pp.

Porcella, R., E. Etheredge, R. Maley, and J. Switzer (1987). Strong-motion data from the Superstition Hills earthquakes of 0154 and 1315 (GMT), November 24, 1987, *U.S. Geol. Surv., Open-File Rept. 87-672*, 56pp.

Reasenberg, P. and D. Oppenheimer (1985). FPFIT, FPPLOT, and FPPAGE: computer programs for calculating and displaying earthquake fault-plane solutions, *U.S. Geol. Surv., Open-File Rept. 85-739*, 46pp.

Richter, C. F. (1958). *Elementary Seismology*, W. H. Freeman, San Francisco, 768 pp.

Robinson, P. T., W. A. Elders, and L. J. P. Muffler (1976). Quaternary volcanism in the Salton Sea geothermal field, Imperial Valley, California, *Geol. Soc. Am. Bull.* **87**, 347-360.

Sanders, C., H. Magistrale, and H. Kanamori (1986). Rupture patterns and preshocks of large earthquakes in the southern San Jacinto fault zone, *Bull. Seism. Soc. Am.* **76**, 1187-1206.

Scholz, C. H. (1989). *The Mechanics of Earthquakes and Faulting*, Cambridge University Press, (in press).

Scholz, C. H., M. Wyss, and S. W. Smith (1969). Seismic and aseismic slip on the San Andreas fault, *J. Geophys. Res.* **74**, 2049-2069.

Schwartz, S.Y., J.W. Dewey, and T. Lay (1989). Influence of fault plane heterogeneity on the seismic behavior in the Southern Kurile Islands Arc, *J. Geophys. Res.* **94**, 5637-5649.

Sharp, R. V. (1967). San Jacinto fault zone in the Peninsular Ranges of southern California, *Bull Geol. Soc. Am.* **78**, 705-730.

Sharp, R. V. (1972). Tectonic setting of the Salton trough, in *The Borrego Mountain earthquake of April 9, 1968, U.S. Geol. Surv. Profess. Paper 787*, 3-15.

Sharp, R. V. (1982). Tectonic setting of the Imperial Valley region, in *The Imperial Valley, California, earthquake of October 15, 1979, U.S. Geol. Surv. Profess. Paper 1254*, 5-14.

Sharp, R. V. and M. M. Clark (1972). Geologic evidence of previous faulting near the 1968 rupture on the Coyote Creek fault, in *The Borrego Mountain earthquake of April 9, 1968, U.S. Geol. Surv. Profess. Paper 787*, 131-140.

Sharp, R. V., J. J. Lienkaemper, M. G. Bonilla, D. B. Burke, B. F. Fox, D. G. Herd, D. M. Miller, D. M. Morton, D. J. Ponti, M. J. Rymer, J. C. Tinsley, J. C. Yount, J. E. Kahle, E. W. Hart and K. E. Sieh (1982). Surface faulting in the central Imperial Valley, in *The Imperial Valley, California, earthquake of October 15, 1979, U.S. Geol. Surv. Profess.*

Paper 1254, 114-144.

Sharp, R. V., M. J. Rymer, and J. J. Lienkaemper (1986). Surface displacement on the Imperial and Superstition Hills faults triggered by the Westmorland, California, earthquake of 26 April 1981, *Bull. Seism. Soc. Am.* **76**, 949-965.

Sharp, R.V., K.E. Budding, J. Boatwright, M.J. Ader, M.G. Bonilla, M.M. Clark, T.E. Fumal, K.K. Harms, J.J. Lienkaemper, D.M. Morton, B.J. O'Neill, C.L. Ostergren, D.J. Ponti, M.J. Rymer, J.L. Saxton, and J.D. Sims (1989). Surface faulting along the Superstition Hills fault zone and nearby faults associated with the earthquakes of 24 November 1987, *Bull. Seism. Soc. Am.* **79**, 252-281.

Sharp, R. V. and J. L. Saxton (1989). Three-dimensional records of surface displacement on the Superstition Hills fault zone associated with the earthquakes of 24 November 1987, *Bull. Seism. Soc. Am.* **79**, 376-389.

Sipkin, S.A. (1989). Moment-tensor solutions for the 24 November 1987 Superstition Hills, California earthquake, *Bull. Seism. Soc. Am.* **79**, 493-499.

Wald, D.J. and P.G. Somerville (1988). Simulation of accelerograms of the 1987 Superstition Hills earthquake sequence (abstract), *Seism. Res. Lett.* **59**, 49.

Wesson, R. L. (1988). Dynamics of fault creep, *J. Geophys. Res.* **93**, 8929-8951.

Williams, P.L. and H.W. Magistrale (1989). Slip along the Superstition Hills fault associated with the 24 November 1987 Superstition Hills, California, earthquake, *Bull. Seism. Soc. Am.* **79**, 390-410.

Woodard, G. D. (1974). Redefinition of Cenozoic stratigraphic column in Split Mountain Gorge, Imperial Valley, California, *AAPG Bull.* **58**, 521-526.

Chapter 7

A Three-Dimensional Velocity Model of Southern California for Locating Earthquakes in the Los Angeles Basin

7.1 Introduction

Southern California earthquakes are routinely located using one-dimensional velocity models to represent the crust. These models have uniform layers for all of southern California, with each layer having a given velocity, usually with seismic velocity increasing as a function of depth. The southern California crust is composed of a variety of geologic provinces, each with a variety of rock types. Different rock types have different seismic velocities, suggesting that a one-dimensional crustal velocity model may not adequately represent the actual variation of seismic velocities in the crust. A three-dimensional crustal velocity model, with velocity a function of depth and horizontal position, is required.

The recent occurrence of the 1987 Whittier earthquake, the 1988 Malibu earthquake, the 1989 Pasadena earthquake, other nearby earthquakes, and the role of these earthquakes in the models of Los Angeles basin as a fold and thrust belt (Davis *et al.*, 1989) make accurate earthquake locations desirable. Good earthquake locations in Los Angeles basin are difficult to achieve because of the large differences in the crustal seismic velocities between the sediments of the Los Angeles basin, the crystalline rocks of the Peninsular and Transverse ranges south, east, and north of the basin, and thinner crust of the offshore region to the west of the basin. Accurate earthquake locations require an accurate representation of seismic velocities. An accurate crustal

velocity model also provides realistic take-off angles of seismic ray paths from the earthquake source to the seismographs, resulting in better focal mechanisms. In this chapter, the construction and calibration of a three-dimensional crustal velocity model used to locate earthquakes in the Los Angeles basin is described. The improved earthquake locations and focal mechanisms help to define seismogenic structures that are difficult to map from the surface of the earth.

Previous studies of the velocity structure of the southern California crust (*e.g.*, Hearn, 1985, Hadley, 1978) recognized the lateral variations of seismic velocity. Recent studies of earthquakes in the Los Angeles basin (Hauksson, 1987, Hauksson and Jones, 1989) have attempted to correct for the presence of the thick sequence of seismically slow sediments not accounted for in standard one-dimensional velocity models by using hybrid one-dimensional models. Elsewhere in California, workers have developed three-dimensional models of small areas (*e.g.*, Michelini *et al.*, 1989, for Parkfield and Eberhart-Phillips, 1989, for Coalinga). The current work is the first attempt to create a three-dimensional velocity model of all of southern California. The results of the earthquake locations in the three-dimensional velocity structure will be discussed in Chapter 8.

The three-dimensional velocity model of southern California was constructed to operate in the earthquake location program REL3D written by Roecker and co-workers (Roecker 1981, 1982, Shedlock 1986, Shedlock and Roecker 1987, Roecker *et al.*, 1987). The velocity model is expressed as rectangular blocks, each block having a given velocity. The blocks are defined by orthogonal vertical and horizontal interfaces. The code calculates ray paths by finding the average one-dimensional structure between source and receiver

Table 7.1
Provinces for 3-D Model

Number	Province	Reference
1	Los Angeles Basin	Suppe, unpublished data
		Kanamori, written communication
2	Santa Barbara Channel	Crandel *et al.* (1983)
3	Ventura Basin	Corbett and Johnson (1982)
4	Borrego Valley	Hamilton (1970)
5	Coast Ranges, east of San Andreas fault	Eaton *et al.* (1970)
6	Coast Ranges, west of San Andreas fault	Walter and Mooney (1982)
7	San Jacinto Valley	Hadley and Combs (1974)
8	San Fernando Valley	Suppe, unpublished data
		Healy (1963)
9	Great Valley	Colburn and Mooney (1986)
10	Mojave	Kanamori and Hadley (1975)
11	East Mojave	Hadley (1978)
12	San Gabriel Mountains	Hadley and Kanamori (1977)
13	San Bernadino Mountains	Hadley and Kanamori (1977)
14	Little San Bernadino Mountains	Hadley and Kanamori (1977)
15	Imperial Valley	Fuis *et al.* (1982)
16	Coachella Valley	Fuis *et al.* (1982)
		Hadley (1978)
17	Santa Monica Mountains	Stierman and Ellsworth (1976)
18	Peninsular Ranges	Kanamori, written communication
19	Sierra Nevada	Dollar and Jones (1986)
20	Tehachapi Mountains	Malin, in preparation
21	Catalina Island	Corbett (1984)
22	North Continental Borderland	Corbett (1984)
23	South Continental Borderland	Corbett (1984)

and tracing rays through that average structure. Once the ray path with the smallest travel time in the average one-dimensional structure is found, that ray path is followed through the three-dimensional structure to calculate travel time and partial derivatives of hypocenters with respect to travel times. The use of the average one-dimensional velocity structure to find the raypath is called approximate ray tracing.

7.2 Constructing the Three-Dimensional Velocity Model

The scheme to generate the three-dimensional velocity model was to partition southern California into geologic provinces, with each province having a consistent one-dimensional velocity structure. The one-dimensional velocity structures of each region were then assembled into a three-dimensional model. Travel times of explosions were then calculated in the three-dimensional model, compared to the observed travel times, and the model adjusted in a forward sense until the observed and calculated travel times agreed satisfactorily. An observed travel time minus a calculated travel time is called a residual.

The three-dimensional model was constructed by dividing southern California into geologic provinces based on surface geology and tectonic elements. Nineteen geologic provinces were originally defined. During the calibration procedure it became apparent that, for a few provinces, part of the province had residuals consistently different than the rest of the province, and so should be split into a separate province. Four new provinces were created, resulting in a total of twenty-three provinces (Table 7.1). The one-dimensional model for each geologic province was taken from the literature. The one-dimensional models are based mostly on seismic refraction studies,

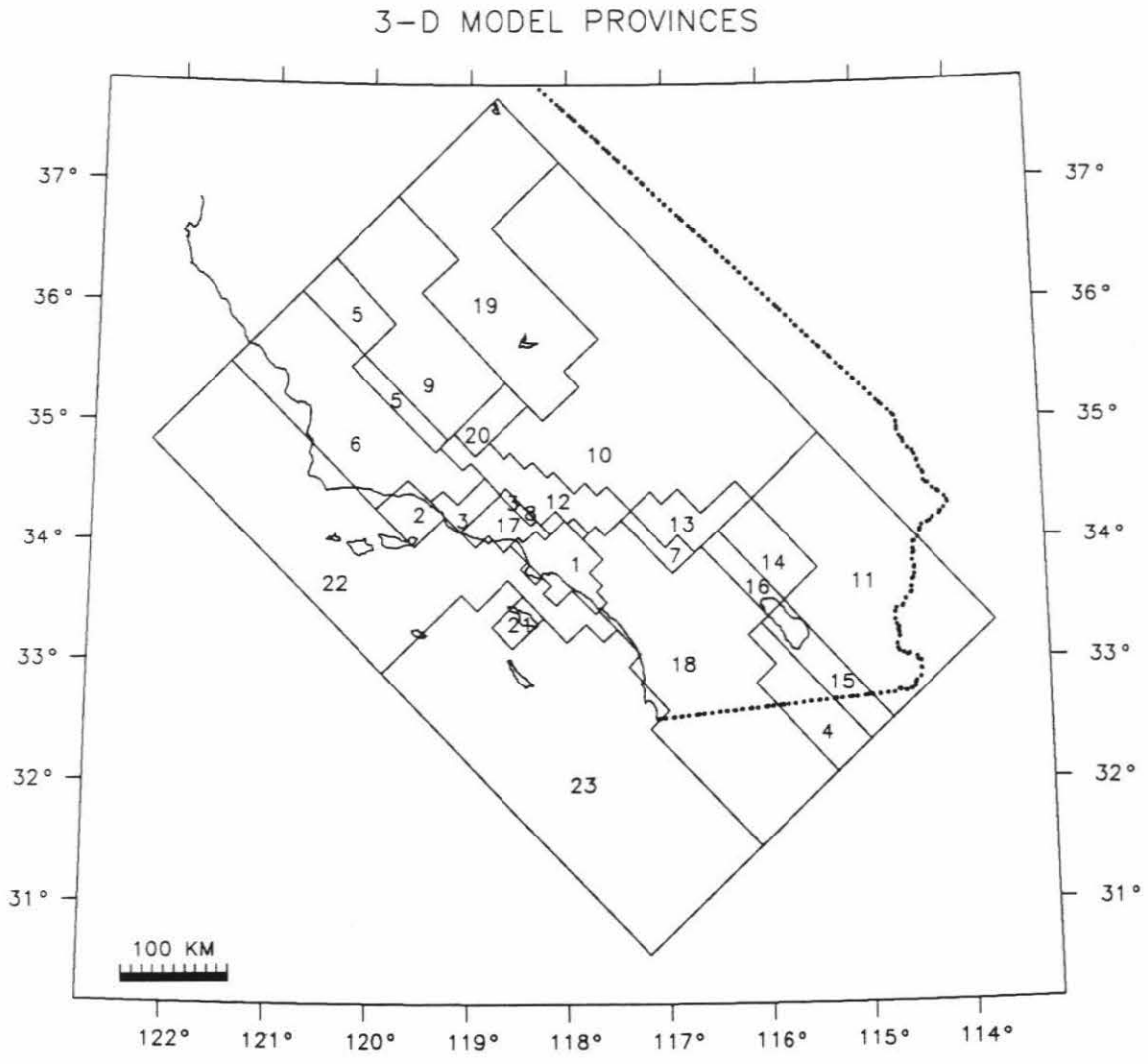

Figure 7.1 Three-dimensional velocity model provinces superposed on an outline of southern California. The numbers labeling the velocity provinces are keyed to the numbers in Table 7.1. Note greater detail of velocity province boundaries close to Los Angeles basin (center) and detail decreasing towards edge of model. Dotted line is California state border.

and some are models that were developed for detailed local earthquake studies. In many cases, several one-dimensional models of a province were tried and rejected during the calibration procedure described below. The one-dimensional (Figure 7.2, Table 7.2) models were assembled into a three-dimensional structure to locate earthquakes in the Los Angeles basin.

The geologic provinces are outlined by vertical block interfaces. The smallest interface spacings, and hence smallest blocks, were used to outline the Los Angeles basin and the provinces nearest to the basin (Figure 7.1). This gives the three-dimensional model the most detail in and near the Los Angeles basin. Interface spacing and block size increases away from the basin. This is acceptable because the number of seismic stations recording Los Angeles basin earthquakes decreases with distance from the basin. Many horizontal interfaces are used to capture the vertical detail of the constituent one-dimensional models. Twenty northwest-striking and twenty-one northeast-striking vertical interfaces and 24 horizontal interfaces were defined, for a total of 9120 blocks. Independent P-wave and S-wave velocity models can be used in the location code, but because of a lack of S-wave velocity information, a constant V_p / V_s of 1.73 was used to derive the S-wave velocity structure from the P-wave velocity structure.

A province by province discussion of the constituent one-dimensional models tested and used follows. The final one-dimensional velocity models are shown in Figure 7.2 and Table 7.2.

Los Angeles basin. The Los Angeles basin has thick Tertiary sediments on a basement surface of large topographic relief. The configuration of the basement surface is well known but the nature of the basement rocks is not (Yerkes *et al.*, 1965). To model the velocity structure of the sediments, the

velocity models of Teng *et al.*, (1973), and Duke *et al.*, (1971, in Vidale, 1987) were tried and found unsatisfactory. The model of Teng *et al.* was from a well-log, and the model of Duke *et al.* was based on a compilation of well-log data, geologic cross sections, and short aperture refraction data. A velocity-depth function from Suppe (unpublished data), with the surface layer modified to fit the travel times of the Whittier explosion, was used. The velocity-depth function is based on logs from oil wells.

It was assumed that the basement rocks of the Los Angeles basin at a given depth had the same velocity as rocks at the same depth in the Peninsular Ranges. The velocity models of the Peninsular Ranges, discussed below, were tried at appropriate depths under the Los Angeles basin. The model of Hauksson (1987), from the inversion of earthquake travel times, was also tried. Below the sediments, all these models are similar to the average southern California structure of Hadley and Kanamori, (1977). The model used is from Kanamori (written communication), based on a large Corona quarry blast recorded in the Peninsular Ranges.

Originally, the three-dimensional model was set up with a 3 km deep, flat bottomed basin. After the velocities of sediments above 3 km depth were correctly modeled by matching explosion travel times, the topography of the basement surface was included. The depth to basement information came from Yerkes *et al.*, (1965). Where sediment extended to between 3 and 4 km depth, blocks were assigned sediment velocities determined from the velocity-depth function of Suppe (unpublished data). In places where the basement is deeper than about 4 km, the sediment velocity-depth function produced inappropriate velocities for the sediments greater than those of the basement rocks. Two maximum velocities for the sediments deeper than 4 km were

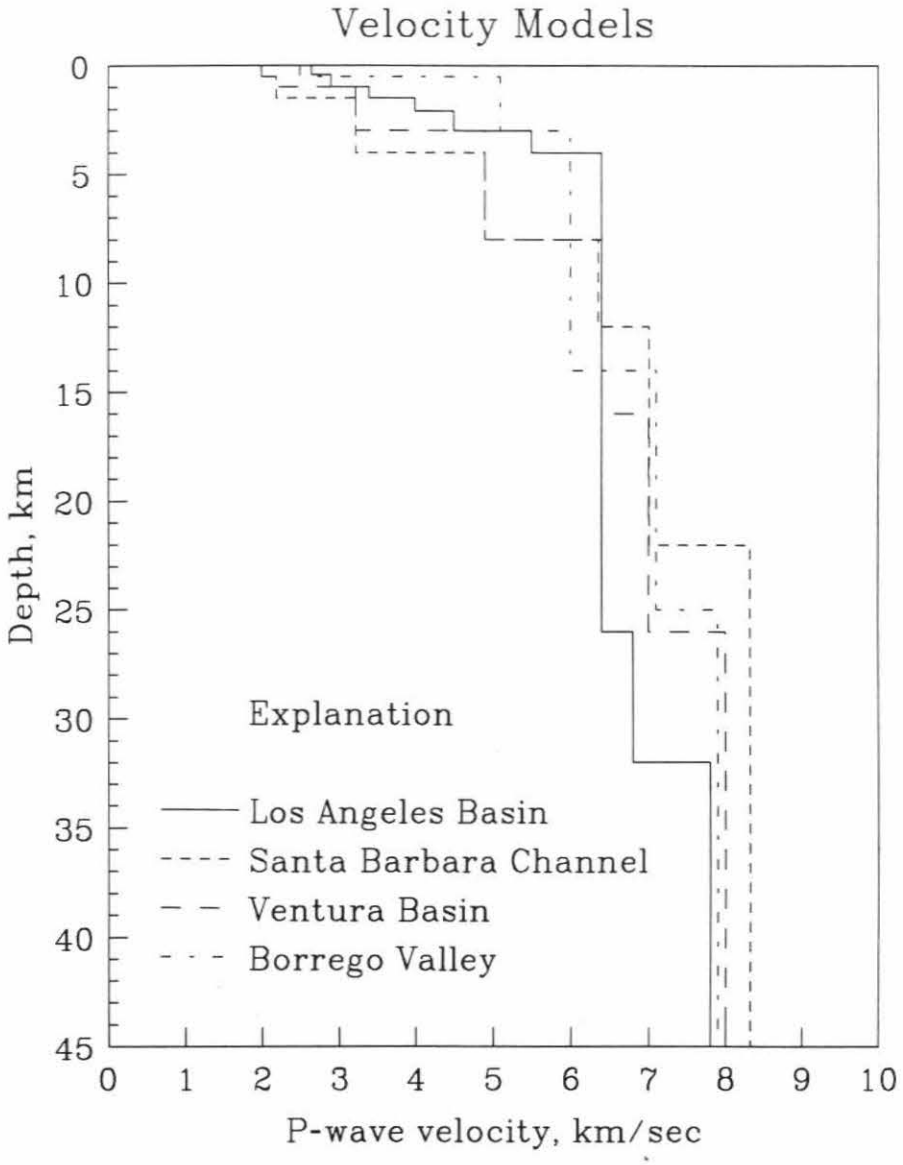

Figure 7.2 One-dimensional velocity models used to construct three-dimensional model. See also Table 7.2. Different line patterns represent different models as indicated in the explanation for each panel.

tried. The first, 5.5 km/sec, is a typical figure from a laboratory measurement of sandstone under pressure from Dobrin (1976, Figure 2-20). The other, 4.9 km/sec, is based on Faust's Law (in Dobrin, Figure 2-24), an empirical relation between seismic velocity, depth, and age. The 4.9 km/sec deep sediment velocity worked best.

Santa Barbara Channel. This area was originally defined to include the onshore Ventura basin, which was later split into a separate province. The model used for the Santa Barbara Channel is from Crandell *et al.*, (1983, Table 11b), and is based on a marine seismic refraction profile. The blocks of the three-dimensional velocity model do not correspond well to the physiographic boundaries of the channel, but that is of little importance because no seismographs lie within the channel province.

Ventura basin. The velocity model used was developed by Corbett and Johnson (1982) for a detailed study of the 1978 Santa Barbara earthquake. Their model is a composite of the sediment velocities from the model of Crandell *et al.*, (1983), described above, and lower crustal velocities from the long reversed refraction line parallel to the California coast studied by Healy (1963). Healy used explosions as seismic sources, and his model is an average for the Coast Ranges.

Borrego Valley. The velocity model comes from Hamilton (1970), and is based on an explosion refraction study. Hamilton used this model to locate aftershocks of the 1968 Borrego Mountain earthquake (Hamilton, 1972).

Coast Ranges, east of the San Andreas fault. This model is a composite. Above 5 km depth, the model from a short aperture refraction study by Eaton *et al.*, (1970) was used. Below 5 km depth, the velocity structure from the long aperture explosion refraction study of Healy (1963) was used.

Seismograph readings from this province contribute little to the location of Los Angeles basin earthquakes.

Coast Ranges, west of the San Andreas fault. The velocity model of Eaton *et al.*, (1970) was tried for this province, but the more recent results of Walter and Mooney (1982, Figure 5, model 1) worked better. The structure is based on ray trace modeling of previously collected seismic refraction data. The refraction data was collected on a line north of the edge of the three-dimensional model. The few, scattered seismographs in this province contribute little to Los Angeles basin earthquake locations.

San Jacinto Valley. The velocity model comes from Hadley and Combs (1974). They developed the model by modifying the model of Gutenberg (1955) to fit a short refraction line and mine blast observations. Hadley and Combs made their observations in the San Bernardino Valley, which in the current work was originally defined as a separate province. The San Bernardino Valley province was later added to the Peninsular Ranges province because of the similarity of their bedrock velocities. The seismographs in the San Bernardino Valley are generally on exposures of bedrock, so a separate province, with low velocity sediment surface layers, was not needed.

San Fernando Valley. The San Fernando Valley contains sediments of widely varying thickness. To model this small province, the sedimentary velocity structure of Duke *et al.*, (1971, in Vidale, 1987) on top of the basement velocity structure of Hauksson (1987) was tried and found unsatisfactory. The average Coast Ranges structure of Healy (1963) also was tried. The velocity-depth function from Suppe (unpublished data) on top of the lower layers of Healy (1963) worked best. This province was originally

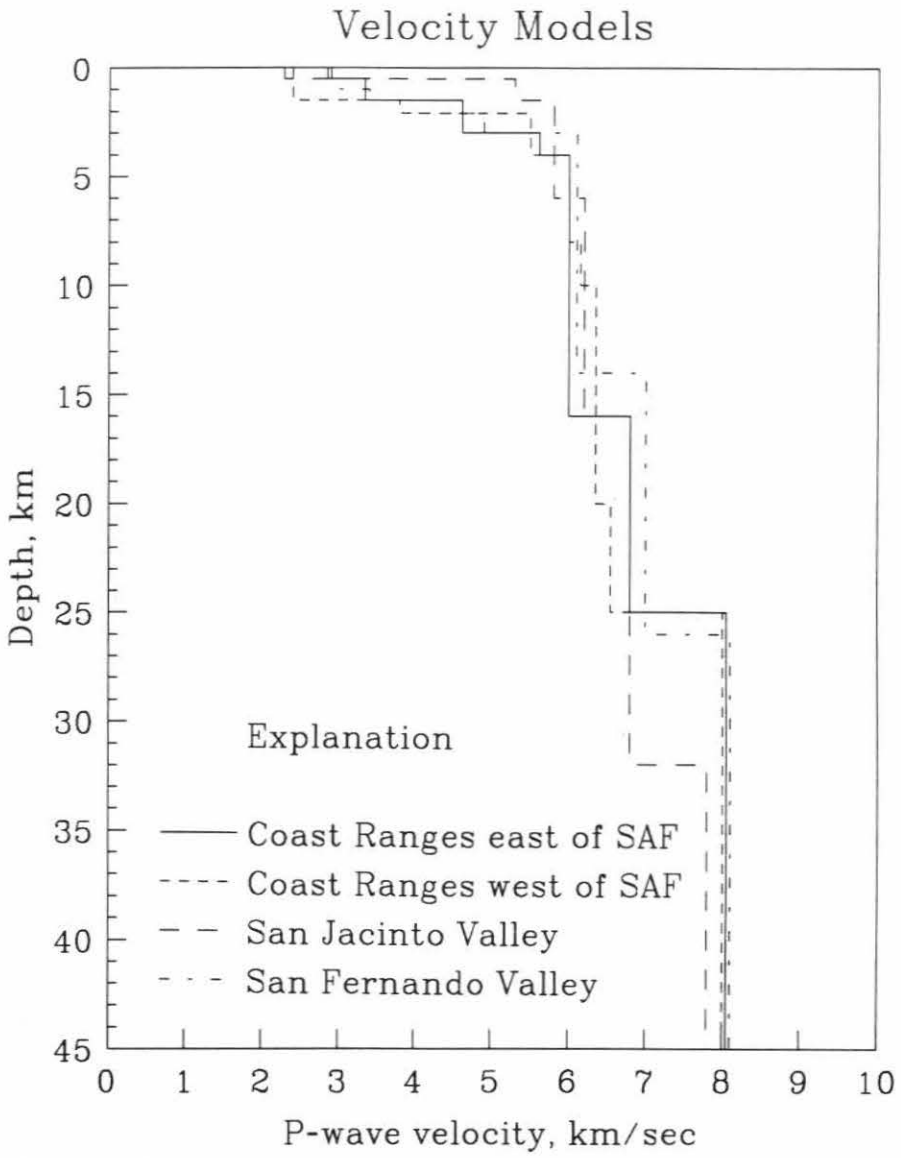

Figure 7.2 continued.

thought to be important to model accurately because of its proximity to the Los Angeles basin, but its small size (only one block) and lack of seismographs lessens its importance.

Great Valley. The model of Colburn and Mooney (1986, average of Table 3) was used. This structure is based on ray trace modeling of a partly reversed seismic refraction profile. The refraction data was collected on a line north of the edge of the three-dimensional model. There are no seismographs in this province due to the lack of hard rock sites, and few seismic rays pass through this province going elsewhere, so it is not of critical importance to the location of Los Angeles basin earthquakes.

Mojave. The model of Louie (1987) was tried and discarded. The velocity structure of Kanamori and Hadley (1975, Figure 3b) is used. That model comes from quarry blast travel time observations and is quite successful in modeling travel times of the explosions used in the current work. Some blocks in the surface layer were assigned velocities appropriate for sediments on the basis of the gravity map of Mabey (1960). A few seismograph stations lie within those blocks. The large number of seismographs in this province recording Los Angeles basin earthquakes make this an important province to model accurately.

East Mojave. This province was split off from the Mojave province on the basis of Moho velocities from the studies of Hadley (1978). The crustal velocity structure is the same as the Mojave province above, but with a higher Moho velocity.

San Gabriel, San Bernardino, and Little San Bernardino Mountains. These three transverse range provinces have velocity structures taken from Hadley and Kanamori (1977). The model was based on explosion and

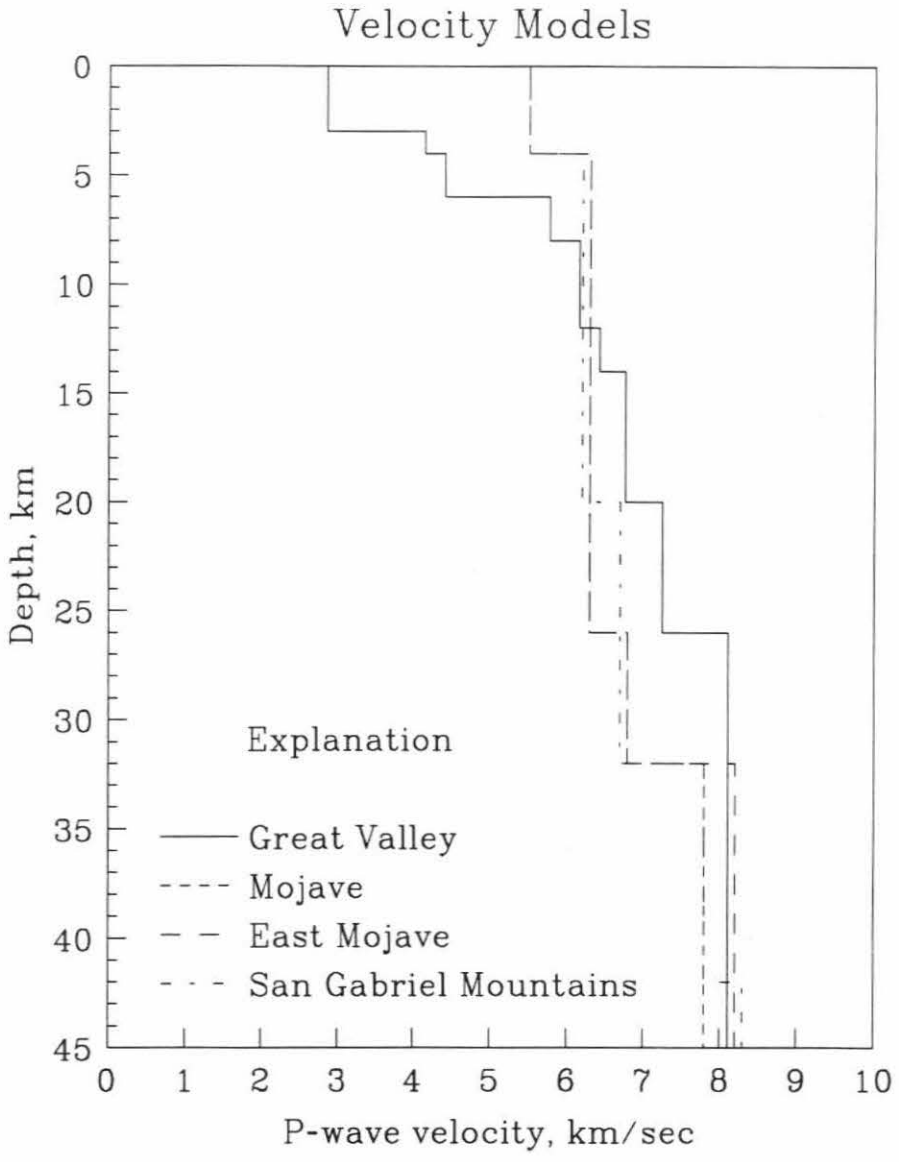

Figure 7.2 continued.

earthquake travel time observations. The province models vary from west to east in crustal layer thickness, depth to Moho, and depth to a fast, subcrustal body defined from teleseismic data. The Little San Bernardino Mountain province does not have the fast, subcrustal body. Two blocks between the Los Angeles basin and the San Gabriel Mountains (unlabeled in Figure 7.1) were given a velocity structure similar to the Little San Bernardinos. The proximity of the San Gabriel and San Bernardino Mountains to the Los Angeles basin, and the large number of seismographs in these provinces, make these important provinces to model well. The velocity structures are successful in modeling travel times of the explosions used in the current work.

Imperial Valley. The model used is from Fuis *et al.*, (1982, Figure 22) based on ray trace modeling of seismic refraction profiles. The upper layers of sediment were given a higher velocity in the current work to better match explosion travel times. The Imperial and Coachella Valleys originally were lumped together as a Salton trough province, but later split to better model the lower crust and Moho.

Coachella Valley. The sediment thickness for this province was taken from Biehler *et al.*, (1964), and although the Coachella Valley is outside the area studied by Fuis *et al.*, (1982), the sediment and upper crustal seismic velocities were taken from that study. The lower crustal velocities are from Hadley (1978), based on earthquake and explosion travel time observations.

Santa Monica Mountains. This province is adjacent to the Los Angeles basin and contains many seismograph stations, and so is important to model accurately. The Coast Ranges velocity model of Healy (1963) was tried and discarded. The sediment seismic velocities of Duke *et al.*, (1971, in Vidale, 1987) on top of the crustal model of Hauksson (1987) were also tried without

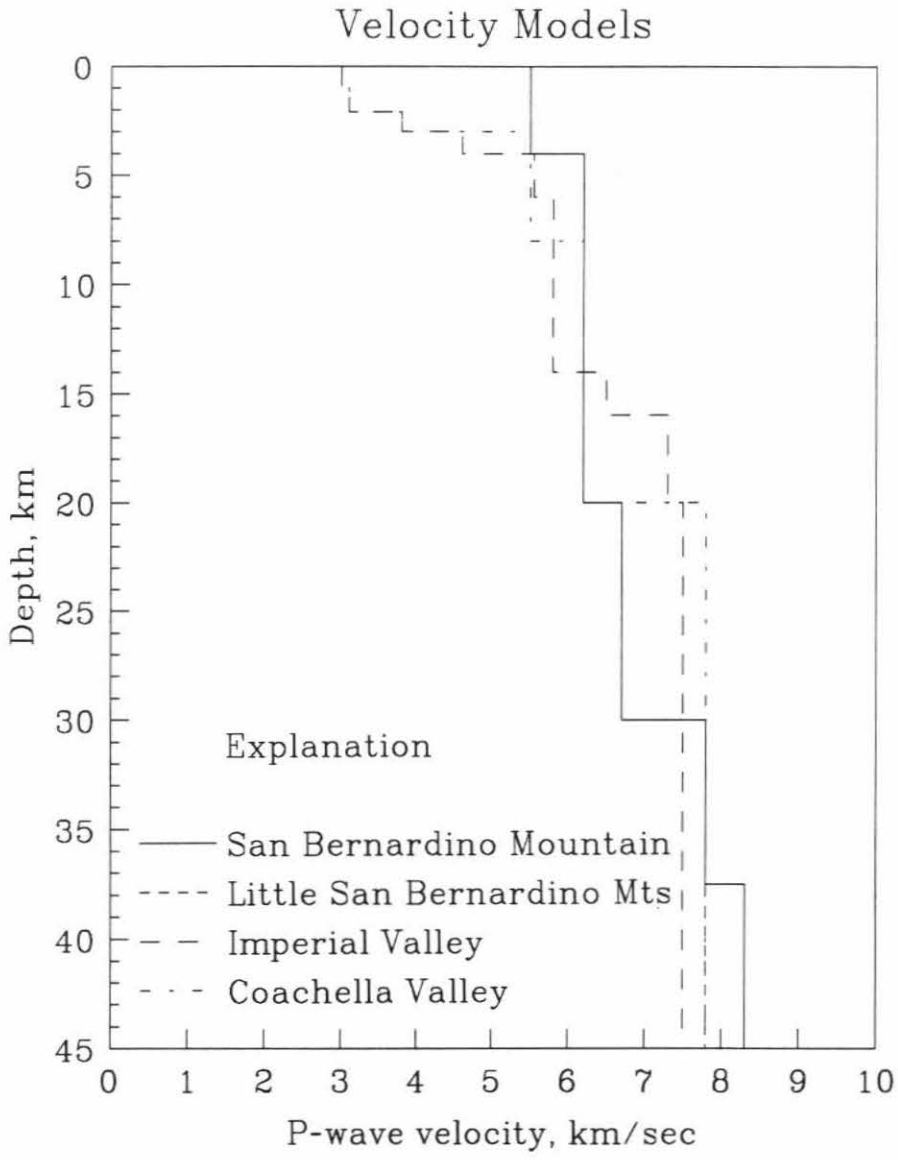

Figure 7.2 continued.

satisfaction. The best fit was that of the velocity model of Stierman and Ellsworth (1976). This model was based on nearby blast and earthquake travel time observations with the Moho depth from Healy (1963). The Palos Verdes peninsula is included as part of the Santa Monica Mountain province.

Peninsular Ranges. This province is also adjacent to the Los Angeles basin, and contains many seismograph stations, and so must be well modeled. Several velocity models were tried and rejected, including the Hadley and Combs (1974) velocity structure from a refraction study in San Bernardino valley (tried here without slow surface sediments), a model by Nava and Brune (1982), based on travel times from a large quarry explosion observed along a line partially reversed by travel times from an earthquake, and a summary model from Hadley (1978) based on earthquake and explosion travel times, and Rayleigh-wave dispersion data. Various subdivisions of the Peninsular Ranges were tried, and rejected, with different velocity models in each subdivision. The model finally used is from Kanamori (written communication), based on travel times of the large Corona blast mentioned above. The blast was recorded on specially deployed portable seismographs and carefully timed. The same blast was used as one of the calibration events to tune the three-dimensional model. The Peninsular Ranges velocity model is similar to the standard model used in routine earthquake locations, but has slightly higher mid-crustal and Moho velocities.

Sierra Nevada. The model used for this province is from Jones and Dollar (1986, Table 1, model A), based on work by Eaton (personal communication cited in Jones and Dollar, 1986). They used this model for a detailed local earthquake study after comparing earthquake travel time residuals of several velocity models. The Sierra Nevada province contains many seismograph

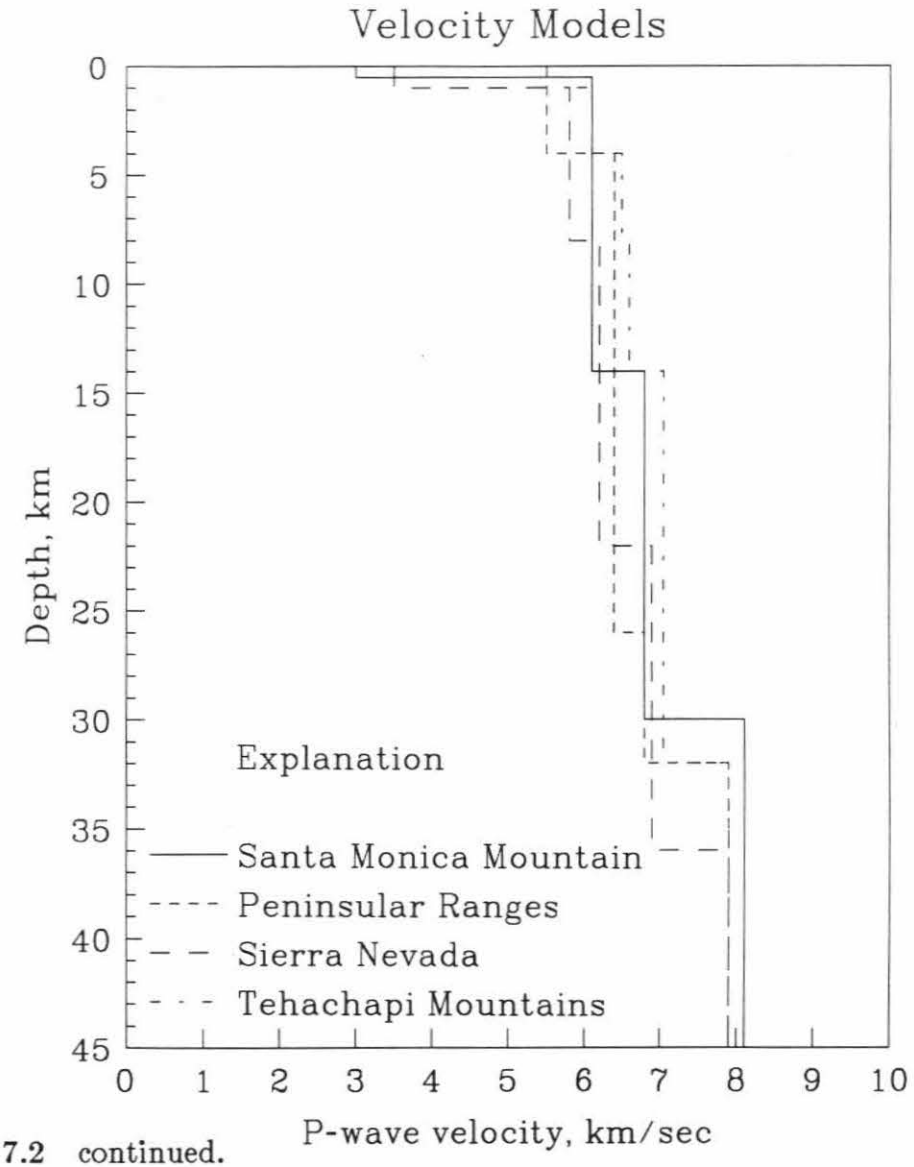

Figure 7.2 continued.

stations but is far from the Los Angeles basin and so contributes little to the locations of basin earthquakes.

Tehachapi Mountains. This province was originally part of the Sierra Nevada province, but was partitioned when a more detailed velocity model based on Calcrust data became available (Malin, in preparation). The model is based on a vibroseis seismic line.

Catalina Island, North Continental Borderland, and South Continental Borderland. The offshore area, while large, has few seismographs. A velocity model of Shor and Raitt (1958) was tried for the entire offshore area, but rejected in favor of the models of Corbett (1984). He based those models on travel time observations from a large quarry explosion on Catalina Island. The models vary slightly with azimuth from the quarry. The same explosion is used as a calibration event for the three-dimensional velocity model. After calibration, the south Continental Borderland model used has a higher Moho seismic velocity than Corbett's original model.

Some of the constituent one-dimensional velocity models used to construct the three-dimensional model are not from the literature. These are the models for the Peninsular Ranges, the Tehachapi Mountains, and the sediments of the Los Angeles basin. The Peninsular Ranges model came from Corona explosion data collected over an appropriate azimuth range by Kanamori (written communication). The same data has been reinterpreted by Nava and Brune (1982). The Tehachapi Mountains model is from Calcrust data analyzed by Malin and co-workers, who have published interpretations of the data (*e.g.*, Goodman and Malin 1988), but not the actual velocity model. The Los Angeles basin sediment model is from Suppe (personal communication), who culled it from much multi-channel seismic refraction

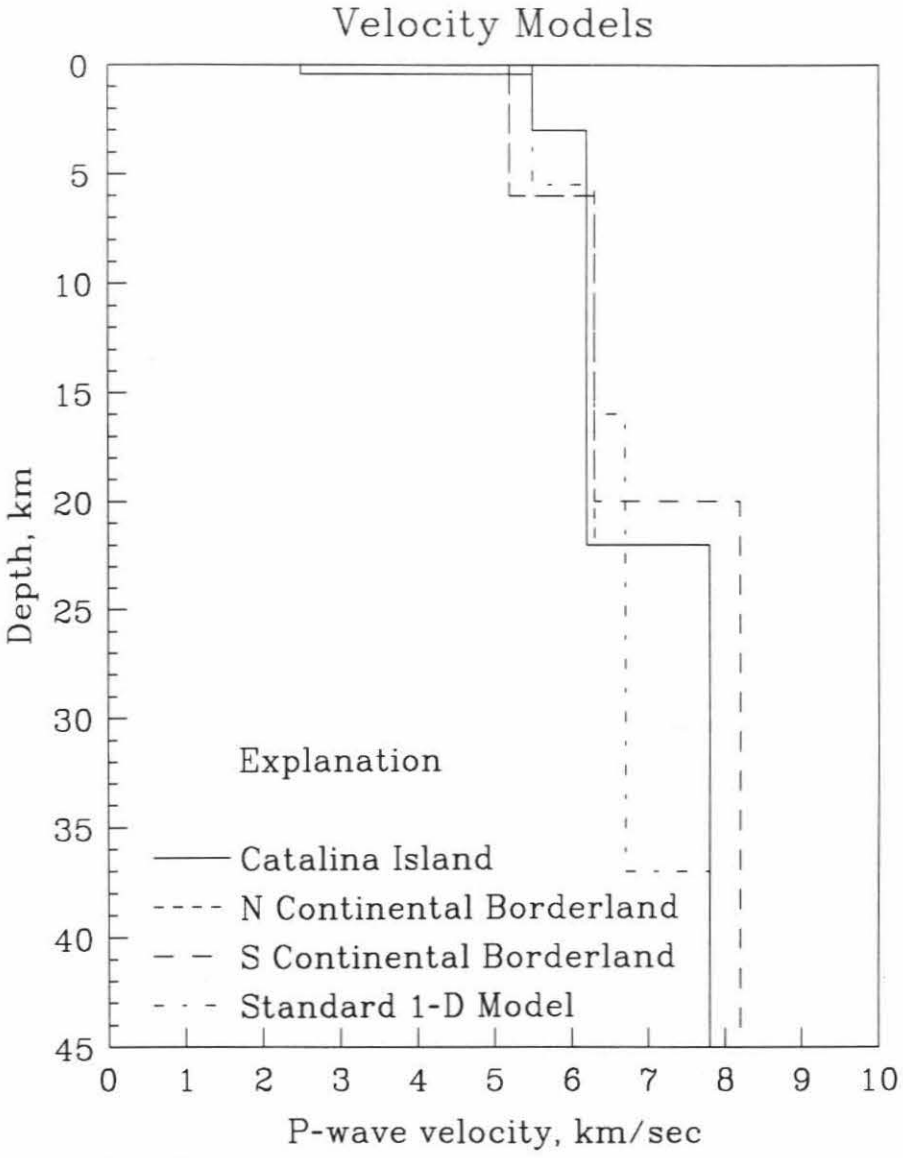

Figure 7.2 continued.

Table 7.2
Velocity Models

Los Angeles Basin		Santa Barbara Channel		Ventura Basin	
Velocity	Depth	Velocity	Depth	Velocity	Depth
2.65	0.0	2.00	0.0	2.00	0.0
2.90	0.4	2.19	0.5	2.20	0.5
3.40	1.0	3.23	1.5	3.23	1.0
4.00	1.5	4.90	4.0	4.90	3.0
4.50	2.1	6.36	8.0	6.40	8.0
5.50	3.0	7.01	12.0	7.00	16.0
6.40	4.0	8.33	22.0	8.00	26.0
6.80	26.0				
7.80	32.0				

Borrego Valley		Coast Ranges E of SAF		Coast Ranges W of SAF	
Velocity	Depth	Velocity	Depth	Velocity	Depth
2.50	0.0	2.85	0.0	2.40	0.0
5.10	0.5	3.34	0.5	3.80	1.5
6.00	3.0	4.62	1.5	5.50	2.1
7.10	14.0	5.62	3.0	6.00	4.0
7.90	25.0	6.00	4.0	6.15	8.0
		6.80	16.0	6.35	10.0
		8.05	25.0	6.55	20.0
				8.00	25.0

San Jacinto Valley		San Fernando Valley		Great Valley	
Velocity	Depth	Velocity	Depth	Velocity	Depth
2.29	0.0	2.90	0.0	2.85	0.0
5.30	0.5	3.40	1.0	4.14	3.0
5.80	1.5	4.00	1.5	4.41	4.0
6.20	6.0	4.90	2.1	5.77	6.0
6.80	16.0	6.10	3.0	6.16	8.0
7.80	32.0	7.00	14.0	6.43	12.0
		8.10	26.0	6.77	14.0
				7.25	20.0
				8.11	26.0

Mojave		East Mojave		San Gabriel Mountains	
Velocity	Depth	Velocity	Depth	Velocity	Depth
5.50	0.0	5.50	0.0	5.50	0.0
6.30	4.0	6.30	4.0	6.20	4.0
6.80	26.0	6.80	26.0	6.70	20.0
7.80	32.0	8.20	32.0	7.80	32.0
				8.30	42.0

Velocity is P-wave velocity in km/sec, Depth is depth to top of layer in km.

Table 7.2, continued
Velocity Models

San Bernardino Mtns		Little San Bernardinos		Imperial Valley	
Velocity	Depth	Velocity	Depth	Velocity	Depth
5.50	0.0	5.50	0.0	3.00	0.0
6.20	4.0	6.20	4.0	3.10	1.0
6.70	20.0	6.70	20.0	3.80	2.1
7.80	30.0	7.80	30.0	4.60	3.0
8.30	37.5			5.55	4.0
				5.80	6.0
				6.50	14.0
				7.30	16.0
				7.50	20.0
Coachella Valley		Santa Monica Mtns		Peninsular Ranges	
Velocity	Depth	Velocity	Depth	Velocity	Depth
3.00	0.0	3.00	0.0	5.50	0.0
3.10	1.0	6.10	0.5	6.40	4.0
3.80	2.1	6.80	14.0	6.80	26.0
5.50	3.0	8.10	30.0	7.90	32.0
6.20	8.0				
7.80	20.0				
Sierra Nevada		Tehachapi Mountains		Catalina Island	
Velocity	Depth	Velocity	Depth	Velocity	Depth
3.50	0.0	5.50	0.0	2.50	0.0
5.80	1.0	5.90	0.5	5.50	0.4
6.20	8.0	6.10	1.0	6.20	3.0
6.90	22.0	6.50	4.0	7.80	22.0
7.90	36.0	6.60	8.0		
		7.05	14.0		
		7.90	32.0		
North Cont Borderland		South Cont Borderland		Standard 1-D Model	
Velocity	Depth	Velocity	Depth	Velocity	Depth
5.20	0.0	5.20	0.0	5.50	0.0
6.30	6.0	6.30	6.0	6.30	5.5
7.80	22.0	8.20	20.0	6.70	16.0
				7.80	37.0

Velocity is P-wave velocity in km/sec, Depth is depth to top of layer in km.

data.

7.3 Calibrating the Three-Dimensional Velocity Model

The three-dimensional velocity model was calibrated by comparing travel times of explosions calculated by the model to the observed travel times. Explosions are useful because the origin times and locations are accurately known. In refraction studies, from which most of the one-dimensional models were taken, receivers may be placed on any type of surface material, including less competent material of low seismic velocities. In contrast, the seismograph stations that record earthquakes in southern California are generally placed on competent material with higher seismic velocities. The explosion calibration allows corrections to surface seismic velocities, or to any layer velocities that may have been interpreted incorrectly in a refraction study.

The calibration was done by examination of explosion travel time residuals (observed travel time minus calculated travel time). The three-dimensional model was improved by trial and error. Some of the constituent one-dimensional velocity models were discarded in favor of another model that produced lower residuals. A few new provinces were added to improve residuals that were consistently large over a coherent area. Some blocks along province boundaries were reassigned from one province to the adjacent province. For many source-receiver pairs it was possible to determine that a refractor within a province required an adjustment of velocity.

Three explosions, in Corona, Catalina, and the Whittier Narrows, were used (Figure 7.3). These explosions were chosen because they were in or nearby the Los Angeles basin, were widely recorded, and were accurately timed. Being close to the Los Angeles basin, the explosions can

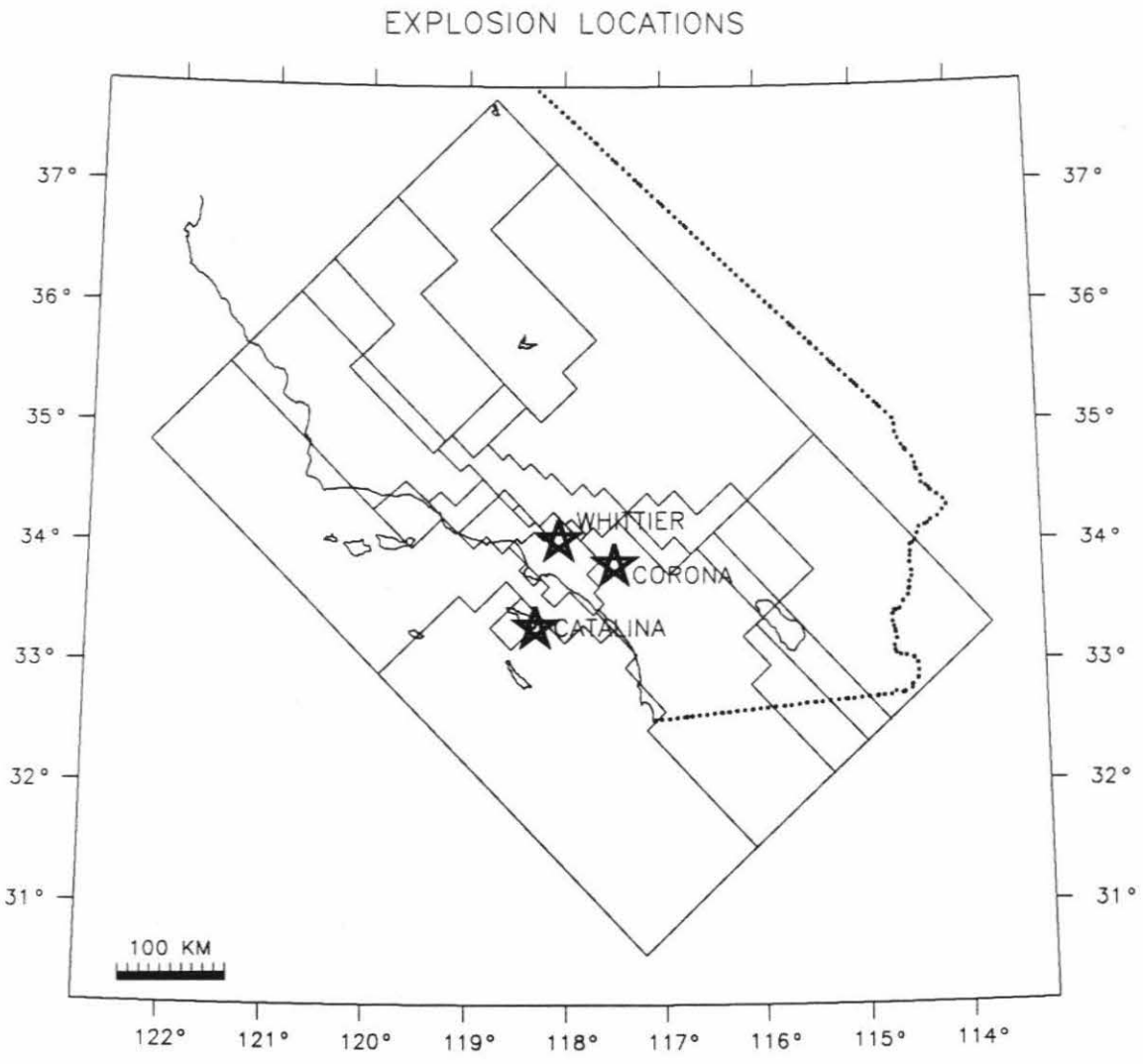

Figure 7.3 Locations of explosions used to calibrate three-dimensional model. Stars indicate explosion locations. Also shown are the velocity province boundaries and the outline of southern California.

contribute greatly to the calibration of the velocity provinces that contain the seismographs that most often record earthquakes occurring in the basin. The explosions are discussed individually below.

Most of the explosion arrival times used in the calibration were determined with an accuracy better than ± .1 sec. In areas of sparse station coverage some explosion arrival times picked with an accuracy of ± .3 sec were used. The earthquake location program downweights arrival times with large travel time residuals. The residual cutoff for downweighting is adjustable. The travel time residual rms and variances for the explosions given below incorporate weights calculated for identical residual cutoffs. The three-dimensional velocity model is compared to the standard one-dimensional used in routine earthquake locations. The standard one-dimensional model is based on Hadley and Kanamori (1977) and is shown in Figure 7.2 and Table 7.2.

Whittier Narrows explosion. On 8 November 1987, a small explosion was shot by the U.S.G.S. in the Whittier Narrows area to calibrate seismic velocities in the epicentral region of the 1 October 1987 Whittier earthquake (Perkins, 1988). The blast was recorded by nearby elements of the southern California seismic array and 60 portable seismometers deployed by the U.S.G.S. for the occasion. The explosion arrivals were timed interactively on a CRT (Hauksson, personal communication). The blast was within the Los Angeles basin province and was recorded as far as 100 km away in 10 velocity provinces.

The residuals of the Whittier blast for the three-dimensional velocity model and the standard one-dimensional velocity model are shown in Figure 7.4. The residuals of the standard model are large and positive, indicating

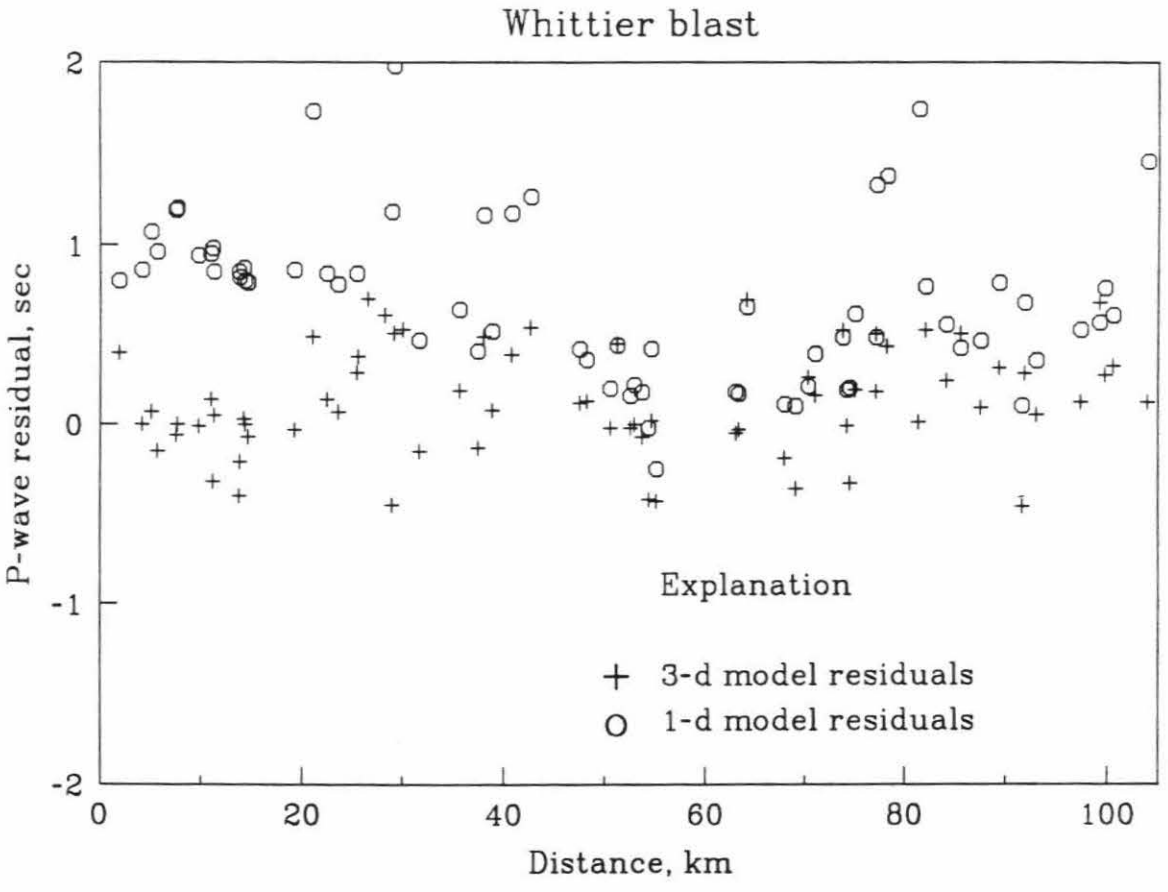

Figure 7.4 P-wave travel time residuals of the Whittier explosion calculated in the three-dimensional velocity model (crosses) and in the standard one-dimensional velocity model (circles). Note large positive residuals for the standard model, and small residuals of the three-dimensional model.

that the standard model is too fast with respect to the observed travel times. This is due in part to the lack of low velocity sediments in the standard model such as exist in the Los Angeles basin. About 70 per cent of the residuals of the three-dimensional model are less than .2 sec. The one-dimensional model has a travel time residual rms and variance of .771 sec and .170 sec^2 , respectively. The three-dimensional model rms and variance are .215 sec and .060 sec^2, respectively, representing a variance reduction of 65 per cent.

Corona explosion. This very large explosion was fired in a quarry on 10 January 1975. It was recorded by 70 permanent seismometers of various institutions and 25 portable seismometers deployed by Kanamori (written communication). The portable seismometers used high speed paper recorders with radio time signals for extremely accurate arrival time readings. The explosion was in the Peninsular Ranges province and was recorded out to 400 km in 16 velocity provinces.

Figure 7.5 shows the Corona explosion residuals for the three-dimensional model and the standard one-dimensional model. Both models show scatter in the residuals, but the three-dimensional model less so, especially within about 150 km. Residuals of the three-dimensional model are smaller than the residuals of the standard model at all distances. Travel time residual rms and variance of the standard model are .330 sec and .209 sec^2, respectively, versus .207 sec and .127 sec^2 for the three-dimensional model, a variance reduction of 40 per cent. This explosion was used by Kanamori (written communication) to define the velocity model used in the current work for the Peninsular Ranges province.

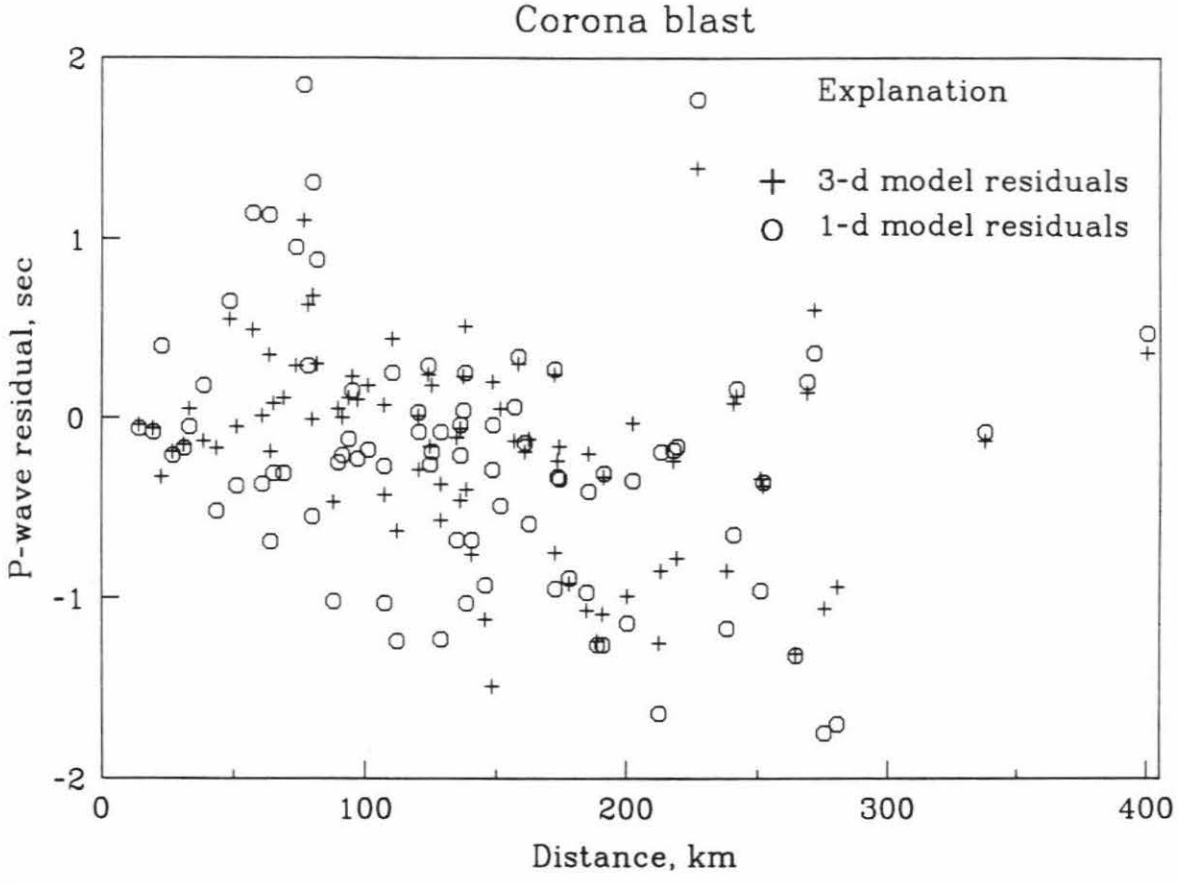

Figure 7.5 P-wave travel time residuals of the Corona explosion calculated in the three-dimensional velocity model (crosses) and in the standard one-dimensional velocity model (circles). Note scatter of residuals for both models, but overall lower residuals for three-dimensional model. See text for discussion.

Catalina explosion. This very large blast was detonated in a quarry on Catalina Island on 8 November 1981. It was recorded by the southern California seismic array and a few portable seismometers deployed on the island. The arrivals were timed interactively on a CRT (Given and Koesterer, 1983). The blast occurred in the Catalina Island province and was recorded out to 300 km in 19 velocity provinces.

The Catalina explosion residuals are shown in Figure 7.6. Again, residuals calculated in both the three-dimensional and one-dimensional velocity models have scatter, but those of the three-dimensional model have less. Residuals of the three-dimensional model are smaller than the residuals of the standard model at all distances. The residuals of the standard model are mostly negative, indicating that the standard model is too slow with respect to the observed travel times. Travel time residual rms and variance in the standard model are .529 sec and .353 sec^2, respectively, and .507 sec and .240 sec^2 for the three-dimensional model, a 32 per cent reduction of the variance. Corbett (1984) used this blast to define the velocity models of the Catalina Island and north and south Continental Borderland provinces used in the current work.

7.4 Discussion

The results of locating Los Angeles basin earthquakes using the three-dimensional velocity structure of southern California are presented in Chapter 8. There it is shown that the variance of P-wave travel time residuals for 1055 Los Angeles basin earthquakes relocated in the three-dimensional model is 47 per cent smaller than for the standard locations. The calibrated three-dimensional model is a vast improvement over the standard one-dimensional

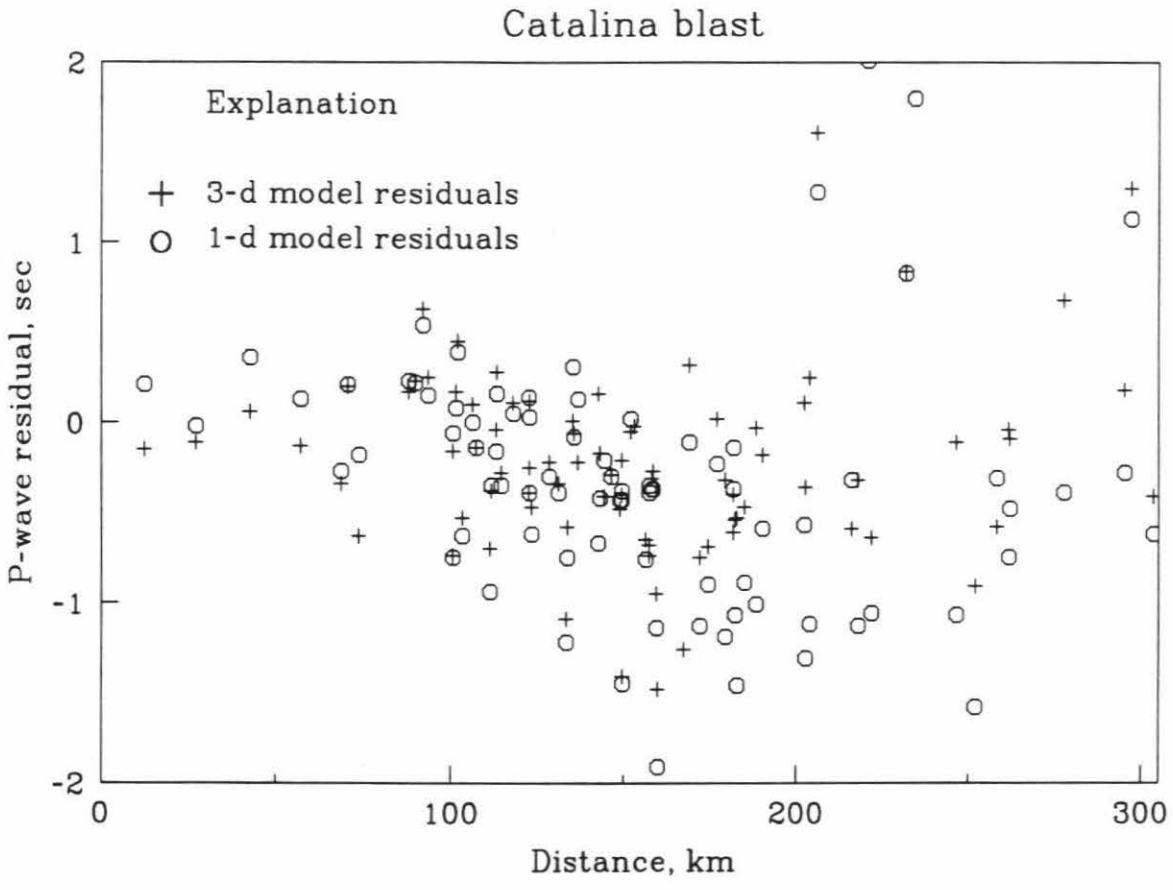

Figure 7.6 P-wave travel time residuals of the Catalina explosion calculated in the three-dimensional velocity model (crosses) and in the standard one-dimensional velocity model (circles). Note scatter of residuals for both models, but overall lower residuals for three-dimensional model. See text for discussion.

model, but it has some problems. Some areas have very few seismograph stations and so cannot be adequately calibrated. An example is the continental borderland region, a large area of complicated geology adjacent to the Los Angeles basin. The other velocity provinces near the Los Angeles basin that contain most of the seismographs that commonly record earthquakes occurring in the basin have adequately calibrated upper crustal layers. It is more difficult in the forward modeling to assign errors in the lower crust. To sample the lower crust, widely spaced source-receiver combinations spanning more than one velocity province must be used. The contributions to travel time residuals from the basement rocks under the Los Angeles basin are difficult to sort out from contributions from adjacent provinces.

The calibration explosions do not sample much of the upper layers of the velocity provinces far from the Los Angeles basin because the seismic rays refract along the lower crustal or Moho layers. Moho arrivals generally have large residuals in the three-dimensional model (Figures 7.4, 7.5, and 7.6). The Moho depth and velocity vary widely in the three-dimensional model (Table 7.2) and the approximate ray tracing scheme used by the location program does not handle the Moho well. Also, the explosion arrivals are harder to pick at P_n distances.

These problems will be addressed in Chapter 9, where the three-dimensional velocity forward model will be used as an initial model in an inversion of earthquake and explosion travel time data to produce a refined three-dimensional model. The earthquakes used in the inversion are well distributed over southern California, so nearly all the upper crustal blocks of the velocity model are sampled.

The three-dimensional velocity model for southern California constructed here is expressed as blocks, each block having a given velocity. It is the first three-dimensional velocity model of southern California that has actually been used to locate earthquakes. The model could be recast from a block model to, say, a model that specifies velocities at nodes. A node velocity model could be used in an earthquake locating program utilizing true ray-tracing or in a finite difference program (Vidale, 1989). Thus the three-dimensional model should be useful in any earthquake location scheme.

Chapter 8

Earthquake Locations in the Three-Dimensional Velocity Model

8.1 Introduction

In this chapter the three-dimensional crustal velocity model developed in Chapter 7 is used to relocate earthquakes in the Los Angeles basin. The improved earthquake locations and focal mechanisms help to define seismogenic structures that are difficult to map from the surface of the earth.

Previous studies of the velocity structure of the southern California crust (*e.g.*, Hearn, 1985, Hadley, 1978) recognized the lateral variations of seismic velocity. Recent studies of earthquakes in the Los Angeles basin (Hauksson, 1987, Hauksson and Jones, 1989) have attempted to correct for the presence of the thick sequence of seismically slow sediments not accounted for in standard one-dimensional velocity models by using hybrid one-dimensional models. Elsewhere in California, workers have developed three-dimensional models of small areas (*e.g.*, Michelini *et al.*, 1989, for Parkfield and Eberhart-Phillips, 1989, for Coalinga). The current work is the first three-dimensional velocity model of all of southern California.

First, ≈1000 earthquakes lying in a band from Palos Verdes to the San Andreas fault are relocated to show the improvement of earthquake locations in the three-dimensional model relative to a standard one-dimensional model. Also, these earthquake relocations are compared to the structural cross section constructed by Davis (1987) and Davis *et al.* (1989) based on the notion of Los Angeles basin as a fold and thrust belt. Then, several larger, recent

earthquakes and their aftershocks are relocated. These are the 1987 M_L 5.9 Whittier earthquake, the 1988 M_L 4.9 Pasadena earthquake, the 1989 M_L 4.5, 4.3 Montebello earthquakes, and the 1989 M_L 5.0 Malibu earthquake. The relocations reveal interesting details about the structures on which these earthquakes occurred.

8.2 Data and Method

The earthquakes were recorded on the Caltech-USGS seismic network in southern California. Routine processing (Given *et al.*, 1986) of the recorded events produced the P- and S-wave arrival times and first motions used here. During this processing, hypocenters are determined and archived. These hypocenters are called the catalog locations. The catalog locations were calculated in the standard one-dimensional velocity model based on the results of Hadley and Kanamori (1977). That model is shown in Table 7.2 and Figure 7.2.

The earthquakes are relocated in the three-dimensional structure constructed in Chapter 7 using the program REL3D written by Roecker and co-workers (Roecker 1981, 1982, Shedlock 1986, Shedlock and Roecker 1987, Roecker *et al.*, 1987). Details of the code are discussed in their papers. The form of the three-dimensional velocity model and some aspects of the location code were discussed in Chapter 7. The version of the code used here was modified to include the ability to downweight arrivals from stations beyond a given distance (S. Roecker, personal communication) and to use a data format compatible with the format that the network data are stored in (C. Jones, personal communication). The distance downweighting is specified as a distance at which an arrival is given a weight of e^{-1} the weight of an arrival

from zero distance. Between zero and the cutoff distance, the downweighting is nearly linear, and beyond the cutoff distance, the weight drops quickly to nothing. The cutoff distance used here is 100 km. This number was determined from Figures 7.4, 7.5, and 7.6, which show that the calibration explosion travel times are best fit by the three-dimensional model at distances out to about 100 km. Arrivals with large residuals are also downweighted in a similar way. (A travel time residual is the observed travel time minus the travel time calculated in a given model). The residual cutoff is set from 3 to 1 sec for the first to last iteration. S-wave arrivals are given one-half the weight of P-wave arrivals, and a V_p / V_s ratio of 1.73 is assumed. No station delays are used.

When the southern California array data are processed, the arrival time picks are assigned qualities according to the maximum error in the timing of the pick. The qualities and maximum timing errors are shown in Table 8.1. The location program REL3D, and the program HYPIT used for inversion of earthquake travel times for velocity structure in Chapter 9, use arrival time weights as though the weights were inversely proportional to the variance of the arrival time errors. To calculate the actual weights used in the location program (Table 8.1), it is here assumed that the maximum errors correspond to the standard deviation of the arrival time errors. The lowest maximum error, .02 sec, is the absolute arrival time picking accuracy determined by the array digitization rate. The actual weight used for that quality pick assumes a maximum error of .03 sec, a realistic value that avoids overweighting the best quality picks. All statistics given below were calculated with the same arrival time weighting scheme.

Table 8.1
Arrival Time Weights

Arrival quality	Maximum error, *sec*	Weight used in 3D codes
0	.02	1111
1	.05	400
2	.10	100
3	.30	11
4	$>.30$	0

It is assumed that the assigned maximum timing errors are standard deviations, σ, of the timing errors. For quality 0 the weight used assumed a maximum error of .03 sec instead of .02 sec. The weights used in the three-dimensional codes are $(\sigma^2)^{-1}$.

Focal mechanisms are determined for some earthquakes that have more than 15 first motions by the grid searching program FPFIT (Reasenberg and Oppenheimer, 1985) after correcting the polarities of reversed seismometers with the information of Norris *et al.* (1986).

8.3 Results

Improvement of earthquake locations in the three-dimensional velocity model. 1055 earthquakes of all magnitudes whose catalog locations are within a 45 km wide band from Palos Verdes to the San Andreas fault (Figure 8.1) were relocated in the three-dimensional velocity model. The earthquakes occurred between 1983 and 1987, and include the 1987 Whittier sequence, discussed in more detail below. Most of the earthquakes are in the Los Angeles basin, with the rest in the San Gabriel Mountains and offshore. The relocations are useful to judge the improvement of earthquake location quality in the three-dimensional model over the standard one-dimensional model.

Figure 8.1 shows the new locations of the band of earthquakes. Earthquakes relocated in the three-dimensional model cluster more tightly along the Newport-Inglewood and San Andreas faults, and the Whittier sequence is more compact, with a more sharply defined aftershock zone. (The epicenter alignments along the San Andreas fault are interesting because they do not lie on the surface trace of the fault. They are not on the Punchbowl fault, which is east of 118^{o}.) Cross sections of the earthquake locations are shown in Figures 8.2a. Again, earthquakes along the San Andreas fault cluster more tightly and the Whittier sequence is more compact in the three-dimensional relocations. The Newport-Inglewood fault does not appear clearly in the cross section because the cross section intersects that fault at a

Figure 8.1. (Following page.) Left, 1055 earthquake locations from the Caltech catalog from 1983 to 1987. Right, the same earthquakes relocated in the three-dimensional velocity model. All magnitude earthquakes are plotted with the same size symbol. The 1987 Whittier earthquake sequence, discussed in the text, is the cluster centered at $34^o\ 3'$, $118^o\ 6'$. AA' is the location of the cross section of Figure 8.2. Abbreviations: SAF, San Andreas fault, SGF, San Gabriel fault, SMF, Sierra Madre fault, SM-RF, Santa Monica-Raymond fault, WF, Whittier fault, NIF, Newport-Inglewood fault, PVF, Palos Verdes fault.

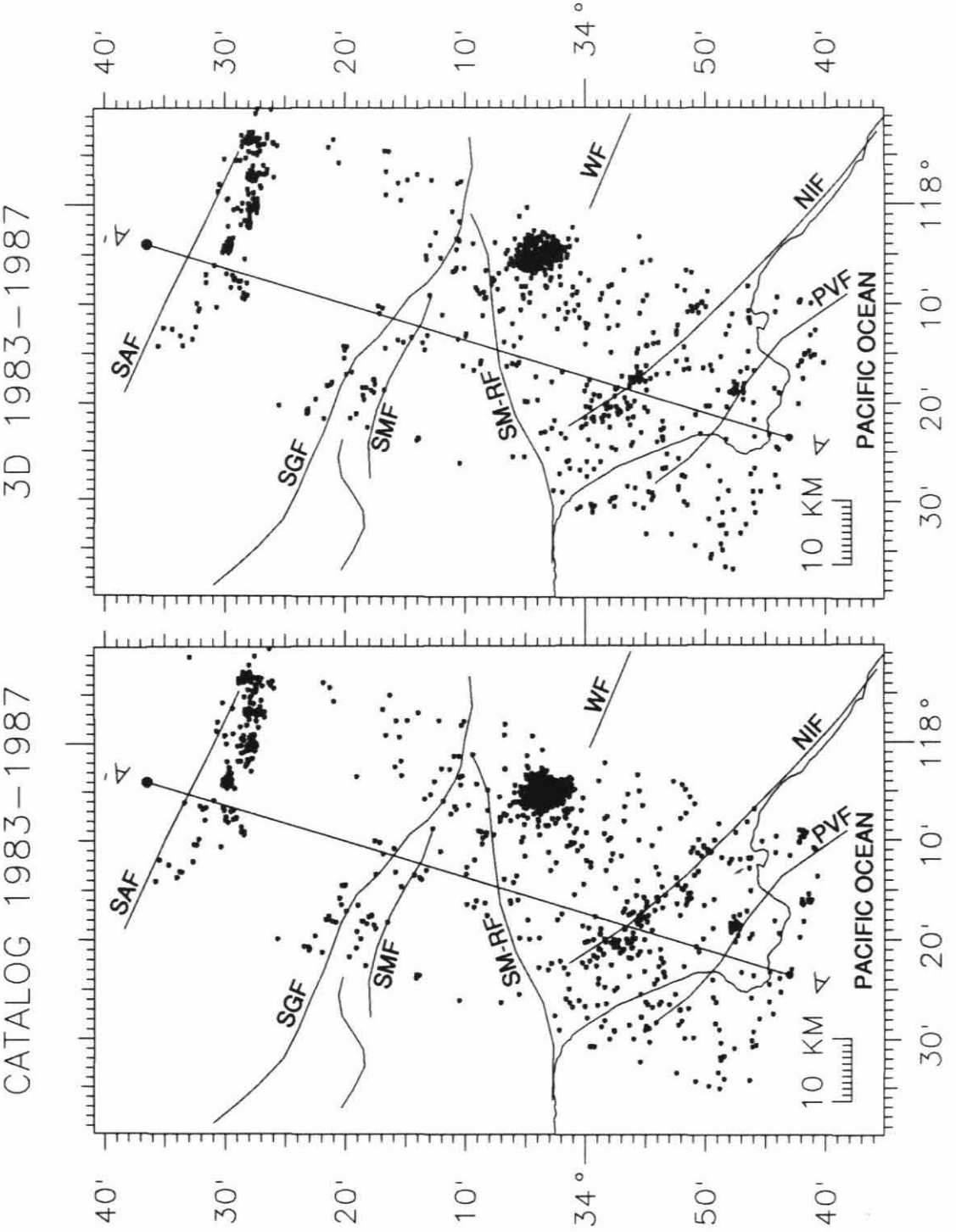
CATALOG 1983–1987
3D 1983–1987
SAF
SGF
SMF
SM-RF
WF
NIF
PVF
PACIFIC OCEAN
10 KM
40'
30'
20'
10'
34°
50'
40'
30'
20'
10'
118°

low angle and because of the more diffuse seismicity associated with that fault compared to the San Andreas fault. The line of hypocenters at 6 km depth in the catalog location cross section is due to the fixed depth of poorly constrained earthquakes.

To compare the catalog locations, locations found in the standard one-dimensional model, and locations found in the three-dimensional model, the earthquakes in Figure 8.1 were relocated in both velocity models using REL3D and the distance and residual cutoffs described above. First, the earthquakes were held fixed at their catalog locations to determine the travel time residuals of the catalog locations in the standard one-dimensional model. The variance of the P-wave travel time residuals for the catalog locations is .06876 sec^2. Next, the earthquakes were allowed to move as they were relocated in the one-dimensional model. In this case, the variance of the P-wave travel time residuals is .05107 sec^2. Finally, the earthquakes were relocated in the three-dimensional model. The variance of the P-wave travel time residuals is .03620 sec^2, a reduction of 29 per cent from the relocations in the one-dimensional model and 47 per cent from the catalog locations. Recall from Chapter 7 that the three-dimensional model was calibrated using P-waves only, and a fixed V_p / V_s was used to determine the S-wave velocity structure. However, similar improvements in the variance of the S-wave travel time residuals (17 and 48 per cent) were found. The three-dimensional velocity model is a clear improvement for the location of earthquakes in and around the Los Angeles basin.

Earthquakes along a structural cross section. Davis *et al.* (1989) have constructed a retrodeformable structural cross section through the Los Angeles basin from Palos Verdes to the San Andreas fault. They use stratigraphic

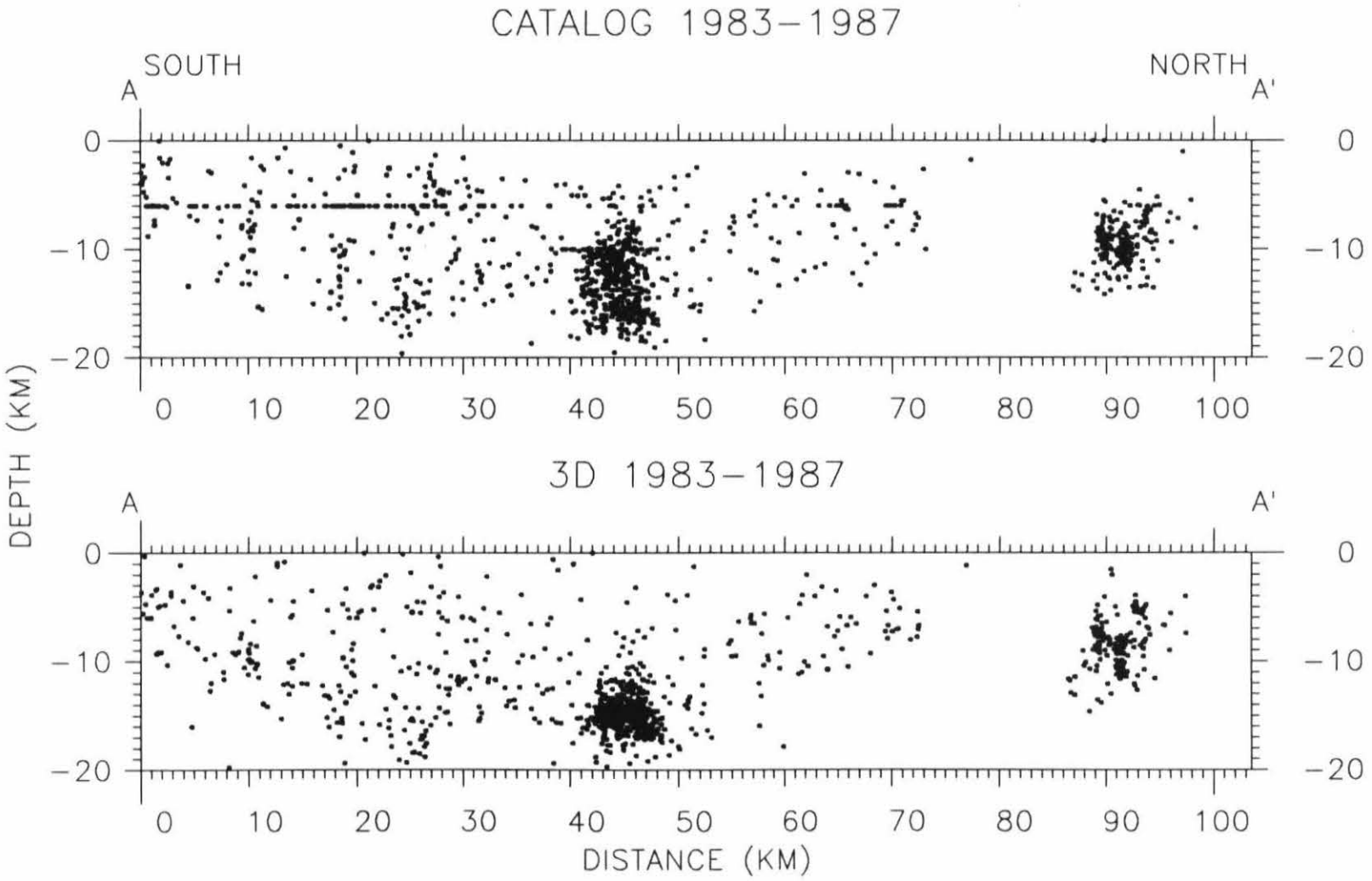
CATALOG 1983–1987
SOUTH
NORTH
A
A'
0
−10
−20
0
10
20
30
40
50
60
70
80
90
100
3D 1983–1987
A
A'
DEPTH (KM)
DISTANCE (KM)

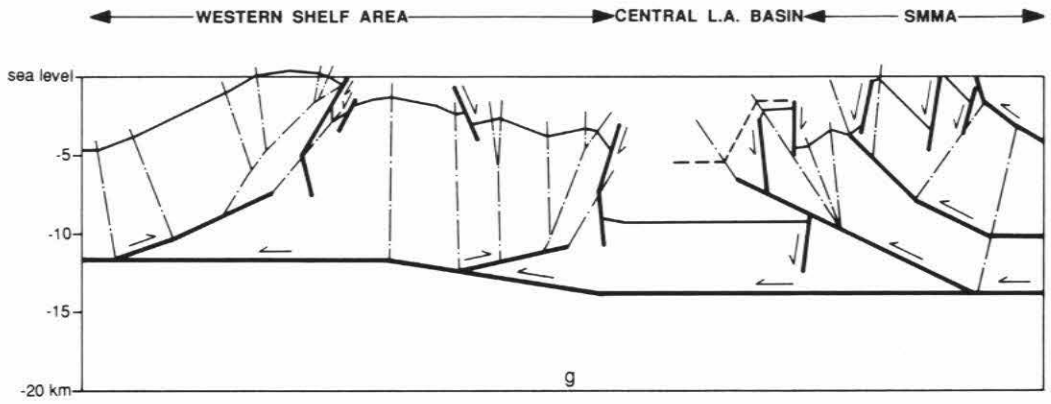

Figure 8.2a. (Previous page). The earthquakes of Figure 8.1 projected onto the plane AA'. Top are the catalog locations and bottom are the three-dimensional relocations. All magnitude earthquakes are plotted with the same size symbol. The 1987 Whittier earthquake sequence, discussed in the text, is the cluster centered at km 45.

Figure 8.2b. (Above). Figure 4g from Davis *et al.*, (1989), a simplified version of their Plate 1. Heavy lines are top of basement. Left side of figure coincides with left side of Figure 8.2a. Abbreviation: SMMA, Santa Monica Mountains anticlinorium.

and structural data to interpret the Pliocene to Quaternary deformation as a developing fold and thrust belt. This interpretation requires thrust ramps splaying off a master detachment underlying the Los Angeles area. The structural cross section has proved very useful in providing a framework for interpretation of the tectonics of the Los Angeles basin (*e.g.*, Hauksson and Stein, 1989). Figure 8.2b is a reproduction of the structural cross section by Davis *et al.* (1989, Figure 4g). The seismic cross section in Figure 8.2a corresponds in location to the structural cross section. It is of interest to compare the seismic cross section to the structural cross section.

Away from the Whittier sequence and the San Andreas fault, the background seismicity in the cross section is diffuse. There is no correspondence of the background seismicity to the buried thrust faults of the structural cross section. Overall, near the Los Angeles basin, the maximum depth of earthquakes is greater than the depth of the detachment surface. The maximum depth of earthquakes varies from about 12 km at the south end of the cross section to nearly 20 km at 25 km north of the south end of the seismic cross section. This deepening of earthquakes corresponds to a deepening of the inferred detachment from 11.5 to 14 km depth. There are few earthquakes in the sediments of the central Los Angeles basin. Under the central basin the deepest earthquakes are only 15 km deep while the detachment remains flat at 14 km. The Whittier sequence occurs at a major north dipping blind thrust fault in the structural cross section, but the earthquakes are deeper than the fault and extend beneath the detachment. The sense of slip of the Whittier earthquake agrees with the structural cross section. Another structural cross section (Figure 9 in Davis *et al.*, 1989) places the thrust fault deeper and so agrees well with the Whittier earthquake

depths, but the rapid change in depth of the thrust fault and detachment from the nearby cross section of Figure 4g of Davis *et al.* is not explained. There are few earthquakes under the San Gabriel Mountains. The maximum depth of seismicity near the San Andreas fault (14 km) agrees with the depth of the detachment.

Davis *et al.* (1989) suggest that the master detachment underlying the Los Angeles basin may correspond to the brittle-ductile transition in the crust. The depth of the detachment is inferred from geometric constraints imposed by fold shapes observed at and near the surface. The maximum depth of seismicity presumably corresponds to the brittle-ductile transition. The deeper earthquakes in Figure 8.2a are below the depth of the detachment, suggesting the detachment is too shallow. Alternatively, the detachment may not extend under the Los Angeles basin (a possibility permitted by Davis *et al.*, 1989), or the detachment does not correspond to the brittle-ductile transition.

Large thrust events such as the Whittier and San Fernando earthquakes imply the existence of thrust faults under the Los Angeles basin. Hauksson (1988) has determined thrust focal mechanisms for many $M_L \geq 2.5$ earthquakes in the Los Angeles basin and has defined in map view two broad east-west trending bands containing those earthquakes. It may be that each band consists of numerous small thrust faults difficult to image with the background seismicity in a single cross section. The earthquake locations in the three-dimensional velocity model do image the thrust fault on which the Whittier earthquake occurred, which may indicate that small earthquakes do not occur on the deep thrust faults except as aftershocks following larger thrust earthquakes.

Whittier earthquake. The 1 October 1987 M_L 5.9 Whittier earthquake was a deep thrust event in the Los Angeles basin. It was followed by both thrust and strike-slip aftershocks. The causative thrust fault does not extend to the surface, but had been inferred from fold structures observed at the surface (Davis, 1987). No surface rupture was observed (Hauksson *et al.*, 1988). The hypocenter relocations in the three-dimensional velocity model presented here define the structures on which the mainshock and aftershocks occurred. The Whittier sequence locations and focal mechanism parameters are listed in Table 8.2. Hauksson and Jones (1989) have presented a detailed analysis of the Whittier sequence using a data set similar to that used here.

Figure 8.3 is a map showing the Whittier sequence from 1 October 1987 to 1 December 1988. Note the small area of the aftershock zone (about 6 by 7 km) and the uneven distribution of aftershocks. Few events are in the middle of the aftershock zone, as if the high stress drop mainshock (Bent and Helmberger, 1989) had broken that area cleanly. Many aftershocks are along the west side of the aftershock zone, and fewer are along the east side. Interestingly, some aftershocks approach the location of the 3 December 1988 Pasadena earthquake (Figure 8.7). Also, a small (M_L 2.7) aftershock on 12 April 1988 occurred at the future location of the 12 June 1989 Montebello earthquakes (Figure 8.11).

Figure 8.4 shows cross sections of the sequence east and west of longitude $118^o 5'$. In the eastern cross section, the depth range of earthquakes is small, from 14 to 17 km. Note the mainshock at 14.5 km depth. The main thrust plane can be defined by the rough alignment of hypocenters dipping north from the mainshock. This alignment is nearly parallel to the north dipping plane of the mainshock focal mechanism (Figure 8.5). In the western cross

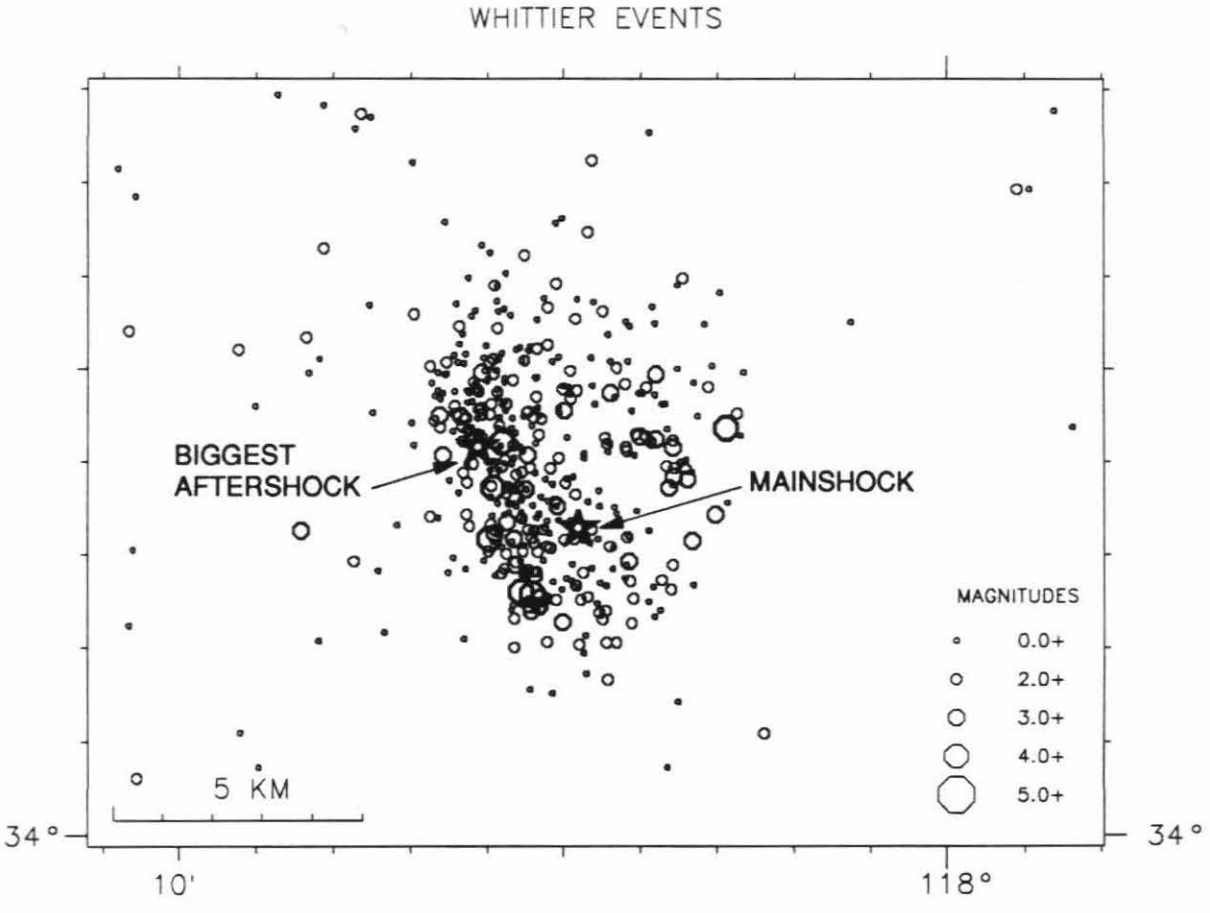

Figure 8.3. Earthquakes of the Whittier sequence from 10/1/87 to 12/1/88. Note mainshock and largest aftershock (stars), and uneven distribution of earthquakes, with more events on the west side of the aftershock zone. Earthquake symbol size is proportional to earthquake magnitude. Earthquake locations are listed in Table 8.2.

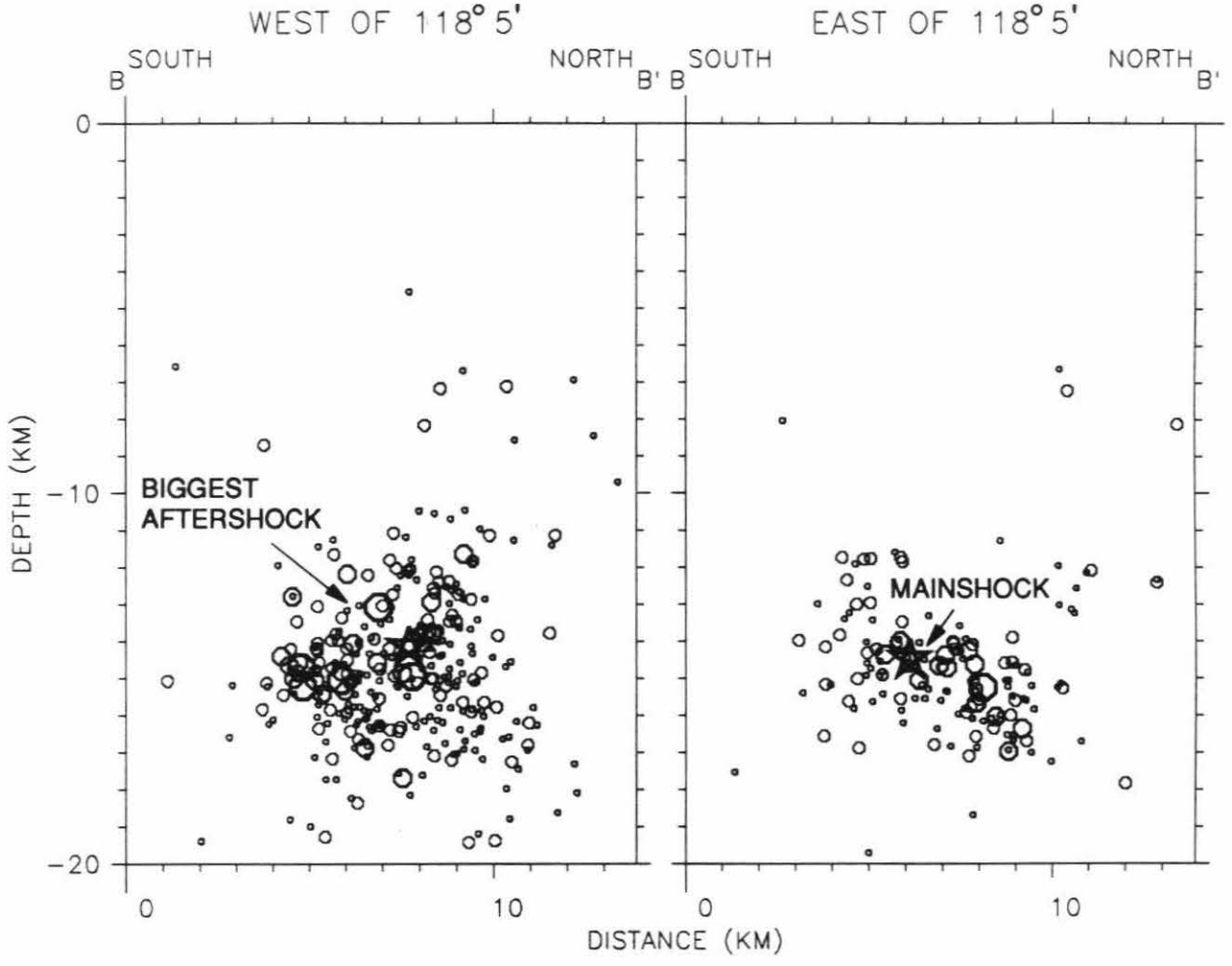

Figure 8.4. The earthquakes of Figure 8.3 in north-south cross section, west (left), and east (right) of 118° 5′. Note mainshock and largest aftershock (stars), and the narrower depth range of the eastern events compared to the western events. Earthquake symbol size is proportional to earthquake magnitude.

section the depth range of earthquakes is larger, from 11 to 17 km. Note the largest aftershock, a M_L 5.3 strike-slip event, at 14 km depth. The difference in depth range between the cross sections is due to the presence of a near vertical strike-slip fault along the west side of the aftershock zone.

Figures 8.5 and 8.6 respectively show thrust and strike-slip focal mechanisms of $M_L \geq 2.5$ events of the Whittier sequence. The mainshock was a thrust event (Figure 8.5) on a 20° north dipping plane striking 230°. This plane is similar to that defined by the hypocenter alignment in the eastern cross section of Figure 8.4. Many aftershocks have thrust mechanisms similar to the mainshock. Southwest of the mainshock are several events that were thrusts on north-south striking planes. The largest aftershock was a right-lateral strike-slip event (Figure 8.6). The strike-slip aftershocks have an organized distribution suggesting that they lie along vertical, or near vertical, fault planes. South of the largest aftershock (and the north-south oriented thrusts) are left-lateral strike-slip mechanisms. The right-lateral and left-lateral strike-slip mechanisms define a single fault plane along the west side of the mainshock thrust plane. Few thrust events occur to the west of the strike-slip fault plane. To stay consistent with the sense of motion on the thrust plane, the sense of displacement on the strike-slip fault changes as it passes from the hanging wall to the foot wall of the thrust. There is a space problem where right-lateral meets left-lateral that is solved by the odd north-south oriented thrust mechanisms. These represent east over west motion on the shallowly east-dipping planes. One of these was an M_L 4.7 event, one of the largest aftershocks. Another strike-slip structure may be represented by the large, M_L 4.7, easternmost strike-slip aftershock on 11 February 1988. It is hard to determine which of the focal planes is the active fault.

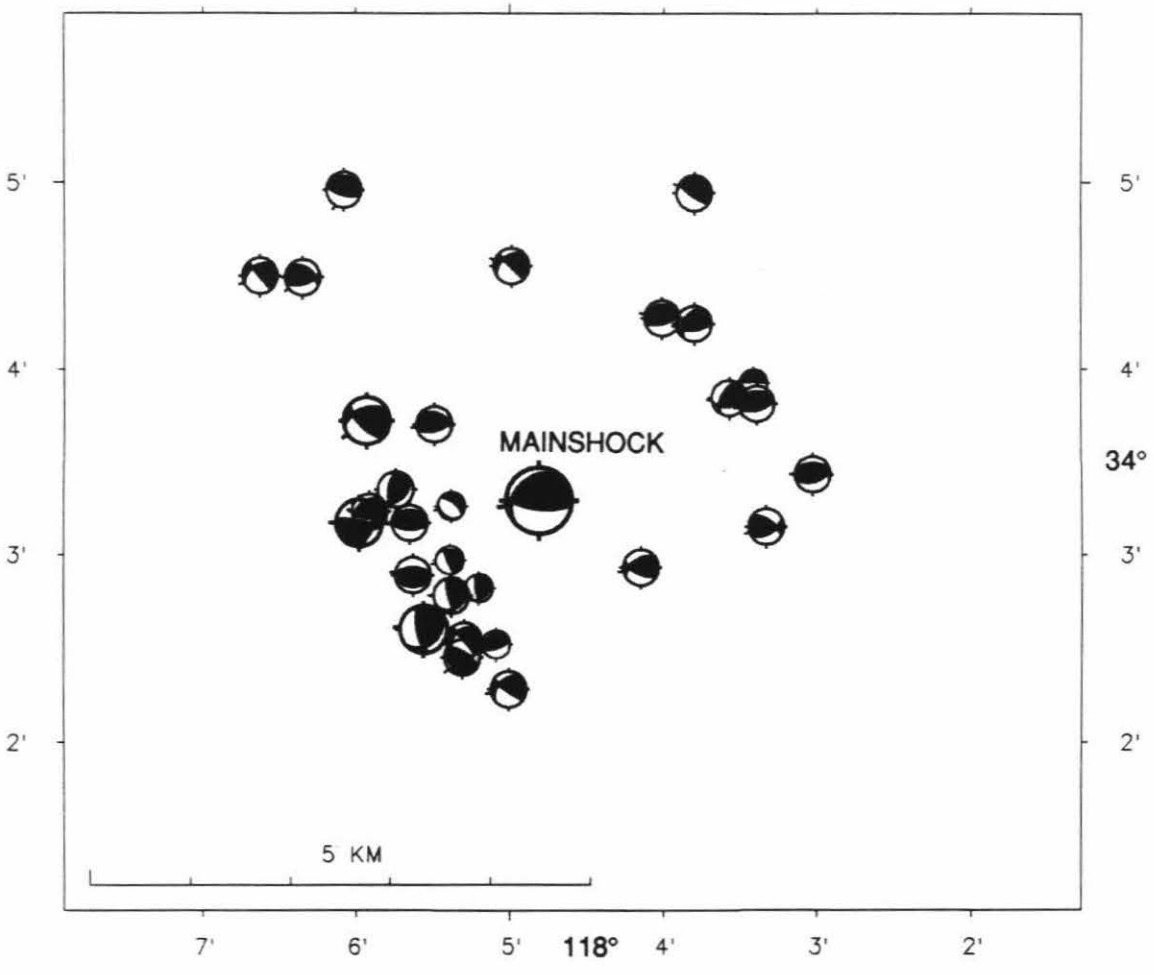

Figure 8.5. Focal mechanisms (lower hemisphere, compressional quadrants shaded) of $M_L \geq 2.8$ thrust events from 10/1/87 to 11/23/88. Note mainshock. Focal parameters are listed in Table 8.2. Earthquake symbol size is proportional to earthquake magnitude.

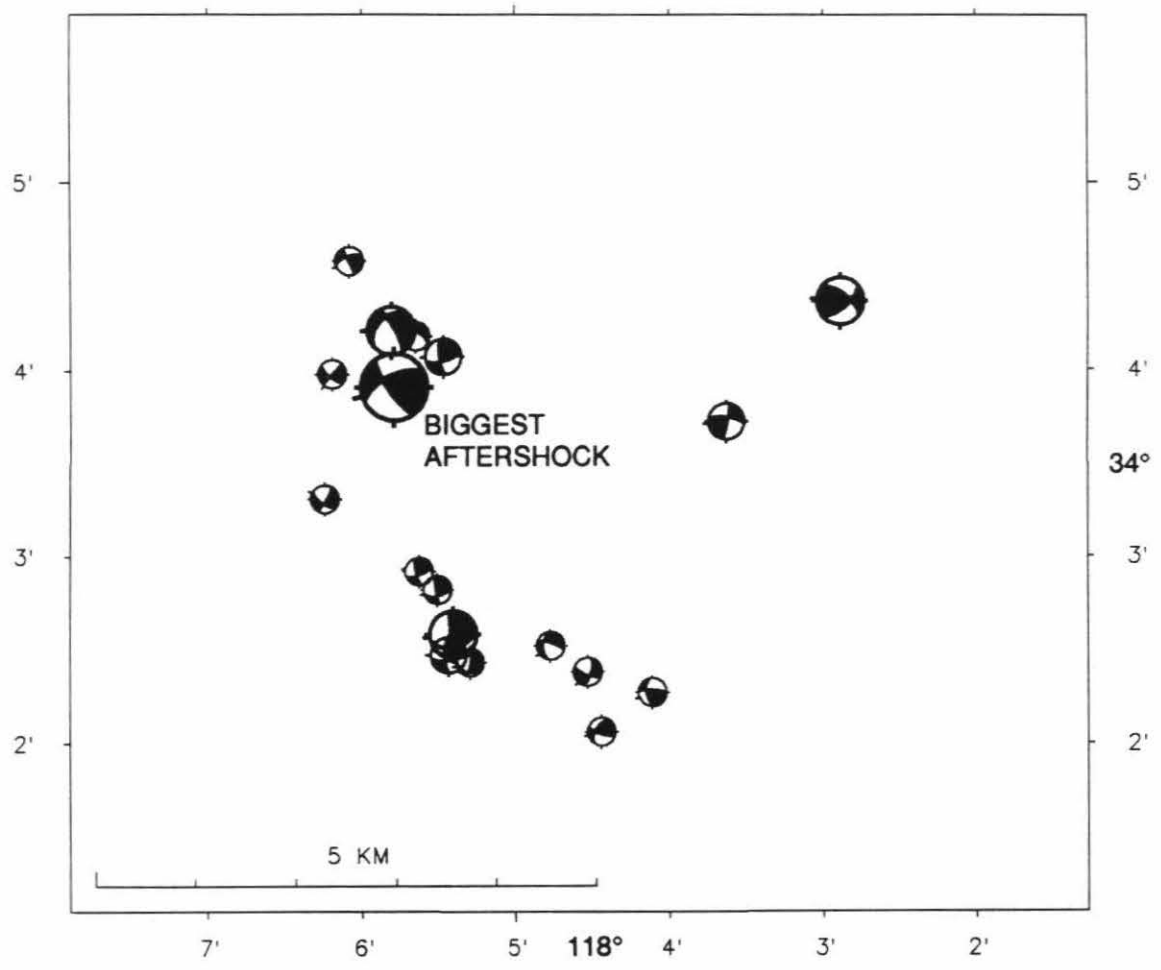

Figure 8.6. Focal mechanisms (lower hemisphere, compressional quadrants shaded) of $M_L \geq 2.5$ strike-slip events from 10/1/87 to 11/23/88. Note largest aftershock. Focal parameters are listed in Table 8.2. Earthquake symbol size is proportional to earthquake magnitude.

Table 8.2

$M_L \geq 2.5$ Whittier Earthquakes

Yr-Mo-Da	HrMn	Sec	Lat		Long		Depth	Mag	rms	npick	Ddir	Dip	Rake
87-10- 1	1442	19.6	34	3.29	118	4.81	14.5	5.9	0.19	97	185	70	110
87-10- 1	1445	41.3	34	3.17	118	5.98	15.1	4.7	0.10	26	10	85	130
87-10- 1	1448	2.8	34	4.21	118	5.81	14.9	4.1	0.13	43			
87-10- 1	1449	5.8	34	3.72	118	5.93	13.1	4.7	0.10	37	225	65	130
87-10- 1	1451	28.9	34	4.55	118	4.99	16.0	3.6	0.17	59	225	85	130
87-10- 1	1452	18.7	34	4.15	118	3.58	14.3	3.2	0.05	11			
87-10- 1	1454	14.3	34	5.21	118	9.23	20.1	2.5	0.00	2			
87-10- 1	15 5	34.1	34	3.35	118	5.74	14.1	3.0	0.18	59	135	40	120
87-10- 1	15 8	7.5	34	2.45	118	5.31	12.8	3.2	0.15	38	235	25	-70
87-10- 1	1512	31.3	34	2.60	118	5.56	15.2	4.7	0.22	97	135	35	140
87-10- 1	1513	59.0	34	2.40	118	5.42	14.6	3.2	0.13	28			
87-10- 1	1517	46.3	34	2.89	118	5.63	15.4	3.4	0.19	83	180	35	90
87-10- 1	1518	35.3	34	3.73	118	5.74	15.5	2.5	0.05	7			
87-10- 1	1520	2.5	34	3.81	118	3.39	14.4	3.0	0.14	67	165	60	80
87-10- 1	1522	21.0	34	2.28	118	5.01	14.4	3.2	0.17	75	215	80	130
87-10- 1	1525	40.7	34	3.92	118	3.41	14.0	2.9	0.14	51	230	10	-40
87-10- 1	1526	29.0	34	3.52	118	5.08	16.9	3.2	0.02	6			
87-10- 1	1526	47.9	34	3.26	118	5.38	14.2	2.8	0.13	49	220	20	-90
87-10- 1	1529	46.9	34	3.70	118	5.49	14.6	3.1	0.14	65	165	60	70
87-10- 1	1536	1.2	34	2.38	118	4.53	12.4	2.5	0.13	43			
87-10- 1	1539	48.9	34	3.26	118	5.90	15.9	2.5	0.08	16			
87-10- 1	1544	36.8	34	2.06	118	4.44	14.2	2.5	0.12	29			
87-10- 1	1548	31.5	34	4.27	118	3.92	15.3	2.7	0.13	28	135	65	70
87-10- 1	1554	36.7	34	4.07	118	5.47	14.9	3.0	0.14	59			
87-10- 1	1557	42.8	34	2.53	118	4.09	15.0	2.5	0.08	36	165	55	70
87-10- 1	1558	15.3	34	2.52	118	5.09	13.5	2.8	0.12	47	160	65	100
87-10- 1	1559	53.2	34	2.58	118	5.41	14.7	4.0	0.18	83			
87-10- 1	1614	54.2	34	5.54	118	4.84	15.3	2.5	0.02	6			
87-10- 1	1619	16.6	34	2.92	118	5.63	15.5	2.9	0.13	31			
87-10- 1	1621	10.6	34	4.94	118	3.80	16.4	3.4	0.15	82	215	75	100
87-10- 1	1632	50.5	34	3.43	118	3.03	15.1	3.0	0.12	66	165	55	80
87-10- 1	1633	33.0	34	2.54	118	5.30	14.6	3.3	0.23	78	50	90	-130
87-10- 1	1639	33.0	34	3.26	118	8.42	12.2	3.0	0.09	4			
87-10- 1	1649	33.8	34	4.98	118	4.91	14.8	2.7	0.11	32	255	10	-120
87-10- 1	1720	14.9	34	3.17	118	5.65	14.8	3.4	0.15	77	180	60	90
87-10- 1	1720	48.5	34	3.84	118	3.57	14.7	3.1	0.09	25	170	50	130
87-10- 1	1747	25.9	34	2.47	118	5.44	15.0	3.6	0.19	89			
87-10- 1	1824	59.4	34	2.40	118	4.45	15.6	2.7	0.12	32	160	60	120
87-10- 1	1911	37.6	34	3.23	118	5.91	15.3	3.6	0.15	86	180	60	110
87-10- 1	1927	8.0	34	4.07	118	6.59	17.7	3.0	0.03	6			
87-10- 1	2040	20.4	34	4.24	118	3.80	14.6	3.3	0.15	83	170	60	120
87-10- 2	019	4.3	34	2.27	118	4.11	13.8	2.5	0.11	42			
87-10- 2	242	19.0	34	2.93	118	4.15	14.4	3.0	0.13	61	205	60	130
87-10- 2	325	31.9	34	5.07	118	5.98	15.9	2.5	0.07	38	170	10	-100
87-10- 2	333	0.5	34	4.80	118	3.12	14.6	2.5	0.04	7			
87-10- 2	724	11.1	34	2.53	118	5.22	14.8	2.7	0.12	54	165	45	40
87-10- 2	1023	5.8	34	3.27	118	5.26	14.9	2.7	0.11	50	230	85	100
87-10- 2	1124	16.6	34	2.07	118	5.21	15.1	2.5	0.13	45	255	65	-50
87-10- 2	19 3	35.2	34	4.74	118	4.39	17.0	3.0	0.03	8			
87-10- 3	044	25.5	34	2.52	118	4.77	13.0	2.7	0.13	57			
87-10- 3	3 3	41.2	34	3.72	118	3.63	14.7	3.1	0.13	64			
87-10- 3	957	0.3	34	4.04	118	5.06	16.3	2.5	0.05	33			
87-10- 3	10 5	7.4	34	4.78	118	5.01	17.2	2.5	0.05	7			
87-10- 3	1752	26.3	34	4.29	118	5.32	15.1	2.5	0.11	45	240	50	130
87-10- 3	2220	19.2	34	2.04	118	4.79	16.6	2.7	0.12	49	165	55	80

87-10- 3	2323	16.8	34	3.15	118	3.33	14.0	3.0	0.13	72	150	55	40
87-10- 4	238	25.8	34	2.82	118	5.51	14.1	2.7	0.15	50			
87-10- 4	255	16.4	34	2.82	118	5.35	13.1	2.8	0.15	66	135	30	140
87-10- 4	255	53.4	34	3.57	118	5.11	12.2	2.6	0.24	31	270	50	-50
87-10- 4	256	16.2	34	2.78	118	5.38	15.1	3.0	0.17	68	140	30	150
87-10- 4	1059	37.8	34	3.19	118	5.79	14.1	5.3	0.21	94	235	75	150
87-10- 4	11 8	41.8	34	4.96	118	6.08	11.6	3.0	0.14	48	195	65	90
87-10- 4	1154	41.0	34	4.18	118	5.65	12.1	2.5	0.15	56			
87-10- 4	1339	24.1	34	4.47	118	6.28	13.7	2.7	0.09	30	165	65	110
87-10- 4	14 5	52.2	34	4.50	118	6.63	13.8	3.5	0.18	86	230	85	130
87-10- 5	7 5	11.2	34	4.49	118	6.35	12.9	3.2	0.17	83	165	60	60
87-10- 5	2359	21.4	34	5.07	118	6.54	12.9	2.7	0.12	55	215	75	110
87-10- 6	2335	58.9	34	3.13	118	5.38	14.0	2.7	0.16	56			
87-10- 9	623	36.9	34	2.82	118	5.39	14.3	2.9	0.15	72	250	75	110
87-10-11	1 1	36.4	34	3.41	118	6.75	18.4	2.7	0.05	5			
87-10-11	1 9	59.1	34	6.47	118	4.68	17.8	2.7	0.00	4			
87-10-11	2234	7.7	34	4.58	118	6.08	13.7	2.6	0.13	63			
87-10-11	2350	48.8	34	5.22	118	5.34	14.9	2.6	0.01	5			
87-10-14	2327	4.5	34	4.12	118	4.18	15.9	2.6	0.03	8			
87-10-16	810	41.2	34	1.67	118	4.42	14.0	2.8	0.15	77	185	65	140
87-10-16	812	20.7	34	4.62	118	5.74	7.2	2.6	0.06	6			
87-10-20	532	41.3	34	2.43	118	5.30	14.2	2.8	0.13	70			
87-11- 1	9 4	34.6	34	2.85	118	5.78	14.6	2.9	0.06	7			
87-11- 6	927	21.2	34	2.31	118	4.49	11.7	2.6	0.16	55	50	65	-140
87-11-22	641	55.4	34	3.18	118	5.41	13.4	2.7	0.12	43	215	80	70
88-01-19	2315	31.8	34	4.27	118	4.01	15.6	3.5	0.14	45	165	65	90
88-04-12	1210	3.9	34	0.61	118	10.56	15.1	2.7	0.13	57	180	55	90
88-04-30	1840	37.5	34	5.59	118	6.96	7.1	2.7	0.13	58	295	75	-70

Lat, Long are latitude and longitude in degree, minutes. Depth is in kilometers. Mag is M_L magnitude. Rms is the rms travel time residual. Npick is the number of P and S times used in the earthquake location. Ddir, Dip, Rake are focal mechanism parameters dip direction, dip, and rake. Parameters may refer to auxiliary plane.

The thrust fault plane of the Whittier mainshock is bound in part by strike-slip faults. Two of the largest aftershocks occurred on these strike-slip faults. The strike-slip fault to the west is a major structure, capable of M_L 5+ earthquakes, as in the case of the largest aftershock. This fault cuts both the hanging and foot wall of the thrust. The strike of the strike-slip fault, as defined by the focal plane of the largest aftershock, is perpendicular to the strike of the thrust fault as defined by the mainshock focal plane. The strike-slip faults apparently controlled the extent of the thrust rupture, constraining the size of the small aftershock zone.

Pasadena earthquake. The 3 December 1988 M_L 4.9 Pasadena earthquake was a left-lateral strike-slip event on the Raymond fault. It occurred close in space and time to the Whittier earthquake (Figure 8.7). The Pasadena earthquake locations and focal mechanism parameters are listed in Table 8.3.

Figure 8.8 shows the area of the Pasadena earthquake from 3 to 18 December 1988. Note the linear aftershock zone, about 4 km long, and the small number of aftershocks, all less than M_L 2.5. Some small earthquakes occurred within the Whittier aftershock zone following the Pasadena earthquake. The linear body of aftershocks generally parallels the Raymond fault. Cross sections are shown in Figure 8.9. These events occupy about the same depth range as the Whittier events, 14 to 17 km, with the deeper events to the east. The mainshock was at 15.5 km depth. In the north-south cross section the hypocenters define a nearly vertical plane.

Focal mechanisms of the mainshock and a few of the aftershocks are shown in Figure 8.10. They all have strike-slip mechanisms. Comparing the aftershock lineation and the focal mechanisms, the left-lateral fault plane

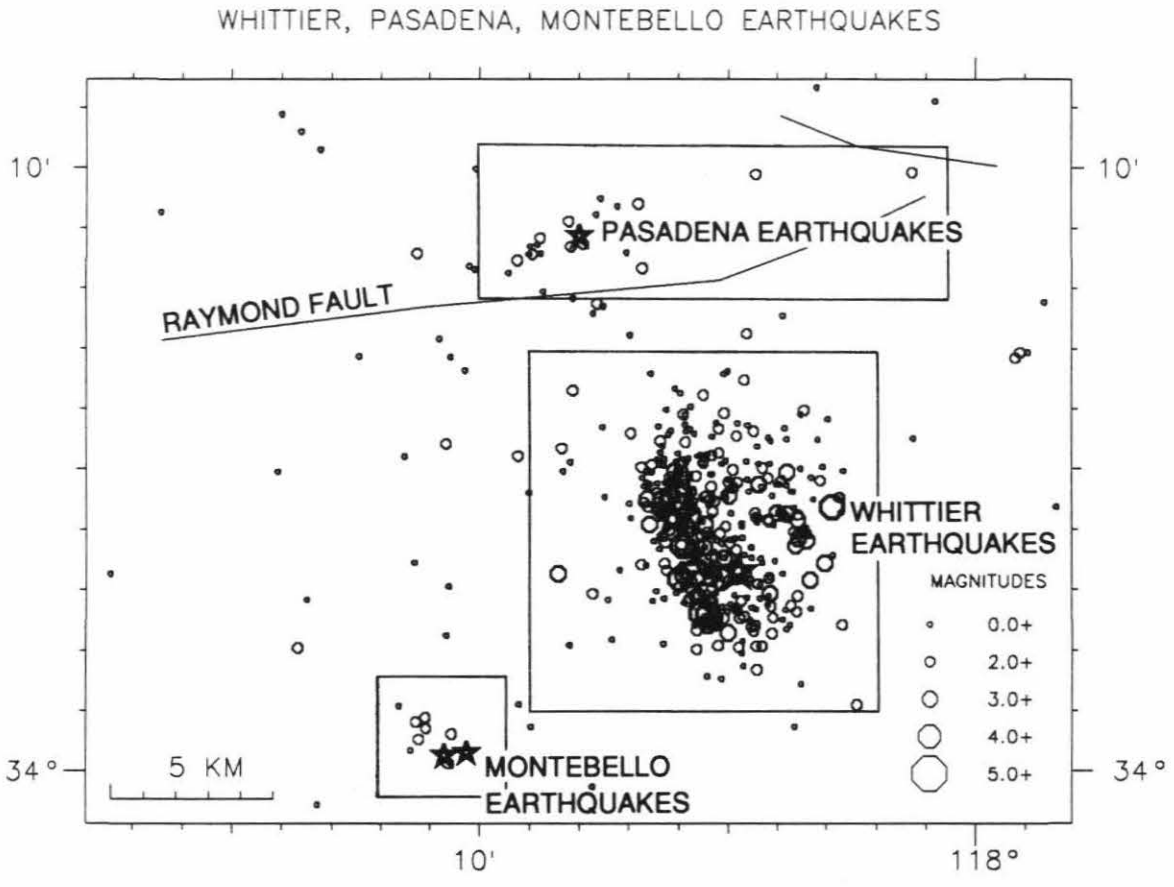

Figure 8.7. The 1987 Whittier, 1988 Pasadena, and 1989 Montebello earthquakes sequences. Earthquakes shown were between 10/1/87 and 6/17/89. Note how close in time and space the earthquakes were. Earthquake symbol size is proportional to earthquake magnitude. Boxes are search windows for the earthquakes shown in Figure 8.18.

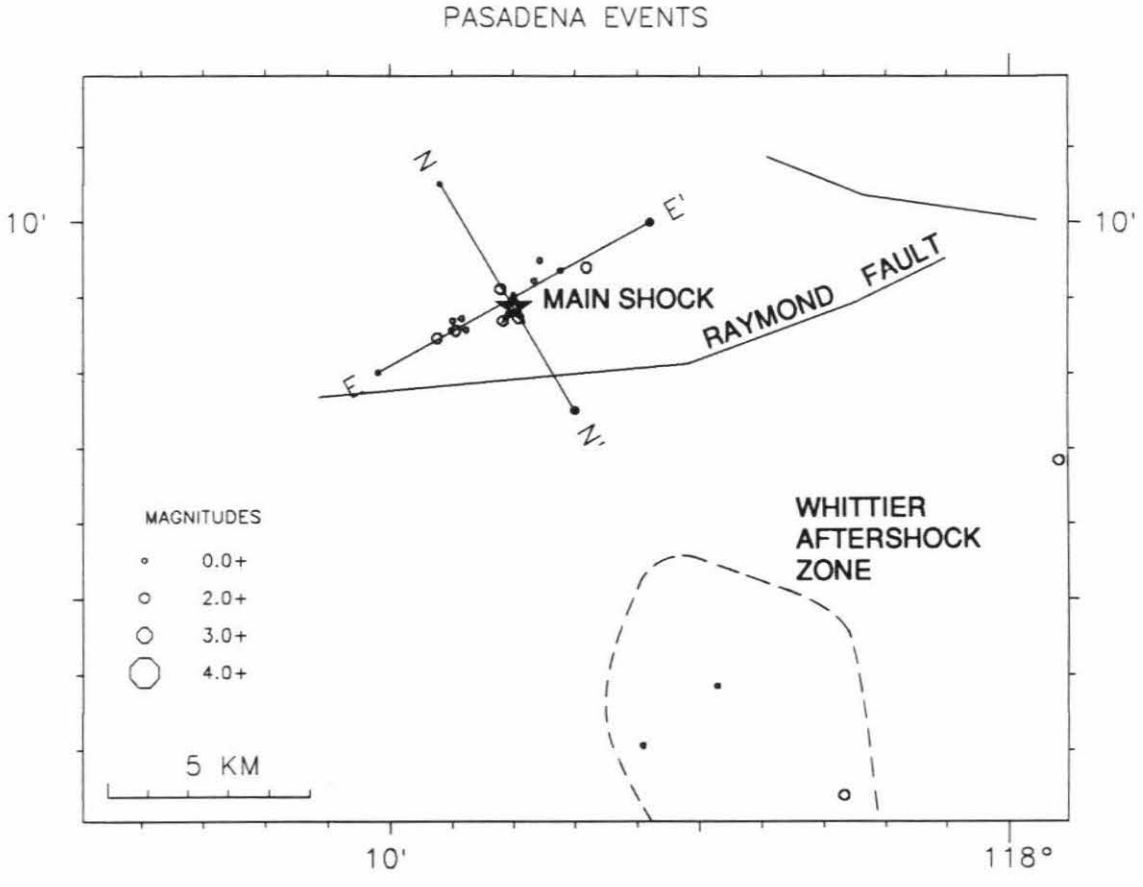

Figure 8.8. Pasadena earthquakes from 12/3/88 to 12/18/88. Note main aftershock zone nearly parallel to Raymond fault, and the aftershocks within the Whittier aftershock zone. Lines EE' and NN' show location of cross sections of Figure 8.9. Note that the Raymond fault is poorly digitized. Earthquake locations are listed in Table 8.3. Earthquake symbol size is proportional to earthquake magnitude.

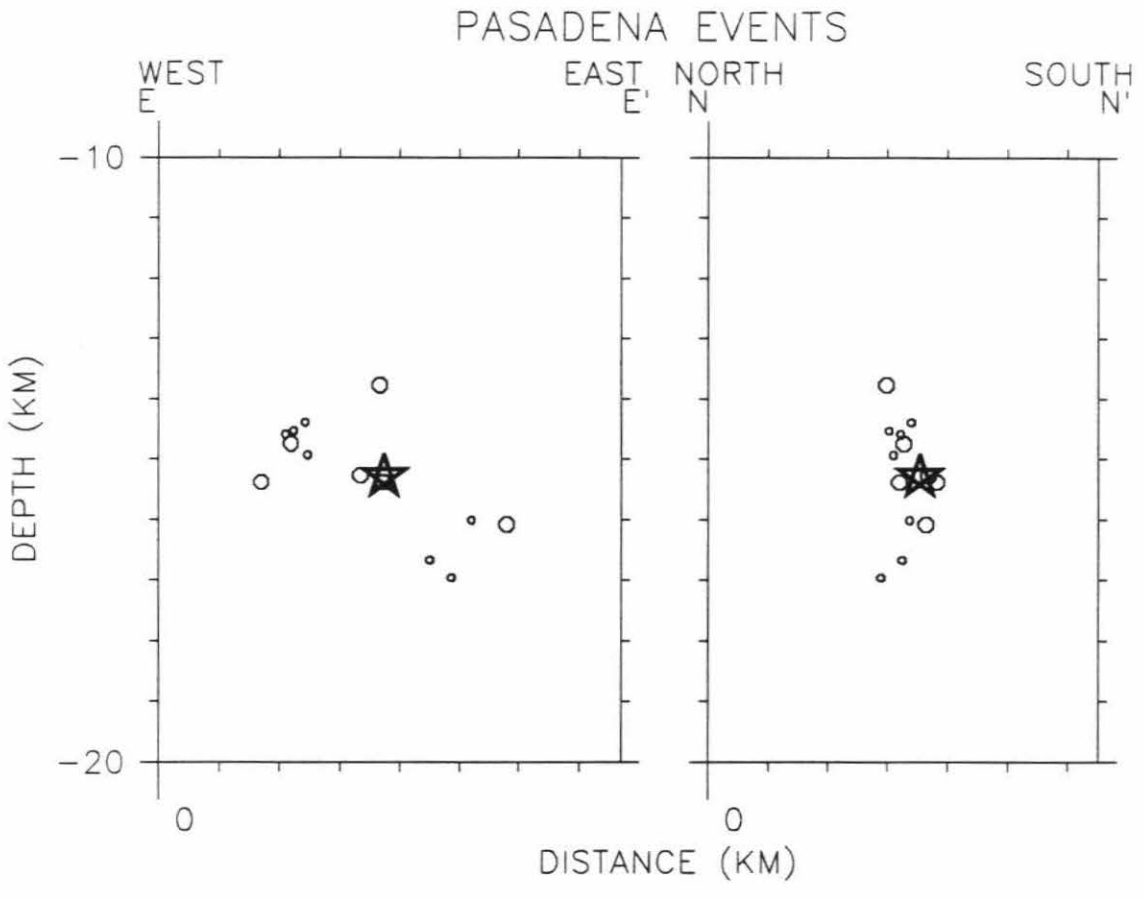

Figure 8.9. Pasadena earthquakes of Figure 8.8 in cross section. Note near vertical dip of aftershocks in north-south cross section (right). Earthquake symbol size is proportional to earthquake magnitude.

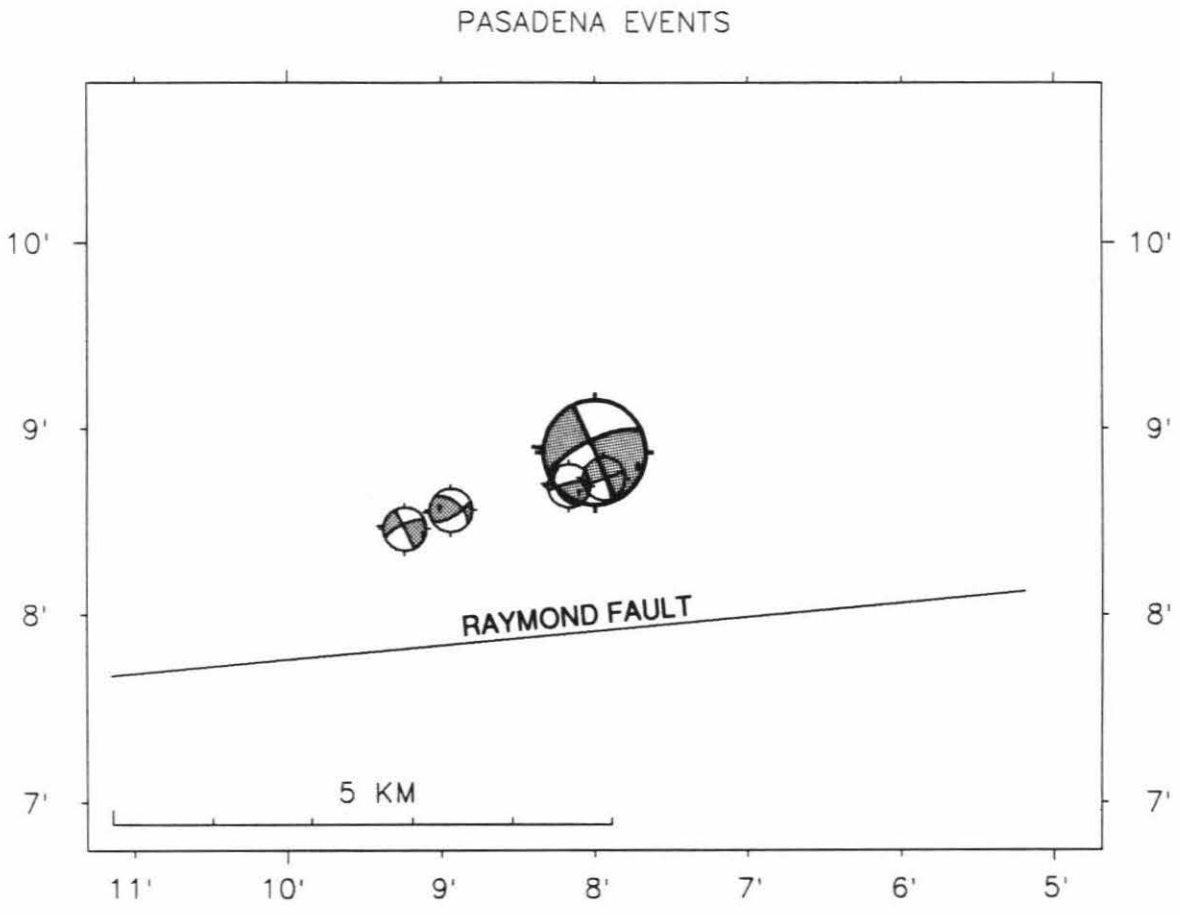

Figure 8.10. Focal mechanisms (lower hemisphere, compressional quadrants shaded) of some $M_L \geq 2.0$ Pasadena events. Mainshock is large mechanism. Focal parameters are listed in Table 8.3.

Table 8.3

Pasadena Earthquakes

Yr-Mo-Da	HrMn	Sec	Lat		Long		Depth	Mag	rms	npick	Ddir	Dip	Rake
88-12- 3	1138	26.2	34	8.87	118	8.00	15.3	4.9	0.21	103	65	90	-160
88-12- 3	1149	13.3	34	8.46	118	9.24	15.4	2.2	0.12	50	65	90	-160
88-12- 3	1156	13.3	34	8.73	118	7.94	15.1	2.4	0.12	58	70	85	180
88-12- 3	12 8	46.2	34	9.22	118	7.66	16.7	1.9	0.07	33			
88-12- 3	1213	11.7	34	8.55	118	9.01	14.6	1.9	0.04	17			
88-12- 3	1215	38.3	34	8.56	118	8.94	14.7	2.4	0.17	71	150	65	40
88-12- 3	1334	41.3	34	8.69	118	8.99	14.5	1.7	0.04	15			
88-12- 3	1336	13.4	34	9.49	118	7.57	17.0	1.7	0.07	20			
88-12- 3	1446	46.4	34	8.57	118	8.77	14.4	1.8	0.11	33			
88-12- 3	17 3	32.8	34	9.36	118	7.23	16.0	1.8	0.05	6			
88-12- 4	8 1	59.0	34	8.69	118	8.17	15.3	2.0	0.06	41	240	40	160
88-12- 5	22 5	22.8	34	9.11	118	8.21	13.8	2.0	0.04	16			
88-12- 8	251	49.6	34	9.41	118	6.81	16.3	2.3	0.08	41			
88-12-18	917	48.1	34	8.72	118	8.84	14.9	1.8	0.04	16			

Lat, Long are latitude and longitude in degree, minutes. Depth is in kilometers. Mag is M_L magnitude. Rms is the rms travel time residual. Npick is the number of P and S times used in the earthquake location. Ddir, Dip, Rake are focal mechanism parameters dip direction, dip, and rake. Parameters may refer to auxiliary plane.

solutions are preferred. The mainshock fault plane strikes 65° and dips 70° north. That dip projects up to the surface at the Raymond fault. From the alignment of hypocenters and focal planes parallel to the Raymond fault, it is concluded that the Raymond fault was the causative structure of the Pasadena earthquake.

The total amount of vertical and horizontal offset of the Raymond fault is unknown (Crook *et al.*, 1987). The recurrence interval of earthquakes causing surface rupture along the fault is about 3000 yr (Crook *et al.*, 1987), so the occurrence of the Pasadena earthquake was somewhat unexpected. The great depth and relatively small size of the earthquake precluded any surface rupture. The surface expression of the fault is marked by north and (mostly) south facing scarps. From surface exposures it has long been thought to be a reverse fault (Buwalda, 1940), so the pure strike-slip nature of the Pasadena earthquake was also unexpected. The dip of the fault at the surface, 58°, (Buwalda, 1940), compared to the dip of the mainshock focal plane, and the hypocenter alignment in cross section (Figure 8.9) indicates the fault steepens with depth.

The Pasadena earthquake showed the Raymond fault to be an active, left-lateral strike-slip fault. The relatively large depth of the earthquake shows the fault width to be larger than expected, with implications for the estimation of seismic hazard in that the larger the width, the greater the maximum expected earthquake. Also, the structural cross section of Davis *et al.* (1989) shows the Raymond fault as an unimportant feature extending to only 5 km depth, yet apparently the fault is active at large depths.

Montebello earthquakes. The 12 June 1989 Montebello earthquakes were two nearly co-located thrust events, a M_L 4.5 mainshock and M_L 4.3

aftershock, 25 minutes apart, followed by a few small aftershocks. The specific causative fault is unknown, but it may be part of the same thrust system that caused the Whittier earthquake. The Montebello earthquake locations and focal mechanism parameters are listed in Table 8.4.

The Montebello earthquake locations are shown in Figure 8.11, covering the time 12 to 17 June 1989. The two larger events are very close together, and the aftershock zone trends northwest from the mainshocks. The aftershock zone may be the downdip continuation of the thrusts, as in seen in the cross section of Figure 8.12. These events are at depths similar to the Whittier events, 15 to 16.5 km. The focal mechanisms are shown in Figure 8.13. The two mainshocks are thrusts. If these events are similar to the Whittier earthquake, 10 km to the east (Figure 8.7), then the north dipping focal planes represent the causative fault, dipping 30^o and striking 255^o. The aftershock locations support the north dipping focal plane as the active fault.

Note in Figure 8.11 that after the Montebello earthquakes two later earthquakes occurred near the six month earlier Pasadena earthquake. One, an M_L 2.3, event on 17 June, has the same epicenter as the Pasadena mainshock. The other, a M_L 2.2 on 15 June, was 11 km east of the Pasadena mainshock along strike of the Raymond fault. Both have left-lateral strike-slip focal mechanisms similar to the Pasadena event (Figure 8.13). The strikes of the focal planes parallel the local strike of the Raymond fault. Recall from above that the Whittier earthquake had a small, M_L 2.7, aftershock on 12 April 1988 at the location of the Montebello earthquakes. That event had a thrust mechanism similar to the Montebello earthquakes.

In the area of the Whittier earthquake, the fold structures used to infer the presence of buried thrust faults strike northwest (Davis *et al.*, 1989).

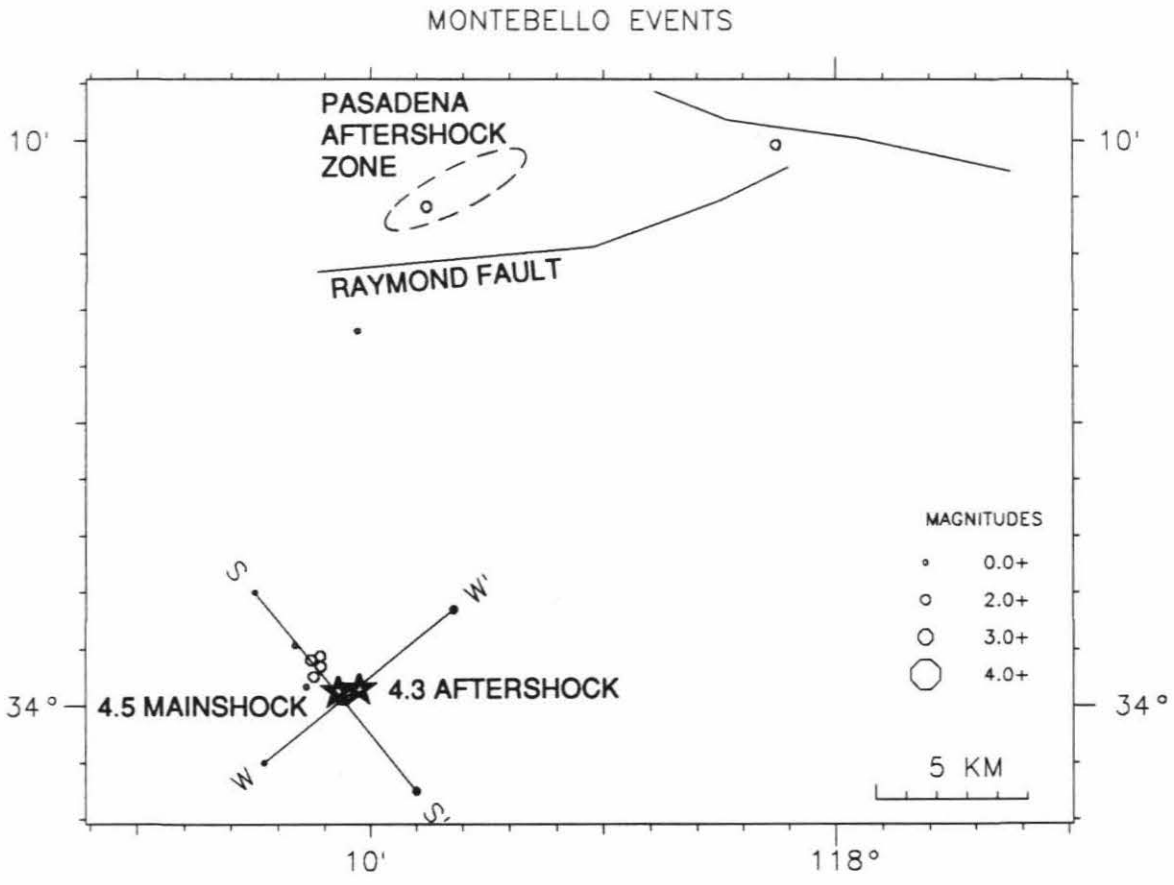

Figure 8.11. Montebello earthquakes from 6/12/89 to 6/17/89. Note small aftershocks northwest of mainshock, the large aftershock, and the aftershocks in and near the Pasadena aftershock zone. Lines SS' and WW' show location of cross sections of Figure 8.9. Note that the Raymond fault is poorly digitized. Earthquake locations are listed in Table 8.4. Earthquake symbol size is proportional to earthquake magnitude.

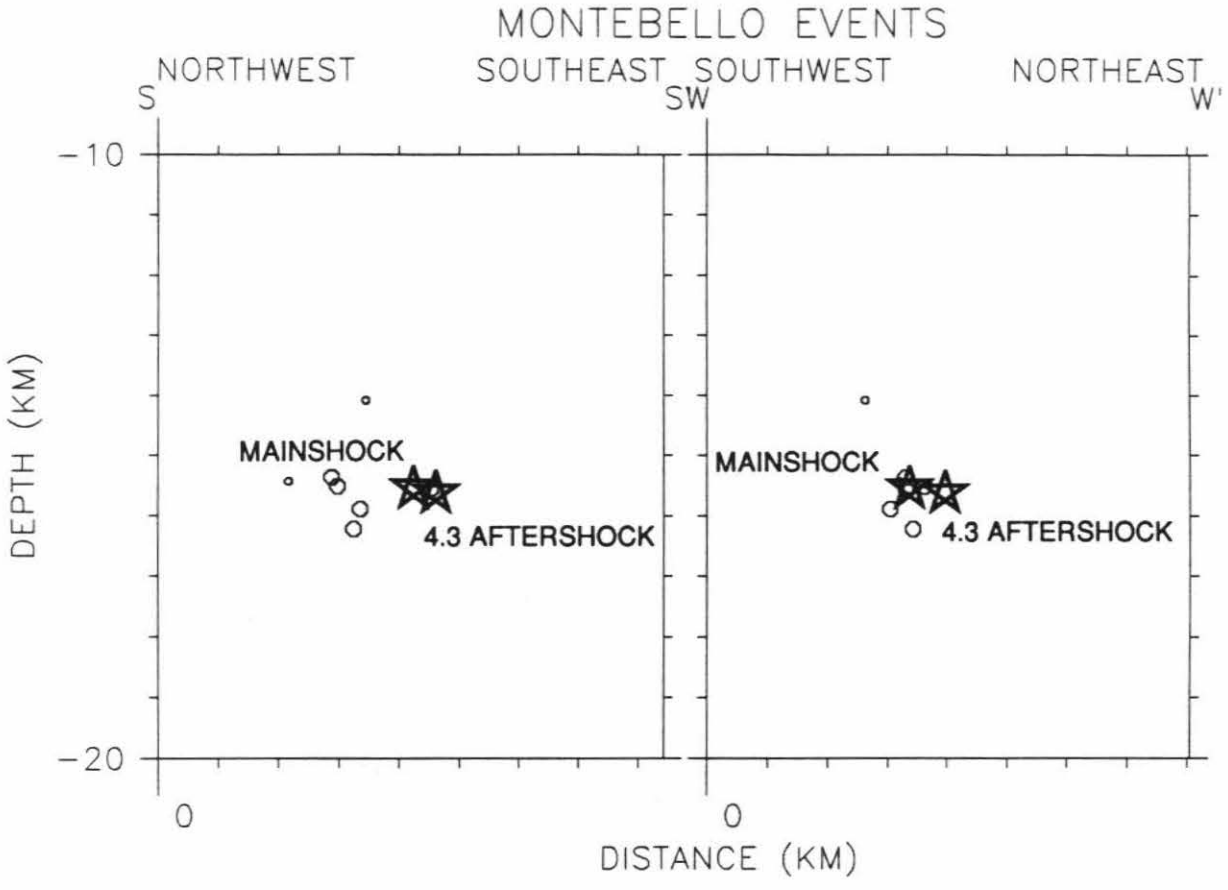

Figure 8.12. Montebello earthquakes of Figure 8.11 in cross section. Earthquake symbol size is proportional to earthquake magnitude.

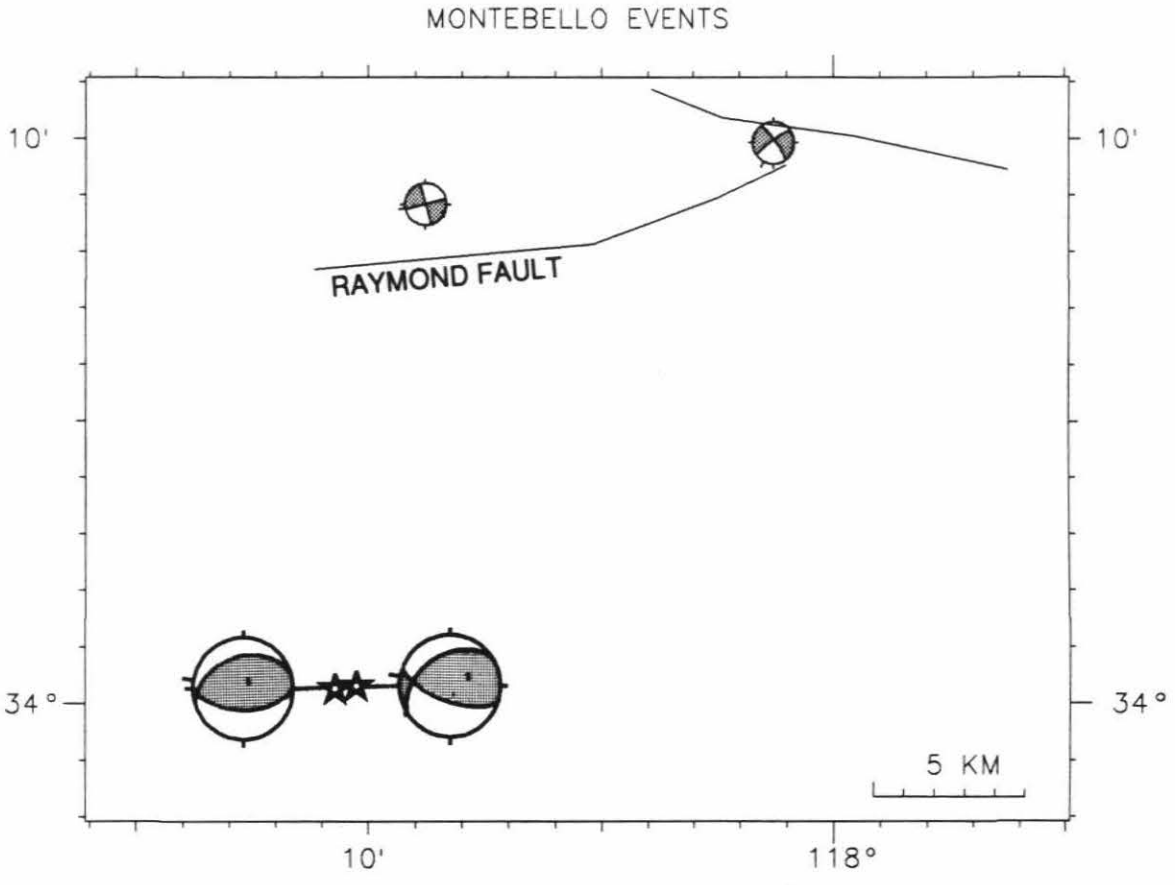

Figure 8.13. Focal mechanisms (lower hemisphere, compressional quadrants shaded) of some Montebello events. Note mechanisms along Raymond fault. Focal parameters are listed in Table 8.4.

Table 8.4

Montebello Earthquakes

Yr-Mo-Da	HrMn	Sec	Lat	Long	Depth	Mag	rms	npick	Ddir	Dip	Rake
89- 6-12	1657	18.4	34 0.26	118 10.71	15.5	4.5	0.22	83	180	55	100
89- 6-12	1722	25.4	34 0.31	118 10.26	15.6	4.3	0.22	88	200	65	120
89- 6-12	1738	21.2	34 0.81	118 11.29	15.4	2.0	0.06	17			
89- 6-12	1743	49.8	34 0.70	118 11.08	16.2	2.1	0.03	13			
89- 6-12	1748	5.5	34 0.12	118 10.62	15.6	2.0	0.07	18			
89- 6-12	1926	45.7	34 0.88	118 11.09	15.5	2.0	0.07	13			
89- 6-13	056	18.0	34 0.34	118 11.40	14.1	1.8	0.06	8			
89- 6-13	633	53.2	34 6.63	118 10.29	10.3	1.8	0.09	20			
89- 6-13	2039	39.4	34 1.07	118 11.64	15.4	1.2	0.03	9			
89- 6-15	041	40.0	34 9.92	118 1.28	11.5	2.2	0.08	25	55	80	-170
89- 6-15	843	24.0	34 0.52	118 11.23	15.9	2.1	0.06	20			
89- 6-17	1256	51.2	34 8.83	118 8.78	14.4	2.3	0.09	31	165	90	0

Lat, Long are latitude and longitude in degree, minutes. Depth is in kilometers. Mag is M_L magnitude. Rms is the rms travel time residual. Npick is the number of P and S times used in the earthquake location. Ddir, Dip, Rake are focal mechanism parameters dip direction, dip, and rake. Parameters may refer to auxiliary plane.

While the Whittier and Montebello earthquakes had similar focal mechanisms, the location of the Montebello earthquakes southwest of, and at the same depth as, the Whittier earthquake makes it unlikely that the events were on the same fault. The thrust fault should track the strike of the fold belt, putting the thrust fault too far north to cause the Montebello events. The Montebello earthquakes occurred on a similar, but different fault than the Whittier mainshock, suggesting fragmentation of the buried thrust faults in that area.

Malibu earthquakes. The 19 January 1989 M_L 5.0 earthquake was a thrust or oblique slip event under the Santa Monica Bay, close to the epicenter of the 1 January 1979 M_L 5.0 Malibu earthquake (Figure 8.14). The 1979 event was a thrust (Hauksson and Saldivar, 1986, 1989). The Malibu earthquake locations and focal mechanism parameters are listed in Table 8.5.

Figure 8.14 shows the 1989 Malibu events and the aftershock zone of the 1979 earthquake. Note that the 1989 aftershocks include a patch of earthquakes 20 km west of the 1989 mainshock. The western events started with a M_L 3.8 event on 2 February 1989 and continued for eight days. The main 1989 aftershock zone abuts, but does not overlap, the 1979 aftershock zone. (The 1979 mainshock and aftershock zone is taken from Hauksson and Saldivar, 1989.) A close up of the 1989 events is shown in Figure 8.15. The mainshock appears to be in the midst of the aftershocks, but in cross section (Figure 8.16) most of the aftershocks are seen to be west of the mainshock. Most surprising is the shallow depth of the mainshock (10 km) with respect to the aftershocks, mostly deeper than 10 km.

There is a problem in determining the depth of the Malibu earthquakes because there are few close stations due to the underwater location of the

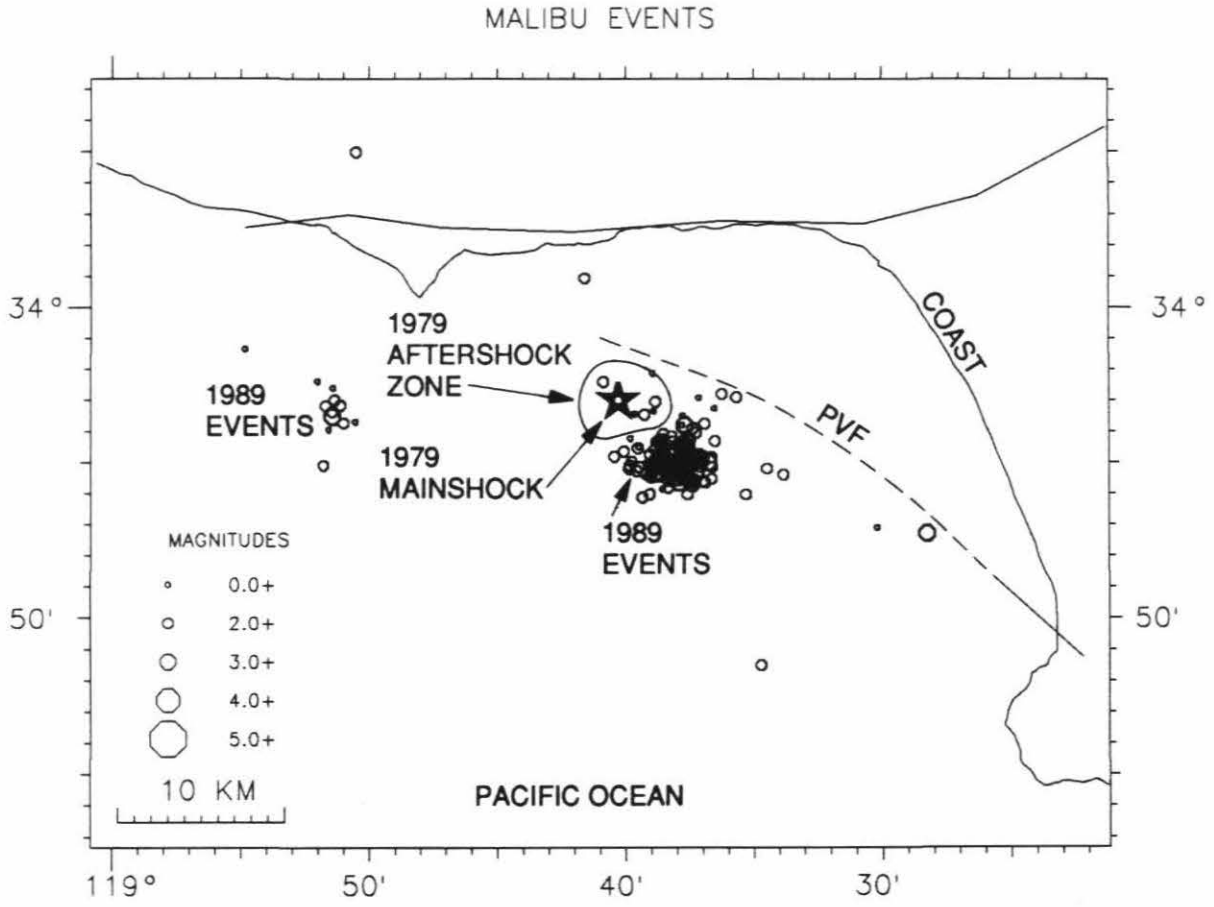

Figure 8.14. Malibu earthquakes from 1/19/89 to 3/2/89. Note the group of aftershocks off to west of main body of aftershocks. The 1989 mainshock is obscured by aftershocks. The 1979 Malibu mainshock and aftershock zone are shown; 1979 event locations are from Hauksson and Saldivar (1989). Abbreviation: PVF, Palos Verdes fault, from Junger and Wagner (1977) in Hauksson and Saldivar (1989). Earthquake locations are listed in Table 8.5. Earthquake symbol size is proportional to earthquake magnitude.

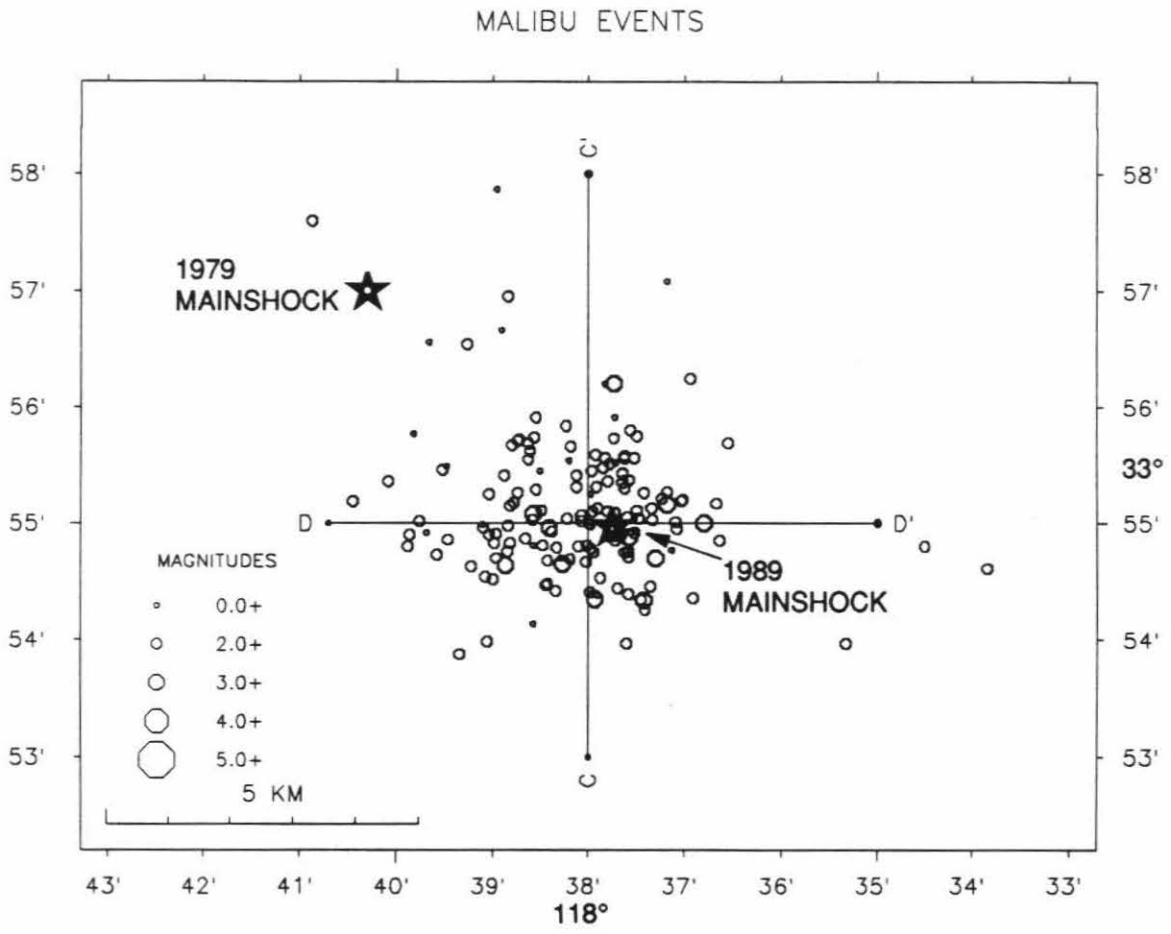

Figure 8.15. Malibu earthquakes from 1/19/89 to 3/2/89. Note 1989 and 1979 mainshocks (stars); 1979 event location is from Hauksson and Saldivar (1989). Lines CC' and DD' show location of cross sections of Figure 8.16. Earthquake symbol size is proportional to earthquake magnitude.

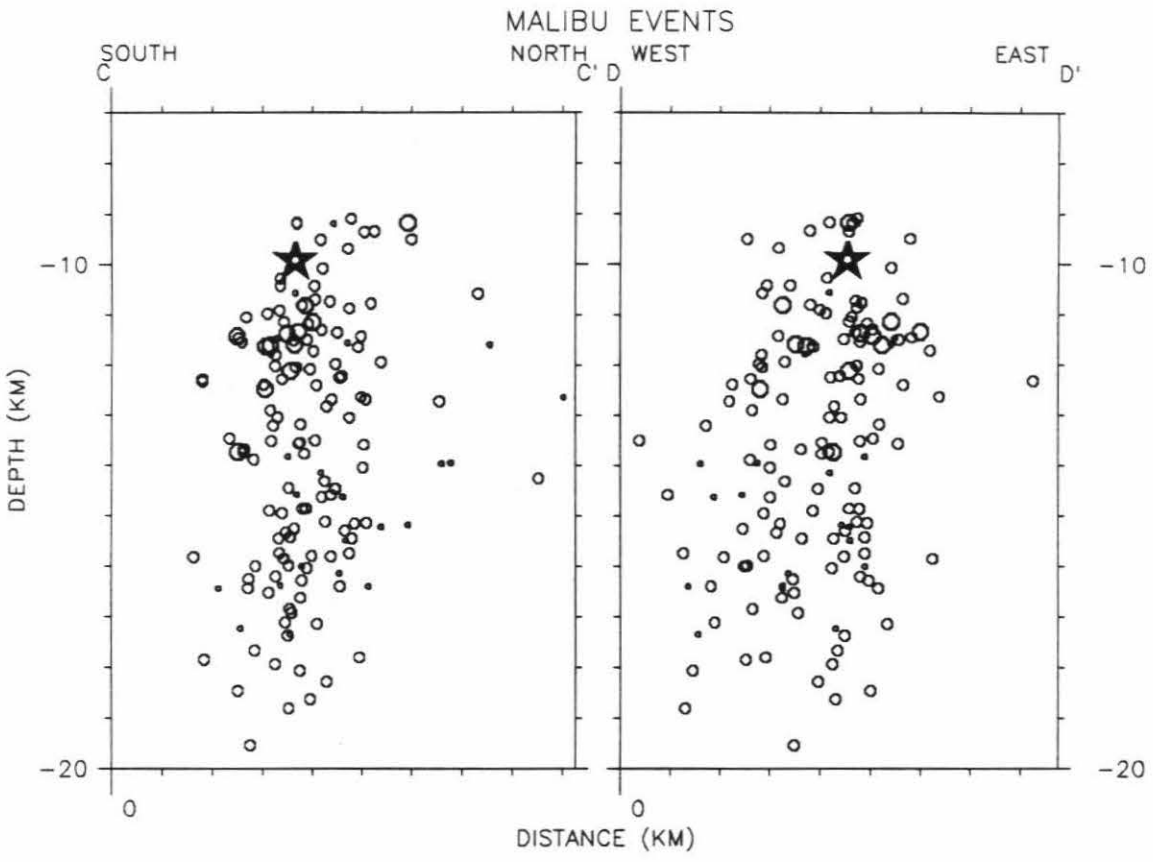

Figure 8.16. Malibu earthquakes of Figure 8.15 in cross section. Note mainshock shallower than most of the aftershocks. Earthquake symbol size is proportional to earthquake magnitude.

events. Only one station is within 20 km, and only three are within 35 km. It is unusual for a mainshock to be shallower than its aftershocks as appears to be the case here. This may suggest depth control problems, but the stations are just as far from the aftershocks as from the mainshock. The variance of the mainshock travel time residuals is minimum for a 10 km depth but varies only slowly with depth. Fortunately, azimuthal coverage is such to ensure reasonable latitude and longitude control.

The poor depth control affects the tectonic interpretation because the focal mechanism of the mainshock varies with depth. For a 10 km depth, a thrust mechanism with steeply dipping planes is found. At a 14 km depth, a strike-slip mechanism is found. Both focal mechanisms, and mechanisms for the $M_L \geq 3$ aftershocks, are shown in Figure 8.17. Only the mainshock was tested for mechanism variations with depth. Most of the aftershocks have thrust mechanisms, similar to the thrust version of the mainshock but two aftershocks just west of the mainshock are strike-slip, with mechanisms similar to the strike-slip version of the mainshock. If the mainshock is a thrust, the 1989 events can be considered to be a continuation of the 1979 rupture of a thrust plane. Hauksson and Saldivar (1986) concluded the 1979 event ruptured a north dipping continuation of the east-west striking Anacapa-Dume fault, but Hauksson and Saldivar (1989) suggest instead that the event broke a buried north dipping thrust fault. The 1989 aftershock locations in cross section do not define any plane, but nearly all the focal mechanisms have a southwest dipping, northwest striking plane. This suggests that a southwest dipping fault plane is worth considering. The Palos Verdes fault has a southwest dip and a northwest strike that could explain both the focal mechanisms of the 1989 earthquakes and the location of the

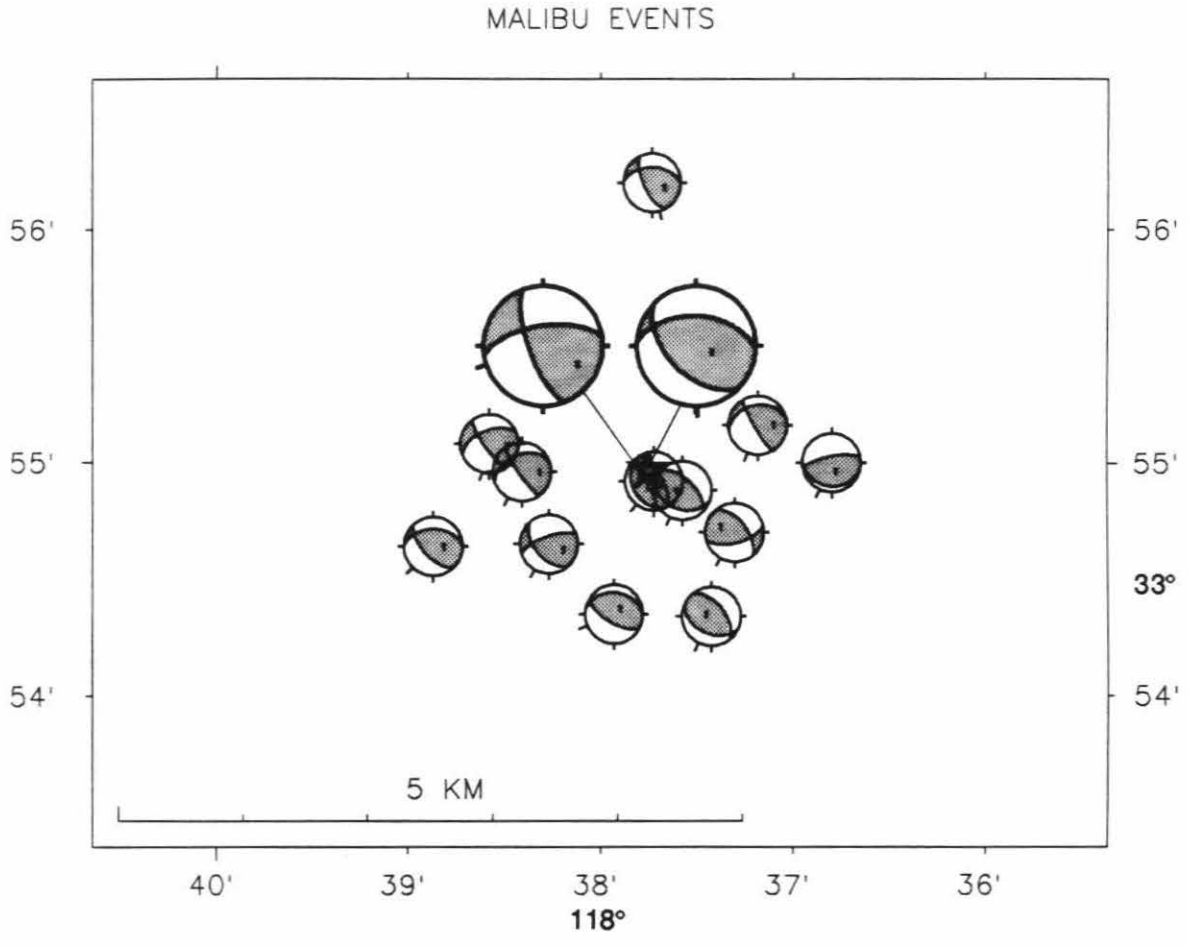

Figure 8.17. Focal mechanisms (lower hemisphere, compressional quadrants shaded) of some $M_L \geq 3.0$ Malibu events. Mainshock is indicated by large mechanisms, two alternate solutions are shown (see text). Focal parameters are listed in Table 8.5.

Table 8.5

$M_L \geq 2.5$ Malibu Earthquakes

Yr-Mo-Da	HrMn	Sec	Lat	Long	Depth	Mag	rms	npick	Ddir	Dip	Rake
89- 1-19	653	28.7	33 54.97	118 37.75	9.9	5.0	0.23	82	250	70	150
									225	50	120
89- 1-19	659	37.1	33 54.34	118 37.42	11.4	3.0	0.21	34	205	40	70
89- 1-19	7 0	53.1	33 54.88	118 37.57	11.4	3.1	0.23	38	200	35	70
89- 1-19	7 2	47.1	33 54.64	118 38.87	12.5	3.1	0.15	33	0	40	50
89- 1-19	7 6	18.2	33 55.04	118 38.22	10.8	2.6	0.16	12			
89- 1-19	738	50.5	33 54.83	118 38.99	12.3	2.5	0.17	31			
89- 1-19	744	21.8	33 54.65	118 38.27	11.6	3.0	0.20	37	230	50	150
89- 1-19	747	13.1	33 54.44	118 37.69	11.0	2.8	0.23	36			
89- 1-19	755	18.7	33 54.39	118 37.58	11.5	2.7	0.20	35			
89- 1-19	758	1.2	33 53.88	118 39.35	15.8	2.6	0.15	29			
89- 1-19	810	5.5	33 54.92	118 37.72	12.1	3.2	0.17	41	240	25	90
89- 1-19	815	22.6	33 55.19	118 37.03	10.7	2.9	0.19	40			
89- 1-19	9 4	6.1	33 55.35	118 37.64	10.7	2.5	0.16	17			
89- 1-19	9 9	22.1	33 55.01	118 37.09	13.6	2.5	0.12	22			
89- 1-19	943	29.7	33 55.43	118 37.64	11.3	2.5	0.16	14			
89- 1-19	1018	28.4	33 55.13	118 37.34	12.1	2.6	0.17	28			
89- 1-19	1025	8.5	33 55.00	118 36.80	11.3	3.3	0.26	50	190	20	110
89- 1-19	1050	23.9	33 54.69	118 38.19	14.9	2.7	0.12	21			
89- 1-19	1118	30.2	33 54.26	118 37.41	13.5	2.5	0.11	20			
89- 1-19	1159	44.6	33 55.37	118 37.57	12.7	2.5	0.14	22			
89- 1-19	1448	1.0	33 55.16	118 37.18	11.1	3.1	0.21	48	240	80	120
89- 1-19	17 4	21.0	33 54.80	118 38.10	10.9	2.8	0.31	37			
89- 1-19	21 2	35.7	33 55.84	118 38.23	9.3	2.6	0.15	25			
89- 1-19	22 1	57.8	33 54.96	118 38.41	11.6	3.8	0.20	77	235	80	130
89- 1-19	22 3	27.2	33 55.62	118 38.61	15.1	2.5	0.08	10			
89- 1-19	22 9	41.6	33 55.08	118 38.58	10.8	3.5	0.21	50	235	75	140
89- 1-19	2211	34.2	33 54.99	118 37.98	9.2	2.8	0.20	14			
89- 1-19	2322	8.7	33 55.11	118 37.49	11.2	2.7	0.17	32			
89- 1-20	325	21.9	33 54.70	118 37.30	11.6	3.0	0.24	42	165	60	40
89- 1-20	1722	3.6	33 53.97	118 35.33	12.3	2.5	0.14	24			
89- 1-21	726	1.0	33 54.85	118 37.72	11.1	2.5	0.20	33			
89- 1-21	1845	48.5	33 54.75	118 37.62	12.0	2.6	0.19	30			
89- 1-22	1759	55.3	33 53.97	118 37.60	12.3	2.5	0.24	21			
89- 1-25	1944	6.8	33 55.17	118 36.67	11.7	2.7	0.17	17			
89- 1-27	2126	4.5	33 54.35	118 37.93	13.7	3.0	0.13	24	210	65	100
89- 1-28	122	50.1	33 55.73	118 37.73	9.4	2.8	0.23	35			
89- 2- 2	451	54.3	33 56.47	118 51.46	8.9	3.8	0.21	64	210	40	130
89- 2- 2	453	22.9	33 54.90	118 51.80	10.1	2.5	0.16	7			
89- 2- 2	517	50.8	33 56.63	118 51.47	9.4	2.9	0.22	31			
89- 2- 3	419	19.7	33 56.24	118 36.94	9.5	2.9	0.18	38			
89- 2- 5	2028	20.8	34 4.99	118 50.52	9.8	2.5	0.25	28			
89- 2-25	1 0	18.8	33 56.20	118 37.73	9.2	3.7	0.24	70	245	65	130
89- 3- 2	19 3	24.8	33 55.03	118 37.33	13.2	2.5	0.11	22			

Lat, Long are latitude and longitude in degree, minutes. Depth is in kilometers. Mag is M_L magnitude. Rms is the rms travel time residual. Npick is the number of P and S times used in the earthquake location. Ddir, Dip, Rake are focal mechanism parameters dip direction, dip, and rake. Alternate solutions are given for the mainshock. Parameters may refer to auxiliary plane.

1989 event southeast of the 1979 earthquake.

If the 1989 mainshock is a strike-slip event, the 1979 thrust and 1989 strike-slip earthquakes could have the same relation as the Whittier thrust mainshock and the largest strike-slip Whittier aftershock. The strike-slip fault aligns with the east edge of the 1979 thrust aftershock zone and may have controlled the extent of the thrust rupture.

8.4 Discussion

Shared aftershock zones?. The Whittier earthquake had an aftershock at the location of the Montebello earthquakes. Following the Pasadena earthquake small earthquakes occurred in the Whittier aftershock zone. Following the Montebello earthquake small earthquakes occurred in and near the Pasadena aftershock zone. To investigate the response of the Whittier, Pasadena, and Montebello earthquake aftershock zones to the nearby earthquakes, the occurrence through time of all events in each aftershock zone are plotted in Figure 8.18. That figure shows earthquakes in the Pasadena aftershock zone following the Montebello event, and earthquakes in the Whittier aftershock zone following the Pasadena event, yet at all times both aftershock zones contain earthquakes apparently unrelated to any nearby large earthquake. It appears that nearby large earthquakes have no influence on the aftershock zones of prior nearby earthquakes.

Strike-slip faults associated with thrust faults. Concurrent strike-slip and thrust focal mechanisms of small earthquakes have been reported from fold-and-thrust belts in Taiwan (Tsai, 1986) and the Los Angeles basin (Hauksson, 1988). Hauksson (1988) suggested that the strike-slip mechanisms may represent faults that segment the thrust faults, but did not actually observe

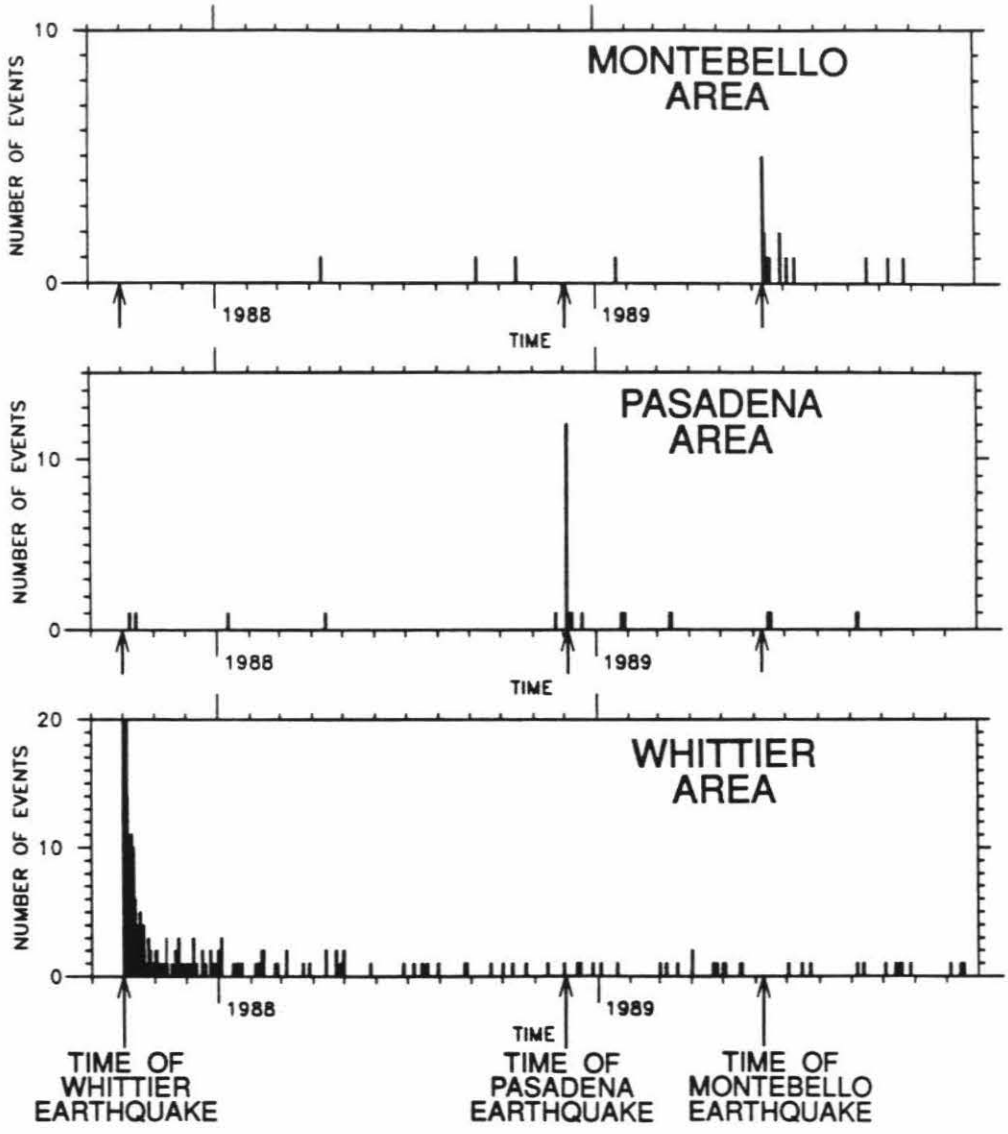

Figure 8.18. Number of earthquakes per day in the aftershock zones of the Whittier, Pasadena, and Montebello earthquakes. Search window of earthquakes shown in Figure 8.7.

that happening in the small earthquakes studied. Here, at least two cases of a thrust rupture being limited in extent by a strike-slip fault are discussed.

The Whittier earthquake sequence involved a strike-slip fault cutting the hanging and foot wall of the main thrust fault plane. The strike-slip fault served to limit the rupture along the west edge of the thrust. To stay consistent with the sense of motion on the thrust plane, the sense of displacement on the strike-slip fault changed from right-lateral in the hanging wall to left-lateral in the foot wall of the thrust. A similar strike-slip feature was seen in the 1971 San Fernando earthquake sequence. The 1971 M_L 6.4 mainshock was a thrust. Whitcomb (1973) did a detailed study of the aftershocks and used focal mechanisms to define a left-lateral strike-slip fault in the foot wall of the thrust. The strike-slip fault coincided with an offset in the thrust fault plane defined by Allen *et al.* (1975). Whitcomb (1973) pointed out that the strike-slip fault was near the west edge of the thrust plane and that it limited the initial thrust plane rupture. The 1989 Malibu earthquake may have been on a strike-slip fault that limited the eastern extent of the 1979 Malibu earthquake thrust rupture, but the tectonic interpretation of the 1989 event is ambiguous. If the 1989 Malibu earthquake was a thrust event, the abutting but separate aftershock zones of the 1979 and 1989 earthquakes still indicate some sort of fault segmentation.

At least two of the largest recent thrust earthquakes (San Fernando and Whittier) in the Los Angeles basin have had the extent of their thrust plane ruptures limited by strike-slip faults. This suggests that the buried thrust faults underlying the Los Angeles basin required by the recent structural cross sections (Davis *et al.*, 1989) are segmented by strike-slip faults. The segmentation scale length would be determined by the separation of the

strike-slip faults, which is unknown. Both the strike-slip faults defined in the Whittier and San Fernando sequences had no surface expression. One approach is to use the typical separation of the strike-slip faults that do have a surface expression in the Los Angeles basin. The cross strike separation of the Palos Verdes, Newport-Inglewood, Whittier, and Chino faults averages about 20 km. This is about the size of the San Fernando earthquake aftershock zone, the largest thrust event known in the Los Angeles basin. It appears that entire buried thrust faults under the Los Angeles basin are unlikely to rupture in very large earthquakes, but instead rupture in moderate sized earthquakes on thrust fault segments.

The initiation point of both the Whittier (Figures 8.5 and 8.6) and the San Fernando thrust mainshocks (Whitcomb, 1973) were located within a km of the intersection of the thrust and strike-slip fault planes. More work is needed to understand the interaction of the thrust faults and the segmenting strike-slip faults.

The three-dimensional crustal velocity model has proved useful in delineating seismogenic structures by improving earthquake locations and focal mechanisms.

Chapter 9

Inversion of Earthquake Travel Times for a Three-dimensional Velocity Structure of Southern California

9.1 Introduction

The three-dimensional crustal velocity model developed in Chapter 7 and applied in Chapter 8 proved useful in locating earthquakes in the Los Angeles basin, an area of large lateral variations of seismic velocities. It was an improvement over the standard one-dimensional model. That three-dimensional velocity model was calibrated by forward modeling of relatively few P-wave travel times from three explosions. There is a great deal of earthquake travel time data available from the southern California seismic array. In this chapter, earthquake and explosion P-wave travel times are inverted for a three-dimensional velocity structure of southern California. The forward model of Chapter 7 is used as a starting model in the inversion.

The velocity structure produced by the inversion can be useful in two ways. First, it can be employed to locate earthquakes. Second, the seismic velocities determined may help to define the types of rocks in areas presently inaccessible, for example, the basement rocks under the Los Angeles basin.

9.2 Method

The inversion is performed using the codes REL3D and HYPIT written by Roecker and co-workers (Roecker 1981, 1982, Shedlock 1986, Shedlock and Roecker 1987, Roecker *et al.*, 1987). Details of the codes are discussed in their papers. The inversion procedure minimizes travel time residuals in a damped

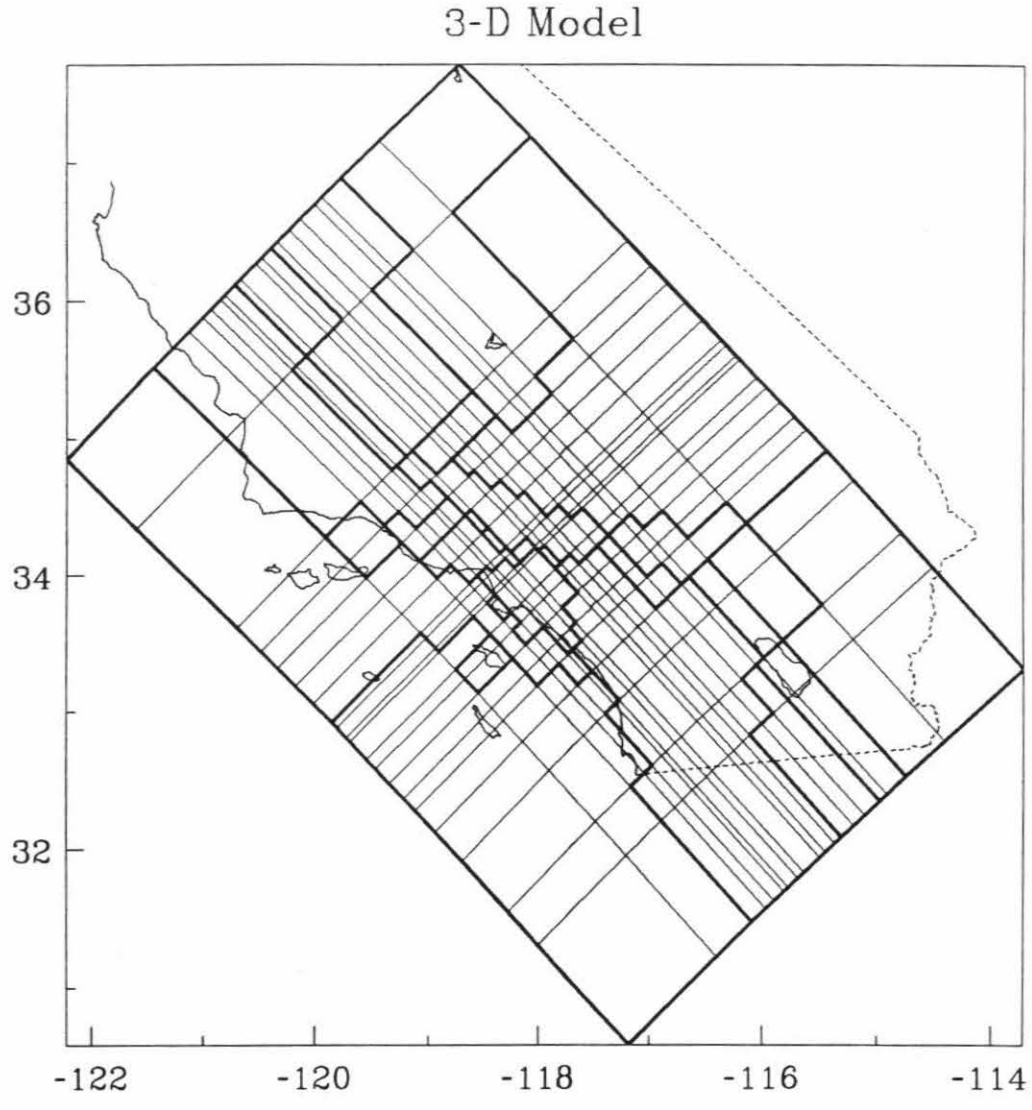

Figure 9.1. The block model from Chapter 8. Heavy lines outline the geologic provinces, and light lines outline blocks. The blocks are arranged the same way in each layer.

least squares sense. The three-dimensional velocity model is expressed as blocks, as discussed in Chapter 7. The inversion adjusts the seismic velocities of each block and the location of each earthquake. The method of parameter separation is used to ease computational requirements, so the earthquake location adjustments by REL3D alternate with the block velocity adjustments done by HYPIT. Separate P- and S-wave velocity models may be determined, but only P-wave models are investigated here because of insufficient coverage of the S-wave data.

The three-dimensional forward model developed in Chapter 7 was based on the idea of partitioning southern California into geologic regions. Many vertical and horizontal interfaces were used to define the edges and layers of the geologic regions (Figure 9.1) in detail. This produced 9120 blocks in the model, but most columns of blocks within a geologic region had the same seismic velocities. This number of blocks is too large for the inversion, so the block model is reparameterized in two ways. First, the blocks within a given layer of a geologic province were connected together to form 'superblocks'. Thus, each geologic region is modeled as one superblock per layer. The outline of the superblocks is the same in each layer. Note that the constituent blocks of a superblock need not be contiguous. During the inversion, the superblock seismic velocities are changed. The superblocks are shown in Figure 9.2. The alterations to the codes to handle the superblocks were written by G. Abers (personal communication). The terms block and superblock are used interchangeably below.

The superblock reparameterization cannot resolve velocity variations over distances smaller than the size of the superblocks. However, it uses the same assumption made in the construction of the forward model, that is, the

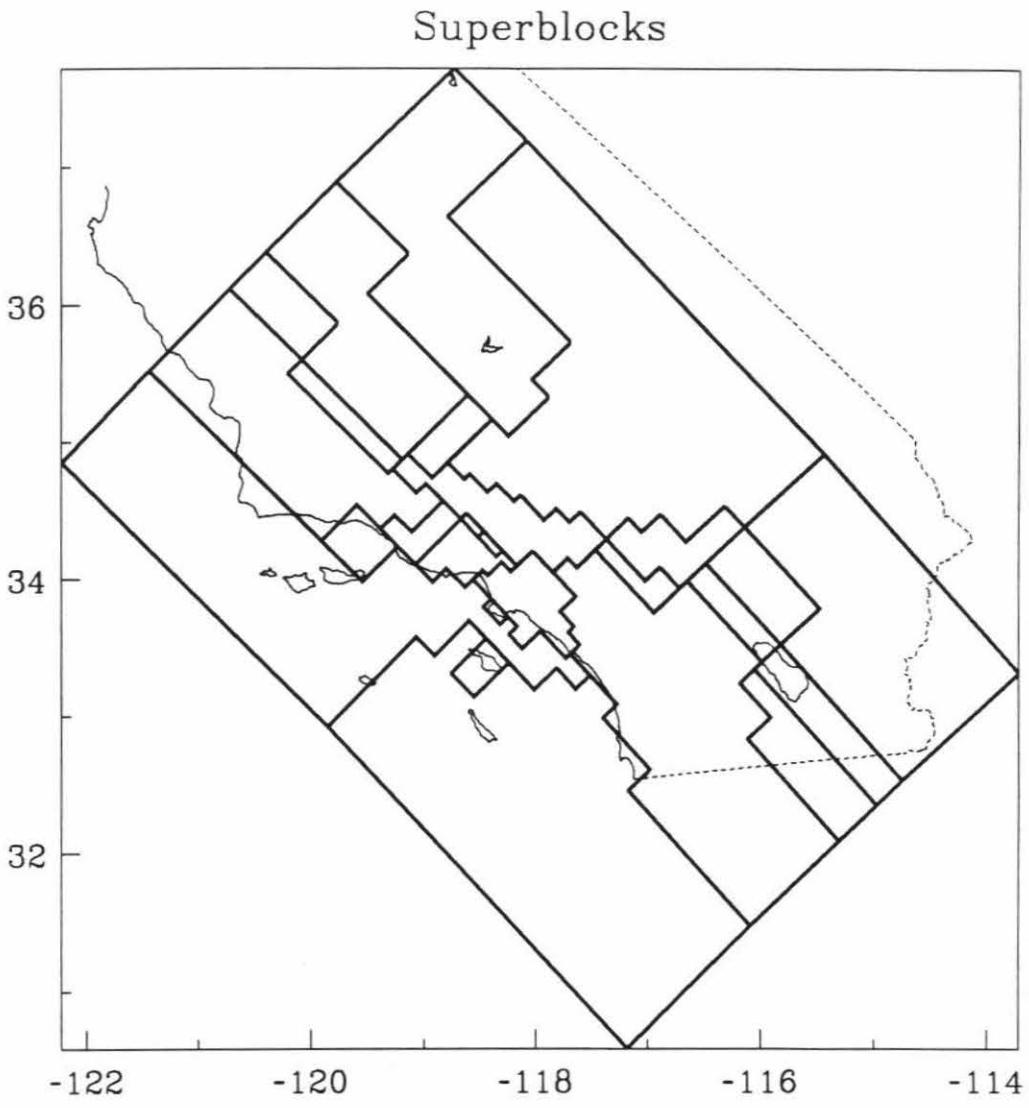

Figure 9.2. The block model of Figure 9.1 reparameterized into superblocks, shown by heavy lines. Each superblock represents a geologic province. The superblocks are arranged the same way in each layer.

seismic velocities within a geologic region will be laterally constant. To test the influence of small scale, near receiver variations in seismic velocity, trial inversions were run that incorporated station corrections. The station corrections were calculated for each station from the average travel time residuals determined in the starting model.

The second reparameterization of the velocity model was to reduce the number of layers from 24, as in the forward model, to 8. Trial inversions indicated difficulty with some of the thin layers in the 24 layer model. Sampling of the blocks by seismic rays is much better in the 8 layer model. All the crustal layers are about the same thickness, 4 to 6 km. With 8 layers and 23 superblocks per layer, the velocity inversion block model has 184 blocks. The positions of the interfaces defining the blocks are fixed during the inversion.

A block must be sampled by 200 or more seismic rays for its velocity to be inverted. Blocks with fewer than 200 hits simply keep the velocity of the input model. An approximate ray tracing technique is used, that is, the code calculates ray paths by finding the average one-dimensional structure between source and receiver and tracing rays through that average structure. Once the ray path with the smallest travel time in the average one-dimensional structure is found, that ray path is followed through the three-dimensional structure to calculate travel times.

The inversion is damped by adding a constant damping parameter to the diagonal of the matrix of normal equations. The damping parameter should be equal to the inverse of the model variance. Estimations of the model variance were made, and the damping parameter tested in trial inversions. The final damping parameter used corresponds to a variation of about 5 per

cent in a 6.5 km/sec block.

When the southern California array data are processed, the arrival time picks are assigned qualities according to the maximum error in the timing of the pick. The qualities and maximum timing errors are shown in Table 8.1. The location program REL3D and the inversion program HYPIT use arrival time weights inversely proportional to the variance of the arrival time errors. To calculate the actual weights used in the location program (Table 8.1), it is here assumed that the maximum errors correspond to the standard deviation of the arrival time errors. The lowest maximum error, .02 sec, is the absolute arrival time picking accuracy determined by the array digitization rate. The actual weight used for that quality pick assumes a maximum error of .03 sec, a realistic value that avoids overweighting the best quality picks.

The codes downweight arrivals from stations beyond a given distance. The distance downweighting is specified as a distance at which an arrival is given a weight of e^{-1} the weight of an arrival from zero distance. Between zero and the cutoff distance, the downweighting is nearly linear, and beyond the cutoff distance, the weight drops quickly to nothing. The cutoff distance was varied as explained below. Arrivals with large residuals are also downweighted in a similar way. The residual cutoff is set from 3 to 1 sec for the first to last iteration in the location program.

The scheme is to take earthquakes well located in the forward velocity model, invert the travel times to change the velocity model, then relocate the earthquakes in the new velocity structure, invert the travel times to further change the velocity model, and so on. The variance of the travel time residuals is monitored at each step. The inversion procedure is stopped when the variance of the travel time residuals stops decreasing. The seismic rays

are retraced at each step. Different distance cutoffs were used for the earthquake relocations and the velocity inversion steps. For the earthquake locations, the distance cutoff was 100 km to get the best quality locations. With that cutoff, the seismic rays used for the locations sample only the better constrained parts of the velocity model (the middle and upper crust). For the inversion the distance cutoff was set to 900 km, purposely larger than the model. This was done to include all P_n arrivals in the inversion to help constrain the relatively poorly sampled lower crust and uppermost mantle.

The codes can invert for separate P- and S-wave velocity models. Trial inversions were run with both P- and S-wave data, but the S-wave data had spotty coverage. This unrealistically forced all the changes of the S-wave velocity model into the relatively few blocks with good coverage, resulting in an unsatisfactory model. The final inversions discussed below inverted the P-wave data only.

During the process of selecting earthquakes to include in the inversion, earthquake relocations were run using both P- and S-wave data. The S-wave velocity model was generated from the P-wave model by using a fixed V_p / V_s ratio of 1.73. During the relocations S-wave arrivals were given one-half the weight of P-wave arrivals.

9.3 Data

The raw data were earthquake arrival times. The earthquakes were recorded on the Caltech-USGS seismic network in southern California between 1978 and 1988. Figure 9.3 shows the station distribution. About 300 stations are shown, some of them temporarily deployed to record the explosions described in Chapter 7. Routine processing (Given *et al.*, 1986) of the

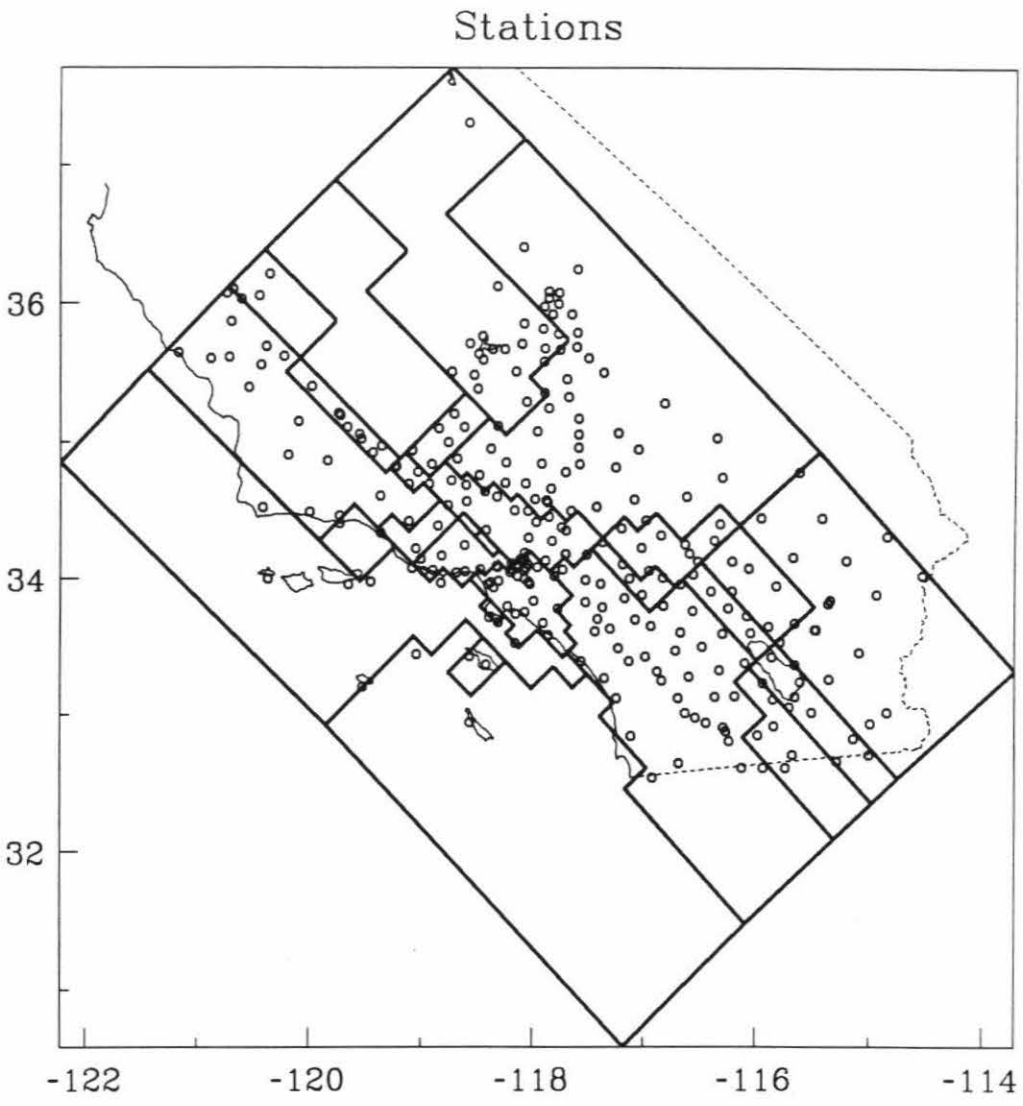

Figure 9.3. The 300 stations (circles) recording travel times used in the inversion. Block outlines as in Figure 9.2.

recorded events produced the earthquake P-wave arrival times. The processing chooses the first P-wave arrivals, which may be direct, P_g, or P_n arrivals, depending on the distance between the source and receiver.

The earthquake catalog was sorted to find earthquakes well distributed in latitude, longitude, and depth. The sort produced about 3000 earthquakes. Earthquakes with fewer than ten S- and P-wave arrivals were discarded, and multicomponent arrival times were combined into a single component with the best quality arrivals from all the components. The latter step avoids overweighting of multicomponent stations that may have several arrival time picks. This left about 1450 earthquakes. These earthquakes were relocated in the forward three-dimensional model of Chapter 7 (with 24 layers). The results of the relocations were edited to discard earthquakes with horizontal or vertical location errors of $\geq$ 10 km, an azimuthal gap to receivers of $\geq 180^o$, or a large condition number. The first two criteria directly indicate poor quality locations and the third warns of lack of control over one of the hypocenter parameters. After this editing, 1041 earthquakes were left, with about 21300 P-wave travel times. The earthquakes are shown in Figure 9.4. These earthquakes were relocated in the 8-layer model with the superblock reparameterization to generate the travel times used in the first iteration of the inversion.

A modification of the inversion code was made to allow the inclusion of travel times from explosions or other events of known location and origin time (S. Roecker, personal communication). 245 travel times from three explosions were used. The explosions are discussed in Chapter 7 and the locations shown in Figure 7.3.

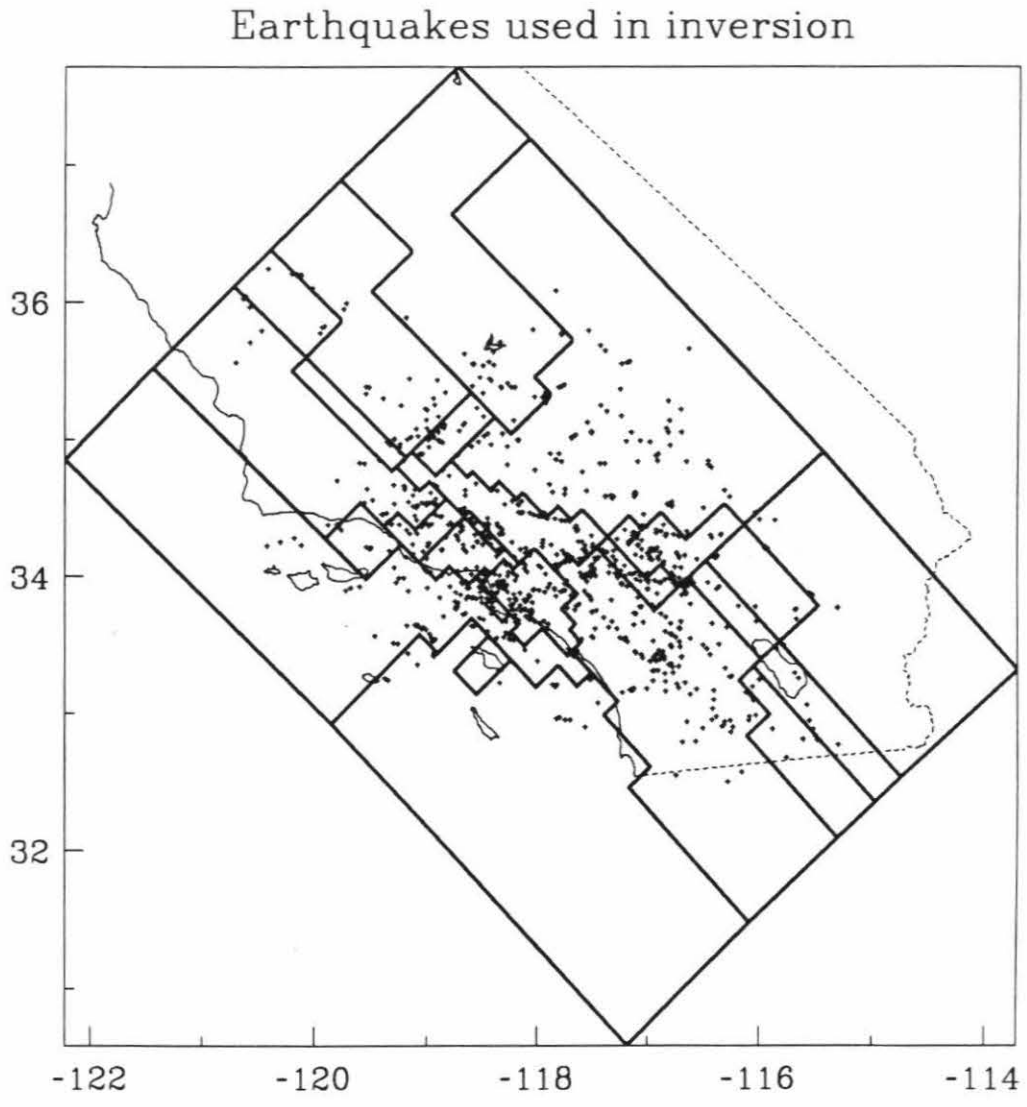

Figure 9.4. The 1041 earthquakes (crosses) that generated travel times used in the inversion. The locations are from the catalog. Block outlines as in Figure 9.2.

The goal was to have well-located earthquakes in order to have accurate travel times to put into the inversion. Travel time residuals of poorly located earthquakes may reflect location errors rather than the velocity variations of interest. The earthquakes that were discarded for poor location quality were mostly around the edge of the southern California seismic array. Those earthquakes have poor azimuthal coverage and few close stations. In general, earthquakes near the center of the array are the best located. The three-dimensional model is centered over the array, so the lack of earthquakes and stations near the edges of the model means that few seismic rays go through the blocks near the edge of the model, especially blocks representing the lower crust and Moho. Those blocks will be poorly constrained in the inversion.

Blocks containing earthquakes tend to be well constrained during the inversion. The maximum depth of earthquakes in southern California is about 20 km. Blocks representing the crust and Moho deeper than 20 km, and some blocks representing the very top of the crust, above most earthquakes, may thus not be well constrained during the inversion. Figure 9.5 shows the depth distribution of the earthquakes used. The depths shown are from the catalog. Some of the deepest events ($\geq$20 km) are suspect. The banding in depth in Figure 9.5 is a result of the depth selection intervals from which earthquakes were selected from the catalog.

The P-wave travel times used in the inversion are displayed in Figure 9.6. Note that both P_g and P_n can been seen beyond about 150 km. Recall that only first arrivals are picked during processing. This means that for some arrivals, the first arrival P_n was missed due to small amplitude and the later arriving, larger amplitude P_g was picked instead. This may influence the inversion by forcing P_n velocities to be slower than reality. Closer than 150

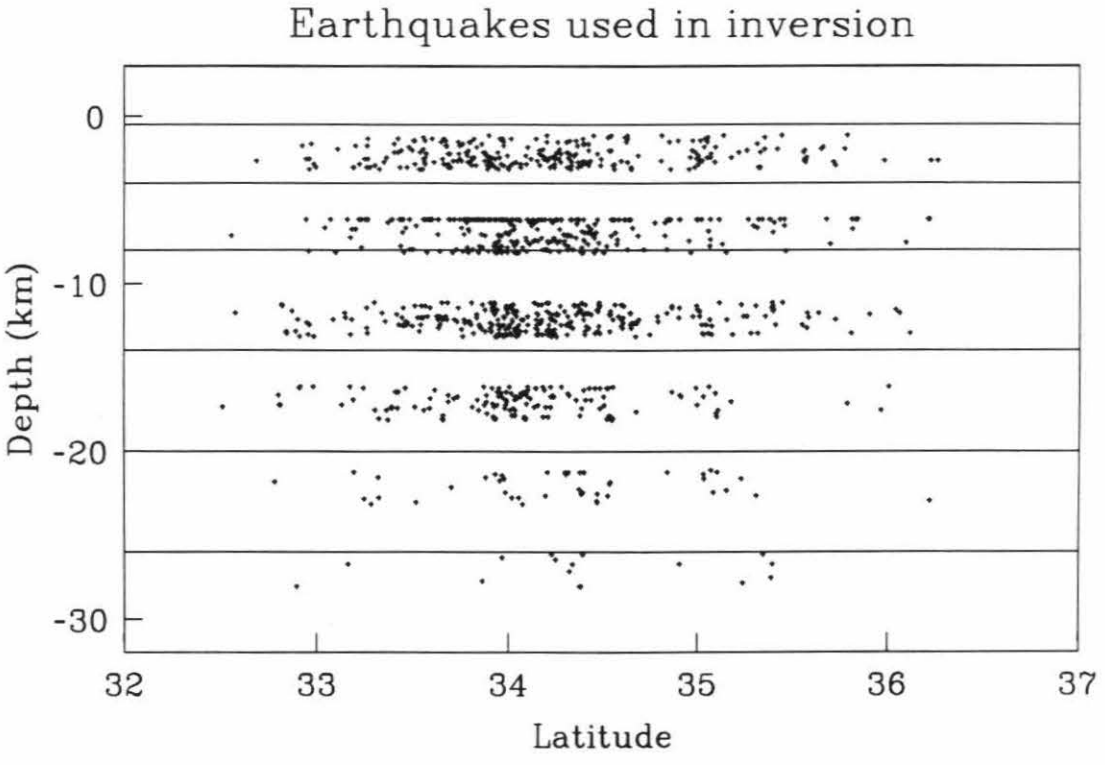

Figure 9.5. Depth distribution of the earthquakes (crosses) from Figure 9.4. The depths are from the catalog. The horizontal lines are the interfaces of the 8 layer velocity model discussed in the text.

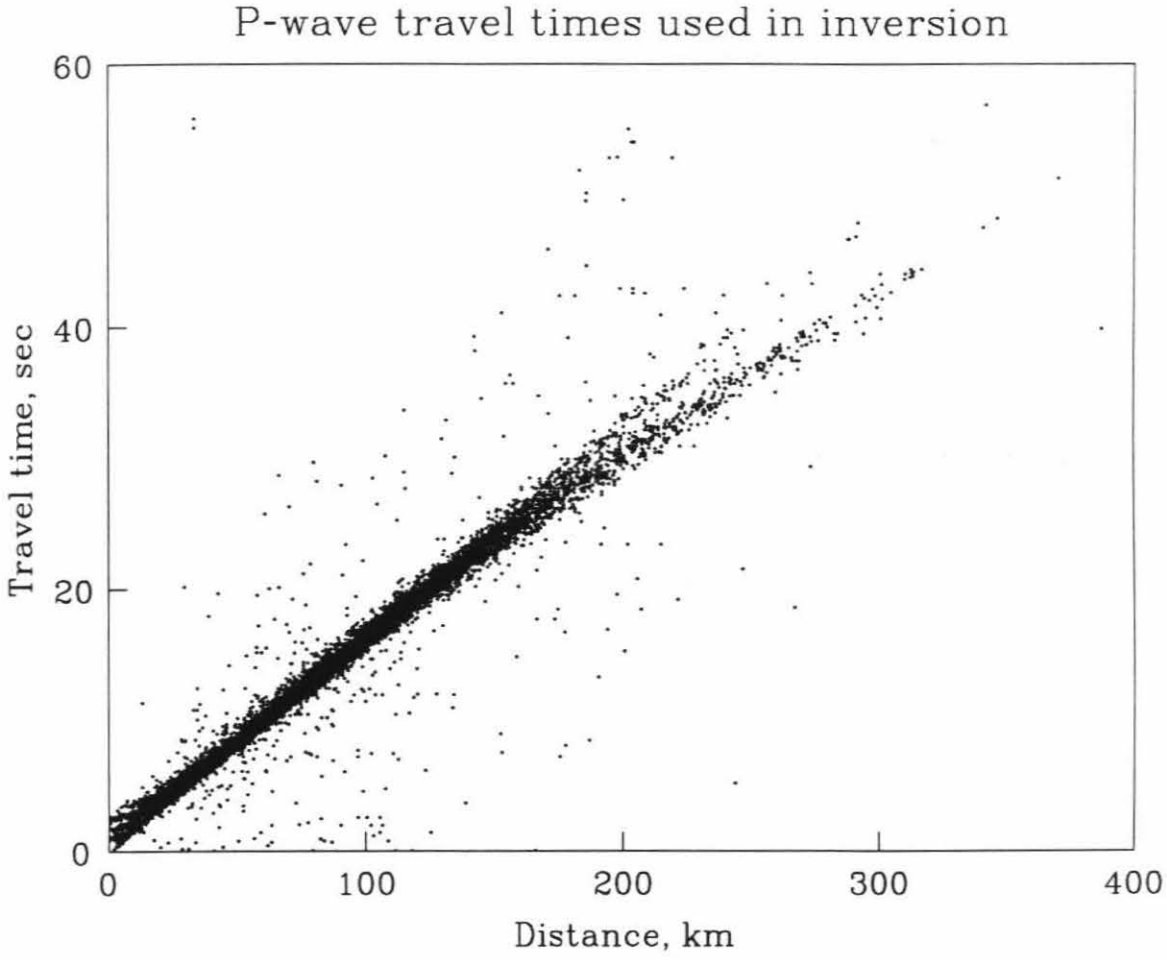

Figure 9.6. The travel times used in the inversion. About 21300 points are shown. Note that both P_n and P_g are present beyond about 150 km.

km the data are generally well-behaved. The data far off the P branch are ignored by the inversion via the large residual cutoff.

The starting model of the inversion was an 8-layer version of the 24-layered forward model developed in Chapter 7. Fewer layers were needed because many thin layers in the forward model were either poorly sampled by seismic rays or poorly resolved and acted unstablely in trial inversions. Also, reducing the number of layers in the model reduced the number of blocks, allowing the inversion to run much quicker. See Chapter 7 for details of the construction of the forward model. The model was modified by choosing 8 layers of nearly equal thickness that best generalized the many original layers. Velocities in the top two layers of the 8-layer model were determined by matching the travel time of a vertical ray passing through the many thin upper layers of the 24-layer model. The 24-layer model allowed closely spaced variations in Moho depth, but the 8-layer starting model has the Moho at 32 km everywhere. Some velocity interface depths of the 24-layer model had to be changed to fit the 8-layer model. This lost the differences between the starting models of some geologic provinces (the San Gabriel and the San Bernardino mountains), but velocities of those provinces evolved differently during the inversion. In the 24-layer model, the Los Angeles basin had sediments of variable thickness but in the 8-layer model the basin is flat bottomed with a 4 km thickness of sediments. The 8-layer starting model of each geologic province (each corresponding to a superblock) is shown in Figure 9.7.

The codes account for station elevations during the calculations. The top layer of the model is extended above zero depth to a height above all the stations so rays can be traced to the stations. Note that this means the blocks

in the top layer will be sampled only by up- and down-going rays, unlike the other layers, which are also sampled by rays refracting along the layer interfaces. The layer interfaces in the 8-layer model are at -3, 0.5, 4, 8, 14, 20, 26, and 32 km depth. The layer interfaces are shown in Figure 9.5.

To investigate the influence of near receiver velocity variations smaller than the scale of the superblocks, station corrections were determined. The station corrections were calculated from the weighted average residuals of the earthquake travel times in the starting 8-layer model. They are listed in Table 9.1. The station corrections do not have a non-zero average over any superblock, so they are not simply reflecting an incorrect velocity of the superblock on which the stations stand, but represent conditions truly local to the station. The inversion was run with and without the station corrections. Using the station corrections is a conservative approach that minimizes the magnitude of the starting travel time residuals, thus minimizing the changes to the velocity structure. The station corrections immediately decreased the variance of the travel time residuals by about 10 per cent, so the inversion with the corrections started with a lower variance, but the percentage variance decrease during each iteration of the inversion was similar for the runs with and without the corrections. This confirms that the station corrections account for local conditions only. The results of the inversion run with the station corrections are preferred over the results without the station corrections.

9.4 Results

Five iterations of earthquake relocations and superblock velocity adjustments were run. The last iteration's results did not vary significantly

from the penultimate iteration. The variances of the travel time residuals in the starting model with and without the station corrections were .092 sec^2 and .101 sec^2, respectively. The variances in the final models were .048 sec^2 and .055 sec^2, reductions of 47 and 46 per cent, respectively. The results for the inversions with and without the station corrections are presented in Figure 9.7. Table 9.2 lists the results for the inversion with the station correction. With the station corrections, 157 of the 184 superblocks of the model were inverted, and 156 superblocks were inverted in the runs without the station corrections. Recall that a block requires a minimum hit count to be inverted. Only blocks that had a sufficient hit count for every iteration are discussed. Recall also that the block boundaries are fixed during the inversion, so the resulting velocities are averages for the block. If, for example, a block straddles the Moho, its velocity will represent an average of the true lower crust and Moho velocities.

The reliability and believability of the inversion results can be judged in several ways. The resolution matrix is calculated. The resolution matrix maps the true least squares solution into the calculated solution. Roecker (personal communication) notes that the most useful interpretation of the resolution matrix is that suggested by Jackson and Matsu'ura (1985). They say that diagonals of the resolution matrix that are less than .5 indicate the *a priori* starting model is controlling the result (that is, the block is poorly resolved), and diagonals greater than .5 mean that the data control the result (that is, the block is well resolved). The resolution of each superblock is given in Table 9.2. Most blocks are well resolved. Some, mostly in the top layer and bottom two layers, are not well resolved, due to poor ray coverage. The top layer is sampled, as noted above, only by up- and down-going rays. Blocks in

the bottom layers contain few sources, and are sampled only by P_n. It is easy for the P_n coverage to be biased. For example, if a block is long and narrow in map view, P_n will only be recorded in the long direction, that is, all the rays sampling that block are traveling in the same direction. Thus a block may have an adequate hit count, but still be poorly resolved. It is also useful to monitor the off diagonal elements of the resolution matrix. A large off diagonal element indicates that a block velocity is not uniquely isolated from that of another block. This sometimes happened between blocks in the first and second layers of a province.

Another measure of reliability of the results comes from examining the behavior of each block velocity during the inversion process. Well-behaved blocks had the largest adjustments of velocity during the first two iterations and changed little after that. The results may be considered more robust if the same velocity is determined for a block in each of the two inversion runs (with and without station corrections). Most well resolved blocks in layers representing the mid crust had very similar results from the two runs.

To estimate how accurately the velocity of a well resolved block is determined by the inversion, the following test was made. A well resolved (resolution=.99) block representing the Los Angeles basin at depths of 8 to 14 km was chosen. Both inversion runs agreed on the block's velocity (6.4 km/sec) within .02 km/sec. New velocity models were made by changing that block's velocity by $\pm$ 1, 5, and 10 per cent. All the earthquakes were relocated in the new velocity models, and the variance of the travel time residuals in each new model was calculated. Note that not every ray samples that block. The results are plotted in Figure 9.8. A significant increase of the variance of the travel time residuals is seen by changing the block's velocity by only 1 per

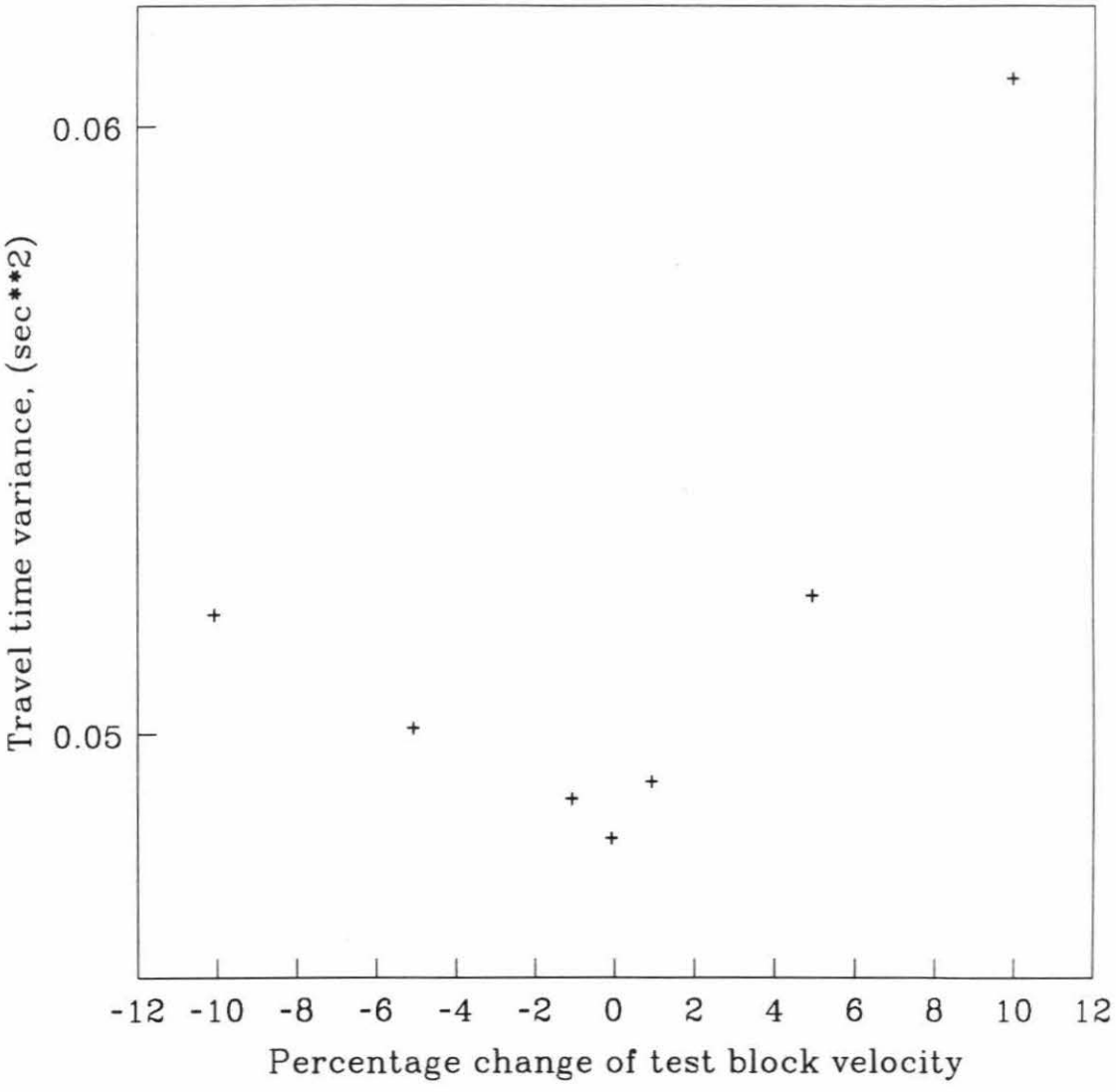

Figure 9.8. Variance of all the travel time residuals calculated in velocity models in which the velocity in one block under the Los Angeles basin was perturbed by the amount shown (± 1, 5, 10 per cent). See text for discussion.

cent. This suggests that the velocities of the well resolved blocks are determined to $\pm$ 1 per cent.

Another way to judge the inversion results is to see how well the final velocity model fits the explosion travel times. Explosions are useful because the origin times and locations are accurately known. Of course, the explosion travel times were used in the inversion, but constituted only a tiny fraction of the data used. The explosion travel time residuals for the starting and final 8 layer velocity models are shown in Figure 9.9. The residuals calculated in the final model appear smaller. The variance of the explosion travel time residuals in the starting model was .343 sec^2, and in the final model .251 sec^2, a reduction of 27 per cent.

A brief discussion of the behavior of each geologic province during the inversion follows. See Figure 7.1 for the province names, and Figure 9.7 for the start and final velocities. Layers 1, 2, 3, 4, 5, 6, 7, and 8 correspond to depths of -3 to .5, .5 to 4, 4 to 8, 8 to 14, 14 to 20, 20 to 26, 26 to 32, and greater than 32 km depth, respectively. The Santa Barbara channel and the Imperial Valley did not have enough hits to be inverted.

All layers of the Los Angeles basin were inverted, with all but the top layer having good resolution. Block velocities changed little after the second iteration. The top layer, however, was well constrained by the Whittier explosion during the forward modeling, so the final velocity of the top layer is reasonable. Layer 2, representing the basin sedimentary fill, did not change much from its starting velocity. Layers 3 to 8, representing hard rock basement, started with the same velocities as the Peninsular Ranges for each depth. Layer 3 ended up much slower, due to sediments extending to depth in some parts of the basin. Layers 4 and 5 changed little from the starting model

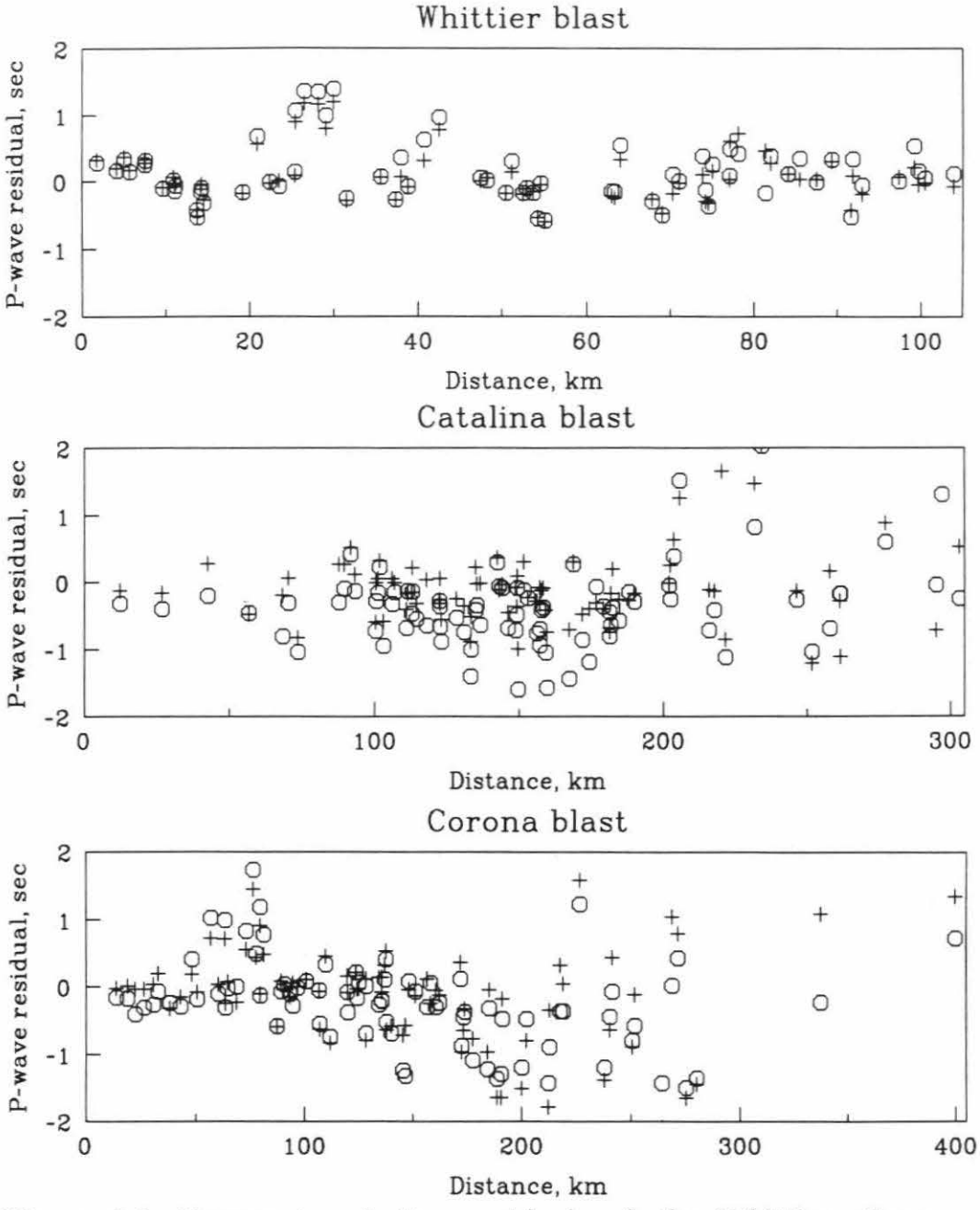

Figure 9.9 P-wave travel time residuals of the Whittier, Corona, and Catalina explosions calculated in the final velocity model (crosses) and in the starting velocity model (circles). Note smaller residuals for the final model.

and layer 6 increased. Layer 7 is nearly typical Moho velocity, and may represent an average of a fast lower crustal velocity and the Moho velocity seen in layer 8. This suggests the Moho is between 26 and 32 km depth.

All but the lower two layers of the Ventura basin were inverted. All but the top two layers had good resolution; the top two layers traded off velocities, so the final velocity of layer 1 is probably too slow and of layer 2 too fast. Layers 3 to 6 changed much from the starting model, which for those layers was based on an average for the entire Coast ranges. Layers 3 and 4 ended up relatively slow, and layers 5 and 6 are relatively fast. Layer 6 is quite fast and so may include some Moho velocity averaged in.

Only the top three layers of Borrego Valley were inverted, and only the third layer has good resolution. The final velocities of layers 2 and 3 are close to the starting model.

In the Coast Ranges east of the San Andreas fault only the top 4 layers were inverted, and only layers 3 and 4 are reliable. The top two layers have small resolutions and were linked with large off-diagonal terms of the resolution matrix. The final velocities are much different from the starting model, taken from a study to the north of the area inverted here. The Coast Ranges west of the San Andreas fault had better coverage; six layers were inverted. Again, the top two layers are poorly resolved, but the other layers have good resolution. The final model differs little from the starting model except the velocity jump in the lower crust is bigger in the final model. The Coast ranges east and west of the San Andreas fault have large differences in their velocity structures.

All but the bottom two layers were inverted for the San Jacinto valley. All layers except the top are well resolved. The final model differs greatly from

the starting model only in layers 3 and 5. The velocities at every depth are slower than the Peninsular Ranges results, compatible with the notion that the San Jacinto valley is a down-dropped block.

The San Fernando Valley had only layers 3 and 4 inverted, both of fair resolution. The final velocities are faster than the velocities at the same depth in the Ventura basin but slower than the velocities in the Los Angeles basin.

In the Great Valley, layers 2 to 6 were inverted, but only layers 4 to 6 are well resolved. The final velocities are much faster than the starting model. Layer 6 is particularly fast for the crust.

All layers in the Mojave were inverted, and all but layers 6 and 7 have good resolution. Layers 1 to 5 ended up with velocities similar to the starting model, but with a gradient in velocity instead of a thick layer of a single velocity. Layers 6 and 7 have lower velocities than the layers above them, but have low resolution and suffer from sampling problems, so those velocities are not to be believed. The Moho velocity found in layer 8 is high for the Mojave as a whole, but has been observed in the easternmost Mojave. That difference in Moho velocity is why an east Mojave province was defined separately for this study, however for the east Mojave only the top five layers were inverted. All but layer 2 are well resolved, and are similar to the starting model, but with the same velocity gradient as seen in the Mojave. That layer 2 is slower than layer 1 is doubtful.

In the San Gabriel mountains all the layers were inverted. All layers except layer 7 have good resolution. The final model, except for layer 7, is similar to the starting model, but with slightly faster mid-crust and Moho velocities. Layer 7 has an unbelievably low final velocity. Layer 7 here, and layers 6 and 7 of the Mojave discussed above, have a sampling problem. In

the starting model, rays prefer to refract either on top of the block above, or on top of the block below. In other words, these blocks are rarely seen in the first arrivals and so are little constrained in the inversion.

The San Bernardino mountains had the same starting model as the San Gabriel mountains, but had different results. All layers were inverted, and all but layer 7 have good resolution. Layer 7 resolution is marginal. The final velocities for the San Bernardino mountains are slower than the velocities at the same depths in the San Gabriel mountains. The bottom layer velocity is a bit slower than expected for the Moho, perhaps indicating that the Moho is a bit deeper than 32 km here. Only the top four layers of the Little San Bernardinos were inverted. Resolution is fair to good. The final velocities are more like the San Gabriel mountains than the San Bernardino mountains.

The Coachella Valley had layers 3 to 5 inverted. Resolution is good in layers 3 and 4 and marginal in layer 5. The starting model was taken from the Imperial Valley, so the difference in the starting and final models reflects the differences in the depth to basement and the nature of the basement between the two valleys. The lower velocity of layer 5 relative to layer 4 is unexplained.

All layers except layer 7 were inverted for the Santa Monica mountains. Resolution is good except for layer 1. Where resolution is good, the final model differs from the starting model only in having a gradient in velocities rather than sharp jumps between thick layers of uniform velocity. Moho is seen clearly in layer 8.

All layers in the Peninsular Ranges were inverted, and resolution is good for all layers. Layers 1 to 5 end up with velocities similar to the starting model, but with gradients instead of thick layers of the same velocity. Layers

6 and 7 have much faster final velocities than the starting model, and layer 8, the supposed Moho, ended up much slower. Layers 7 and 8 are too fast to be normal crust, yet too slow to be Moho. It may be that the thickness of the crust varies a lot in this region, so the velocities of layers 7 and 8 are some average of lower crustal and Moho velocities. Also, as pointed out in the discussion of the travel time data, some P_n arrivals may have been missed and P_g picked instead for source-receiver distances appropriate to sample the lower crust and mantle. That mispicking would force slower Moho velocities, which may be happening here.

The top six layers of the Sierra Nevada were inverted. All but layer 1 had good resolution. The final model is somewhat faster than the starting model. The Tehachapi mountains had the top five layers inverted. Resolution is good for layers 3 to 5, fair for layer 2, and bad for layer 1. Layers 1 and 2 traded off velocity changes during the inversion. The final model for layers 3 to 5 is slower than the starting model, but faster than the final Sierra Nevada model.

Only the top three layers of Catalina Island were inverted. Resolution is bad for the top layer and fair for layers 2 and 3. The final model does not differ much from the starting model. The north continental borderland had all layers inverted; resolution is good except for the top layer. Layers 2 to 5 ended up with faster velocities than the starting model. The starting model had a very shallow Moho (20 km), but the inversion puts it deeper (20 to 26 km) with a higher Moho velocity. The south continental borderland had the upper six layers inverted. Resolution is good for layers 3, 4, and 6, marginal for layers 2 and 5, and bad for layer 1. Moho is shallow, at 20 km, but slower than the input starting model. The final crustal velocities are faster than the

starting model. The north continental borderland, Catalina Island, and the south continental borderland have different velocity structures.

9.5 Discussion

The inversion was successful in determining a crustal P-wave velocity model to better fit the earthquake travel times. By the measures of the resolution, agreement between the two inversion runs with and without station corrections, and the rapid convergence of the block velocities during the inversion, most of the blocks representing the upper and mid crust were well constrained. In some regions, good control of the lower crustal and Moho velocities was possible. The variance of the residuals of the P-wave travel times was reduced by 47 per cent during the inversion. The inversion was stopped when the variance no longer decreased. Significant variance remains; some must be due to noise in the data, but the rest cannot be reduced by the inversion due to the parameterization of the model. Large blocks are used, but in some areas the geology must vary over a wavelength smaller than the block size. An example might be the variation in the Moho depth under the Peninsular Ranges.

The final crustal velocity model determined here should be useful for earthquake locations. The blocks representing the lower portions of the model that were not well constrained can be avoided by the use of a station distance cutoff in the earthquake location scheme.

A principal motivation for this study was to understand the velocity structure of the Los Angeles basin. The inversion had good data coverage and resolution in the blocks representing the Los Angeles basin, except the top block, which had poor resolution. However, the velocity of that block was well

constrained by the Whittier explosion travel time data during the forward modeling in Chapter 7. The velocity structure of the Los Angeles basin thus appears well enough known to justify a crude geologic interpretation. The top layer, from 3 km above sea level to .5 km depth, has a P-wave velocity of 2.6 km/sec. This is a velocity typical of unindurated sediments (Dobrin, 1976), in agreement with the known surface geology (*e.g.*, Yerkes *et al.*, 1965). From .5 to 4 km depth the velocity is 4.1 km/sec. This velocity represents indurated sediments filling the basin. The third layer, from 4 to 8 km depth, has a velocity of 6.0 km/sec. Recall the basin was modeled as having a flat bottom 4 km deep, but it actually varies from 0 to about 10 km depth (*e.g.*, Yerkes *et al.*, 1965). The velocity for this layer can be expected to be an average of the velocities of deeply buried sediments and the basement rocks on which the sediments lie. The velocities of the next two layers, from 8 to 14 and 14 to 20 km depth, are 6.4 and 6.5 km/sec, respectively. The velocities are typical of granitic rocks at this depth (see figure 12 in Kanamori and Hadley, 1975) and so the basin may be underlain with granitic rocks. The next layer, 20 to 26 km depth, has a velocity of 6.8 km/sec. The higher velocity is presumably due to a higher mafic content than the layers above. The layer below, from 26 to 32 km depth, has a velocity of 7.7 km/sec. This is nearly a typical Moho velocity. One possibility is that the Moho is between 26 and 32 km depth, and the 7.7 km/sec velocity represents an average of the lower crustal and Moho velocities. McCulloh (1960) used gravity data to model the Moho at 32 km depth under the central Los Angeles basin. The velocity of the lowest layer, deeper than 32 km, is 8.0 km/sec. This layer represents the uppermost mantle.

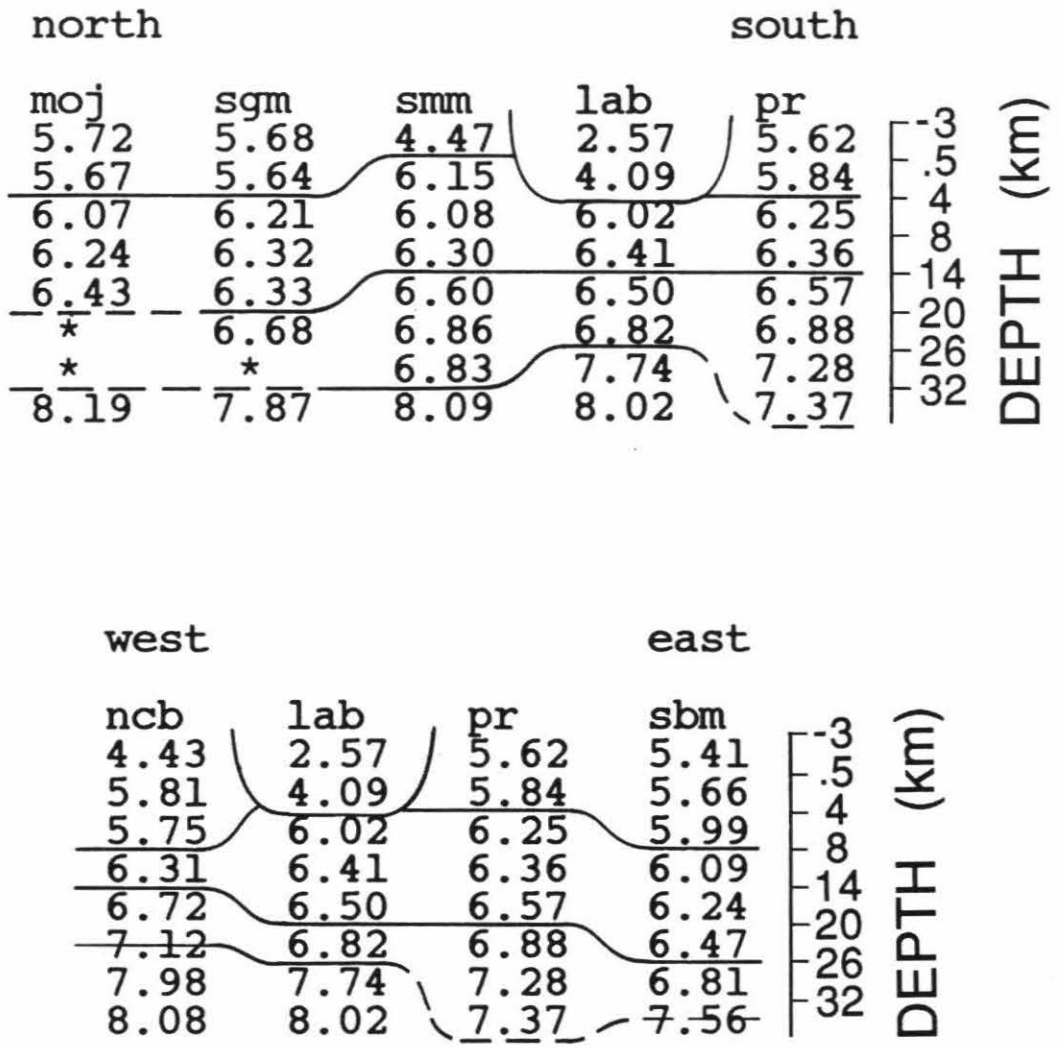

Figure 9.10 Cross sections of the velocity profiles for some of the geologic regions. Lines contour crustal P-wave velocities of $\leq$4, 4 to 6, 6 to 6.5 and $>$6.5 km/sec, dashed where approximately located. Moho location is inferred from the velocities shown. Abbreviations of geologic provinces: moj, Mojave, sgm, San Gabriel mountains, smm, Santa Monica mountains, lab, Los Angeles basin, pr, Peninsular Ranges, ncb, north continental borderland, sbm, San Bernardino mountains. * indicates poorly resolved blocks.

It is interesting to compare the velocities determined for the Los Angeles basin to the velocities found for nearby regions. Figure 9.10 shows north-south and east-west cross sections of the velocity structure from the inversion. The sediment filled basin stands out, defined by low velocities. The upper crustal layer defined by velocities of 6 to 6.5 km/sec thins from north to south, and the faster, lower crustal layer of >6.5 km/sec thickens from north to south, in general agreement with Hadley and Kanamori (1977). The east-west cross section shows the eastward thickening crust. The depths to the 6.0 to 6.5 km/sec upper crustal layer, and the >6.5 km/sec lower crustal layer, seem to increase as the Moho depth increases going west to east. The crustal velocity structure below 8 km under the Los Angeles basin is most similar to that under the Santa Monica mountains and the Peninsular Ranges.

Three-dimensional representations of crustal velocities are clearly superior to the typical one-dimensional velocity model. Three-dimensional velocity models will become more common in the future. The most useful extension to this work will be the implementation of a true three-dimensional ray tracing code that is now available. For southern California it would be nice to include regional P_n data to help constrain the Moho and lower crust velocities. It would be interesting to focus on smaller areas of large lateral velocity contrasts, such as the Ventura basin, or the Salton trough, to generate accurate velocity models for detailed earthquake studies. It would also be interesting to model in detail the Peninsular Ranges to see if the seismic velocities vary along with the geochemical variations in that area.

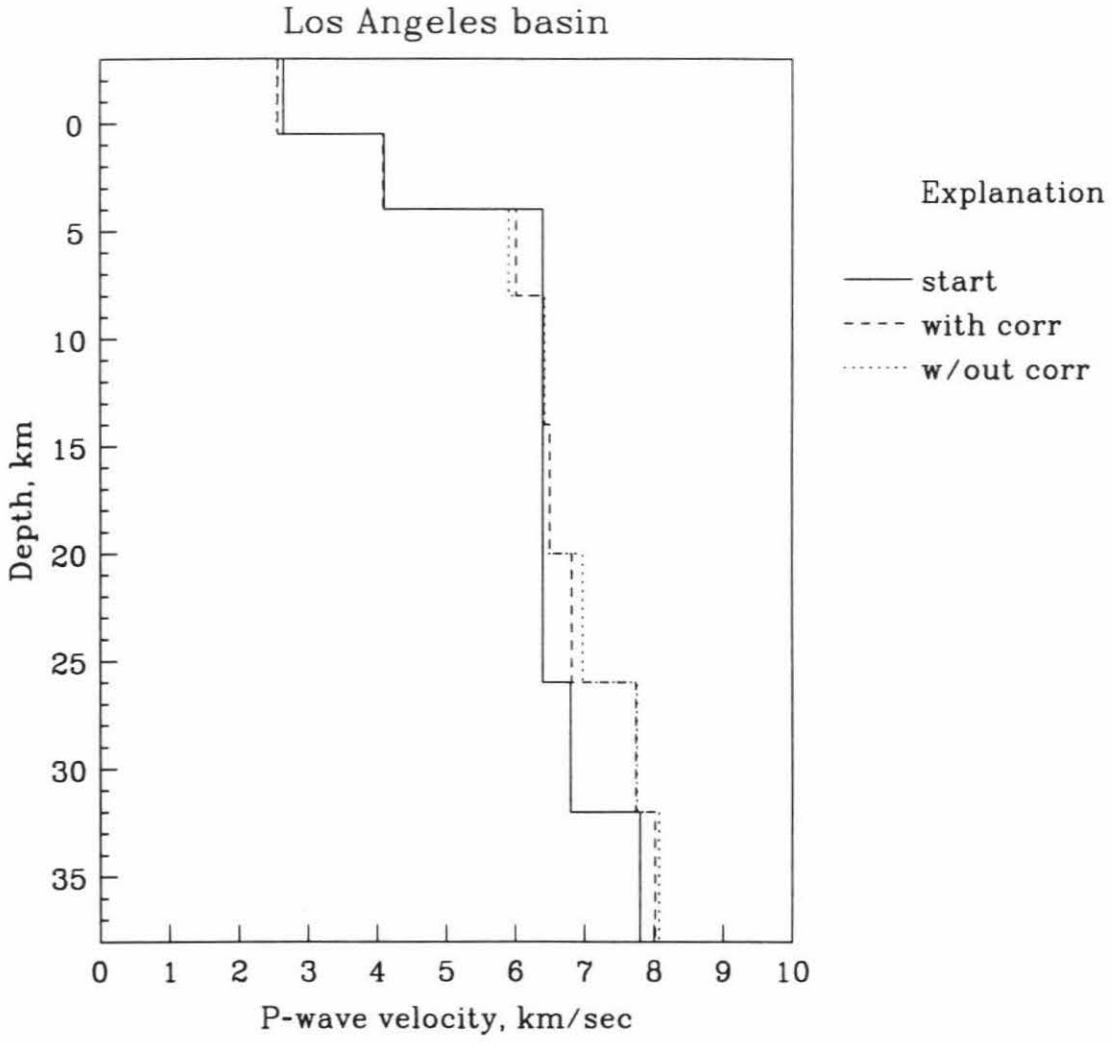

Figure 9.7. The starting (solid line) and final (dotted lines) P-wave velocity models. The final velocities are shown for inversions run both with (with corr) and without (w/out corr) the station corrections. If a block did not have its velocity inverted, nothing is shown for the final velocity.

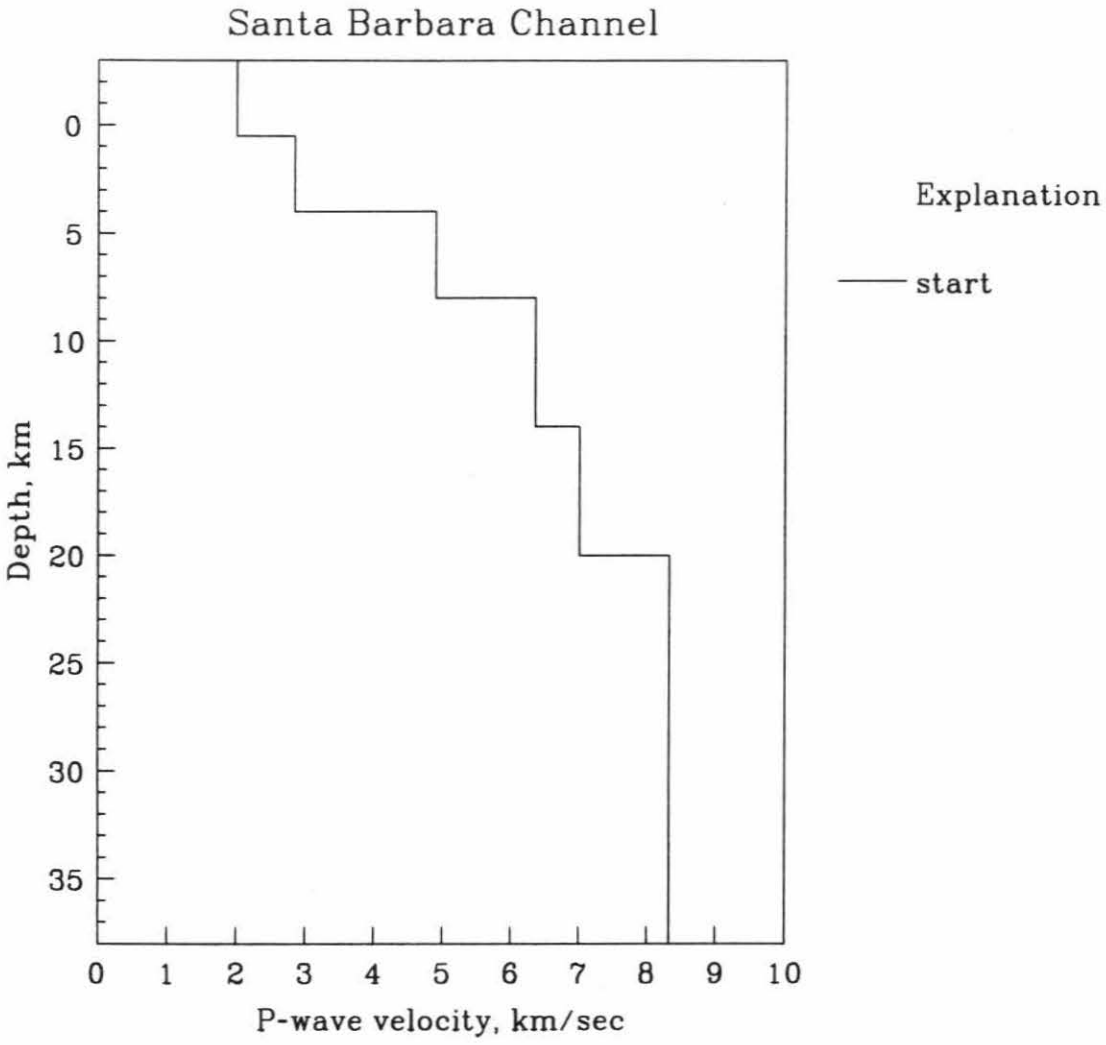

Figure 9.7 continued.

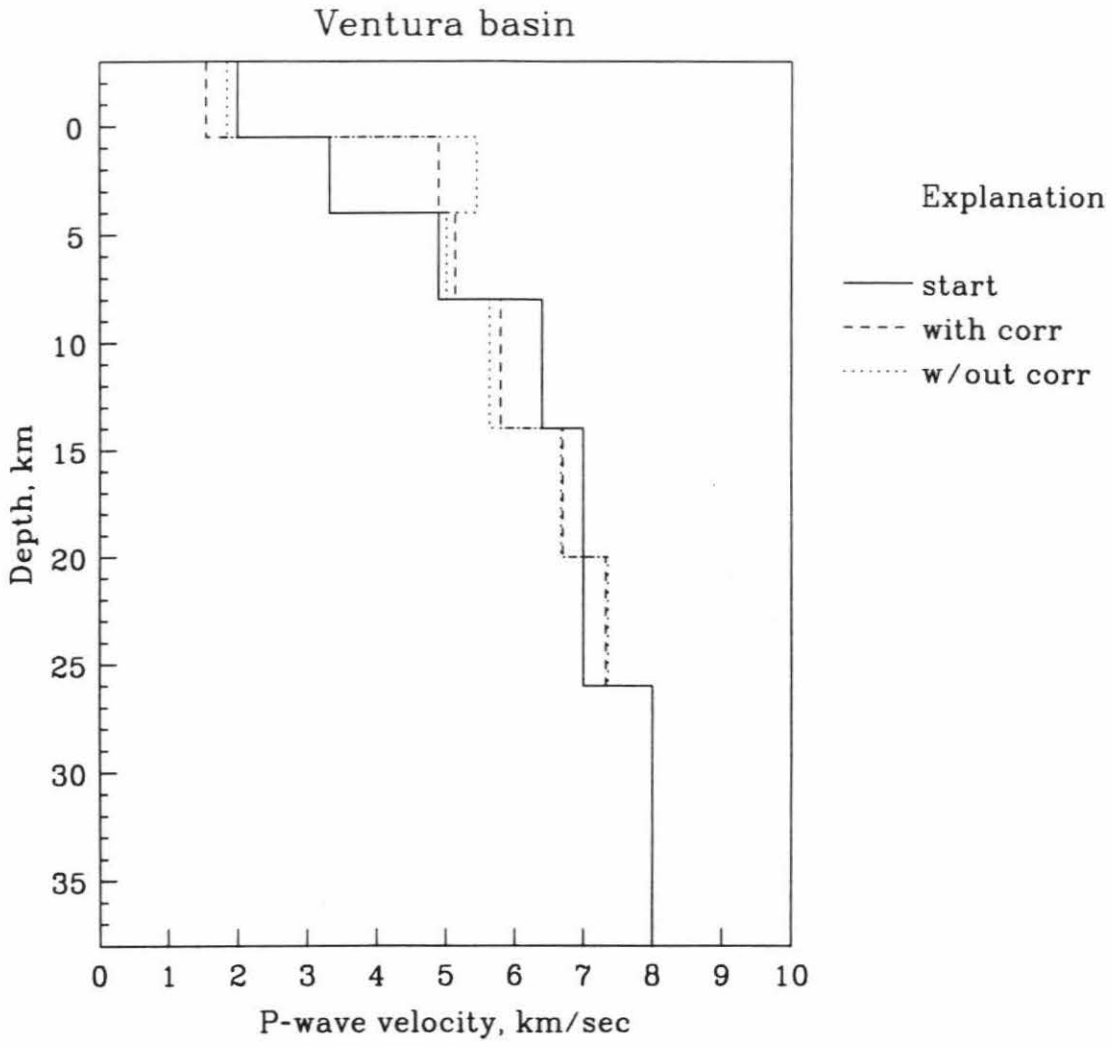

Figure 9.7 continued.

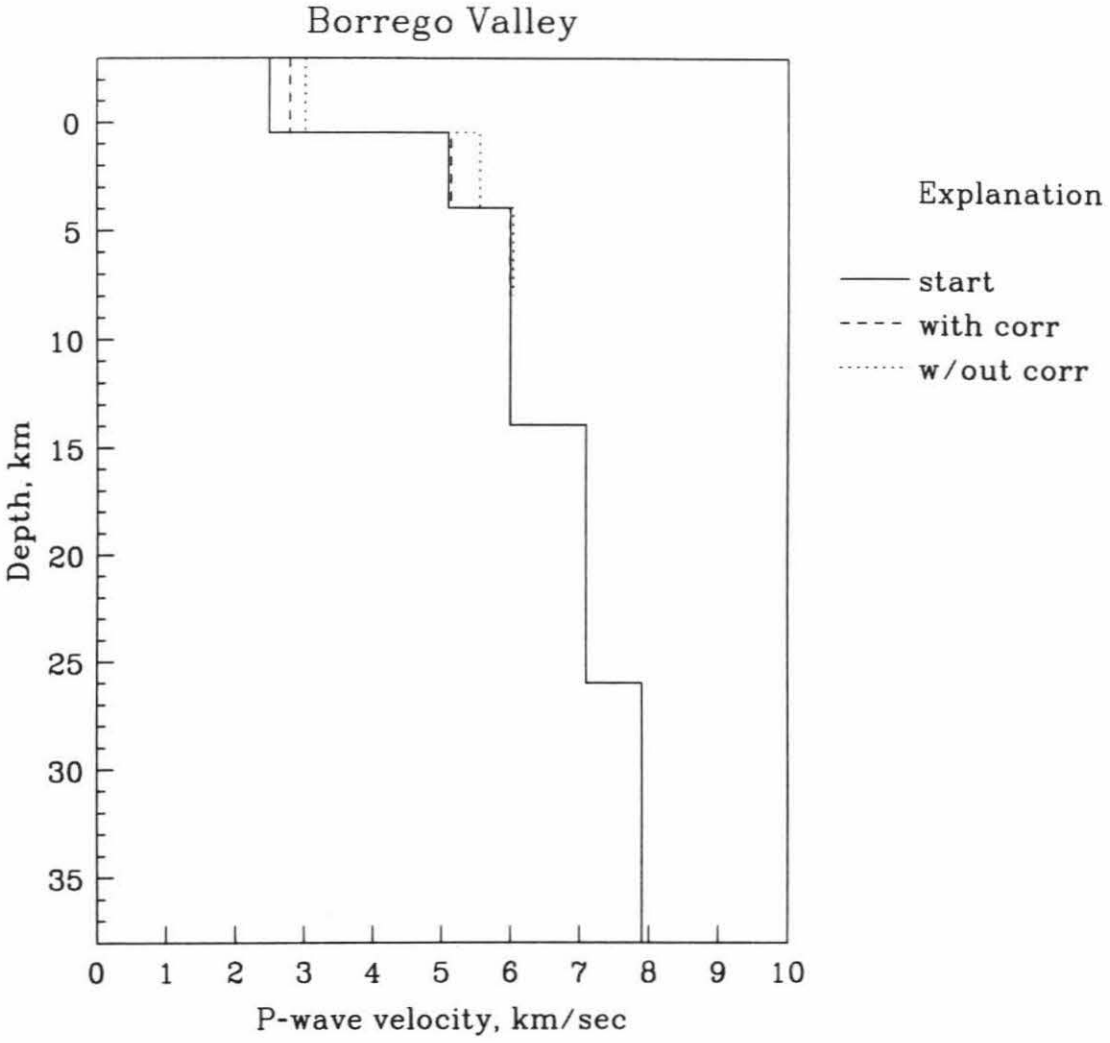

Figure 9.7 continued.

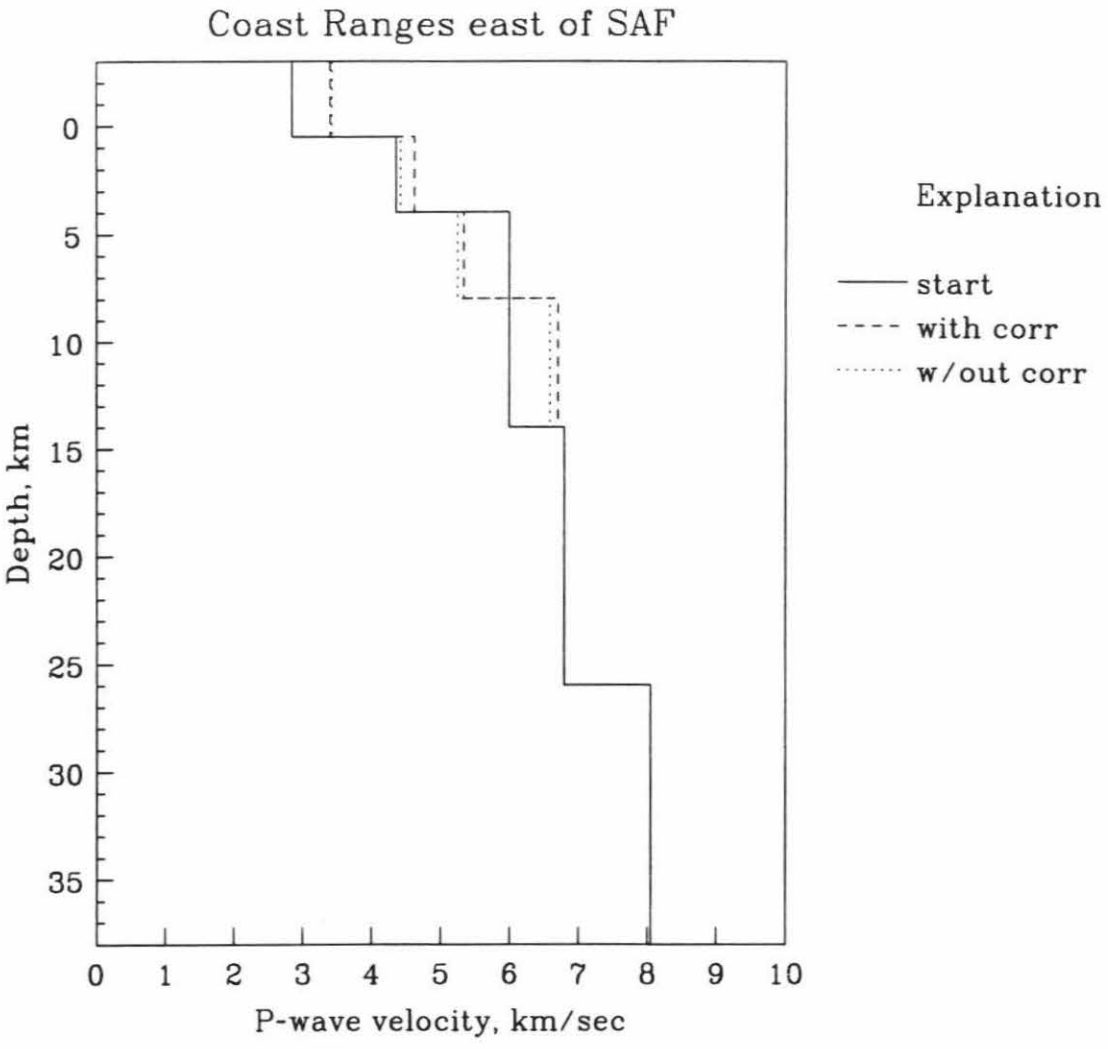

Figure 9.7 continued.

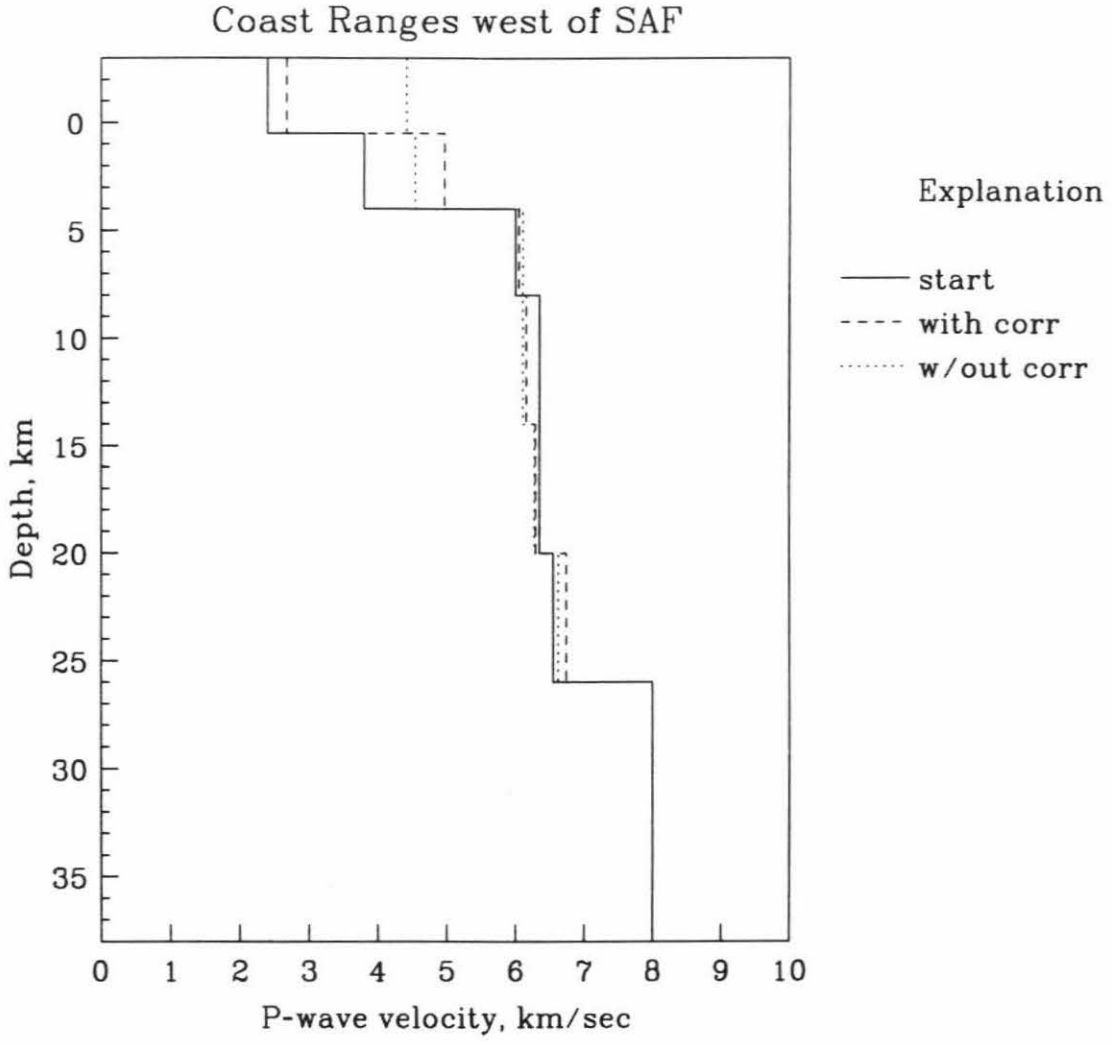

Figure 9.7 continued.

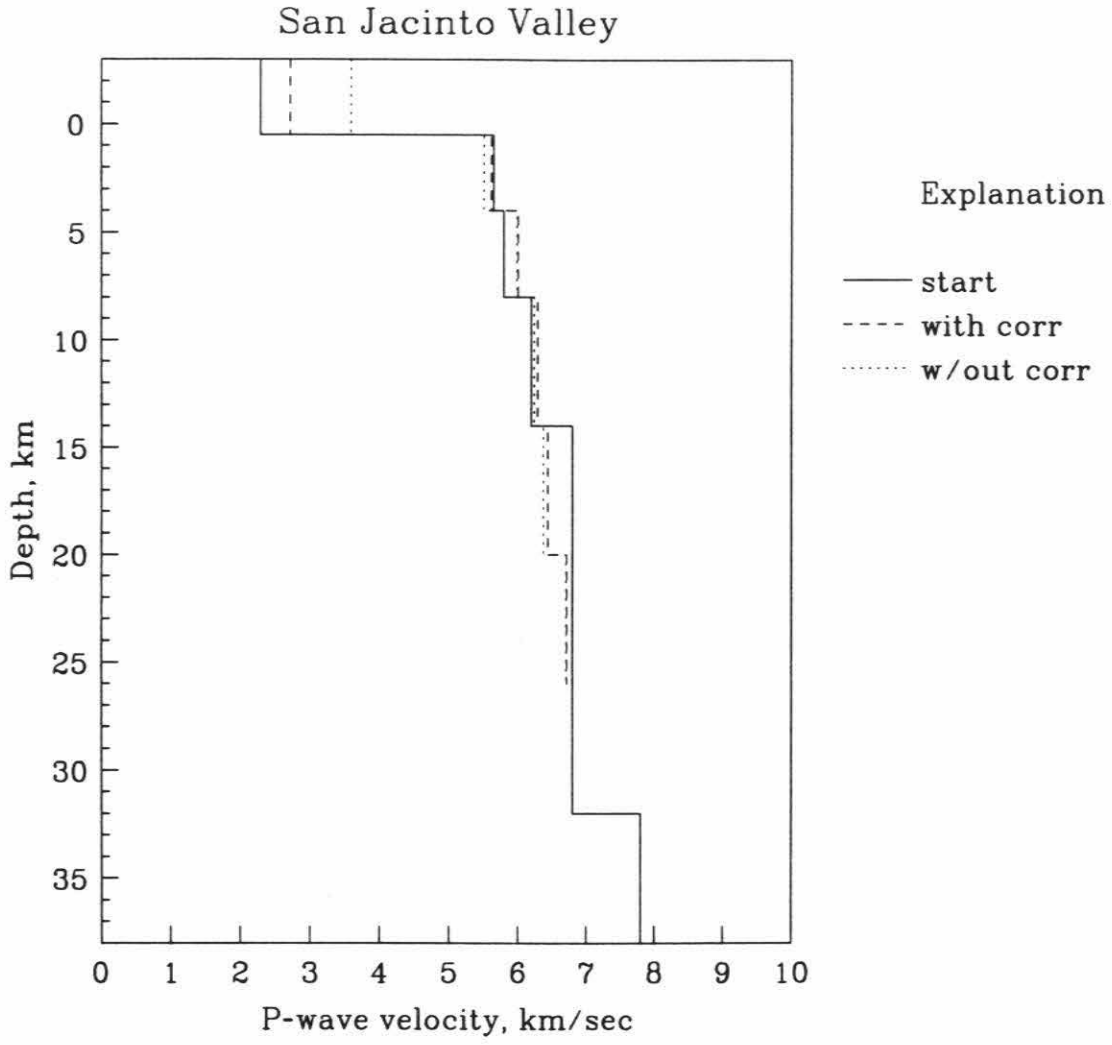

Figure 9.7 continued.

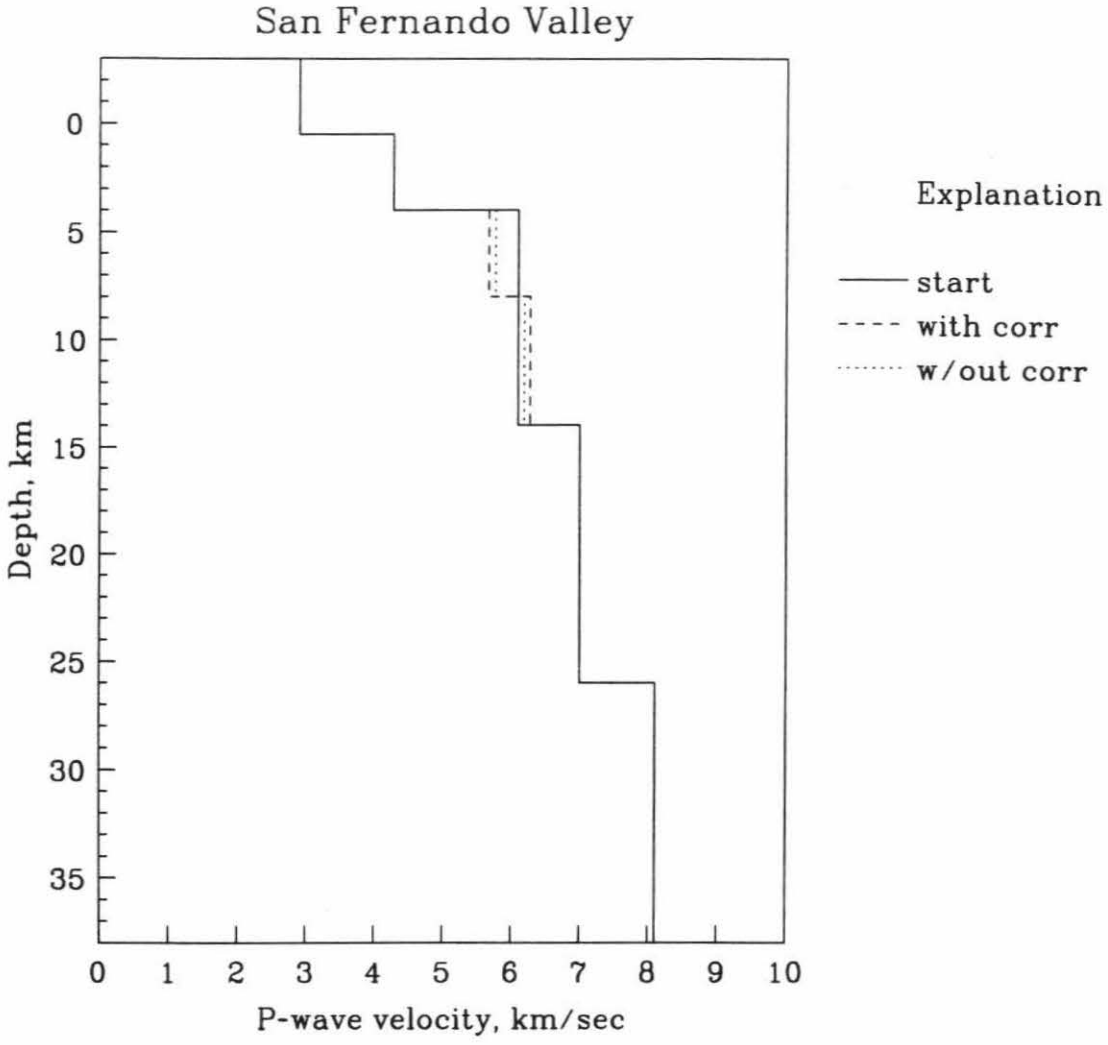

Figure 9.7 continued.

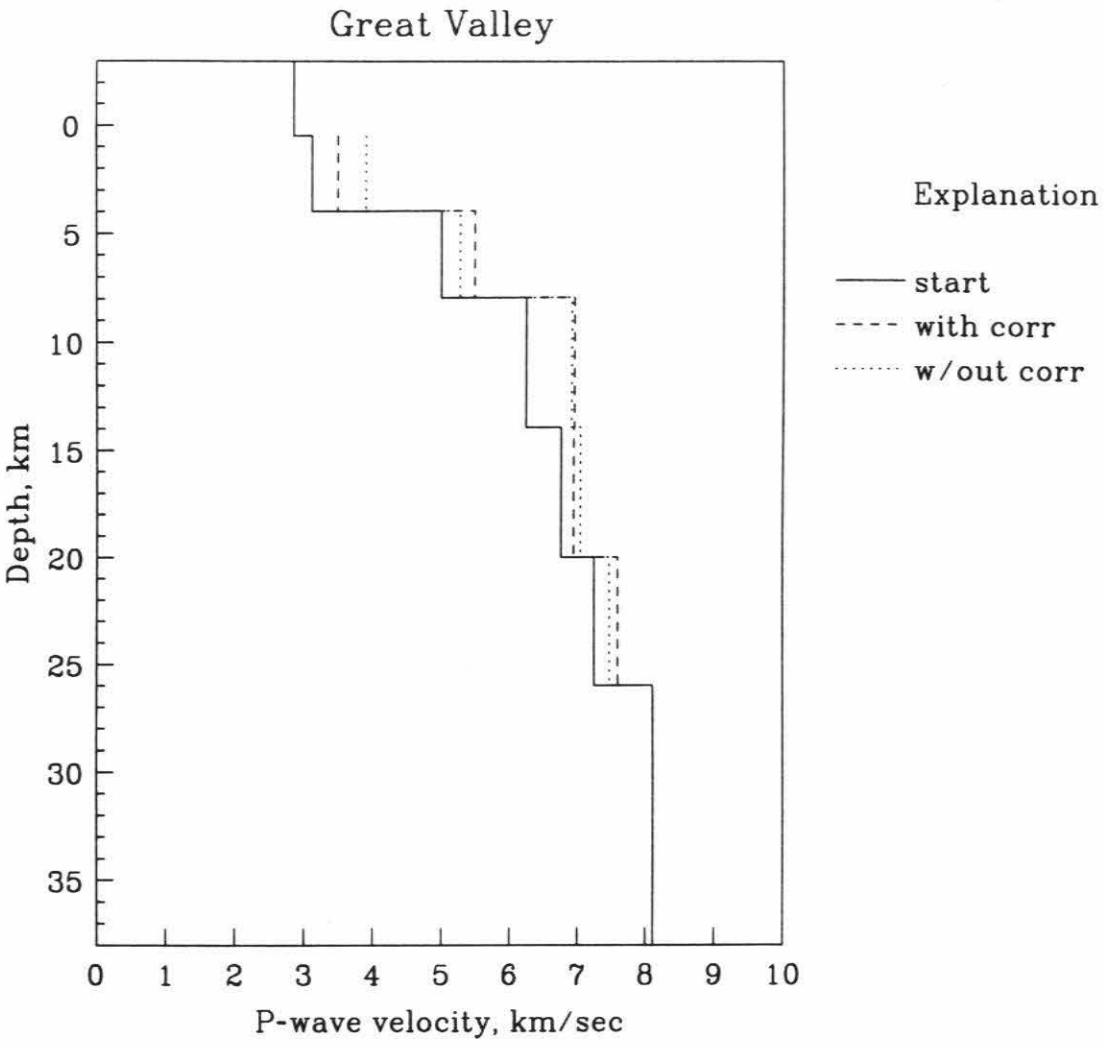

Figure 9.7 continued.

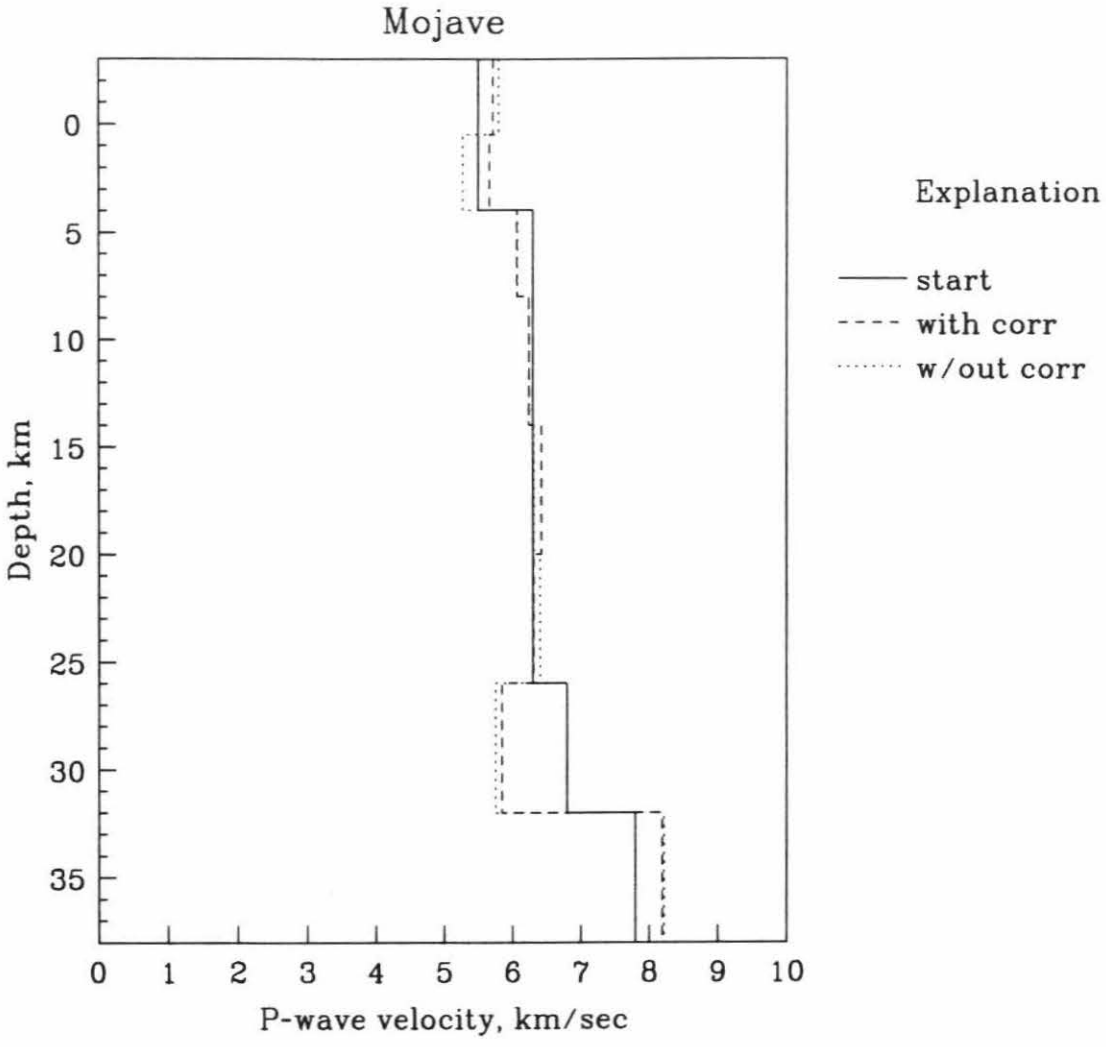

Figure 9.7 continued.

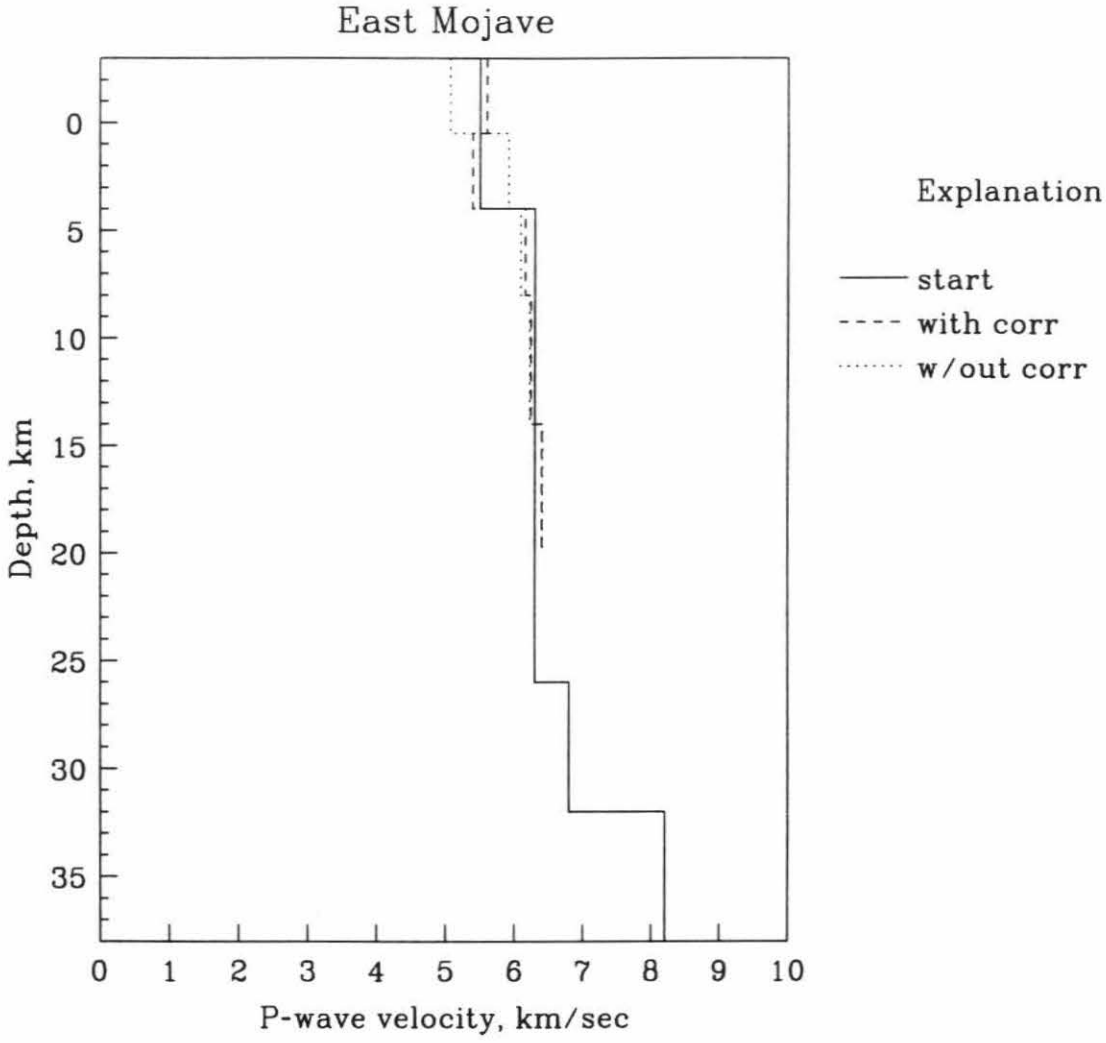

Figure 9.7 continued.

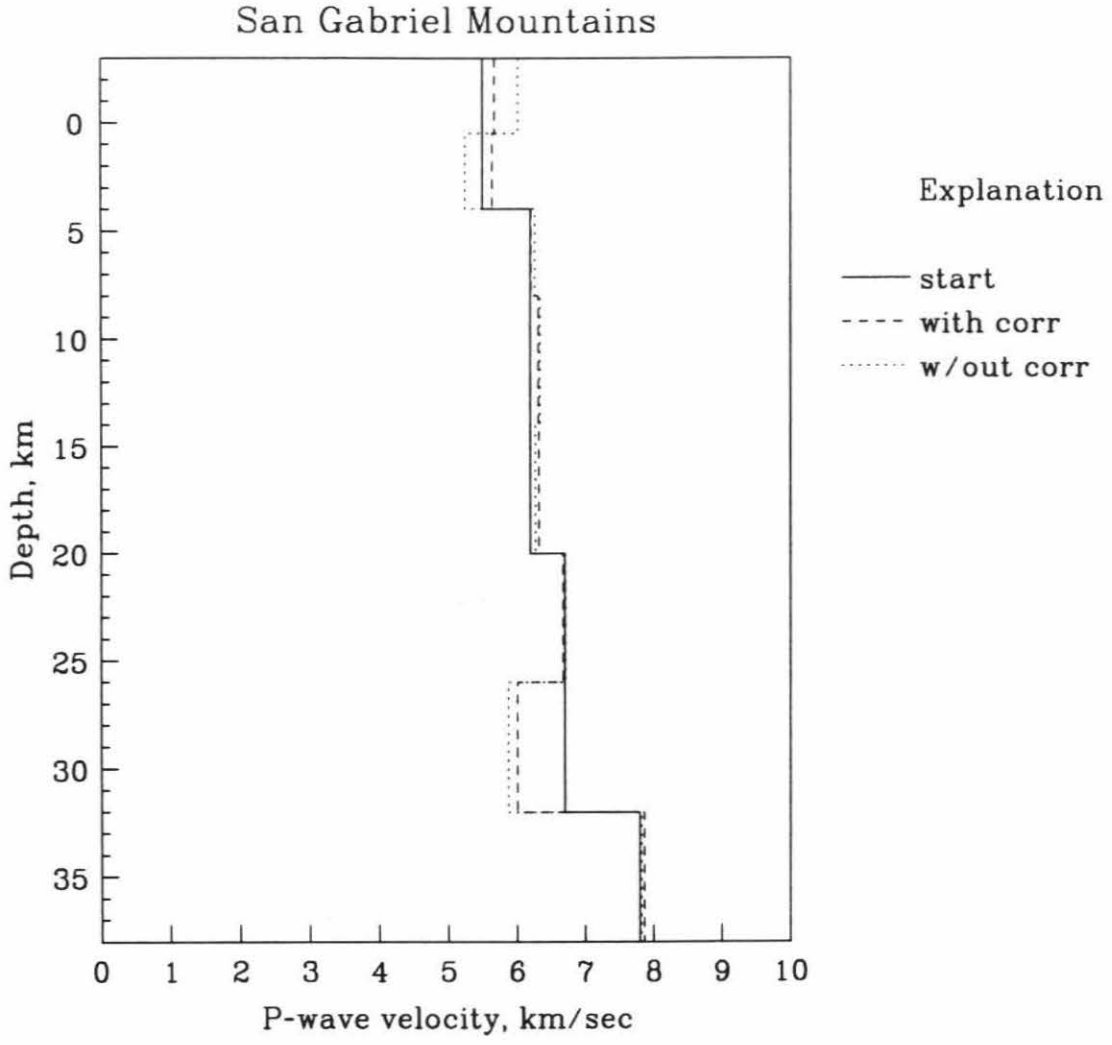

Figure 9.7 continued.

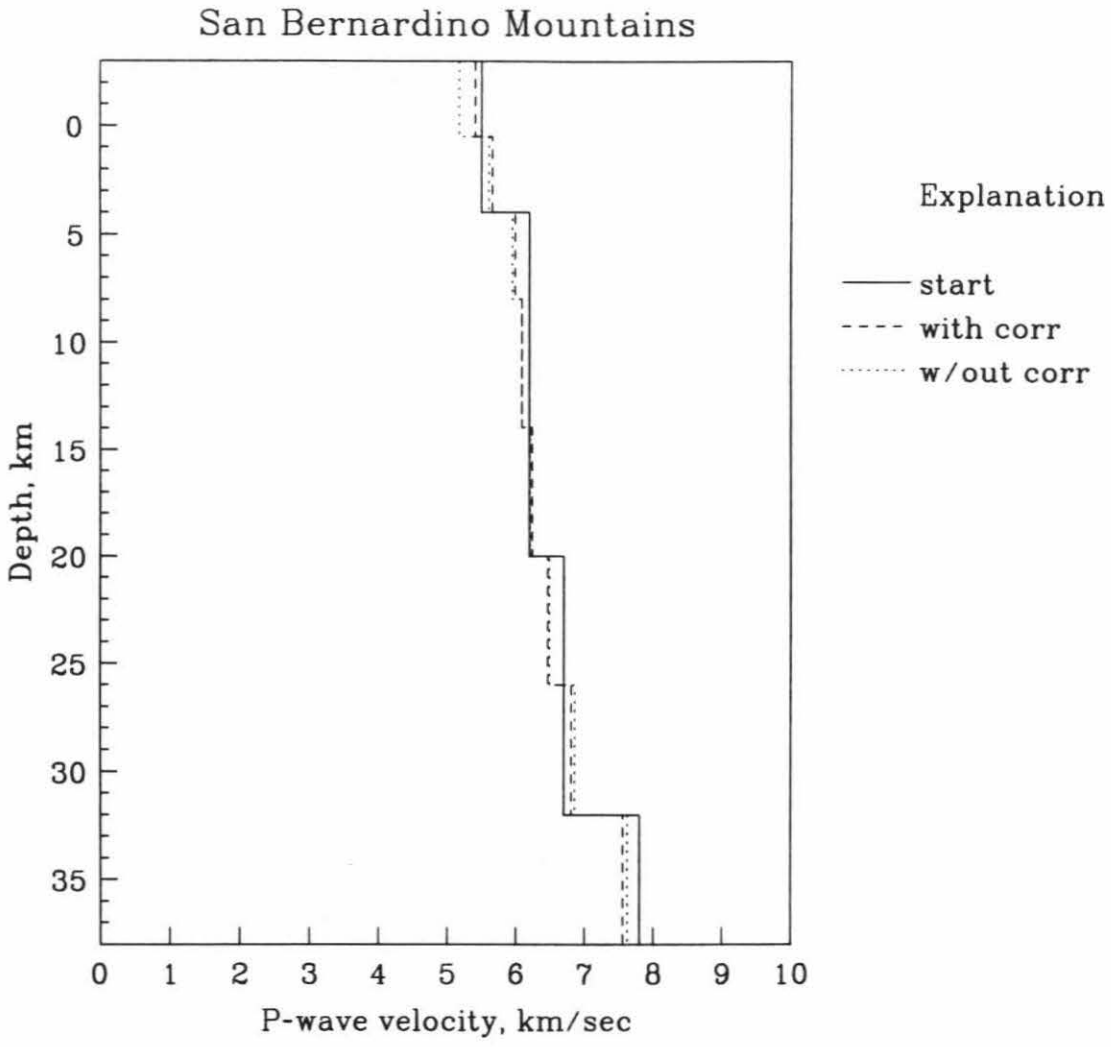

Figure 9.7 continued.

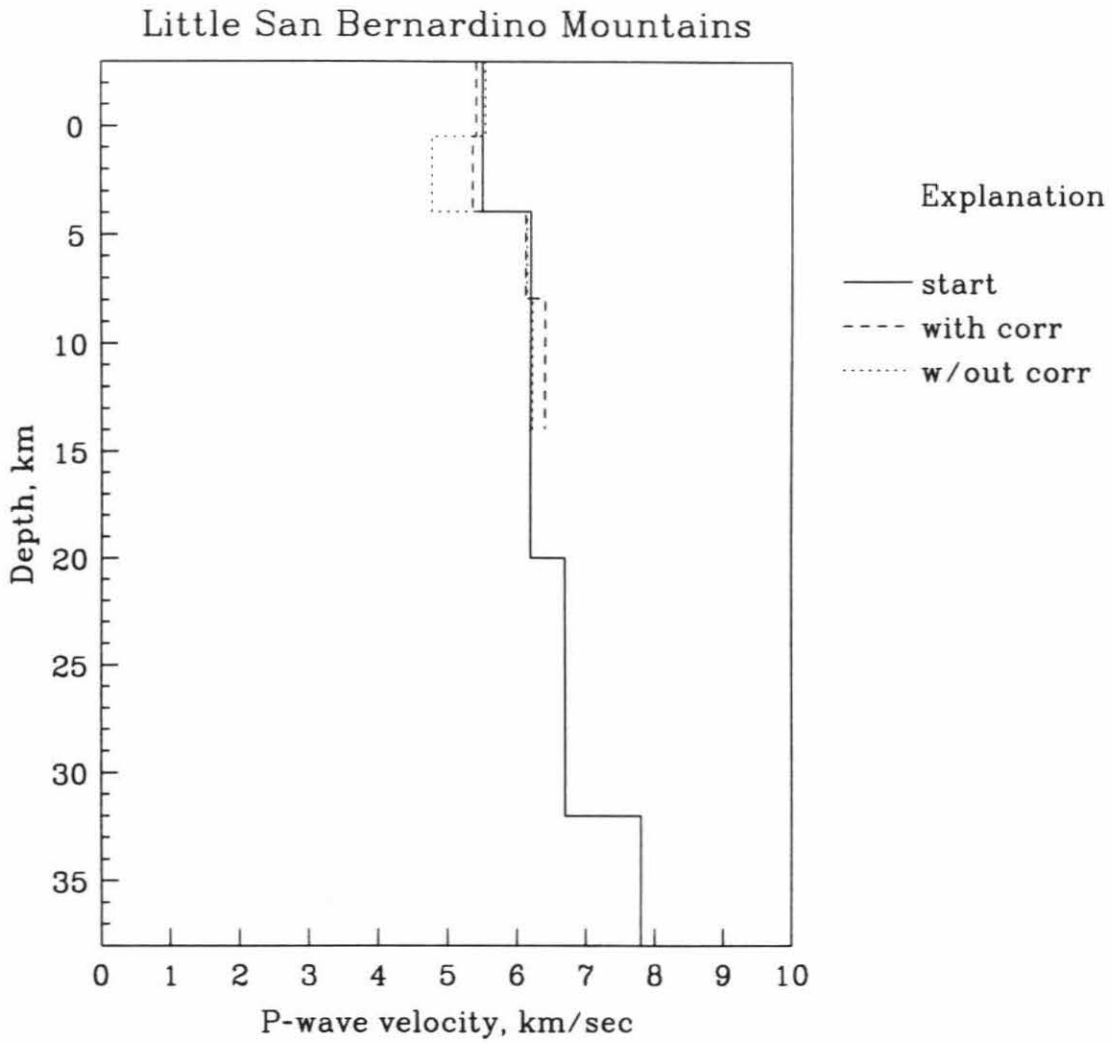

Figure 9.7 continued.

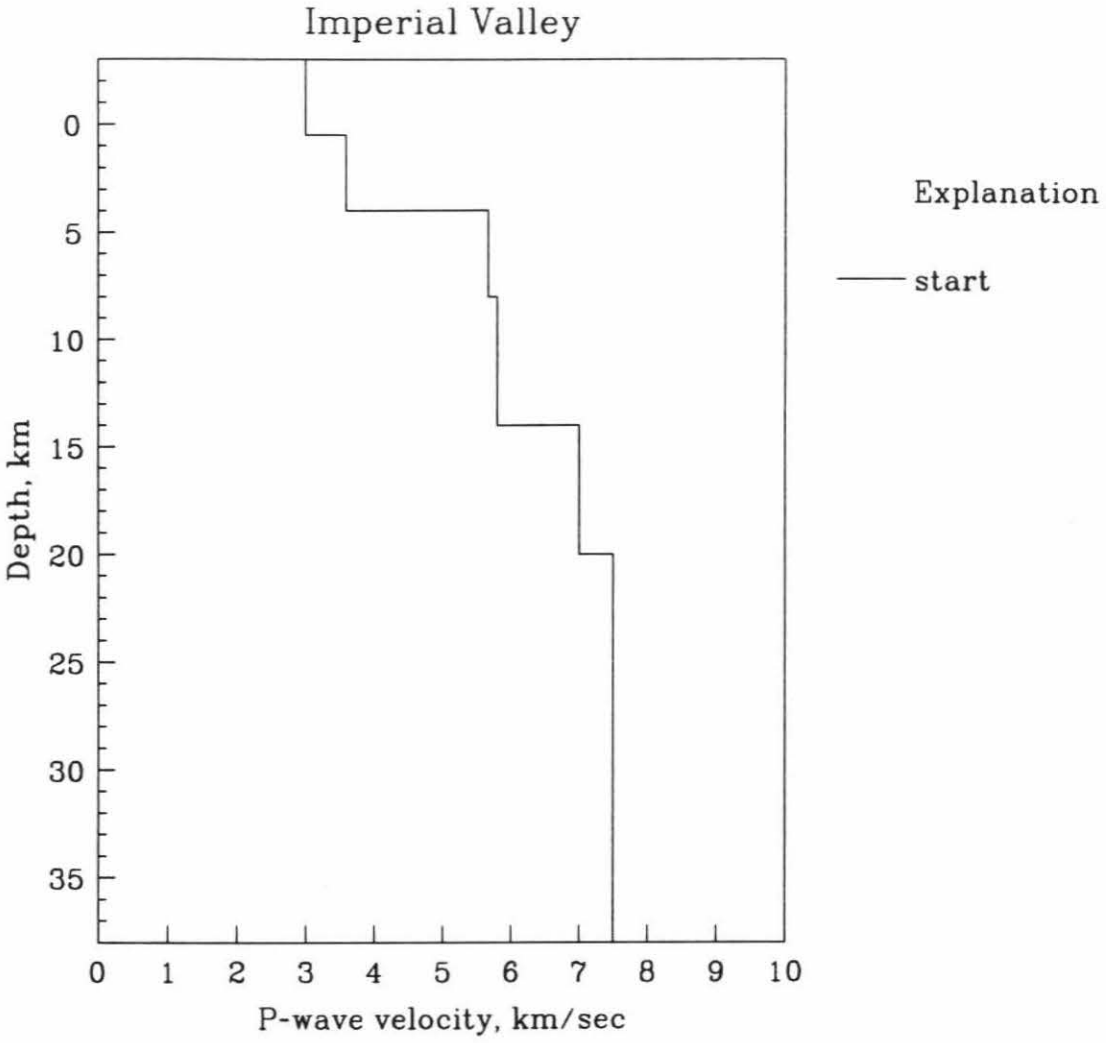

Figure 9.7 continued.

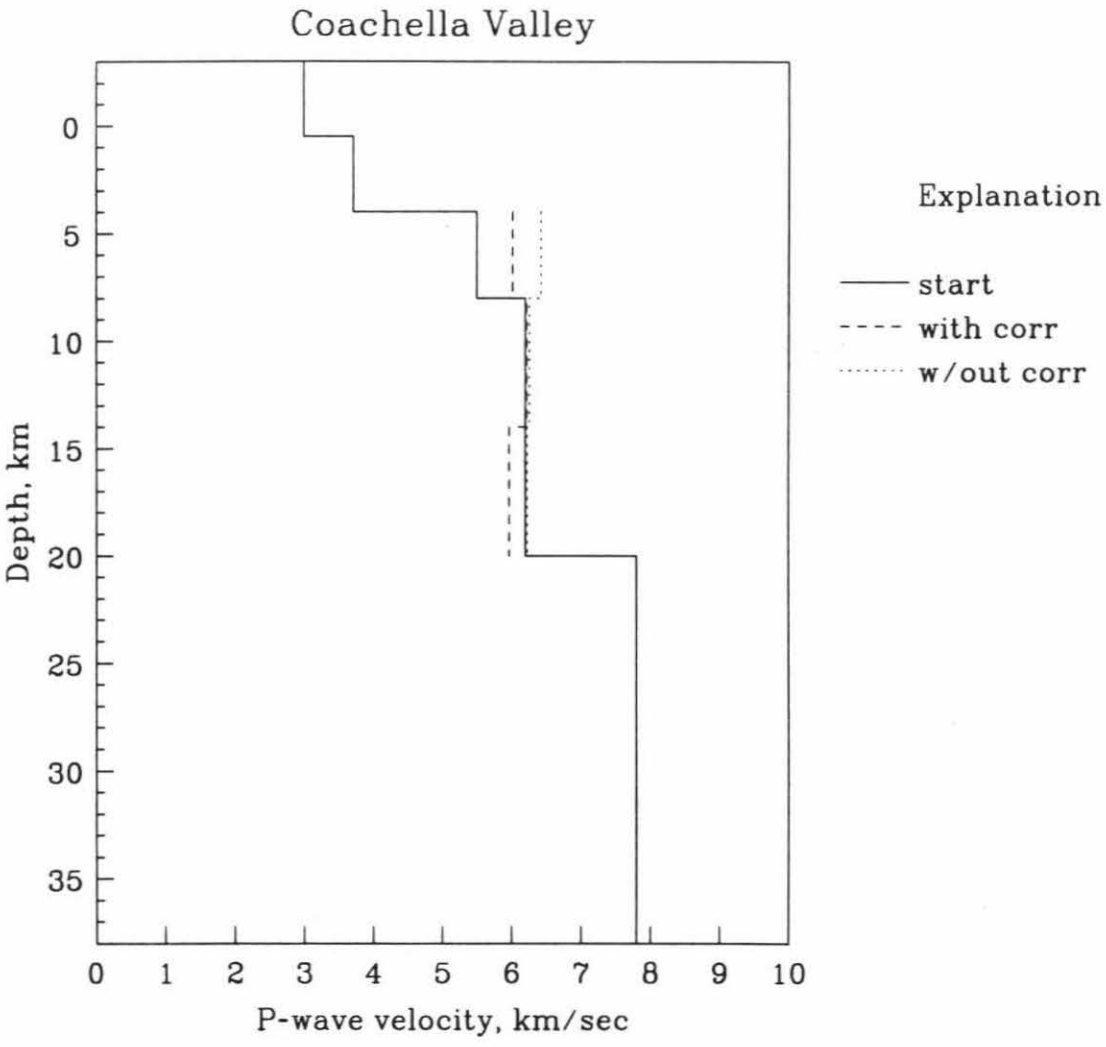

Figure 9.7 continued.

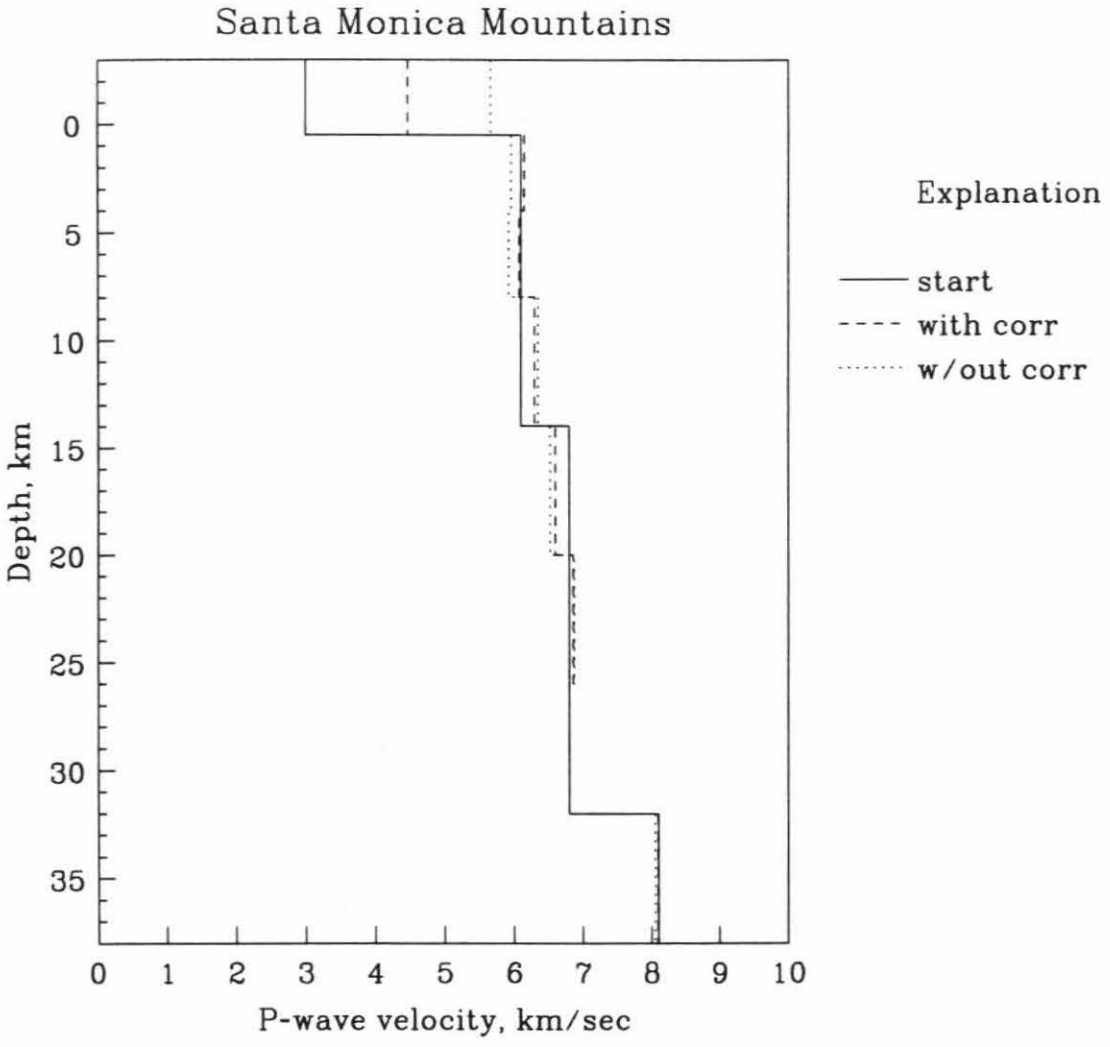

Figure 9.7 continued.

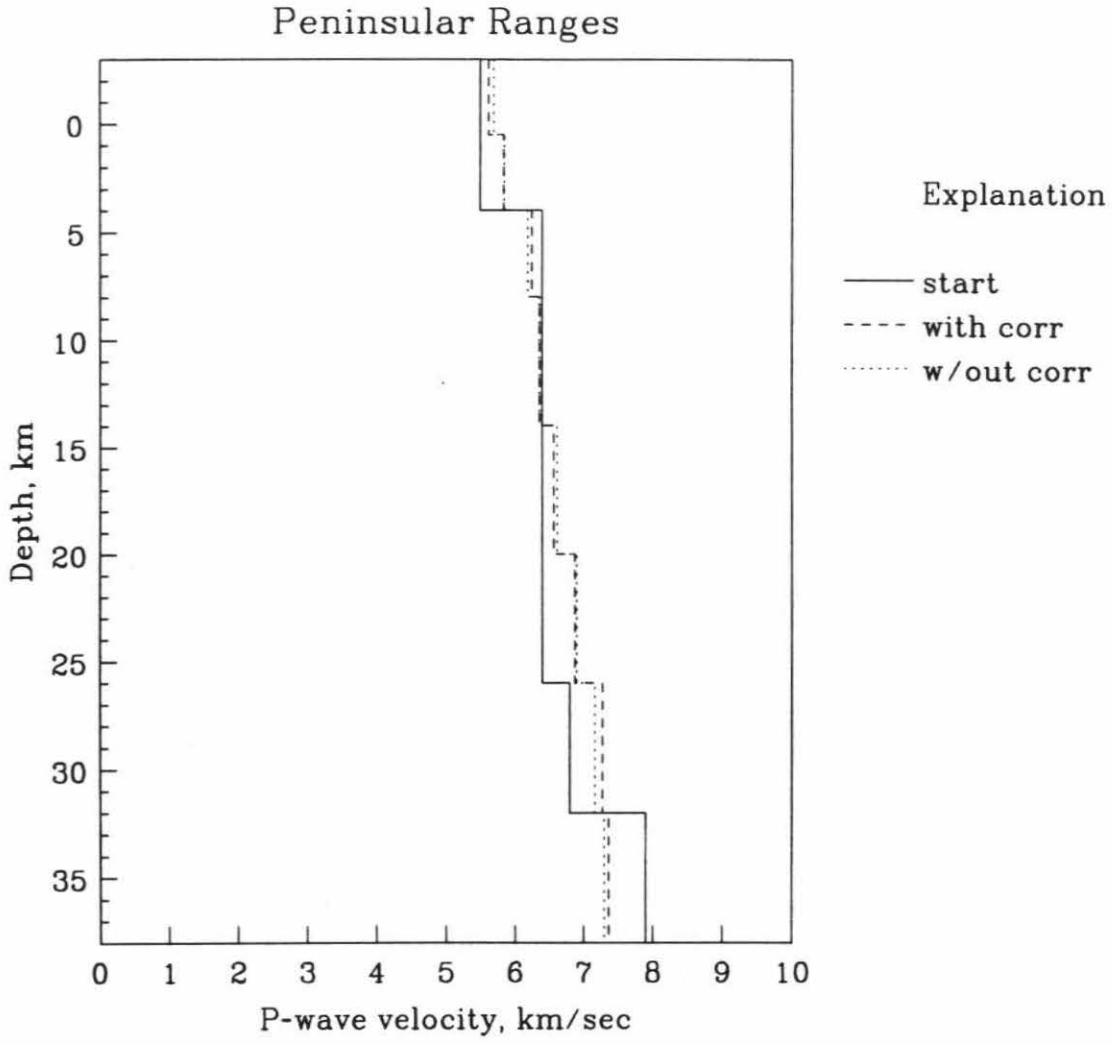

Figure 9.7 continued.

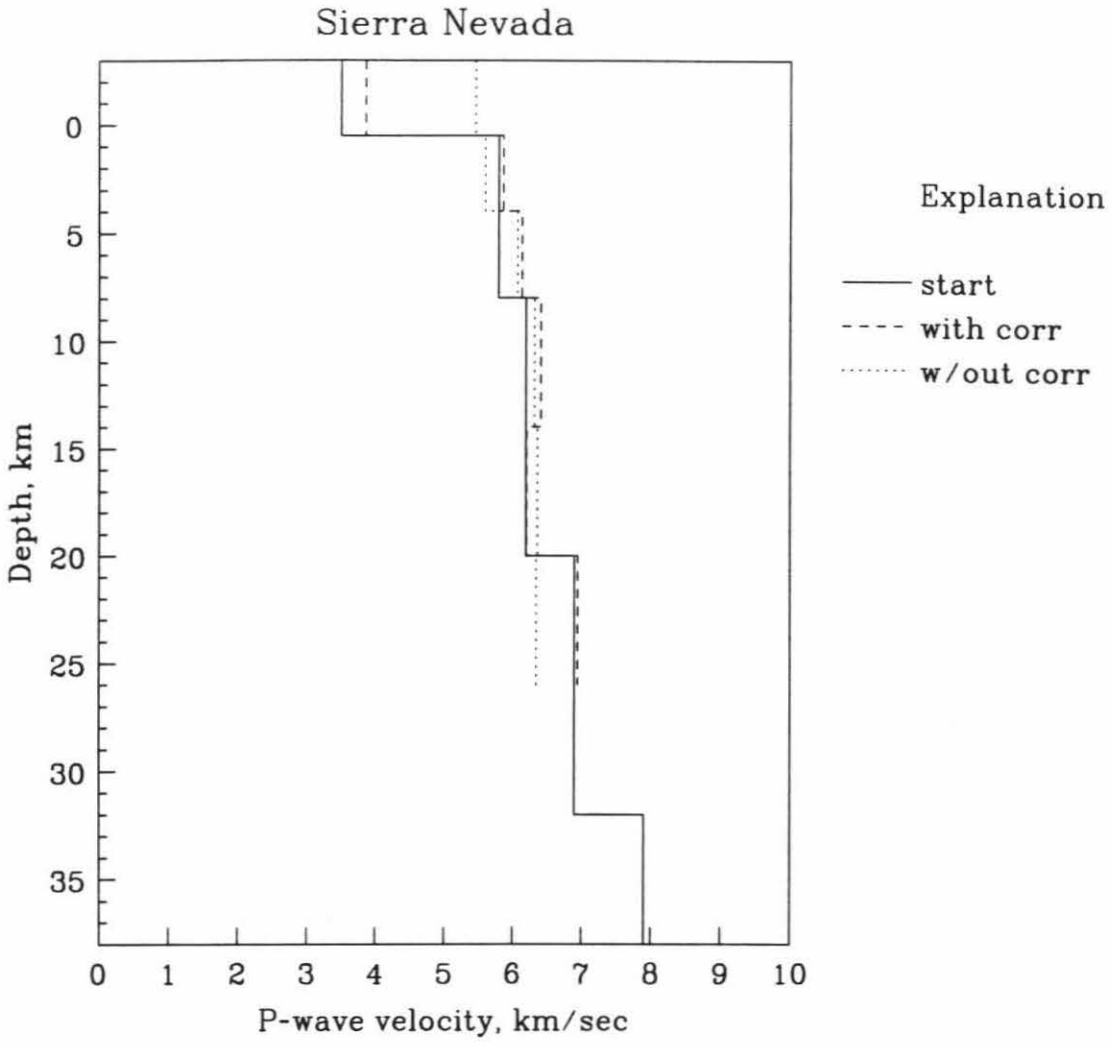

Figure 9.7 continued.

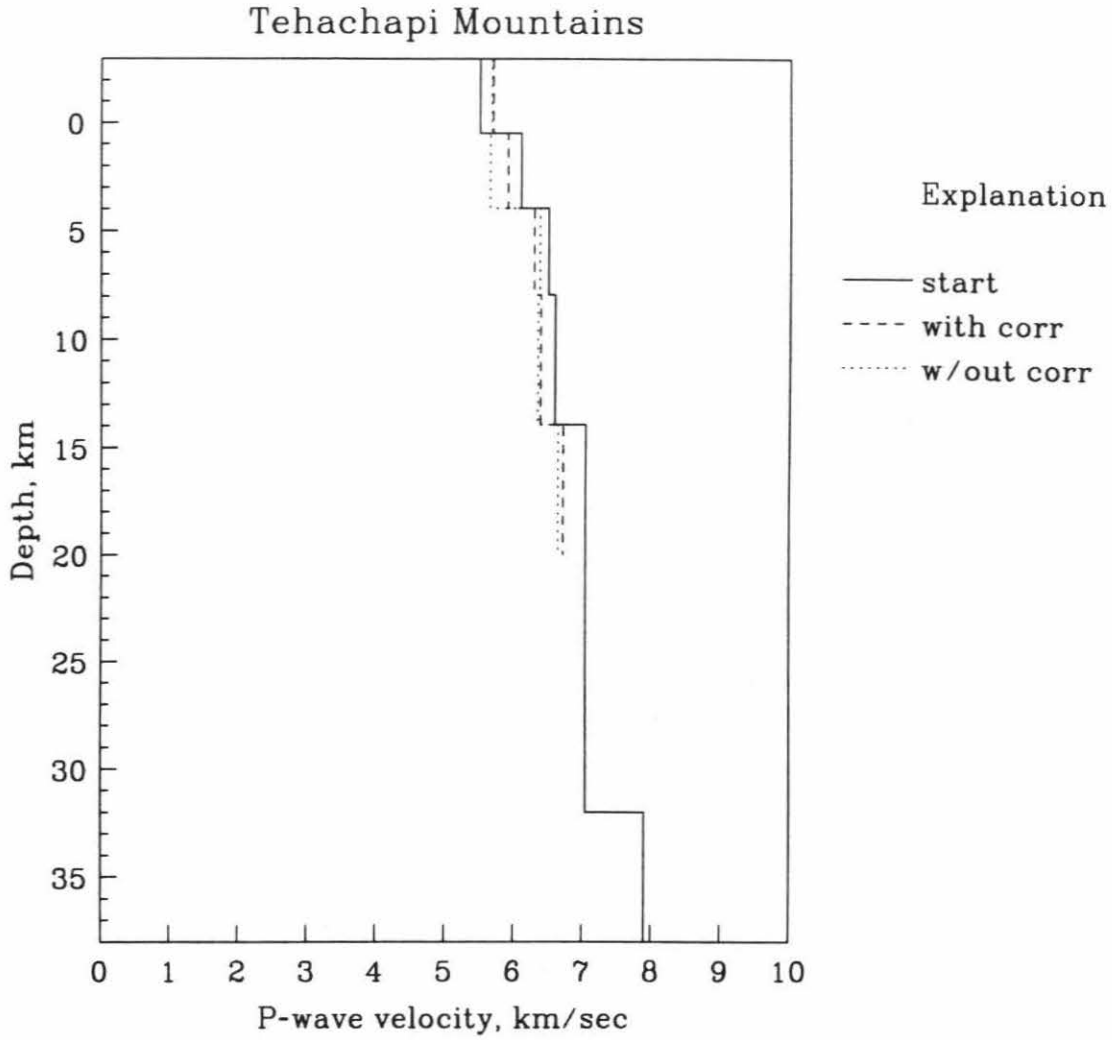

Figure 9.7 continued.

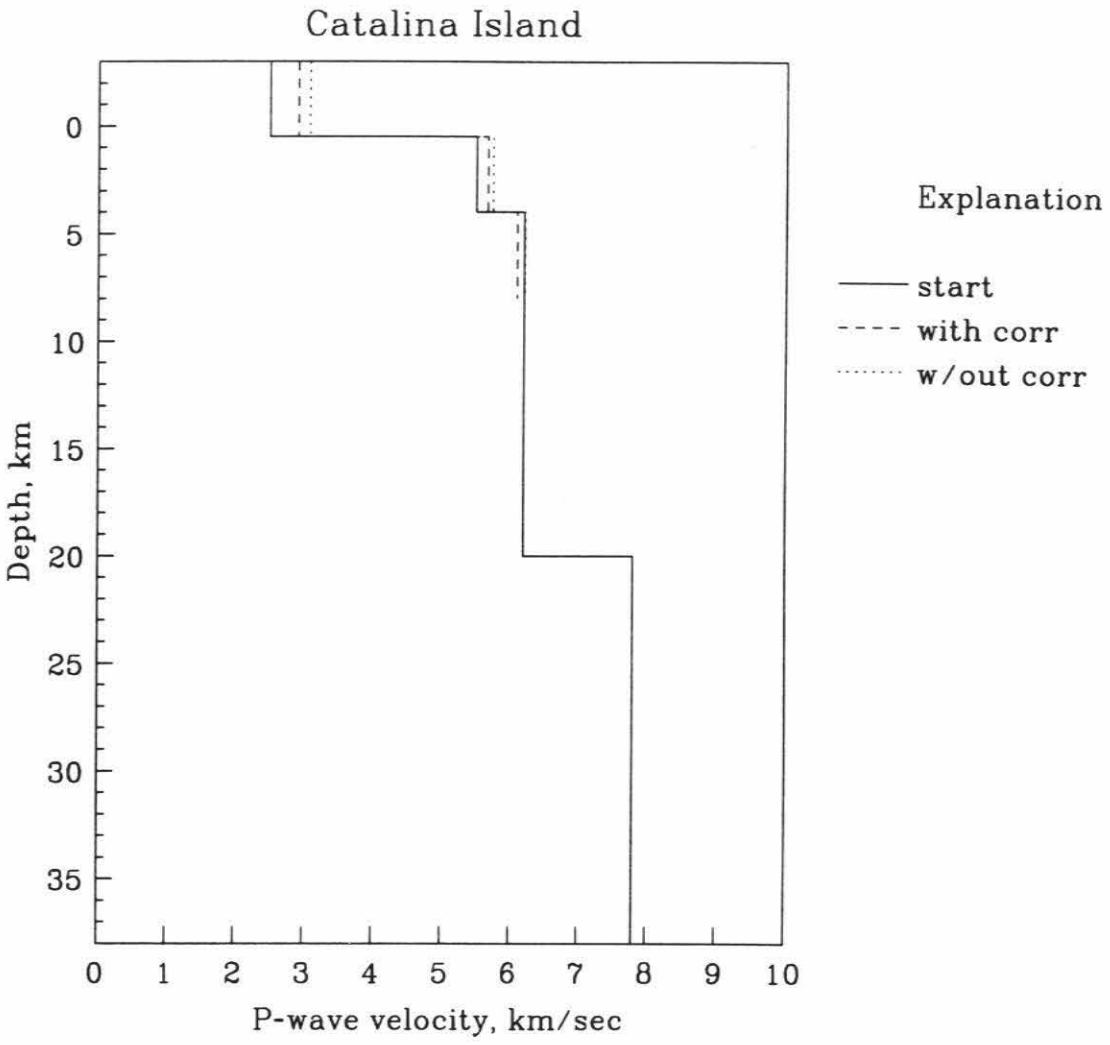

Figure 9.7 continued.

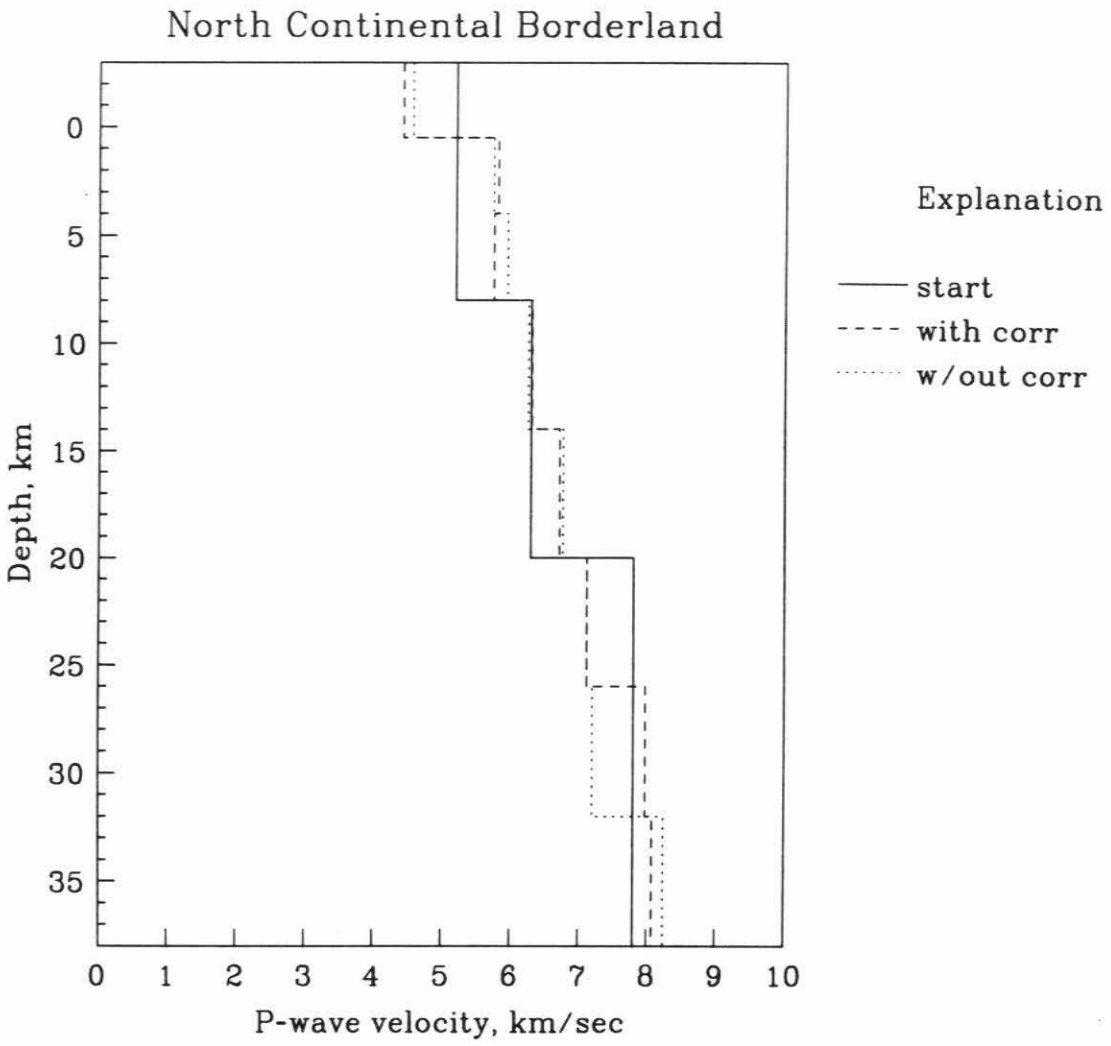

Figure 9.7 continued.

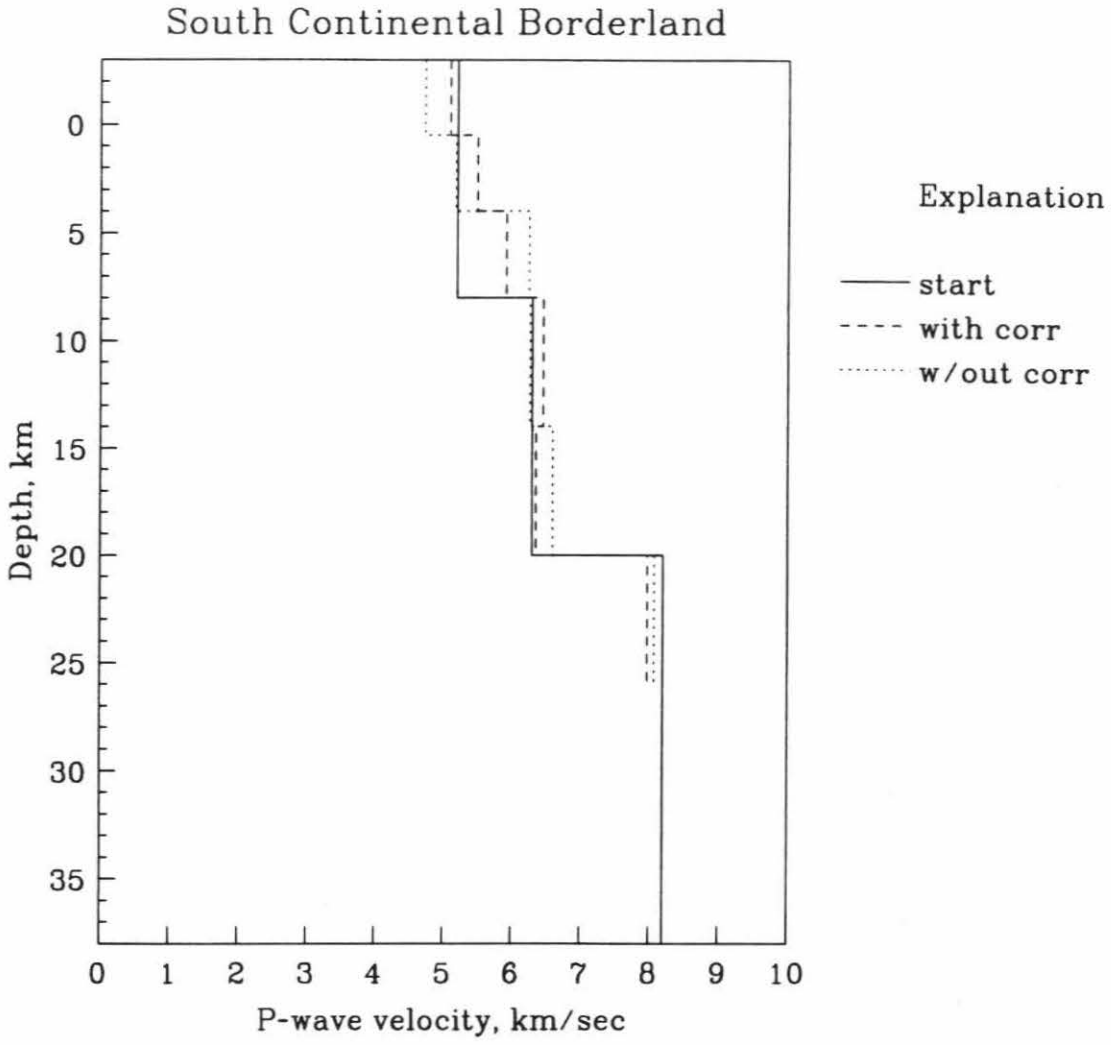

Figure 9.7 continued.

Table 10.1

Station Name	Latitude	Longitude	Station Correction (sec)
ABL	34.85083	-119.22083	-0.06
ACO	34.07983	-118.18767	0.00
ADL	34.55633	-117.41700	0.24
AGC	32.94117	-116.27550	0.00
ALB	33.73617	-117.40266	0.00
ARC	34.11533	-118.04217	0.00
ARV	35.12717	-118.82933	0.19
BAR	32.68000	-116.67167	-0.06
BAT	33.45900	-115.84100	-0.07
BC2	33.65700	-115.46117	0.05
BCH	35.18500	-120.08417	-0.14
BCM	33.65533	-115.44800	0.00
BHM	34.27883	-116.61517	0.00
BHR	34.00850	-118.36200	0.00
BLK	35.08800	-117.21850	-0.04
BLU	34.40667	-117.72684	-0.04
BMT	35.13583	-118.59683	-0.02
BON	32.69450	-115.26850	0.09
BOO	34.86800	-117.91033	0.21
BOW	32.84200	-116.22533	0.00
BRG	33.17117	-116.17400	0.24
BRT	34.61150	-117.96300	-0.03
BTL	34.25717	-117.00484	0.06
CAG	32.97783	-116.42683	0.00
CAH	33.50367	-116.69850	-0.12
CAL	35.10350	-117.94767	0.10
CAM	34.25450	-119.03333	-0.32
CAV	35.05233	-116.33916	0.00
CBK	32.91567	-116.25267	0.16
CFL	34.33283	-118.02300	-0.09
CFT	34.03517	-117.11100	-0.12
CH2	33.29617	-115.33617	-0.34
CHA	33.01333	-116.52617	0.00
CIS	33.40667	-118.40334	-0.03
CIW	33.46533	-118.55167	-0.06
CJP	34.18200	-118.98650	0.00
CJV	34.53050	-118.14450	-0.05
CKC	34.13633	-117.17467	0.10
CLC	35.81667	-117.59666	0.09
CLP	34.08883	-118.96416	0.00
CO2	33.84717	-115.34467	-0.11
COA	32.86350	-115.12267	-0.28
COQ	33.86050	-117.50967	0.02

COX	33.87250	-115.32800	0.00
COY	33.36050	-116.30933	0.11
CPC	34.85767	-119.20834	0.00
CPD	34.95383	-119.41833	0.00
CPE	32.88000	-117.10000	-0.07
CPM	34.15400	-116.19666	0.27
CPT	33.30333	-117.34000	-0.15
CRG	35.24217	-119.72334	0.19
CRR	32.88633	-115.96833	-0.05
CSP	34.29783	-117.35550	-0.04
CTW	33.67967	-115.87183	0.03
CWC	36.43917	-118.07800	0.46
CZA	35.05416	-119.51950	0.00
CZB	35.14150	-119.64633	0.00
CZC	35.22467	-119.70966	0.00
DAC	36.27700	-117.59367	0.00
DB2	33.73500	-117.06200	-0.09
DBM	34.97900	-118.36050	0.07
DRS	33.46400	-116.97017	0.00
DTP	35.26750	-117.84534	-0.14
DYC	33.28517	-116.82250	0.00
ECF	34.45800	-119.09067	-0.05
ECP	34.17683	-118.09634	0.00
EES	34.98333	-117.57883	0.00
ELM	34.52617	-117.64017	0.07
ELR	33.14734	-115.83250	0.32
ELS	33.64783	-117.42717	-0.04
EMS	32.74133	-114.98783	0.00
ERP	32.74350	-115.66267	0.00
EWC	33.93733	-116.38100	-0.27
FAL	34.30983	-117.80917	-0.15
FIL	34.42383	-118.83450	-0.07
FLA	33.87133	-117.97550	0.23
FLS	34.97033	-117.03850	-0.02
FMA	33.71250	-118.29117	0.16
FMP	35.19183	-117.57650	0.00
FOX	34.73300	-118.23067	0.10
FRG	33.75717	-116.06150	0.06
FRK	33.40083	-115.63683	-0.04
FTC	34.87083	-118.89183	-0.05
GAV	34.02250	-117.51234	-0.01
GFP	34.12933	-118.30983	-0.08
GLA	33.05167	-114.82667	-0.07
GOH	34.72850	-118.91067	0.00
GRI	34.11833	-118.29833	0.00
GRP	34.80433	-115.60450	0.04
GSA	34.13700	-118.12700	0.04
GSC	35.30167	-116.80500	0.17
GST	34.13700	-118.12700	0.00
GVF	34.05000	-118.11884	0.25
GVR	34.05000	-118.11884	0.20
HAY	33.70667	-115.63667	-0.05

HCM	33.99400	-118.38300	0.00
HDG	34.42883	-116.30500	0.02
HOD	34.83883	-117.24583	0.01
HOT	33.31417	-116.58167	0.00
HUN	34.12900	-118.11667	0.00
HYS	34.86383	-117.56866	0.00
IKP	32.64883	-116.10800	0.07
IND	33.81617	-116.22967	-0.32
INS	33.93567	-116.19434	-0.15
IPC	33.97066	-118.33450	0.00
IRC	34.38850	-118.40150	0.02
IRN	34.16000	-115.18400	-0.07
ISA	35.66333	-118.47334	-0.14
JAW	35.31583	-118.04483	-0.06
JFS	35.35083	-117.67000	0.06
JNH	34.44750	-117.95450	-0.07
JRH	34.80833	-117.69167	0.00
JUL	33.04833	-116.61283	-0.13
KEE	33.63833	-116.65317	0.08
KIN	34.18167	-118.08067	0.00
KYP	34.10183	-118.87950	-0.10
LAN	34.72700	-118.05100	0.19
LAQ	33.62800	-116.27966	0.19
LAV	34.76583	-116.28650	-0.04
LCL	33.83300	-118.20700	-0.06
LCM	34.01783	-118.28700	0.00
LED	34.46767	-115.93650	0.02
LEO	34.63133	-118.30367	-0.11
LHU	34.67167	-118.41167	-0.03
LJB	34.59117	-117.84800	-0.01
LLN	34.48450	-117.84050	-0.03
LNA	33.78917	-118.05450	0.00
LOK	34.72450	-119.09133	0.10
LOW	34.81183	-119.01667	0.00
LRM	35.47733	-117.68916	-0.01
LRR	34.52600	-118.02766	0.10
LTC	33.48900	-115.07000	-0.33
LTM	33.91500	-114.91833	0.80
LUC	34.45500	-116.96300	0.00
LVB	34.60533	-117.86467	0.00
MAR	35.00250	-119.33933	-0.07
MDA	33.91300	-116.99950	-0.16
MEC	33.63533	-116.02850	0.16
MIR	33.41617	-116.08100	0.19
MLL	34.09133	-116.93633	-0.01
MON	34.13650	-118.02500	0.00
MOV	34.15583	-116.50166	0.10
MRV	34.06133	-116.54300	-0.31
MTU	37.35333	-118.56350	0.00
MWC	34.22333	-118.05833	0.04
NAR	34.03200	-118.05483	0.00
NW2	33.09050	-115.69234	0.05

OBB	33.16733	-115.63667	-0.24
OLY	33.43133	-117.11750	-0.09
ORK	33.56617	-115.76917	0.00
PAD	35.63933	-120.86433	-0.05
PAR	36.24917	-120.34200	0.13
PAS	34.14917	-118.17150	0.06
PCF	34.05317	-117.79066	0.07
PCR	36.09383	-120.43467	-0.02
PEC	33.89183	-117.16000	0.03
PEM	34.16733	-117.86967	0.12
PHC	35.68217	-121.15250	0.00
PIR	33.52367	-117.21300	0.00
PIV	35.90650	-120.68233	0.12
PKM	34.89583	-119.81883	-0.25
PLE	34.96850	-119.06800	0.29
PLM	33.35333	-116.86166	0.04
PMC	35.72467	-120.37050	0.07
PMG	35.42983	-120.52033	0.00
PNM	33.97733	-115.80083	0.08
POB	33.68667	-116.92333	-0.03
POC	34.10000	-117.71433	0.00
PPR	35.64767	-120.70067	0.02
PPT	36.10833	-120.72117	-0.15
PRI	36.14167	-120.66500	-0.14
PSH	35.59083	-120.41534	-0.06
PSM	36.06967	-120.59467	-0.01
PSP	33.79383	-116.54884	-0.01
PTD	34.00417	-118.80634	0.05
PTR	35.65467	-120.21117	0.14
PVR	33.75217	-118.37050	0.04
PYR	34.56800	-118.74167	0.11
QAL	34.74967	-118.71467	-0.01
RAY	34.03633	-116.81116	0.03
RCH	34.30733	-116.35050	0.01
RCP	33.77767	-118.13333	0.01
RDM	34.40000	-117.18500	0.00
RHC	34.00783	-118.02450	0.00
RMR	34.21283	-116.57533	0.04
ROD	34.62967	-116.60484	0.12
ROS	34.09566	-118.06284	0.00
RRC	33.66533	-117.29134	0.00
RUN	32.97217	-114.97717	0.03
RVR	33.99333	-117.37500	0.00
RVS	34.05133	-114.51800	0.20
RYS	34.64333	-119.35167	-0.33
SAD	34.08100	-118.66500	-0.01
SAT	33.70783	-117.89050	0.05
SAY	33.15833	-116.67550	0.00
SBA	34.01333	-119.43716	0.24
SBB	34.68833	-117.82500	0.04
SBC	34.44167	-119.71333	-0.04
SBC	34.93967	-120.17200	-0.07

SBC	34.36867	-119.34383	0.01
SBI	33.48067	-119.02866	0.20
SBK	35.07883	-117.58134	0.01
SBL	34.49650	-119.71350	0.77
SBL	34.11450	-119.06416	0.10
SBL	34.55950	-120.40033	0.29
SBS	33.99467	-119.63316	0.00
SBS	34.03733	-120.35017	0.04
SBS	33.24467	-119.50633	-0.04
SCC	34.93967	-120.17200	0.12
SCD	34.36867	-119.34383	-0.07
SCI	32.98000	-118.54667	0.29
SCY	34.10617	-118.45417	0.03
SDL	35.38050	-117.88667	0.00
SDW	34.60917	-117.07417	-0.07
SFD	34.11833	-117.94317	0.00
SGL	32.64917	-115.72533	-0.05
SHH	34.18767	-115.65450	-0.03
SIL	34.34783	-116.82667	0.05
SIP	34.20400	-118.79900	0.10
SJQ	33.62000	-117.84500	0.00
SLC	34.49650	-119.71350	-0.15
SLG	34.11450	-119.06416	-0.21
SLP	34.55950	-120.40033	0.00
SLT	33.26483	-115.92316	0.00
SMD	34.17400	-118.05350	0.00
SME	33.82267	-117.35533	-0.02
SMO	33.53584	-116.46167	-0.02
SNC	35.14300	-118.30217	-0.15
SNS	33.43167	-117.54833	0.27
SPA	34.10517	-118.17467	0.00
SPC	33.56300	-118.13950	0.80
SPM	34.47200	-115.40266	0.18
SRT	35.69183	-117.74934	0.33
SS2	34.20767	-117.49966	0.03
SSC	33.99467	-119.63316	0.03
SSK	34.21617	-117.68867	0.11
SSM	34.03733	-120.35017	0.02
SSN	33.24467	-119.50633	0.06
STT	34.78850	-118.46183	0.26
SUN	34.21067	-117.69300	0.05
SUP	32.95517	-115.82383	-0.18
SWM	34.71667	-118.58334	0.02
SYP	34.52717	-119.97784	0.09
SYS	32.57967	-116.91150	0.00
TAM	34.38200	-117.68450	0.00
TCC	33.99450	-118.01283	0.12
TEJ	35.22983	-118.68950	0.17
THC	34.90867	-118.66350	-0.05
TJR	35.02750	-118.74250	-0.04
TMB	35.08733	-119.53467	0.20
TOW	35.80833	-117.76500	0.46

TPC	34.10583	-116.04867	-0.05
TPO	34.87883	-118.22767	0.10
TPR	34.08883	-118.58667	0.00
TTM	34.33533	-114.82750	-1.07
TWL	34.27833	-118.59450	0.21
VG2	33.83183	-116.80917	0.00
VPD	33.81500	-117.76167	-0.05
VST	33.15667	-117.23167	0.02
WAS	35.73817	-118.55700	-0.15
WBM	35.60800	-117.89000	0.11
WBS	35.53700	-118.13950	-0.13
WCH	35.88300	-118.07467	-0.23
WCO	35.62250	-118.43750	0.00
WCP	36.07100	-117.85017	0.06
WCS	36.02633	-117.76683	0.26
WCX	35.71050	-117.59967	-0.02
WHF	35.69617	-118.34850	0.04
WHS	36.10500	-117.76117	0.49
WHV	35.51000	-118.51783	-0.02
WIS	33.27600	-115.59300	-0.01
WJP	35.41083	-118.48067	-0.07
WKT	35.79400	-118.44250	0.06
WLH	36.15233	-118.31167	0.15
WLK	33.05133	-115.49067	0.11
WMF	36.11750	-117.85284	0.32
WNM	35.84283	-117.90483	-0.10
WOF	35.53567	-118.71250	-0.24
WOR	35.69650	-118.24200	0.02
WRC	35.95067	-117.64816	0.25
WRV	36.00783	-117.89034	0.12
WSC	35.70433	-117.88650	-0.09
WSH	35.63267	-117.49167	-0.17
WSP	34.59617	-118.57867	-0.01
WVP	35.94967	-117.81700	0.18
WWP	35.73550	-118.08700	-0.06
WWR	33.99183	-116.65600	0.00
XMS	35.52333	-117.35467	0.06
YAQ	33.16800	-116.35000	0.19
YEG	35.43633	-119.95934	0.26
YUH	32.64767	-115.92300	0.10

Table 10.2

Los Angeles Basin

Layer Number	Starting Velocity	Final Velocity	Resolution
1	2.65	2.57	.14
2	4.11	4.09	.88
3	6.40	6.02	.96
4	6.40	6.41	.99
5	6.40	6.50	.97
6	6.40	6.82	.88
7	6.80	7.74	.94
8	7.80	8.02	.97

Santa Barbara Channel

Layer Number	Starting Velocity	Final Velocity	Resolution
1	2.00		
2	2.84		
3	4.90		
4	6.36		
5	7.01		
6	8.33		
7	8.33		
8	8.33		

Ventura Basin

Layer Number	Starting Velocity	Final Velocity	Resolution
1	2.00	1.55	.19
2	3.33	4.90	.71
3	4.90	5.14	.83
4	6.40	5.80	.95
5	7.00	6.70	.96
6	7.00	7.33	.94
7	8.00		
8	8.00		

Borrego Valley

Layer Number	Starting Velocity	Final Velocity	Resolution
1	2.50	2.80	.04
2	5.10	5.14	.58
3	6.00	5.99	.90
4	6.00		
5	7.10		
6	7.10		
7	7.90		
8	7.90		

Coast Ranges, east of SAF

Layer Number	Starting Velocity	Final Velocity	Resolution
1	2.85	3.40	.23
2	4.36	4.63	.52
3	6.00	5.34	.70
4	6.00	6.71	.92
5	6.80		
6	6.80		
7	8.05		
8	8.05		

Coast Ranges, west of SAF

Layer Number	Starting Velocity	Final Velocity	Resolution
1	2.40	2.68	.41
2	3.80	4.97	.65
3	6.00	6.05	.94
4	6.35	6.16	.97
5	6.35	6.29	.96
6	6.55	6.74	.95
7	8.00		
8	8.00		

San Jacinto Valley

Layer Number	Starting Velocity	Final Velocity	Resolution
1	2.29	2.72	.52
2	5.65	5.62	.89
3	5.80	6.01	.97
4	6.20	6.29	.98
5	6.80	6.44	.94
6	6.80	6.72	.91
7	6.80		
8	7.80		

San Fernando Valley

Layer Number	Starting Velocity	Final Velocity	Resolution
1	2.90		
2	4.28		
3	6.10	5.67	.63
4	6.10	6.28	.70
5	7.00		
6	7.00		
7	8.10		
8	8.10		

Great Valley

Layer Number	Starting Velocity	Final Velocity	Resolution
1	2.85		
2	3.12	3.49	.39
3	5.00	5.49	.49
4	6.25	6.96	.95
5	6.77	6.95	.90
6	7.25	7.60	.91
7	8.11		
8	8.11		

Mojave

Layer Number	Starting Velocity	Final Velocity	Resolution
1	5.50	5.72	.95
2	5.50	5.67	.93
3	6.30	6.07	.99
4	6.30	6.24	1.00
5	6.30	6.43	.99
6	6.30	6.31	.68
7	6.80	5.85	.58
8	7.80	8.19	.99

East Mojave

Layer Number	Starting Velocity	Final Velocity	Resolution
1	5.50	5.60	.74
2	5.50	5.39	.59
3	6.30	6.16	.97
4	6.30	6.24	.86
5	6.30	6.40	.88
6	6.30		
7	6.80		
8	8.20		

San Gabriel Mountains

Layer Number	Starting Velocity	Final Velocity	Resolution
1	5.50	5.68	.82
2	5.50	5.64	.91
3	6.20	6.21	.99
4	6.20	6.32	1.00
5	6.20	6.33	.98
6	6.70	6.68	.96
7	6.70	6.01	.78
8	7.80	7.87	.99

San Bernardino Mountains

Layer Number	Starting Velocity	Final Velocity	Resolution
1	5.50	5.41	.79
2	5.50	5.66	.90
3	6.20	5.99	.99
4	6.20	6.09	.99
5	6.20	6.24	.96
6	6.70	6.47	.92
7	6.70	6.81	.67
8	7.80	7.56	.95

Little San Bernardino Mountains

Layer Number	Starting Velocity	Final Velocity	Resolution
1	5.50	5.41	.61
2	5.50	5.36	.77
3	6.20	6.13	.98
4	6.20	6.41	.75
5	6.20		
6	6.70		
7	6.70		
8	7.80		

Imperial Valley

Layer Number	Starting Velocity	Final Velocity	Resolution
1	3.00		
2	3.59		
3	5.67		
4	5.80		
5	7.00		
6	7.50		
7	7.50		
8	7.50		

Coachella Valley

Layer Number	Starting Velocity	Final Velocity	Resolution
1	3.00		
2	3.72		
3	5.50	6.02	.93
4	6.20	6.22	.95
5	6.20	5.97	.75
6	7.80		
7	7.80		
8	7.80		

Santa Monica Mountains

Layer Number	Starting Velocity	Final Velocity	Resolution
1	3.00	4.47	.26
2	6.10	6.15	.94
3	6.10	6.08	.95
4	6.10	6.30	.98
5	6.80	6.60	.97
6	6.80	6.86	.95
7	6.80		
8	8.10	8.09	.94

Peninsular Ranges

Layer Number	Starting Velocity	Final Velocity	Resolution
1	5.50	5.62	.77
2	5.50	5.84	.95
3	6.40	6.25	.99
4	6.40	6.36	1.00
5	6.40	6.57	.99
6	6.40	6.88	.99
7	6.80	7.28	.98
8	7.90	7.37	.98

Sierra Nevada

Layer Number	Starting Velocity	Final Velocity	Resolution
1	3.50	3.86	.45
2	5.80	5.87	.83
3	5.80	6.14	.95
4	6.20	6.42	.98
5	6.20	6.21	.81
6	6.90	6.95	.85
7	6.90		
8	7.90		

Tehachapi Mountains

Layer Number	Starting Velocity	Final Velocity	Resolution
1	5.50	5.69	.25
2	6.10	5.91	.73
3	6.50	6.29	.90
4	6.60	6.39	.97
5	7.05	6.73	.96
6	7.05		
7	7.05		
8	7.90		

Catalina Island

Layer Number	Starting Velocity	Final Velocity	Resolution
1	2.50	2.91	.12
2	5.50	5.67	.77
3	6.20	6.10	.68
4	6.20		
5	6.20		
6	7.80		
7	7.80		
8	7.80		

North Continental Borderland

Layer Number	Starting Velocity	Final Velocity	Resolution
1	5.20	4.43	.06
2	5.20	5.81	.94
3	5.20	5.75	.91
4	6.30	6.31	.98
5	6.30	6.72	.96
6	7.80	7.12	.93
7	7.80	7.98	.96
8	7.80	8.08	.93

South Continental Borderland

Layer Number	Starting Velocity	Final Velocity	Resolution
1	5.20	5.09	.02
2	5.20	5.49	.68
3	5.20	5.92	.81
4	6.30	6.46	.93
5	6.30	6.36	.60
6	8.20	7.98	.81
7	8.20		
8	8.20		

Chapter 7 to 9 References

Allen, C. R., T. C. Hanks, and J. H. Whitcomb (1975). Seismological studies of the San Fernando earthquake and their tectonic implications, in San Fernando, California, earthquake of 9 February 1971, *Bull. Calif. Div. Mines* **196**, 257-262.

Bent, A. L. and D. V. Helmberger (1989). Source complexity of the October 1, 1987, Whittier Narrows earthquake, *J. Geophys. Res.* **94**, 9548-9556.

Biehler, S., R. L. Kovach, and C. R. Allen (1964). Geophysical framework of northern end of Gulf of California, in *Marine geology of the Gulf of California*, T. H. van Andel and G. G. Shor Jr. (Editors), AAPG Memoir 3, 126-143.

Buwalda, J. P. (1940). Geology of the Raymond basin (a report to the Pasadena Water Department).

Colburn, R. H. and W. D. Mooney (1986). Two-dimensional velocity structure along the synclinal axis of the Great Valley, California, *Bull. Seism. Soc. Am.* **76**, 1305-1322.

Corbett, E. J. (1984). Seismicity and crustal structure studies of southern California: Tectonic implications from improved earthquake locations, *Pasadena, California Institute of Technology, Ph. D. thesis*, 231pp.

Corbett, E. J. and C. E. Johnson (1982). The Santa Barbara, California, earthquake of 13 August 1978, *Bull. Seism. Soc. Am.* **72**, 2201-2226.

Crandell, G. J., B. P. Luyendyk, M. S. Reichle, and W. A. Prothero (1983). A marine seismic refraction study of the Santa Barbara channel, California, *Marine Geophys. Res.* **6**, 15-37.

Crook, R., C. Allen, B. Kamb, C. Payne, and R. Proctor (1987). Quaternary geology and seismic hazard of the Sierra Madre and associated faults, western San Gabriel mountains, California, in *Recent reverse faulting in the Transverse Ranges, California, U.S. Geol. Surv. Profess. Paper 1339*, 27-63.

Davis, T. L. (1987). National earthquake hazard reduction program summary of technical reports XXIV, *U.S. Geol. Surv. Open-File Rep. 87-374*, 143-147.

Davis, T. L., J. Namson, and R. F. Yerkes (1989). A cross section of the Los Angeles area: Seismically active fold and thrust belt, the 1987 Whittier Narrows earthquake, and earthquake hazard, *J. Geophys. Res.* **94**, 9644-9664.

Dobrin, M. B. (1976). Introduction to geophysical prospecting, New York, McGraw-Hill.

Duke, C. M., J. A. Johnson, Y. Kharraz, K. W. Campbell, and N. A. Malpiede (1971). Subsurface site conditions and geology in the San Fernando earthquake area, *UCLA-ENG-7206, School of Engineering, UCLA.*

Eaton, J. P., M. E. O'Neill, and J. N. Murdock (1970). Aftershocks of the 1966 Parkfield-Cholame, California, earthquake: A detailed study, *Bull. Seism. Soc. Am.* **60**, 1151-1197.

Eberhart-Phillips, E. (1989). Active faulting and deformation of the Coalinga anticline as interpreted from three-dimensional velocity structure and seismicity, *J. Geophys. Res.* **94**, 15565-15586.

Fuis, G. S., W. D. Mooney, J. H. Healey, G. A. McMechan, and W. J. Lutter (1982). Crustal structure of the Imperial Valley region, in *The Imperial Valley, California, earthquake of October 15, 1979, U.S. Geol. Surv. Profess. Paper 1254*, 25-50.

Given, D. D. and C. L. Koesterer (1983). Station arrival data for a quarry blast on Santa Catalina Island, California, *U.S. Geol. Surv., Open-File Rept. 83-462*, 12pp.

Given, D. D., R. Norris, L. M. Jones, L. K. Hutton, C. E. Johnson, and S. Hartzell (1986). The southern California network bulletin January through June, 1986, *U.S. Geol. Surv., Open-File Rept. 86-598*, 28pp.

Goodman, E. D. and P. E. Malin (1988). Comments on the geology of the

Tejon embayment from available seismic, well, and subsurface data, SEPM San Joaquin basin volume.

Gutenberg, B. (1955). Wave velocities in the earth's crust, in *Crust of the Earth*, A. Poldervaart (Editor), *Geol. Soc. Am. Spec. Paper 62*, 19-34.

Hadley, D. M. (1978). Geophysical investigations of the structure and tectonics of southern California, *Pasadena, California Institute of Technology, Ph. D. thesis*, 167pp.

Hadley, D. and J. Combs (1974). Microearthquake distribution and mechanisms of faulting in the Fontana-San Bernardino area of southern California, *Bull. Seism. Soc. Am.* **64**, 1477-1499.

Hadley, D. and H. Kanamori (1977). Seismic structure of the Transverse Ranges, California, *Geol. Soc. Am. Bull.* **88**, 1469-1478.

Hamilton, R. M. (1970). Time term analysis of explosion data from the vicinity of the Borrego Mountain, California, earthquake of 9 April 1968, *Bull. Seism. Soc. Am.* **60**, 367-381.

Hamilton, R. M. (1972). Aftershocks of the Borrego Mountain earthquake from April 12 to June 12, 1968, in *The Borrego Mountain earthquake of April 9, 1968, U.S. Geol. Surv. Profess. Paper 787*, 31-54.

Hauksson, E. (1987). Seismotectonics of the Newport-Inglewood fault zone in the Los Angeles basin, southern California, *Bull. Seism. Soc. Am.* **77**, 539-561.

Hauksson, E. (1988). Thrust faulting and earthquake potential in the greater Los Angeles basin (abstract), *Eos Trans. AGU* **69** 1305.

Hauksson, E., et al. (1988). The 1987 Whittier Narrows earthquake in the Los Angeles metropolitan area, California, *Science* **239**, 1409-1412.

Hauksson, E. and L. M. Jones (1989). The 1987 Whittier Narrows earthquake sequence in Los Angeles, southern California: seismological and tectonic analysis, *J. Geophys. Res.* **94**, 9569-9590.

Hauksson, E. and G. Saldivar (1986). The 1930 Santa Monica and the 1979 Malibu, California, earthquakes, *Bull. Seism. Soc. Am.* **76**, 1542-1559.

Hauksson, E. and G. Saldivar (1989). Seismicity and active compressional tectonics in Santa Monica Bay, southern California, *J. Geophys. Res.* **94**, 9591-9606.

Hauksson, E. and R. Stein (1989). The 1987 Whittier Narrows, California earthquake: a metropolitan shock, *J. Geophys. Res.* **94**, 9545-9547.

Healy, J. H. (1963). Crustal structure along the coast of California from seismic-refraction measurements, *J. Geophys. Res.* **68**, 5777-5787.

Hearn, T. M. (1985). Crustal structure in southern California from array data, *Pasadena, California Institute of Technology, Ph. D. thesis*, 130pp.

Jackson, D. D. and M. Matsu'ura (1985). A Bayesian approach to nonlinear inversion, *J. Geophys. Res.* **90**, 581-591.

Jones, L. M. and R. S. Dollar (1986). Evidence of basin-and-range extensional tectonics in the Sierra Nevada: The Durrwood Meadows swarm, Tulare county, California (1983-1984), *Bull. Seism. Soc. Am.* **76**, 439-461.

Junger, A. and H. Wagner (1977). Geology of the Santa Monica and San Pedro basins, California continental borderland, *U.S. Geol. Surv. Misc. Field Stud. Map MF-820.*

Kanamori, H. and D. Hadley (1975). Crustal structure and temporal velocity change in southern California, *Pageoph.* **113**, 257-280.

Louie, J. N. (1987). Seismic reflection experiments imaging the physical nature of crustal structures in southern California, *Pasadena, California Institute of Technology, Ph. D. thesis*, 275pp.

Mabey, D. R. (1960). Gravity survey of the western Mojave desert, California, *U.S. Geol. Surv. Profess. Paper 316-D*, 51-73.

McCulloh, T. H. (1960). Gravity variations and the geology of the Los Angeles basin of California, *U.S. Geol. Surv. Profess. Paper 400-B*, 320-

325.

Michelini, A., W. Foxall, and T. McEvilly (1989). The Parkfield monitoring program: joint hypocentral and velocity inversion for three-dimensional structure (abstract), *Seism. Res. Lett.* **60**, 31.

Nava, F. A. and J. N. Brune (1982). An earthquake-explosion reversed refraction line in the Peninsular Ranges of southern California and Baja California Norte, *Bull. Seism. Soc. Am.* **72**, 1195-1206.

Norris, R., C. E. Johnson, L. M. Jones, and L. K. Hutton (1986). The southern California network bulletin, *U.S. Geol. Surv., Open-File Rept. 86-96*, 31pp.

Perkins, G. (1988). Data report for the 1987 seismic calibration/refraction survey, Whittier, California, *U.S. Geol. Surv.*, Menlo Park, California, 29pp.

Reasenberg, P. and D. Oppenheimer (1985). FPFIT, FPPLOT, and FPPAGE: Computer programs for calculating and displaying earthquake fault-plane solutions, *U.S. Geol. Surv., Open-File Rept. 85-739*, 46pp.

Roecker, S. W. (1981). Seismicity and tectonics of the Pamir-Hindu Kush region of central Asia, *Cambridge, Massachusetts Institute of Technology, Ph. D. thesis*, 298pp.

Roecker, S. W. (1982). Velocity structure of the Pamir-Hindu Kush region: Possible evidence of a subducted crust, *J. Geophys. Res.* **87**, 945-959.

Roecker, S. W., Y. H. Yeh, and Y. B. Tsai (1987). Three-dimensional P and S wave velocity structures beneath Taiwan: deep structure beneath an arc-continent collision, *J. Geophys. Res.* **92**, 10547-10570.

Shedlock, K. M. (1986). Structure and tectonics of north China, *Cambridge, Massachusetts Institute of Technology, Ph. D. thesis*, 194pp.

Shedlock, K. M. and S. W. Roecker (1987). Elastic wave velocity structure of the crust and upper mantle beneath the North China basin, *J. Geophys. Res.* **92**, 9327-9350.

Shor, G. G. Jr., and R. W. Raitt (1958). Seismic studies in the southern California continental borderland, *Proc., XX Internat. Geolog. Congress, Mexico*, 243-259.

Stierman, D. J. and W. L. Ellsworth (1976). Aftershocks of the February 21, 1973 Point Mugu, California earthquake, *Bull. Seism. Soc. Am.* **66**, 1931-1952.

Teng, T. L., C. R. Real, and T L. Henyey (1973). Microearthquakes and water flooding in Los Angeles, *Bull. Seism. Soc. Am.* **63**, 859-875.

Tsai, Y. B. (1986). Seismotectonics of Taiwan, *Tectonophysics* **125**, 17-38.

Vidale, J. E. (1987). Application of two-dimensional finite-difference wave simulation to earthquakes, earth structures, and seismic hazard, *Pasadena, California Institute of Technology, Ph. D. thesis*, 150pp.

Vidale, J. E. (1989). Earthquake location using finite-difference travel times in arbitrary velocity structures and an example from Bear Valley (abstract), *Seism. Res. Lett.* **60**, 30.

Walter, A. W. and W. D. Mooney (1982). Crustal structure of the Diablo and Gabilan ranges, central California: A reinterpretation of existing data, *Bull. Seism. Soc. Am.* **72**, 1567-1590.

Whitcomb, J. (1973). The 1971 San Fernando earthquake series focal mechanisms and tectonics, *Pasadena, California Institute of Technology, Ph. D. thesis, Part 2*, 343pp.

Yerkes, R. F., T. H. McCulloh, J. E. Schoellhamer, and J. G. Vedder (1965). Geology of the Los Angeles basin, California - an introduction, *U.S. Geol. Surv. Profess. Paper 420-A*, 1-57.